Anatomy of the B-meson Light-Cone Distribution Amplitude

DISSERTATION
zur Erlangung des akademischen Grades
eines Doktors der Naturwissenschaften

vorgelegt von
M.Sc. Philip Carlo Lüghausen

eingereicht bei der Naturwissenschaftlich-Technischen Fakultät
der Universität Siegen
Siegen 2024

Erster Gutachter

Prof. Dr. Thorsten Feldmann
Universität Siegen

Zweiter Gutachter

Dr. Danny van Dyk
University Durham, United Kingdom

Weitere Mitglieder der Prüfungskommission

Prof. Dr. Markus Cristinziani
Universität Siegen

und

Jun.-Prof. Dr. Stefan Nimmrichter
Universität Siegen

Tag der mündlichen Prüfung

25. Juni 2024

Publications

All work presented in this thesis is the author's own work, unless stated otherwise. This includes content previously published in the following articles:

1. T. Feldmann, P. Lüghausen, and N. Seitz. "Strange-quark mass effects in the B_s meson's light-cone distribution amplitude". In: *JHEP* 08 (2023), p. 075. DOI: 10.1007/JHEP08(2023)075. arXiv: 2306.14686 [hep-ph]
2. T. Feldmann, P. Lüghausen, and D. van Dyk. "Systematic parametrization of the leading B-meson light-cone distribution amplitude". In: *JHEP* 10 (2022), p. 162. DOI: 10.1007/JHEP10(2022)162. arXiv: 2203.15679 [hep-ph]
3. D. van Dyk, P. Lüghausen, et al. "EOS: a software for flavor physics phenomenology". In: *Eur. Phys. J. C* 82.6 (2022), p. 569. DOI: 10.1140/epjc/s10052-022-10177-4. arXiv: 2111.15428 [hep-ph]

The above publications are the result of collaborative scientific work by several authors. In the first and second publications, the author of this thesis contributed to the conceptual development, provided the analytic formulas, performed the numerical studies, and created the figures. For the second publication, the aforementioned contributions were divided equally between N. Seitz and P. Lüghausen. The third publication serves as an overview provided by the developers of the `EOS` software, including the author of this thesis whose contributions to this software include the implementation needed for the analysis in Chapter 4.

The results of Chapter 4 are unpublished at the time of writing this thesis.

Abstract

In the Standard Model of particle physics, the strong dynamics of hadronic particles such as the B meson are governed by Quantum Chromodynamics (QCD). Currently, there exists no single method capable of accurately predicting all phenomena associated with QCD. Rather, various specialized methods have emerged to address specific phenomena. Among these approaches, QCD Factorization and QCD Light-Cone Sum Rules are used for exclusive, energetic B decays. Therein, the B-meson Light-Cone Distributions Amplitudes (LCDAs) systematically represent the internal structure of the B meson, and as such, the LCDAs are (presently) inaccessible from first principles. In this thesis, we develop a new systematic framework for phenomenological analyses, focusing on the leading-twist B-meson LCDA which leads to the dominant contribution in predictions. Our framework allows for the integration of various theoretical and experimental constraints to infer the LCDA and derive predictions. While models have been used for the same purpose, our approach makes systematic uncertainties quantifiable and provides greater transparency in the implementation of constraints.

We derive a new systematic parametrization of the leading-twist B-meson LCDA that fulfills established mathematical properties and satisfies a parameter bound to address the issue of truncation in the expansion. We discuss certain practical aspects, such as renormalization group evolution, the implementation of the known short-distance behavior as a fit constraint, and more. In addition, we update the known short-distance behavior with the effect of a non-zero spectator quark mass to improve the effectiveness of our approach for applications with the B_s meson. For this purpose, we perform a generic matching calculation, which further yields a new result for the short-distance behavior of the subleading 2-particle LCDA. To demonstrate the practical utility of our framework, we perform a detailed analysis of the decay mode $B \to \gamma\ell\nu$, which serves as a benchmark for probing the leading-twist B-meson LCDA. To that end, we extended the `EOS` software with experimental observables of this decay and pseudo-observables to accommodate the theoretical short-distance constraint. This enabled a proof-of-concept study using mock data and the Bayesian analysis tools in `EOS` which underscores the utility of the measurement of this decay mode and further demonstrates the effectiveness of the parameter bound in managing truncation errors. This analysis highlights the significant potential of our approach for future research.

Zusammenfassung

Im Standardmodell der Teilchenphysik werden die starken Wechselwirkungen hadronischer Teilchen wie des B-Mesons durch die Quantenchromodynamik (QCD) bestimmt. Derzeit gibt es keine einzelne Methode, die in der Lage ist, alle mit der QCD verbundenen Phänomene genau vorherzusagen. Vielmehr wurden verschiedene spezialisierte Methoden entwickelt, die sich mit bestimmten Phänomenen befassen. Unter diesen Ansätzen werden die QCD-Faktorisierung und QCD-Lichtkegel-Summenregeln für exklusive energetische B-Zerfälle verwendet. Dabei repräsentieren die Lichtkegel-Distributions-Amplituden (LCDAs) des B-Mesons systematisch seine innere Struktur, und als solche sind die LCDAs (derzeit) nicht von grundlegenden Prinzipien ableitbar. In dieser Arbeit entwickeln wir ein neues systematisches Framework für phänomenologische Analysen, das sich auf die B-Meson-LCDA zu führender Twist-Ordnung konzentriert, welche in Vorhersagen den dominanten Beitrag generiert. Unser Framework ermöglicht die Integration verschiedener theoretischer und experimenteller Informationen, um die LCDA abzuleiten und Vorhersagen zu treffen. Modelle wurden bereits für denselben Zweck verwendet, jedoch macht unser Ansatz systematische Unsicherheiten quantifizierbar und bietet größere Transparenz für die Implementierung bekannter Informationen.

Wir leiten eine neue systematische Parametrisierung der B-Meson-LCDA zu führendem Twist ab, die etablierte mathematische Eigenschaften erfüllt und eine Parameterschranke erfüllt, um Trunkierung der Parameterentwicklung handzuhaben. Wir diskutieren bestimmte praktische Aspekte wie Skalenentwicklung durch die Renormierungsgruppe, Einschränkung der LCDA durch das bekannte Verhalten bei geringer Separation (Kurzstreckenverhalten) und mehr. Darüber hinaus erweitern wir das bekannte Kurzstreckenverhalten mit dem Effekt einer von Null verschiedenen Spectator-Quark-Masse, um die Effektivität unseres Frameworks für Anwendungen mit dem B_s-Meson zu verbessern. Zu diesem Zweck führen wir eine generische Matching-Rechnung durch, die zusätzlich ein neues Ergebnis für das Kurzstreckenverhalten der 2-Teilchen-LCDA zu nachfolgender Twist-Ordnung ergibt. Um den praktischen Nutzen unseres Frameworks zu demonstrieren, führen wir eine detaillierte Analyse des Zerfalls $B \to \gamma\ell\nu$ durch, der als Maßstab für die Untersuchung der führenden B-Meson-LCDA gilt. Dazu haben wir die Software `EOS` um experimentelle Observablen dieses Zerfalls und Pseudo-Observablen entsprechend dem theoretische Kurzstreckenverhalten erweitert. Dies ermöglicht eine Machbarkeitsstudie unter Verwendung von Pseudo-Daten und den Bayes'schen Analysewerkzeugen in `EOS`,

welche den Nutzen der Messung dieses Zerfalls unterstreicht und weiterhin die Wirksamkeit der Parameterschranke zur Handhabung von Trunkierungsfehlern demonstriert. Diese Analyse zeigt das signifikante Potenzial unseres Ansatzes für zukünftige Forschung.

Contents

1. Introduction

In this chapter, we briefly introduce essential concepts used in the main text. The overview covers the elements of the strong interaction, heavy quark effective theory, and the role of the leading B-meson light cone distribution amplitude in theoretical predictions.

The field of theoretical particle physics aims to establish a unified framework capable of explaining a wide range of phenomena at the level of the smallest building blocks of the universe. The Standard Model (SM) of particle physics serves as the cornerstone of this field. It describes three of the four known fundamental forces: the electromagnetic interaction, responsible for keeping electrons within atoms; the weak interaction, responsible for nuclear processes like those powering the sun; and the strong interaction, combining quarks and gluons into protons and neutrons, the building blocks of atomic nuclei. The particles involved in these interactions are the quarks, leptons, and various bosons. Contrary to the short-distance phenomena just mentioned, the SM does not include gravity, a force crucial on the opposite end of the length scales in physics, such as the movement of the planets in the solar system.

The SM is tested up to the current technological limit of several 10^{12} electronvolts of collision energy. This, roughly speaking, corresponds to exploring structures as tiny as 10^{-18} meters. One can imagine to zoom in to a level where molecule structures such as DNA become perfectly visible – except that this zoom is applied twice in succession. The physical reality, however, is more complicated due to quantum effects, as many intuitive concepts such as distance, size, and matter lose their conventional meaning. Although the SM has achieved significant success, it is crucial to continue improving our understanding of particle physics: on the one hand, there are still unanswered conceptual questions, such as the nature of dark matter, the hierarchy problem, and the unification of forces. On the other hand, matching the precision of theory predictions with current experimental observations presents new technical challenges. These challenges include the development and refinement of non-perturbative methods, such as those discussed in this thesis.

1.1. Quarks and Gluons

The SM is a quantum field theory containing 17 particles: 6 quarks, 3 charged leptons, 3 neutrinos, the gluon, photon, Z, and W vector bosons and the scalar Higgs boson. In this

thesis, however, we focus on the sector of quarks and gluons. The six types (*flavors*) of quarks are organized in three *generations*,

$$\begin{pmatrix} u \\ d \end{pmatrix}, \quad \begin{pmatrix} c \\ s \end{pmatrix}, \quad \text{and} \quad \begin{pmatrix} t \\ b \end{pmatrix}, \tag{1.1}$$

which are referred to as *up* and *down*, *charm* and *strange*, and *top* and *bottom* (also called *truth* and *beauty*). The gluon is the force-mediating particle of the strong interaction between quarks and also between gluons among themselves.

Quantum Chromodynamics (QCD) is the quantum field theory that describes the properties and strong interactions of quarks and gluons. One notable characteristic of QCD is that quarks and gluons are never found in isolation; they always exist in composite states involving at least two of these particles. This phenomenon arises from the non-Abelian gauge group, $\mathrm{SU}(3)_c$, which permits renormalizable self-interactions among massless spin-1 particles. As a consequence, the interaction between quarks and gluons becomes stronger as the distance between them increases due to a charge screening effect. Objects with color charge, such as quarks and gluons, are bound together by an attractive potential that prevents them from separating. Consequently, only color-neutral (gauge-invariant) objects exist independently. This standout feature of QCD[1] is known as *confinement*.

Unique, tailored approaches are often a necessity to derive predictions from QCD. In contrast, calculations in other sectors of the SM typically rely on only one method: perturbation theory. This method involves expressing physical observables as a power series of the coupling strength. The efficiency of perturbation theory lies in the ability to truncate the series when the expansion parameter is sufficiently small to result in a satisfactory approximation. However, QCD presents a unique challenge in this regard, because the coupling strength is typically sizable (which is related to confinement). In such cases, non-perturbative approaches come into play, ranging from effective field theories to numerical Lattice simulations, sum rules, and factorization theorems. Commonly, these methods (unlike perturbative ones) must be developed and fined-tuned at hand of the specific process to take best advantage.

1.2. Heavy Quark Effective Theory

Effective theories in physics are an essential concept used to describe physical phenomena at a particular scale or energy range, where certain degrees of freedom or interactions dominate, while the effects at different scales can be sufficiently accounted for using a simplified description. Whether or not a particular effect becomes insignificant, such

[1] Although the symmetry group $\mathrm{SU}(2)_L$ of the weak interaction is also non-Abelian, the Higgs mechanism prevents weak confinement through the effective mass terms of the bosons.

that an effective treatment is warranted, depends on the precision of the experimental observation the theory calculation aims to explain. In many cases, physical mechanisms may become irrelevant altogether; for example, the gravitational attraction between the balls on a Billiard table can be neglected for all practical purposes. In more complicated cases, when the complete underlying theory is unknown or too complex to derive predictions efficiently, effective theories can still be successful.

Heavy Quark Effective Theory (HQET) exploits the case where a quark's mass is much larger than all other energy scales in a system, including $\Lambda_{\text{had}} \approx 1\,\text{GeV}$, the hadronization scale. It applies to hadrons with a single b (or, not discussed here, c) and a light u, d, or s. In contrast, the t is too short-lived (due to its mass, $m_t \approx 40\,m_b$) to form bound states before it decays. Systems with two heavy quarks instead of a single one do not admit the limit since the dynamics depend on the (large) mass in an essential way. Notably, although the B_c with a b and c can be considered a heavy-light quark system to some extent, the sizable ratio $m_c/m_b \approx 1/3$ requires additional attention. New symmetries emerge in the infinite quark mass limit of QCD; HQET formalizes the limit and allows to systematically account for symmetry-breaking effects in terms of a systematic expansion; contributions to each order n in the expansion are power-suppressed, $(k/(2m_Q))^n$, where k is the typical momentum scale and m_Q denotes the heavy quark mass. The expansion's primary advantage is the efficiency in calculating the strong interaction effects between weak processes with heavy quarks on the one side and heavy hadrons on the other.

The following text introduces the formal basics of HQET very briefly. Excellent in-depth discussions can be found in many texts, e.g., Refs. [4–6]. The starting point to derive the effective theory is the QCD Lagrangian,

$$\mathcal{L}_{\text{QCD}} = \bar{Q}(i\not{D} - m_Q)Q + \dots\,, \tag{1.2}$$

where Q denotes the field of a heavy quark and the ellipsis stands for terms with light quarks and gluons, which are irrelevant here. It is convenient to formulate the field theory in terms of a particle field that has its lowest energy level shifted by the mass m_Q, such that it remains constant (i.e., zero) in the infinite mass limit [5]. Formally, this corresponds to an appropriate shift of the field's phase. To that end, we consider a decomposition of the heavy quark momentum p into a "non-relativistic" component characterized by a velocity v and a *residual momentum* k,

$$p^\mu = m_Q\, v^\mu + k^\mu\,, \tag{1.3}$$

where the four vector v satisfies $v^2 = 1$. Additionally, the quark field itself can be decomposed into approximate particle and anti-particle solutions through the projectors $P_\pm = (1 \pm \not{v})/2$ to motivate the following definition:

$$Q(x) \equiv \mathrm{e}^{-im_Q\, v\cdot x}\left(h_v(x) + H_v(x)\right). \tag{1.4}$$

The components correspond to the aforementioned projectors, fulfilling $\not{v} h_v = +h_v$ and $\not{v} H_v = -H_v$. The infinite mass limit is related to $k \to 0$ such that the Dirac equation

becomes $(1 - \not{v})Q = 0$, implying $H_v = 0$; this leaves only the field component h_v as a dynamic degree of freedom of the effective theory. Using the decomposition in Eq. (1.4) in the QCD Lagrangian reveals that h_v has no mass term, whereas H_v has mass $2m_Q$. Beyond the infinite mass limit, one defines HQET by integrating out the heavy field H_v using the path integral formalism [4]. This way, HQET systematically separates the dynamical component of the heavy quark field from the one that becomes static in the limit.

Altogether, the HQET Lagrangian follows from the QCD Lagrangian in Eq. (1.2) after integrating out H_v. The resulting Lagrangian, in terms of h_v, and up to power N in the expansion in m_Q^{-1}, takes the form

$$\begin{aligned} \mathcal{L}_{\text{HQET}}^{(N)} &= \bar{h}_v (iv \cdot D) h_v && (\text{“leading power”}) \\ &\quad + \sum_{n=1}^{N} \left(\frac{1}{2m_Q} \right)^n \bar{h}_v \, O^{(n)} \, h_v \, . && (\text{“power corrections”}) \end{aligned} \tag{1.5}$$

Power-correction terms contain covariant Dirac operators $O^{(n)}$ composed of D^μ and v^μ. To leading power, the Feynman rules in momentum space [6] are given by the effective heavy quark propagator,

$$S(k) = \frac{i}{v \cdot k + i\epsilon} \frac{1 + \not{v}}{2} \, , \tag{1.6}$$

and a vertex coupling two quark fields with a gluon, which amounts to

$$\Gamma_{ij}^{\mu;a} = i g_s v^\mu T_{ij}^a \frac{1 + \not{v}}{2} \, . \tag{1.7}$$

Here, g_s is the strong coupling strength, i and j are the color indices of the quark fields, and μ and a are the Lorentz and color indices of the gluon, respectively. Higher-order terms introduce new interaction vertices with two quark fields and (between zero and $N + 1$) gluon fields.

The heavy quark limit, $m_Q \to \infty$, yields two additional symmetries initially absent in QCD. Experiments show their approximate realization in the mass spectrum of hadrons [5]. The first is *heavy flavor symmetry* because QCD treats the quark flavors identically apart from their masses. In the limit, they are interchangeable without affecting the properties of a hadron emerging as a strong bound state. The second, *spin symmetry*, becomes apparent when formalizing the infinite mass limit of QCD, and it predicts the decoupling of the heavy quark spin from the gluon. Since the heavy quark interacts with the other constituents of the system by gluon exchange, the properties of the hadron become independent of spin. The additional symmetries relate (i.e., restrict) the non-perturbative information needed to understand a variety of heavy-light quark systems.

1.3. B-meson Light-cone Distribution Amplitudes

The light-cone distribution amplitudes (LCDA) of the B meson play a crucial role as hadronic input about the internal structure for theoretical descriptions of exclusive B decays into energetic hadrons and photons. These descriptions rely on factorization theorems in QCD, initially formulated for charmless non-leptonic B-decays [7, 8]. Their applications have since expanded to various decay modes, including semi-leptonic and radiative decays; Ref. [9] provides an overview and extensive references of recent literature. Furthermore, light-cone sum rules (LCSR) offer a complementary method, accessing "soft" hadronic matrix elements when initial and final state factorization is incomplete. Integrating the B-meson LCDA already known from factorization also into LCSR, as proposed in Refs. [10–13], facilitates a unified theoretical description, suitable to be confronted with experimental data. This complementary approach has been employed recently for the benchmark decay mode $B \to \gamma\ell\nu$ [14–16], where data is anticipated from the Belle-II experiment [17].

Among the LCDAs, the leading-twist LCDA is the phenomenologically most important one, while the subleading-twist LCDAs are relevant for the improvement of accuracy (cf. Chapter 4). In this work, we aim to establish a new analysis framework, which at this stage is mostly focused on the leading-twist LCDA. In the following, we often refer to this LCDA without specifying the twist.

There are several sources of information about the LCDA. The two theoretical approaches for decay predictions systematically probe different aspects, expressed as weighted integrals of the LCDA's momentum-space representation:

1. QCD factorization features "logarithmic moments", i.e., integrals weighted by powers of logarithms over the entire domain.

2. The LCSR approach depends on weighted integrals over a finite domain of small light-cone momenta.

We defer the quantities' definitions to the main text. On purely theoretical grounds, one can constrain another aspect of the LCDA:

3. The local operator product expansion (OPE) yields the short-distance behavior for the position-space representation of the LCDA at small but finite distances.

This short-distance behavior can be calculated in terms of perturbative coefficients and a set of hadronic parameters. The behavior in position space at short distance is also manifest in momentum space in the regime of large light-cone momenta, where the term "radiative tail" (or "radiation tail") became established jargon.

A detailed discussion of the properties and applications of the LCDA follows in the main text. The objective of this thesis is the development of a tailored approach for the LCDA that combines all available information in a consistent and transparent way.

1.4. Thesis Outline

After the brief introduction presented in this chapter, we will proceed with a detailed discussion in the following chapters. Each chapter represents a comprehensive research project, with each subsequent chapter building on the previous one(s). Except for the final chapter, our considerations include the B_s meson (and to some extent the B_c meson), distinguished by a considerable spectator quark mass.

In Chapter 2, we propose a systematic parametrization for the leading-twist B-meson LCDA, starting with a detailed review of the LCDA's theoretical properties and applications. On that basis, we construct a suitable parametrization with a parameter bound to handle truncation. We examine practical aspects such as the parameter expansions of various quantities and the handling of renormalization group evolution. Testing the parametrization at the hand of several models for the LCDA demonstrates its flexibility and provides heuristic benchmarks for convergence. In a "pseudo-phenomenological" study, we aim to understand the impact of constraints from the short-distance behavior in a global fit.

Chapter 3 is devoted to the short-distance behavior accessed through the operator product expansion (OPE). In particular, we are interested in the effect of the finite spectator quark mass for the case of the B_s meson, previously unconsidered in the literature. To that end, we detail an efficient approach for the matching calculation in position space based on Feynman integrals in momentum space. We derive results up to dimension 4 in the OPE for the leading-twist 2-particle LCDA ϕ_+ and the subleading 2-particle LCDA ϕ_-. Using the "pseudo-phenomenological" setup once more, we estimate the impact of the spectator quark mass, comparing our results with independent results obtained using QCD sum rule estimates. Finally, we look into the potential impact of dimension-5 operators.

Chapter 4 confronts the theoretical considerations with experimental observables from the benchmark decay mode $B \to \gamma\ell\nu$. We review the theoretical understanding of the decay amplitude using QCD factorization, complemented with subleading power corrections accessible via QCD sum rules. We express the decay amplitude through the systematic parametrization, detailing computational methods to streamline this process. After briefly describing the implementation work performed as part of this thesis for the publicly available open-source software `EOS`, we demonstrate how our parametrization can combine theoretical and experimental information in a global analysis using a statistically sophisticated Bayesian framework.

Each chapter is prefaced with a more detailed content overview for the reader's convenience.

2. Systematic Parametrization of the Leading B-meson Light-cone Distribution Amplitude

The main results in this chapter and Appendix A have been published in

> T. Feldmann, P. Lüghausen, and D. van Dyk. "Systematic parametrization of the leading B-meson light-cone distribution amplitude". In: *JHEP* 10 (2022), p. 162. DOI: 10.1007/JHEP10(2022)162. arXiv: 2203.15679 [hep-ph].

Existing analyses involving the B-meson LCDAs have so far relied on models. Model-based analyses are subject to theory bias and unwarranted correlations between the concrete quantities entering the physical description, which ultimately results in unquantifiable uncertainties. A key development of this thesis is a suitable parametrization for the leading-twist LCDA which makes systematic uncertainties quantifiable and incorporates as much model-independent theoretical information as possible.

We derive this systematic parametrization for the LCDA within the framework of heavy-quark effective theory (HQET). In position space, the approach uses a conformal transformation, facilitating a Taylor expansion and an integral bound. This setup effectively provides control over the truncation error. Furthermore, the parametrization yields compact analytical expressions for various derived quantities. At a specified reference scale, the momentum-space representation corresponds to an expansion in associated Laguerre polynomials, which transform into confluent hypergeometric functions ${}_1F_1$ under renormalization-group evolution at 1-loop level. This approach allows to transparently incorporate a range of phenomenological constraints, regardless of their origin. For instance, we can impose theoretical constraints on the expansion coefficients from the short-distance behavior obtained from the local operator product expansion (see also Chapter 3). We demonstrate the feasibility of a consistent global analysis based on inputs of both phenomenological and theoretical origin (see also Chapter 4 for a more rigorous analysis based partially on mock data in lieu of upcoming measurements).

This chapter is organized as follows: in Section 2.1, we present a comprehensive overview of the leading-twist B-meson light-cone distribution amplitude, establishing the notation for the purposes of this chapter. In particular, we discuss the analytical properties of the

LCDA, renormalization at the 1-loop level, logarithmic moments, and we define quantities that characterize the low-momentum behavior.

In Section 2.2, we derive a novel parametrization of the leading-twist B-meson LCDA in position space, $\tilde{\phi}_+(\tau)$. After applying a conformal transformation from τ to y, mapping the real τ axis onto the unit circle in the complex y-plane, we perform a Taylor expansion in y. The coefficients of this expansion adhere to an integral bound, crucial to manage truncation. We translate the parametrization to the so-called dual space and momentum space, where it is expressed through expansions in associated Laguerre polynomials. We further elaborate on the computation of logarithmic moments, the incorporation of renormalization group evolution effects, and the adaptation of our framework to higher-twist LCDAs within the Wandzura-Wilczek approximation.

In Section 2.3, we test the versatility of our expansion by analyzing its convergence in four different, representative models from existing literature, showcasing the efficacy of our approach.

In Section 2.4, as a first consistency study, we perform a series of rudimentary pseudo-fits related to the photo-leptonic $B \to \gamma\ell\nu$ decay. The study aims to demonstrate how the parametrization facilitates the simultaneous integration of both theoretical and experimental information in global analyses, without discussing the intricacies of a more sophisticated statistical approach.

In Section 2.5, we summarize our findings and their implications. For ease of reference and further detail, additional formulas are provided Appendix A.

2.1. Preliminaries

The leading-twist 2-particle LCDA of the B-meson is defined as the matrix element of a light-ray operator within HQET. We adopt a definition that uses a normalization against the matrix element of the corresponding local operator, as in Ref. [18]:

$$\tilde{\phi}_+(\tau;\mu) = \frac{\langle 0|\bar{q}(\tau n)\,[\tau n, 0]\,\not{n}\gamma_5\, h_v(0)|B(v)\rangle}{\langle 0|\bar{q}(0)\,\not{n}\gamma_5\, h_v(0)|B(v)\rangle}\,. \tag{2.1}$$

We refer to this function as the "position-space representation" of the LCDA as the argument τ parametrizes the separation between the coordinate arguments of the quark fields. Here, the vector n^μ is defined as light-like, $n^2 = 0$, and the gauge link denoted as $[\tau n, 0]$ represents a straight Wilson line that ensures the gauge invariance of the LCDA. The B meson is characterized by its velocity v^μ, and we simplify our considerations by working in a frame where $v \cdot n = 1$. The LCDA further depends on the renormalization scale μ, which compensates the scale dependence of the perturbative components in the theoretical descriptions of scale-independent observables. Notably, in the HQET framework,

the limit $m_b \to \infty$ has been applied as a fundamental step, such that $\tilde{\phi}_+$ is independent of the heavy-quark mass m_b. Physical amplitudes, in contrast, still acquire an explicit heavy-quark mass dependence due to short-distance functions, which enter as multipliers to the LCDA. This is the case, for example, in the context of QCD factorization calculations. We finally point out that the notion of twist of light-ray operators, as previously established in QCD, has to be modified in HQET (see, for example, Ref. [19]).

2.1.1. Mathematical Properties

We collect the mathematical properties of the position-space LCDA, here denoted as **P1**, **P2** and **P3**, which are discussed in the literature (e.g., in Ref. [20]):

P1: $\tilde{\phi}_+(\tau)$ is analytic in the lower half of the complex plane, $\mathrm{Im}\,\tau < 0$.

P2: $\tilde{\phi}_+(\tau)$ is analytic on the real axis, $\tau \in \mathbb{R}$, except for a single point $\tau = 0$ where it has a logarithmic singularity of measure zero. A branch cut extends from this singular point along the positive direction of the imaginary axis. Therefore $\tilde{\phi}_+(\tau)$ is Lebesgue-integrable with

$$\lim_{\epsilon\to 0^+} \int_{-\infty-i\epsilon}^{\infty-i\epsilon} \mathrm{d}\tau\, \tilde{\phi}_+(\tau,\mu) = 0\,. \tag{2.2}$$

P3: $\tilde{\phi}_+(\tau)$ can be analytically continued from the lower half of the complex plane onto the real τ axis *almost everywhere* (i.e., in all points except for a null set).

We further assume that the Fourier transform exists,

$$\phi_+(\omega;\mu) = \int_{-\infty-i\epsilon}^{\infty-i\epsilon} \frac{\mathrm{d}\tau}{2\pi}\, \mathrm{e}^{i\omega\tau}\, \tilde{\phi}_+(\tau;\mu)\,, \tag{2.3}$$

which we call momentum-space representation of the LCDA. The integration contour lies below the singularities of $\tilde{\phi}_+$ which are located in the upper-half plane. The positions of singularities in the complex τ imply that $\phi_+(\omega)$ vanishes for $\omega < 0$ [18, 21]. It follows from the properties **P1** to **P3** and the Paley-Wiener theorem [22, Theorem 7.2.4] that $\tilde{\phi}_+(\tau)$ is the holomorphic Fourier transform of $\phi_+(\omega)$,

$$\tilde{\phi}_+(\tau;\mu) = \int_0^\infty \mathrm{d}\omega\, \mathrm{e}^{-i\omega\tau}\, \phi_+(\omega;\mu)\,, \tag{2.4}$$

and that ϕ_+ is square-integrable, $\phi_+(\omega) \in L^2$, on the support $[0,\infty)$. By extension, according to Plancherel's theorem, the two-norm of the position-space LCDA exists and

is equal to the two-norm in momentum space. Thus, the inner product exists in both representations:

$$\int_{-\infty}^{\infty} \frac{\mathrm{d}\tau}{2\pi} \left|\tilde{\phi}_+(\tau)\right|^2 = \int_0^{\infty} \mathrm{d}\omega \left|\phi_+(\omega)\right|^2 < \infty \,. \tag{2.5}$$

We further assume the LCDA tends to zero linearly, $\phi_+(\omega;\mu) \sim \omega$, in the limit $\omega \to 0$ at large renormalization scales $\mu \gg \Lambda_{\mathrm{had}}$. An analysis of the renormalization group equation at the 1-loop level shows that the scaling of the LCDA at the origin becomes linear as it evolves to a larger scale [21]. This outcome of RG evolution is independent of how the LCDA behaves at a lower scale. Sum-rule inspired arguments imply the same asymptotic behavior [18, 19]. Translating this behavior to position space through consideration of the Fourier transform leads to the following additional property:

P4: The position-space LCDA falls off asymptotically at least as fast as $1/\tau^2$, i.e.

$$0 \leq \lim_{\tau\to\infty} \left|\tau^2\, \tilde{\phi}(\tau)\right| < \infty \,. \tag{2.6}$$

2.1.2. Renormalization and Eigenfunctions

The B-meson LCDA $\phi_+(\omega)$ can be represented in terms of a continuous set of eigenfunctions of the 1-loop renormalization-group equation, specifically through the Bessel functions of the first kind, J_1 [23, 24]. We call this the "dual-space representation"[1], in addition to the position- and momentum-space representations, which is convenient because of the simple multiplicative solution of its RGE. Here, we adopt the convention used in Ref. [24]:

$$\begin{aligned} \phi_+(\omega;\mu) &= \int_0^{\infty} \mathrm{d}s\, \sqrt{\omega s}\, J_1(2\sqrt{\omega s})\, \eta_+(s;\mu) \\ \Leftrightarrow \qquad s\,\eta_+(s;\mu) &= \int_0^{\infty} \frac{\mathrm{d}\omega}{\omega}\, \sqrt{\omega s}\, J_1(2\sqrt{\omega s})\, \phi_+(\omega;\mu) \,. \end{aligned} \tag{2.7}$$

We note that the corresponding definition of $\rho_+(\omega')$ in Ref. [23], fulfilling the same purpose, is related to the above definition as follows:

$$s\,\eta_+(s;\mu) = \rho_+(\omega' = 1/s;\mu) \,. \tag{2.8}$$

The relation between the LCDA in dual space and position space reads [23]

$$\begin{aligned} s\,\eta_+(s;\mu) &= \int_{-\infty-i\epsilon}^{\infty-i\epsilon} \frac{\mathrm{d}\tau}{2\pi} \left(1 - \mathrm{e}^{-is/\tau}\right) \tilde{\phi}_+(\tau;\mu) \\ \Leftrightarrow \quad \tilde{\phi}_+(\tau;\mu) &= -\frac{1}{\tau^2} \int_0^{\infty} \mathrm{d}s\, \mathrm{e}^{is/\tau}\, s\,\eta_+(s;\mu) \,. \end{aligned} \tag{2.9}$$

[1] The term "spectral function" is also used in the literature due to the notion of a continuous set of eigenfunctions.

The multiplicative RG equation of $\eta_+(s)$ at the 1-loop level,

$$\frac{\mathrm{d}\eta_+(s;\mu)}{\mathrm{d}\ln\mu} = -\left[\Gamma_{\mathrm{c}}(\alpha_s(\mu))\,\ln\left(\mu\, s\,\mathrm{e}^{2\gamma_E}\right) + \gamma_+(\alpha_s(\mu))\right]\eta_+(s;\mu)\,, \tag{2.10}$$

has the following explicit solution:

$$\eta_+(s;\mu) = \mathrm{e}^{V(\mu;\mu_0)}\,\eta_+(s;\mu_0)\,\left(\hat{\mu}_0\, s\right)^{-g(\mu;\mu_0)}\,. \tag{2.11}$$

Here and in the following, we use the convenient short-hand notation

$$\hat{\mu} \equiv \mu\,\mathrm{e}^{2\gamma_E}\,, \tag{2.12}$$

and similar for other quantities. We use the same definitions of the functions $V(\mu;\mu_0)$ and $g(\mu;\mu_0)$ as used, e.g., in Ref. [23]. We give their explicit expressions in Eq. (A.1) and Eq. (A.2), and, for convenience, we quote their RG equations here:

$$\frac{\mathrm{d}V(\mu,\mu_0)}{\mathrm{d}\ln\mu} = -\left[\Gamma_{\mathrm{c}}(\alpha_s(\mu))\,\ln\left(\frac{\mu}{\mu_0}\right) + \gamma_+(\alpha_s(\mu))\right]\,, \qquad \frac{\mathrm{d}g(\mu,\mu_0)}{\mathrm{d}\ln\mu} = \Gamma_{\mathrm{c}}(\alpha_s(\mu))\,. \tag{2.13}$$

Notice that the dual-space LCDA no longer renormalizes multiplicatively at 2-loop order, demonstrated explicitly in Ref. [25].

2.1.3. Logarithmic Moments and Generating Function

In QCD factorization theorems for exclusive B-meson decays [7, 8] the B-meson LCDA enters in terms of so-called logarithmic moments. It is convenient to define these moments directly from the dual-space representation [23, 26]. In the following, we use the convention

$$L_n(\mu,\mu_m) = (-1)^n \int_0^\infty \mathrm{d}s\,\ln^n(\hat{\mu}_m s)\,\eta_+(s;\mu)\,, \tag{2.14}$$

where L_0 is commonly called the zeroth logarithmic moment, λ_B^{-1}. We emphasize that in defining the logarithmic moments L_n with $n \geq 1$, we consider an arbitrary fixed reference scale μ_m. Alternative definitions in the literature use the renormalization scale μ or the inverse zeroth logarithmic moment λ_B, which present special cases of our more general definition. The Mellin transform of $\eta_+(s)$,

$$F_{[\eta_+]}(t;\mu,\mu_m) \equiv \int_0^\infty \mathrm{d}s\,(\hat{\mu}_m s)^{-t}\;\eta_+(s;\mu) \tag{2.15}$$

generates the moments L_n as the coefficients of its Taylor expansion at $t = 0$:

$$L_n(\mu,\mu_m) = \left(\frac{\mathrm{d}}{\mathrm{d}t}\right)^n F_{[\eta_+]}(t;\mu,\mu_m)\Big|_{t=0}\,. \tag{2.16}$$

We analogously define the generating function of the logarithmic moments of the momentum-space LCDA as

$$G_{[\phi_+]}(t;\mu,\mu_m) = \int_0^\infty \frac{\mathrm{d}\omega}{\omega} \left(\frac{\mu_m}{\omega}\right)^{-t} \phi_+(\omega;\mu)\,, \tag{2.17}$$

which is related to its pendant in dual space via the relation

$$\begin{aligned} G_{[\phi_+]}(t;\mu,\mu_m) &= \frac{\Gamma(1+t)}{\Gamma(1-t)}\,\mathrm{e}^{2\gamma_E\,t}\,F_{[\eta_+]}(t;\mu,\mu_m) \\ &= F_{[\eta_+]}(t;\mu,\mu_m)\left(1+\mathcal{O}(t^3)\right)\,, \quad (t<1)\,. \end{aligned} \tag{2.18}$$

The logarithmic moments of η_+ and ϕ_+ are equal for $n = 0, 1, 2$. The function $G_{[\phi_+]}$ already appeared in the analysis of the RG equation for $\phi_+(\omega;\mu)$ [21]. It is further helpful to solve the 2-loop RGE, as shown in Ref. [27], where they refer to it as the Laplace transform of the LCDA. In the following text, we regularly omit the argument μ_m in the logarithmic moments and their generating functionals for brevity. The position-space LCDA yields the logarithmic moments as weighted integrals over the negative imaginary axis. The generating function translates to [28]

$$\int_0^\infty \frac{\mathrm{d}\omega}{\omega} \left(\frac{\mu_m}{\omega}\right)^{-t} \phi_+(\omega,\mu) = \frac{\mathrm{e}^{\gamma_\mathrm{E} t}}{\Gamma(1-t)} \int_0^\infty \mathrm{d}\tau\,(\tau\mu_m\,\mathrm{e}^{\gamma_\mathrm{E}})^{-t}\;\tilde{\phi}_+(-i\tau,\mu)\,. \tag{2.19}$$

The logarithmic moments L_n obey simple coupled RG equations at 1-loop order (see also Ref. [23]),

$$\frac{\mathrm{d}L_n(\mu,\mu_m)}{\mathrm{d}\ln\mu} = \Gamma_\mathrm{c}(\mu)\,L_{n+1}(\mu,\mu_m) - \Gamma_\mathrm{c}(\mu)\,\ln\frac{\mu}{\mu_m}\,L_n(\mu,\mu_m) - \gamma_+(\mu)\,L_n(\mu,\mu_m)\,. \tag{2.20}$$

The equation simplifies in the particular case $\mu_m = \mu_0$, where the solution reads

$$L_n(\mu,\mu_0) = \mathrm{e}^{V(\mu,\mu_0)} \sum_{k=0}^\infty \frac{[g(\mu,\mu_0)]^k}{k!}\,L_{n+k}(\mu_0,\mu_0)\,. \tag{2.21}$$

The general result for an arbitrary μ_m is given by

$$\begin{aligned} L_n(\mu,\mu_m) &= \sum_{i=0}^n \binom{n}{i} L_i(\mu,\mu_0)\,\left(\ln\frac{\mu_0}{\mu_m}\right)^{n-i} \\ &= \mathrm{e}^{V(\mu,\mu_0)}\,\left(\frac{\mu_0}{\mu_m}\right)^{-g(\mu,\mu_0)} \sum_{k=0}^\infty \frac{[g(\mu,\mu_0)]^k}{k!}\,L_{n+k}(\mu_0,\mu_m)\,. \end{aligned} \tag{2.22}$$

The generating function $F[\eta_+](t;\mu,\mu_m)$ is especially convenient because of the simple scale dependence that follows from Eq. (2.11),

$$F_{[\eta_+]}(t;\mu,\mu_m) = \mathrm{e}^{V(\mu;\mu_0)}\,\left(\frac{\mu_0}{\mu_m}\right)^{-g(\mu;\mu_0)} F_{[\eta_+]}(t+g(\mu;\mu_0);\mu_0,\mu_m)\,. \tag{2.23}$$

The corresponding RG equation reads

$$\frac{\partial F_{[\eta_+]}(t;\mu)}{\partial \ln \mu} = -\left(\gamma_+(\mu) + \Gamma_c(\mu)\,\ln\frac{\mu}{\mu_m}\right) F_{[\eta_+]}(t;\mu) + \Gamma_c(\mu)\,\frac{\partial F_{[\eta_+]}(t;\mu)}{\partial t}\,. \tag{2.24}$$

We note that also the 2-loop RG equation for $G_{[\phi_+]}$ is available in the recent literature [27], which easily can be translated to $F_{[\eta_+]}$ via Eq. (2.18).

2.1.4. Behavior at Small Momentum

Theoretical calculations based on the light-cone sum rules approach with B-meson LCDAs [10–13] require information about the low-momentum regime, $\omega \leq s_0/2E$. Here, s_0 is the effective threshold parameter in the hadronic model for the spectral density under consideration, and E is the large recoil energy of the physical process. In such applications, we may expand the LCDA around $\omega = 0$, in terms of its n^{th} derivatives, assuming they exist. This is complementary to the QCD factorization approach, where the theoretical description depends on the logarithmic moments $L_n(\mu)$ instead. The derivatives at the origin and the generating function of the logarithmic moments $F_{[\eta_+]}(t)$ are related as

$$\phi_+^{(n)}(0;\mu) = \frac{(-1)^{n+1}}{\Gamma(n)}\int_0^\infty \mathrm{d}s\, s^n\, \eta_+(s;\mu) = -\frac{(-\hat{\mu}_m)^{-n}}{\Gamma(n)}\, F_{[\eta_+]}(-n;\mu)\,. \tag{2.25}$$

While the derivatives can be represented using the generating function, it is essential to emphasize that the $\phi_+^{(n)}(0)$ values probe the function $F_{[\eta_+]}$ at specific finite (discrete) points, namely at $t = -n$ where $n > 0$. On the other hand, the logarithmic moments L_n probe the expansion coefficients of the function $F_{[\eta_+]}$ at $t = 0$. This distinction leads to a crucial point: the techniques of light-cone sum rules and QCD factorization calculations are sensitive to different aspects of the underlying LCDA $\phi_+(\omega)$, which renders the interpolation of information extracted from those two approaches non-trivial.

To investigate the low-momentum behavior, we propose the "normalized Laplace transform"[2] as the benchmark quantity:

$$\frac{\mathcal{L}[\phi_+](\zeta,\mu)}{\mathcal{L}[\omega](\zeta)} \equiv \frac{\int_0^\infty \mathrm{d}\omega\, \mathrm{e}^{-\zeta\omega}\,\phi_+(\omega,\mu)}{\int_0^\infty \mathrm{d}\omega\, \mathrm{e}^{-\zeta\omega}\,\omega} = \zeta^2\,\tilde{\phi}_+(-i\zeta,\mu)\,. \tag{2.26}$$

The advantage of this quantity is that, in the limit $\zeta \to \infty$, it results in $\phi_+^{(1)}(0;\mu)$[3], but in case the derivative does not exist, it can also probe the regime of small (but non-vanishing) values of ω using large (but finite) values of ζ.

[2] Our use of the term differs to Ref. [27], where it corresponds to our generating function in Eq. (2.17).
[3] To show this, one has to apply partial integration twice.

2.2. Parametrization of the B-meson LCDA

We propose a novel parametrization of the leading-twist B-meson LCDA that satisfies the general properties listed in Section 2.1. While the expansion in terms of any complete set of basis functions is valid as long all orders are taken into account, it is crucial for practical applications to ensure rapid convergence of the series. A bounding condition for the parameters that controls the truncation error is needed to justify taking only a finite number of parameters into account. Such a condition in terms of a set of expansion parameters $\{a_k \,|\, k = 0, 1, \ldots\}$ takes the form

$$\sum_{k=0}^{\infty} |a_k|^2 < \infty \,. \tag{2.27}$$

With this goal in mind, we start with a functional $\chi[r]$ defined as a weighted integral of the position-space LCDA,

$$\chi[r](\mu) \equiv \int_{-\infty}^{\infty} \frac{\mathrm{d}\tau}{2\pi} \left|\tilde{\phi}_+(\tau;\mu)\right|^2 |r(\tau;\mu)|^2 \,, \tag{2.28}$$

where $r(\tau;\mu)$ is a complex-valued weight function to ensure that the integral is finite. In the following, we construct a set of basis functions and choose a weight function such that the above equation poses a suitable bounding condition.

To express the problem in mathematically well-understood terms, we use a conformal map to transform the dimensionful integration variable $\tau \in \mathbb{R}$ to a dimensionless variable y on the complex unit circle:

$$\tau \mapsto y(\tau) \equiv \frac{i\omega_0\tau - 1}{i\omega_0\tau + 1} \qquad \Leftrightarrow \qquad i\omega_0\tau(y) = \frac{1+y}{1-y} \,. \tag{2.29}$$

Here, we introduce an auxiliary parameter ω_0 as a reference scale of the dimensionless variable. This step is not a mere technicality: the introduction of a reference scale is essential to encode physical information using a set of numbers. The variable transform, visualized in Fig. 2.1, features the following properties:

- The point $\tau = 0$ is mapped to $y(0) = -1$.
- The points at $|\tau| \to \infty$ are mapped to $\lim_{|\tau|\to\infty} y(\tau) = +1$.
- The real τ axis is mapped to the unit circle, $|y(\tau)| = 1$, in the complex plane.
- The lower half of the complex plane, $\mathrm{Im}\,\tau < 0$, is mapped onto the open unit disk, $|y| < 1$.

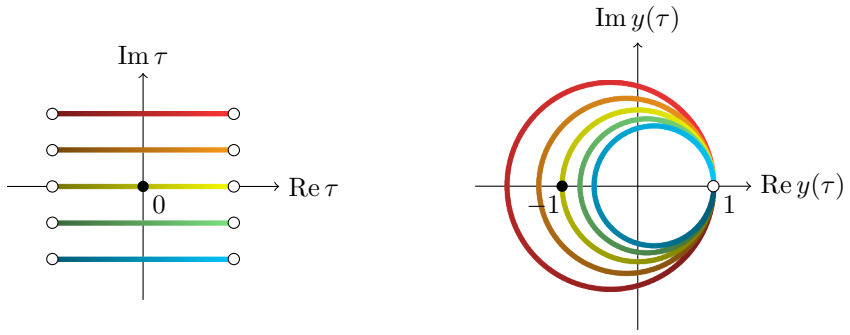

(a) Color-marked domain of τ **(b)** Image in the $y(\tau)$-plane

Figure 2.1.: Visualization of the variable transform $\tau \mapsto y(\tau)$, with τ in units of $1/\omega_0$. The hollow small circles in the left sketch represent points at $\mathrm{Re}\,\tau \to \pm\infty$. The small circles and colored lines correspond to each other in both sketches.

Applying the change of variable to the integral in Eq. (2.28) maps the integration domain onto the boundary of the unit disc, ∂D, which we parametrize using an exponential function:

$$\begin{aligned}\chi[r] &= \oint_{\partial D} \frac{\mathrm{d}y}{2\pi} \left|\tilde{\phi}_+(\tau(y))\right|^2 |r(\tau(y))|^2\, J(\tau(y)) \\ &= \int_{-\pi}^{\pi} \frac{\mathrm{d}\theta}{2\pi} \left|\tilde{\phi}_+(\tau(y))\right|^2 |r(\tau(y))|^2\, (-iy)\, J(\tau(y))\Big|_{y=\mathrm{e}^{i\theta}} .\end{aligned} \tag{2.30}$$

In the above, we denote $\theta = \arg(y)$, and we suppress the argument μ for legibility. The Jacobian $-iyJ$ of the chain of variable transforms amounts to

$$-iy\, J(\tau(y)) = -iy \frac{\mathrm{d}\tau}{\mathrm{d}y} = -\frac{2y}{\omega_0\,(1-y)^2} = \frac{1+\omega_0^2\tau^2}{2\omega_0} . \tag{2.31}$$

Factorizing the LCDA as

$$\tilde{\phi}_+(\tau) \equiv \frac{f_+(y(\tau))}{r(\tau)\,(1+i\omega_0\tau)} , \qquad \tilde{\phi}_+^*(\tau) = \frac{f_+^*(y^*(\tau))}{r^*(\tau)\,(1-i\omega_0\tau)} \tag{2.32}$$

simplifies the expression in Eq. (2.28),

$$\chi = \frac{1}{2\omega_0} \int_{-\pi}^{\pi} \frac{\mathrm{d}\theta}{2\pi}\, |f_+(y)|^2 \Big|_{y=\mathrm{e}^{i\theta}} . \tag{2.33}$$

Expanding f_+ in terms of so-called "orthogonal polynomials on the unit circle" yields the desired form of a bound given in Eq. (2.27). The form above shows similarity to the parametrization of hadronic form factors with unitarity bounds (see, e.g., Ref. [29]). We achieve the bounding condition by expanding in monomials with positive powers, $\{y^n \,|\, n = 0, 1, \ldots\}$. Negative powers of y are excluded from the parametrization of $\tilde{\phi}_+$, as

they induce singularities on the open unit disk and thus violate **P1**. The same holds for positive powers of the complex conjugate y^*. In formal terms, the Taylor expansion of the function $f_+(y)$ corresponds to the Fourier series

$$f_+(y) \equiv \sum_{k=0}^{\infty} a_k\, y^k\,, \qquad f_+(y)\big|_{y=\mathrm{e}^{i\theta}} = \sum_{k=0}^{\infty} a_k\, \mathrm{e}^{i\theta k} \tag{2.34}$$

which yields

$$\chi[r] = \frac{1}{2\omega_0} \sum_{k=0}^{\infty} |a_k|^2\,. \tag{2.35}$$

Since χ is finite, the sequence $\{a_k\}$ is an element of the ℓ^2 space of sequences and must fall off faster than $\sqrt{1/k}$ as $k \to \infty$. This implies the expansion can be truncated at some value $k = K$ while the truncation error is controlled by the parameter bound $2\omega_0\chi$. In particular, when the parameters used for truncation result in a higher level of saturation of the bound, it indicates that the approximation provided by the truncated parameterization is more accurate, because the maximum allowed magnitude of each omitted parameter is monotonously becoming smaller with growing truncation level K. In contrast to the unitarity bounds for hadronic form factors, however, we presently do not know the value of the parameter bound for the LCDA.

Up to this point, we did not assume a specific weight function. Generally, we find that $\chi[r]$ is finite as long as[4]

- $|\lim_{\tau\to\infty} r(\tau;\mu)/\tau| < \infty$, by **P4**; and
- $r(\tau;\mu)$ is regular as $\tau \to 0$, by **P2**.

These conditions alone do not uniquely determine the weight function. While the concrete choice is arbitrary for the entire infinite series, it is critical for the convergence rate of the truncated parametrization.

We select a weight function which is in line with the analyticity requirements of $\tilde{\phi}_+(\tau)$ and that leads to at least a $1/\tau^2$ suppression of $\tilde{\phi}_+(\tau)$ for $|\tau| \to \infty$ (see **P4**),

$$r(\tau;\mu_0) \equiv 1 + i\omega_0\tau\,, \tag{2.36}$$

at a *fixed* reference scale μ_0 for which we require that $\mu_0/\omega_0 \sim \mathcal{O}(1)$. With this, we obtain the following parametrization of the B-meson LCDA in position space,

$$\begin{aligned} \tilde{\phi}_+(\tau;\mu_0) &= \frac{(1-y(\tau))^2}{4} \sum_{k=0}^{K} a_k(\mu_0)\,(y(\tau))^k \\ &= \frac{1}{(1+i\omega_0\tau)^2} \sum_{k=0}^{K} a_k(\mu_0) \left(\frac{i\omega_0\tau - 1}{i\omega_0\tau + 1}\right)^k\,, \end{aligned} \tag{2.37}$$

[4] It is sufficient that $r(\tau;\mu)$ diverges slower than $1/\sqrt{\tau}$ for $\tau \to 0$, i.e., $\lim_{\tau\to 0} \sqrt{\tau}\, r(\tau) = 0$.

which corresponds to an expansion in the point $\tau = -i/\omega_0$. On the one hand, our choice yields simple analytical expressions not only in position space but also in the other relevant representations. On the other hand, one can view this expansion as a systematic extension of the popular phenomenological model proposed in Ref. [18]. For details, see Section 2.3.1. Assuming this model provides a good approximation, one expects numerically small values of the higher-order parameters; data analysis can test this assumption and, most importantly, give quantitative insight into how to improve the simple picture.

The central result of this chapter is the parametrization provided in Eq. (2.37). In the following sections, we develop various useful applications of it, for example, how to (efficiently) account for renormalization group evolution.

2.2.1. Dual-space LCDA and Logarithmic Moments

The dual-space representation of our parametrization follows from the transformation in Eq. (2.9) of the position-space form in Eq. (2.37) as

$$\eta_+(s;\mu_0) = \mathrm{e}^{-s\omega_0} \sum_{k=0}^{K} \frac{(-1)^k\, a_k(\mu_0)}{1+k}\, L_k^{(1)}(2\omega_0 s)\,, \tag{2.38}$$

where $L_k^{(1)}$ denote the associated Laguerre polynomials. We use the orthogonality relations of the polynomials to derive the following integral relation to extract the expansion coefficient a_k for a given η_+:

$$a_k(\mu_0) = 4\,(-1)^k\,\omega_0 \int_0^\infty \mathrm{d}s\,(\omega_0 s)\,\mathrm{e}^{-s\omega_0}\, L_k^{(1)}(2\omega_0 s)\,\eta_+(s;\mu_0)\,. \tag{2.39}$$

The expression for the integral χ in terms of the dual-space LCDA reads

$$\begin{aligned} 2\omega_0\,\chi[r](\mu_0) = \sum_{k=0}^{K} |a_k|^2 &= 2\omega_0 \int_0^\infty \mathrm{d}s \left(\omega_0^2\,|s\eta_+(s;\mu_0)|^2 + \left| \frac{\mathrm{d}}{\mathrm{d}s}\,(s\eta_+(s;\mu_0)) \right|^2 \right) \\ &\equiv 2\omega_0 \int_0^\infty \mathrm{d}s \int_0^\infty \mathrm{d}s' \left(s'\eta_+^*(s';\mu_0)\right) R_{[\eta]}(s',s)\,(s\eta_+(s;\mu_0))\,, \end{aligned} \tag{2.40}$$

with the following distribution R, which we obtain as the corresponding integral transform of our weight factor $|r(\tau;\mu_0)|^2$:

$$R_{[\eta]}(s',s) = \omega_0^2\,\delta(s-s') - \delta''(s-s')\,. \tag{2.41}$$

On this basis, we find the generating function for the logarithmic moments in terms of the parameters,

$$F_{[\eta_+]}(t;\mu_0,\mu_m) = \frac{\Gamma(1-t)}{\omega_0} \left(\frac{\hat{\mu}_m}{\omega_0}\right)^{-t} \sum_{k=0}^{K} a_k\, {}_2F_1(-k,1+t;2;2)\,. \tag{2.42}$$

This expression can be derived using Cauchy's residue theorem, where higher-order poles result in derivatives of the integrand, which results in binomial coefficients. The hypergeometric function with negative first argument $-k$ amounts to polynomials of the variable t to n^{th} order. For instance, the leading three polynomials read

$$\begin{aligned} {}_2F_1(0,1+t;2;2) = 1\,, \quad {}_2F_1(-1,1+t;2;2) = -t\,, \\ {}_2F_1(-2,1+t;2;2) = \frac{1}{3}\left(1+2t^2\right)\,. \end{aligned} \tag{2.43}$$

Generally, they are even functions of t for even k and odd functions of t for odd k. From this, we obtain the expressions for the first few logarithmic moments within our parametrization:

$$L_0(\mu_0) = \frac{1}{\omega_0}\sum_{k=0}^{K}\frac{1-(-1)^{k+1}}{2}\,\frac{a_k(\mu_0)}{k+1} = \frac{a_0 + 1/3\,a_2 + \ldots}{\omega_0}\,, \tag{2.44}$$

$$\begin{aligned} L_1(\mu_0) &= -\left(\ln\frac{\hat{\mu}_m}{\omega_0} - \gamma_{\text{E}}\right) L_0(\mu_0) + \frac{1}{\omega_0}\sum_{k=0}^{K} a_k \left[\frac{\mathrm{d}}{\mathrm{d}t}\,{}_2F_1(-k,1+t;2;2)\right]_{t=0} \\ &= -\left(\ln\frac{\hat{\mu}_m}{\omega_0} - \gamma_{\text{E}}\right) L_0(\mu_0) + \frac{-a_1 - 2/3\,a_3 + \ldots}{\omega_0}\,, \end{aligned} \tag{2.45}$$

$$\begin{aligned} L_2(\mu_0) &= \left[\frac{\pi^2}{6} - \left(\ln\frac{\hat{\mu}_m}{\omega_0} - \gamma_{\text{E}}\right)^2\right] L_0(\mu_0) - 2\left(\ln\frac{\hat{\mu}_m}{\omega_0} - \gamma_{\text{E}}\right) L_1(\mu_0) \\ &\quad + \frac{1}{\omega_0}\sum_{k=0}^{K} a_k \left[\frac{\mathrm{d}^2}{\mathrm{d}t^2}\,{}_2F_1(-k,1+t;2;2)\right]_{t=0}\,, \\ &= \left[\frac{\pi^2}{6} - \left(\ln\frac{\hat{\mu}_m}{\omega_0} - \gamma_{\text{E}}\right)^2\right] L_0(\mu_0) - 2\left(\ln\frac{\hat{\mu}_m}{\omega_0} - \gamma_{\text{E}}\right) L_1(\mu_0) \\ &\quad + \frac{4/3\,a_2 + 4/3\,a_4 + 56/45\,a_6 + \ldots}{\omega_0}\,. \end{aligned} \tag{2.46}$$

The characteristics of the confluent hypergeometric functions in Eq. (2.45) and Eq. (2.46) have the following effect in the particular case $\mu_m = \omega_0\,\mathrm{e}^{-\gamma_{\text{E}}}$: The logarithmic moments L_0 and L_2 solely rely on coefficients a_k with even index k, while the logarithmic moment L_1 exclusively involves the coefficients with odd index. In addition, the sequence produced by the hypergeometric functions and their derivatives forms a null sequence. We highlight the conclusions for the logarithmic moments expressed through the parametrization:

1. At the reference scale $\mu_m = \omega_0\,\mathrm{e}^{-\gamma_{\text{E}}}$, the logarithmic moments L_0 and L_1 are parametrically independent. Thus, the two have no correlation, even for the truncated expansion.

2. The series representation of the logarithmic moments can converge, even if the series $\sum_k a_k$ does not converge.

2.2.2. Momentum-space LCDA and Behavior at $\omega = 0$

We obtain the momentum-space representation by applying the Fourier transform in Eq. (2.3) to the position-space representation in Eq. (2.37),

$$\phi_+(\omega;\mu_0) = \frac{\omega\, \mathrm{e}^{-\omega/\omega_0}}{\omega_0^2} \sum_{k=0}^{K} \frac{a_k(\mu_0)}{1+k}\, L_k^{(1)}(2\omega/\omega_0)\,, \tag{2.47}$$

where $L_k^{(n)}$ denotes the *associated* Laguerre polynomials. The corresponding projection relation to obtain the expansion coefficients reads

$$a_k(\mu_0) = 4 \int_0^\infty \mathrm{d}\omega\ \mathrm{e}^{-\omega/\omega_0}\, L_k^{(1)}(2\omega/\omega_0)\, \phi_+(\omega;\mu_0)\,. \tag{2.48}$$

For analytical calculations, we find it convenient to generate the coefficients through derivatives from a single integral expression:

$$a_k(\mu_0) = \frac{1}{k!}\frac{\partial^k}{\partial t^k} \int_0^\infty \mathrm{d}\omega\, \frac{4}{(1-t)^2}\, \exp\left\{\frac{(t+1)}{(t-1)}\,\frac{\omega}{\omega_0}\right\} \phi_+(\omega;\mu_0)\bigg|_{t=0}\,. \tag{2.49}$$

The integral $\chi[r]$ can be expressed in terms of the momentum-space representation as

$$\begin{aligned} 2\omega_0\, \chi[r](\mu_0) = \sum_{k=0}^{K} |a_k|^2 &= 2\omega_0 \int_0^\infty \mathrm{d}\omega \left(|\phi_+(\omega;\mu_0)|^2 + \omega_0^2 \left| \frac{\mathrm{d}\phi_+(\omega;\mu_0)}{\mathrm{d}\omega} \right|^2 \right) \\ &\equiv 2\omega_0 \int_0^\infty \mathrm{d}\omega \int_0^\infty \mathrm{d}\omega'\ \phi_+^*(\omega';\mu_0)\, R_{[\phi]}(\omega',\omega)\, \phi_+(\omega;\mu_0)\,, \end{aligned} \tag{2.50}$$

with the corresponding Fourier transform of the weight factor $|r(\tau;\mu_0)|^2$,

$$R_{[\phi]}(\omega',\omega) = \delta(\omega-\omega') - \omega_0^2\, \delta''(\omega-\omega')\,. \tag{2.51}$$

The parametrization further warrants the notion of η_+ being a "dual" representation of ϕ_+, because of the mathematical similarities between the expressions for the dual-space and momentum-space representations in Eq. (2.41) and Eq. (2.47).

The leading two Taylor-expansion coefficients of $\phi_+(\omega;\mu_0)$ around $\omega = 0$, in terms of the parameters, read:

$$\begin{aligned} \phi_+'(0;\mu_0) &= \frac{1}{\omega_0^2} \sum_{k=0}^{\infty} a_k\,, \\ \phi_+''(0;\mu_0) &= -\frac{1}{\omega_0^3} \sum_{k=0}^{\infty} (2k+2)\, a_k\,. \end{aligned} \tag{2.52}$$

For the n^{th} derivative, the weights of the coefficients a_k grow power-like as k^{n-1}.

The method of QCD sum rules is sensitive to the low-energy regime since it relies on integrals of $\phi_+(\omega)$ over a finite interval of (small) ω values. Typically, the integrals are computed after Borel transformation, such that the appearing expressions are Laplace transformations of $\phi_+(\omega)$. The normalized Laplace transform, Eq. (2.26), at large values $\zeta \equiv n\,t_0$, in terms of the parameters, reads

$$\ell_n(\mu, t_0) \equiv n^2 t_0^2\, \tilde{\phi}_+(-int_0;\mu) \tag{2.53}$$

$$\ell_n(\mu, 1/\lambda_B) = \frac{1}{\lambda_B^2}\frac{n^2}{(1+n\,\omega_0/\lambda_B)^2}\sum_{k=0}^{\infty} a_k(\mu)\left(\frac{n\,\omega_0/\lambda_B - 1}{n\,\omega_0/\lambda_B + 1}\right)^k \tag{2.54}$$

The series expansion of the quantities ℓ_n converges for $0 < n < \infty$. This follows as the sequence $\{a_k\} \in \ell^2$ is bounded and therefore the weighted sum is finite:

$$\left|\sum_{k=0}^{\infty} a_k(\mu)\left(\frac{n\,\omega_0/\lambda_B - 1}{n\,\omega_0/\lambda_B + 1}\right)^k\right| < \max_{k'}|a_{k'}|\left|\sum_{k=0}^{\infty}\left(\frac{n\,\omega_0/\lambda_B - 1}{n\,\omega_0/\lambda_B + 1}\right)^k\right| < \infty\,, \tag{2.55}$$

Above, $n > 0$, $\omega_0/\lambda_B > 0$ render the geometric series finite.

2.2.3. RG Evolution

The solution of the 1-loop RG equation of the LCDA is multiplicative in the dual-space representation. Explicitly, the relation between η_+ evaluated using two different renormalization scales, μ_0 and μ, in our expansion, reads

$$\eta_+(s;\mu) = \mathrm{e}^{V(\mu,\mu_0)}\,(\hat{\mu}_0 s)^{-g(\mu,\mu_0)}\,\mathrm{e}^{-s\omega_0}\sum_{k=0}^{K}\frac{(-1)^k\,a_k(\mu_0)}{1+k}\,L_k^{(1)}(2\omega_0 s)\,. \tag{2.56}$$

We discuss three different ways of implementing the scale evolution:

1. Transform the above form into momentum or position space. The expansion of the LCDA remains in terms of the coefficients $a_k(\mu_0)$, while the basis functions of the expansion change with the scale μ.

2. Project Eq. (2.56) onto our parametrization using our *default choice* of $r(\tau;\mu_0)$. This yields a matrix relation between the coefficients evaluated μ_0 and at μ:

$$a_{k'}(\mu) \sim \sum_{k=0}^{K}\mathcal{R}_{k'k}\,a_k(\mu_0)\,, \quad k' = 0, 1, \ldots, \infty\,.$$

   The expansion basis of functions remains the same at all scales while the coefficients change. Starting with a truncated (finite) set of coefficients $\{a_k(\mu_0)\,|\,k = 0, \ldots, K\}$ at the initial scale, evolution generates an infinite set of coefficients $\{a_{k'}(\mu)\,|\,k = 0, \ldots, \infty\}$, as the truncated series cannot exactly accommodate for the shape modification. For practical purposes, one has to introduce an additional truncation parameter K' so that $k' \leq K'$.

3. Project Eq. (2.56) onto a *modified* parametrization *with a scale-dependent choice of* $r(\tau,\mu)\equiv\tilde{r}$. We choose the weight function $\tilde{r}$ such that the additional truncation parameter K' of the previous approach is identical to K. This results in a similar coefficient RGE, however, without a second truncation:

$$\tilde{a}_{k'}(\mu)\sim\sum_{k=0}^{K}\tilde{\mathcal{R}}_{k'k}\,a_k(\mu_0)\,,\quad k'=0,1,\dots,K\,.$$

Here, $\tilde{a}_k(\mu_0)=a_k(\mu_0)$, which guarantees that the coefficients remain bounded at any scale, $|\tilde{a}_k(\mu)|<\sqrt{2\omega_0\tilde{\chi}(\mu)}$ with $\tilde{\chi}\equiv\chi[\tilde{r}]$.

From now on we abbreviate $g\equiv g(\mu,\mu_0)$ and $V\equiv V(\mu,\mu_0)$.

For the first option, transforming Eq. (2.56) into momentum space results in

$$\begin{aligned}\phi_+(\omega;\mu)&=\mathrm{e}^V\left(\frac{\hat{\mu}_0}{\omega_0}\right)^{-g}\frac{\omega}{\omega_0^2}\times\\&\times\sum_{k=0}^{K}(-1)^k\,\frac{a_k(\mu_0)}{1+k}\left[\frac{1}{k!}\frac{\mathrm{d}^k}{\mathrm{d}t^k}\left(\frac{1-t}{1+t}\right)^{-g}\frac{\Gamma(2-g)}{(1+t)^2}\,{}_1F_1\left(2-g;2;\frac{t-1}{t+1}\frac{\omega}{\omega_0}\right)\right]_{t=0}\,.\end{aligned}\tag{2.57}$$

The derivatives amount to an expansion in ${}_1F_1(k-g;k;-x)$, where ${}_1F_1(k-g;k;-x)\to\mathrm{e}^{-x}$ for $g\to0$. The coefficients $a_k(\mu_0)$ fulfill a bound obtained at the initial scale μ_0. Numerical calculations using the LCDA involve hypergeometric functions with non-integer parameters, which is challenging to implement.

For the second option, we obtain the following relation:

$$a_{k'}(\mu)=\mathrm{e}^V\left(\frac{\hat{\mu}_0}{2\omega_0}\right)^{-g}\sum_{k=0}^{K}\mathcal{R}_{k'k}(\mu,\mu_0)\,a_k(\mu_0)\tag{2.58}$$

with the matrix components

$$\begin{aligned}\mathcal{R}_{k'k}(\mu,\mu_0)&=\frac{(-1)^{k'+k}}{1+k}\int_0^\infty\mathrm{d}z\;z^{1-g}\,\mathrm{e}^{-z}\,L_{k'}^{(1)}(z)\,L_k^{(1)}(z)\\&=\Gamma(2-g)\,\frac{(-1)^{k'+k}}{(1+k)!k'!}\,\frac{\mathrm{d}^k}{\mathrm{d}u^k}\frac{\mathrm{d}^{k'}}{\mathrm{d}v^{k'}}\,\frac{1}{(1-uv)^2}\left(\frac{1-uv}{(u-1)(v-1)}\right)^g\Bigg|_{u,v=0}\,,\end{aligned}\tag{2.59}$$

where $\mathcal{R}_{k'k}(\mu_0,\mu_0)=\delta_{k'k}$. Notably, the matrix must be calculated only once for fixed $\mu\neq\mu_0$ while the additional dependence on ω_0 is simple and factorizes. The efficiency improvement is beneficial for evaluating the LCDA a large number of times for different values of the $a_k(\mu_0)$ and ω_0, as is required in sampling-based statistical methods. We further find that the "secondary truncation", $K'<\infty$, is justified, as the off-diagonal elements of $\mathcal{R}$ are suppressed by $\mathcal{O}(g,1/|k'-k|)$. In other words, the matrix is approximately

of upper-triangular form, while the other components systematically take small values. We quantitatively test the convergence in a realistic scenario, at the hand of a model, in Section 2.3.2. We further employ this solution for the numerical implementation in Chapter 4.

For the third option, we transform Eq. (2.56) to position space and define a modified expansion basis such that

$$\tilde{\phi}_+(\tau;\mu) = \mathrm{e}^V\,\Gamma(1-g)\,\left(\frac{\omega_0}{\hat{\mu}_0}\right)^g\left(\frac{1-y}{2}\right)^2\left(\frac{1+y}{2}\right)^{-g}\sum_{k'=0}^{K'=K}\tilde{a}_{k'}(\mu)\,y^{k'}\,. \tag{2.60}$$

We emphasize the truncation at $K'=K$. The complementary set of evolved coefficients reads

$$\tilde{a}_{k'}(\mu) = \sum_{k=k'}^{K}\tilde{\mathcal{R}}_{k'k}(\mu,\mu_0)\,a_k(\mu_0)\,, \tag{2.61}$$

with the following (exactly) upper-triangular matrix:

$$\tilde{\mathcal{R}}_{k'k}(\mu,\mu_0) = \begin{cases} \dfrac{(-1)^{1+k}\,\Gamma(k+g-k')}{(1+k)\,\Gamma(g-1-k')\,\Gamma(1+k-k')\,\Gamma(1+k')} & k'\geq k\,, \\ 0 & \text{otherwise.}\end{cases} \tag{2.62}$$

To obtain a bounding condition for the evolved LCDA $\tilde{\phi}_+(\tau;\mu)$, we modify the weight function to compensate the additional factor in Eq. (2.60),

$$\tilde{r}(\tau) \equiv \mathrm{e}^{-V}\,\frac{(i\hat{\mu}_0\tau)^g\,(1+i\omega_0\tau)^{1-g}}{\Gamma(1-g)}\,, \tag{2.63}$$

which results in

$$\tilde{\chi} = \int_{-\infty}^{\infty}\frac{\mathrm{d}\tau}{2\pi}\,\left|\tilde{\phi}_+(\tau;\mu)\right|^2|\tilde{r}(\tau)|^2 = \frac{1}{2\omega_0}\sum_{k'=0}^{K'=K}|\tilde{a}_{k'}(\mu)|^2\,. \tag{2.64}$$

This modification comes at the expense that the basis functions, especially in momentum space, become more complicated as they acquire a non-trivial dependence on g. We remark that even though this third approach works at the 1-loop level, the extension to the 2-loop level is not straightforward since the RG equation in dual space becomes inhomogeneous [25]. Moreover, evolving from μ_0 to a smaller scale $\mu<\mu_0$ results in $g<0$, and therefore the integral bound only exists as long as $g(\mu,\mu_0)$ is larger than $-1/2$, as per the requirements for the weight function. In the contrary case, $\mu>\mu_0$, g remains positive, and the parametrization with the weight function Eq. (2.63) can be used as long as $g<1$.

2.2.4. Application to Higher Twist

A comprehensive description of exclusive processes involves further higher-twist LCDAs. One can and should apply our approach also for these, given that sufficient knowledge about their analytic properties is available. Here, we briefly discuss the implications of our result to the second 2-particle LCDA at twist 3 denoted as $\tilde{\phi}_-(\tau)$. It is commonly split into two terms, $\tilde{\phi}_-(\tau) = \tilde{\phi}_-^{(\mathrm{WW})} + \tilde{\phi}_-^{(\mathrm{tw3})}$: the first term refers to the so-called Wandzura-Wilczek limit and is related to the leading 2-particle LCDA $\tilde{\phi}_+(\tau)$ at twist 2. The second term $\tilde{\phi}_-^{(\mathrm{tw3})}$ is "genuinely of twist-3 origin" related to the 3-particle LCDA at twist 3 [30, 31]. We restrict the following discussion to the 2-particle (Wandzura-Wilczek) contribution while dropping the superscripts in the notation. The corresponding RG equations can be found in Ref. [32] (see also Ref. [33]).

The equation of motion connecting the Wandzura-Wilczek term with the leading-twist LCDA in position space (see, e.g., Ref. [34]) reads

$$\tilde{\phi}_+(\tau) = \tau \frac{\mathrm{d}}{\mathrm{d}\tau} \tilde{\phi}_-(\tau) + \tilde{\phi}_-(\tau)\,. \tag{2.65}$$

It is helpful to reuse the same definitions established during the construction of the parametrization and the bounding condition in Section 2.2. We formulate the differential equation in terms of the variable y and find

$$\frac{\tilde{\phi}_+(\tau(y))}{(1-y)^2} = \frac{1}{2} \frac{\mathrm{d}}{\mathrm{d}y} \left[\frac{1+y}{1-y} \tilde{\phi}_-(\tau(y)) \right] . \tag{2.66}$$

The solution, substituting $\tilde{\phi}_+(\tau(y))$ for $f_+(y)$, simplifies to

$$\begin{aligned} \tilde{\phi}_-(\tau(y)) &= 2\,\frac{1-y}{1+y} \int_{-1}^{y} \mathrm{d}x\; \frac{\tilde{\phi}_+(\tau(x))}{(1-x)^2} = \frac{1}{2}\,\frac{1-y}{1+y} \int_{-1}^{y} \mathrm{d}x\; f_+(x) \\ &\equiv \frac{1}{2}\,\frac{1-y}{1+y}\,\left[f_-(y) - f_-(-1) \right] . \end{aligned} \tag{2.67}$$

Here, we define f_- as the antiderivative of f_+. The local limit of $\tilde{\phi}_+(\tau)$ corresponds to the limit $y \to -1$, which presents a condition that fixes the integration constant and lower boundary. Our parametrisation for $\tilde{\phi}_+$ translates to the following expansion of f_-:

$$f_-(y) = \int_0^y \mathrm{d}x\, f_+(x) = \sum_{k=0}^{K} \frac{a_k}{1+k} y^{1+k}\,. \tag{2.68}$$

The asymptotic behavior of $\tilde{\phi}_-(\tau)$ for $|\tau| \to \infty$ is $1/\tau$. The convergence is improved compared to $\tilde{\phi}_+$ since the coefficients a_k appear with an additional suppression factor $1/(1+k)$. It is straightforward to calculate the Fourier transform of each term in the expansion to obtain the momentum-space representation:

$$\frac{1-y}{1+y} \mapsto \frac{1}{2\omega_0}\,, \quad \frac{1-y}{1+y} y \mapsto \frac{1}{2\omega_0} \left[-1 + 4\mathrm{e}^{-\omega/\omega_0} \right] , \quad \text{etc.} \tag{2.69}$$

Alternatively, we can directly calculate ϕ_- from ϕ_+ in momentum space [31] through the integration of the explicit expressions of the Laguerre polynomials, leading to

$$\begin{aligned}\phi_-(\omega;\mu_0) &= \int_\omega^\infty \frac{\mathrm{d}\omega'}{\omega'}\,\phi_+(\omega';\mu_0) \\ &= \frac{1}{\omega_0}\sum_{k=0}^{K}\frac{a_k(\mu_0)}{1+k}\sum_{i=0}^{k}\frac{(-2)^i}{i!}\binom{k+1}{k-i}\Gamma(1+i,\omega/\omega_0) \\ &= \frac{\mathrm{e}^{-\omega/\omega_0}}{\omega_0}\left\{a_0+\frac{a_2}{3}-\left(a_1+\frac{2a_2}{3}\right)\frac{\omega}{\omega_0}+\frac{2a_2}{3}\frac{\omega^2}{\omega_0^2}+\dots\right\}.\end{aligned} \tag{2.70}$$

2.3. Application to Existing Models

Phenomenological applications often employ simple models of the B-LCDAs at a low scale μ_0, featuring only a few parameters. In this section, we explore the ability of the parametrization to capture certain behaviors using a diverse selection of models. We compare each parametrized model using the dimensionless ratio

$$\xi \equiv \frac{\omega_0}{\lambda_B^{\mathrm{model}}(\mu_0)} > 0\,, \tag{2.71}$$

where ω_0 is the auxiliary scale of the parametrization, and $\lambda_B^{\mathrm{model}}(\mu_0)$ is the value for the inverse moment in the specific model. We extract the expansion coefficients for each model using the projection relation in Eq. (2.48).

To test the parametrization, we study the ratio, for various quantities, between the prediction based on its truncated approximation and the prediction based on the model truth. The ratio saturates (approaches unity) in the limit $K \to \infty$. Formally, we therefore define the saturation of a quantity X as

$$\mathrm{Sat}\,[X]_K \equiv \frac{\sum_{k=0}^{K} X\big|_k}{\sum_{k=0}^{\infty} X\big|_k}\,, \tag{2.72}$$

where $X\big|_k$ is the contribution at order k in the expansion.

We use the following quantities as physical benchmarks:

- the result for the integral χ, which provides the bound for the expansion parameters a_k in our parametrization,

$$\chi\big|_k \equiv \frac{1}{2\omega_0}|a_k|^2\,, \tag{2.73}$$

- the derivative of the momentum-space LCDA at the origin,

$$\phi_+'(0)\big|_k \equiv \frac{1}{\omega_0^2}\,a_k\,, \tag{2.74}$$

- the normalized Laplace transform at $\zeta = n/\lambda_B$,

$$\ell_n\big|_k \equiv \frac{1}{\lambda_B^2} \frac{n^2}{(1+n\xi)^2} \left(\frac{n\xi - 1}{n\xi + 1}\right)^k a_k \,, \tag{2.75}$$

- the inverse logarithmic moment,

$$L_0\big|_k = \lambda_B^{-1}\big|_k \equiv \frac{1}{2\omega_0} \frac{1 + (-1)^k}{1+k} a_k \,, \tag{2.76}$$

- and the normalized first logarithmic moment,

$$\begin{aligned} \sigma_B\big|_k &\equiv -\lambda_B \, L_1(\mu_m = \mathrm{e}^{-\gamma_\mathrm{E}} \, \lambda_B)\big|_k \\ &= \begin{cases} -\ln \xi & k = 0 \,, \\ -\dfrac{a_k}{\xi} \left[\dfrac{\mathrm{d}}{\mathrm{d}t} \, {}_2F_1(-k, 1+t; 2; 2)\right]_{t=0} & k \geq 1 \text{ and odd}, \\ 0 & k \geq 1 \text{ and even}. \end{cases} \end{aligned} \tag{2.77}$$

We omit the fixed renormalization scale $\mu = \mu_0$ for all quantities in this section.

In addition to the saturation, we study the "relative growth" of some of the quantities, which we define as

$$\mathrm{Gr}[X]_K \equiv \frac{X\big|_K}{\sum_{k=0}^{K} X\big|_k} \,. \tag{2.78}$$

The relative growth of the bound indicates the rapidity of convergence (whereas the saturation indicates the level of accuracy). It is independent of the true value (the limit $K \to \infty$), bringing two advantages: First, the relative growth is also helpful if the model renders a quantity ill-defined (e.g., the derivative at the origin). Second, relative growth can be a proxy for saturation in model-independent phenomenological studies because considerable growth indicates an insufficient level of saturation for a given truncation level.

2.3.1. Exponential Model

A popular single-parameter model, commonly serving as a starting point for phenomenological analysis, was proposed in Ref. [18]:

$$\phi_+(\omega, \mu_0) = \frac{\omega}{\lambda_B^2} \mathrm{e}^{-\omega/\lambda_B} \qquad [\text{exp. model}] \,. \tag{2.79}$$

We obtain the expansion coefficients using Eq. (2.48) for general k in closed form:

$$a_k = (k+1) \left(\frac{2\xi}{1+\xi}\right)^2 \left(\frac{\xi - 1}{\xi + 1}\right)^k \qquad [\text{exp. model}] \,. \tag{2.80}$$

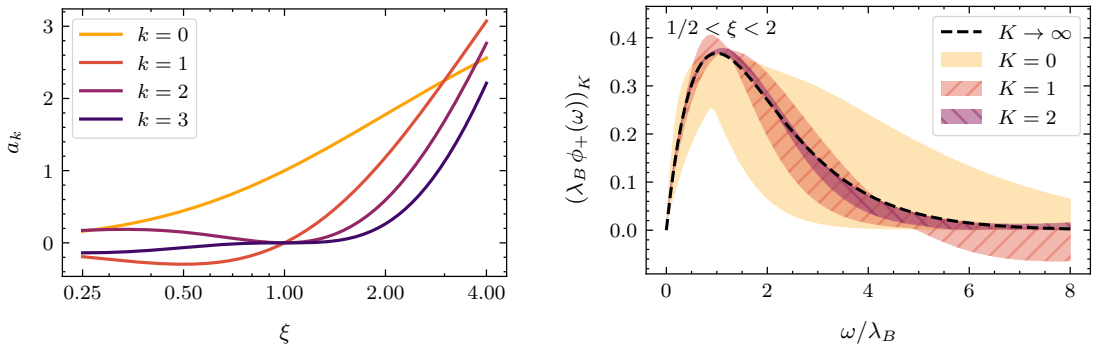

(a) Values for the expansion coefficients a_k

(b) Variability of the momentum-space LCDA for different truncations K in the interval $1/2 < \xi < 2$

Figure 2.2.: Plots illustrating the parametrization's truncation effects for the exponential model in Eq. (2.79). We use the ratio $\xi = \omega_0/\lambda_B$ plotted on a logarithmic scale.

They exhibit exponential suppression for $\xi \neq 1$. For $\xi = 1$, the model trivially matches the parametrization with $a_0 = 1$ and $a_{k>0} = 0$. In Fig. 2.2a, we plot the result for the first few coefficients as a function of ξ. The plot demonstrates the role of the auxiliary scale $\omega_0 = \xi\lambda_B$ that the coefficients are "measured with": at a specific scale, $\xi \approx 1$, we observe optimal convergence, such that higher-order coefficients are very small. Far off this point, the contribution hierarchy breaks down due to large higher-order coefficients or alternating signs while the magnitudes remain similar. Although the measurement scale is arbitrary as long as the entire infinite set of coefficients is accounted for, the truncation error of the series expansion crucially depends on it.

We observe a rapid decrease of the coefficient's magnitudes $|a_k|$ for $k > 2$ in the entire interval

$$1/2 \lesssim \xi \lesssim 2 \qquad \text{[benchmark interval]}\,. \tag{2.81}$$

We use the above interval to define an estimator for the inherent uncertainty of our parametrization, in particular, to compare the efficiency in various scenarios with the exponential model as a reference. The uncertainty estimate based on the benchmark interval is illustrated in Fig. 2.2b, where we show the resulting variation of the shape of the momentum-space LCDA for different truncation levels. Within the benchmark interval, we find that the uncertainty bands form a narrow envelope at $K = 2$.

The resulting integral bound for the exponential model reads

$$2\omega_0\chi = \frac{1}{2}\left(\xi + \xi^3\right) \qquad \text{[exp. model]}\,. \tag{2.82}$$

Fig. 2.3a and Fig. 2.3b show the bound's saturation and relative growth, respectively, for different truncation levels K. We observe that both quantities give comparable insight

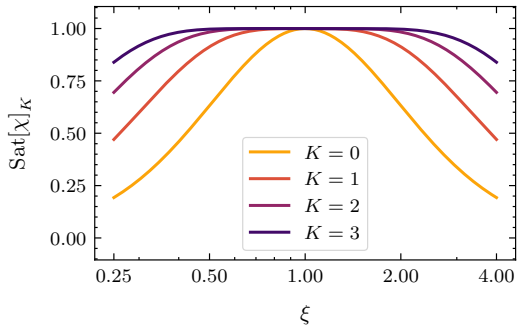

(a) Saturation of the integral bound χ

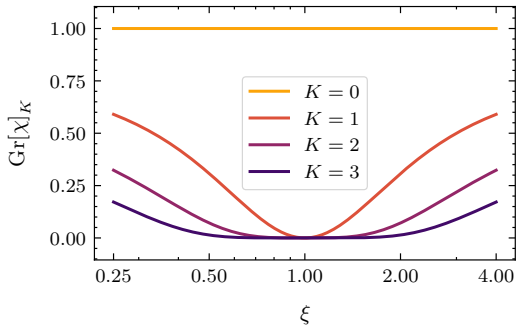

(b) Relative growth of the integral bound χ

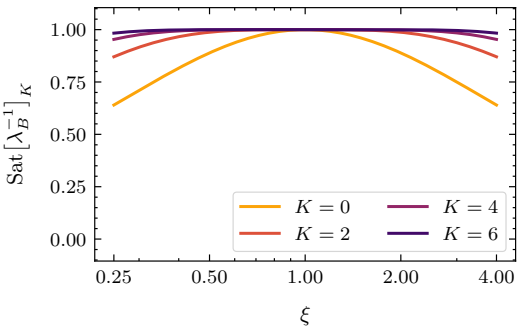

(c) Saturation of the inverse moment $L_0 = \lambda_B^{-1}$

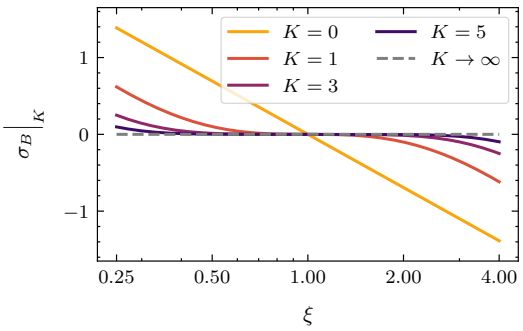

(d) Value of σ_B for different truncation levels K

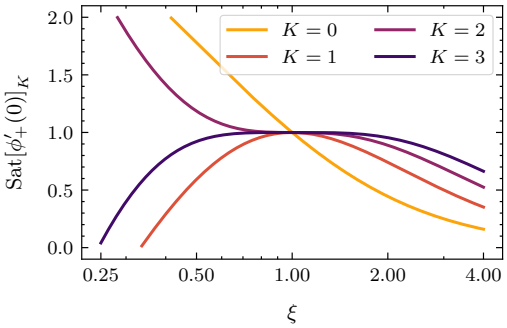

(e) Saturation of the derivative of $\phi_+(\omega)$ at the origin

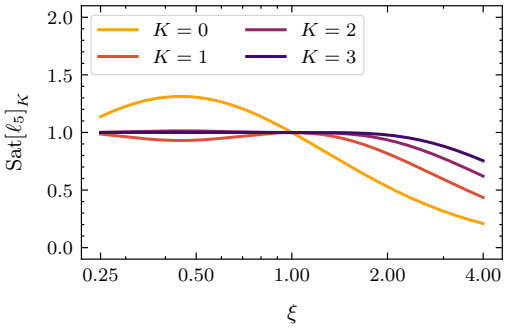

(f) Saturation of the normalized Laplace transform ℓ_5

Figure 2.3.: Plots illustrating the parametrization's truncation effects for the exponential model in Eq. (2.79). We use the ratio $\xi = \omega_0/\lambda_B$ plotted on a logarithmic scale.

about the convergence of the parametrization. Taking $K = 2$, within the benchmark interval, the saturation exceeds 98% and the relative growth is below 7%.

The saturation for the inverse moment $L_0 = \lambda_B^{-1}$ is shown in Fig. 2.3c. Its series expansion also rapidly convergences: for $K = 2$ the saturation within the benchmark interval is better than 98%. It is further instructive to study the normalized first logarithmic moment, which is zero in the model at the scale μ_m,

$$\sigma_B = 0 \qquad [\text{exp. model}]\,. \tag{2.83}$$

In Fig. 2.3d, we show the result as a function of ξ for different truncations K. The accuracy of the truncated expansion improves rapidly and the absolute difference falls below 0.11 for $K = 2$ in the benchmark interval.

Finally, we study the low-momentum behavior using the saturation of the LCDA's derivative at the origin $\omega = 0$ and of the normalized Laplace transform at $n = \zeta\lambda_B$. In the exponential model, they read:

$$\phi_+'(0,\mu_0) = \lim_{n\to\infty} \ell_n = \frac{1}{\lambda_B^2}\,, \quad \ell_n(\mu_0, 1/\lambda_B) = \frac{1}{\lambda_B^2}\,\frac{n^2}{(1+n)^2} \qquad [\text{exp. model}]\,. \tag{2.84}$$

In Fig. 2.3e and Fig. 2.3f, we show the saturation of $\phi_+'(0)$ and ℓ_5, respectively, for different truncations K. For $K = 2$, in the benchmark interval, we find $0.88 < \text{Sat}\left[\phi_+'(0)\right]_K < 1.19$ and $0.93 < \text{Sat}\left[\ell_5\right]_K < 1.02$. The reasonable convergence behavior of $\phi_+'(0)$ is due to the exponential decrease of the coefficients in Eq. (2.80). The plot of ℓ_5 shows that the convergence is improved in comparison to $\phi_+'(0)$, in line with expectations (see the discussion in Section 2.2.2).

We conclude that our parametrization captures the exponential model with high precision even for small K. We remark that the parametrization envelopes the model to any order by construction; however, this study showed that the dependence on the auxiliary scale ω_0 becomes weaker for growing K at a rate suitable for practical applications. We find that $K = 2$ offers sufficient precision for practical applications using the model while varying ω_0 in the benchmark interval. The exponential model presents the ideal test case as the parametrization exactly contains it already at the elementary order. We take it as a reference to study the models in the following sections.

2.3.2. Lee-Neubert Model with Radiative Tail

In Ref. [35], Lee and Neubert extend the exponential model by a "radiative tail", an effect in the high-momentum region stemming from radiative corrections through virtual gluon exchange. They use an operator product expansion to motivate the inclusion of terms with $\ln\omega/\mu$ when $\omega \sim \mu \gg \Lambda_{\text{QCD}}$, where μ is the renormalization scale. The tail is attached to

the exponential low-momentum region using a Heaviside function of the model parameter ω_t:

$$\phi_+(\omega,\mu) = \mathcal{N}\,\frac{\omega\,\mathrm{e}^{-\omega/\bar{\omega}}}{\bar{\omega}^2} + \frac{\alpha_s C_F}{\pi}\,\frac{\theta(\omega-\omega_t)}{\omega}\times \\ \times\left\{\frac{1}{2} - \ln\frac{\omega}{\mu} + 4\,\frac{\bar{\Lambda}_{\mathrm{DA}}}{3\omega}\left(2-\ln\frac{\omega}{\mu}\right)\right\} \qquad \text{[Lee/Neubert]}\,. \quad (2.85)$$

Here, $\bar{\Lambda}_{\mathrm{DA}}$ corresponds to the B meson's binding energy using a convenient renormalon-free scheme (see Ref. [35] for details). The model parameters $\mathcal{N}$, $\bar{\omega}$, and ω_t are fixed by matching the model to a constraint and by requiring continuity between the low- and high-momentum regions. We stress that this model does not aim to be accurate at asymptotically large values $\omega \gg \mu$, which would further require to resum the large logarithms $\ln\omega/\mu$ (see e.g. the discussion in Ref. [26]). With this in mind, we study the parametrization's efficiency to approximate the model for small and intermediate values of ω.

For the following numerical discussion, we adopt the following values provided in Ref. [35] for $\mu_0 = 1$ GeV,

$$\bar{\Lambda}_{\mathrm{DA}} = 519\ \mathrm{MeV}\,, \quad \bar{\omega} = 438\ \mathrm{MeV}\,, \quad \mathcal{N} = 0.963\,, \quad \omega_t = 2.33\ \mathrm{GeV}\,,$$

and we use $\alpha_s(\mu_0) = 0.5$. The model makes the following predictions:

$$L_0 = \lambda_B^{-1} = 1/479\ \mathrm{MeV}^{-1}\,, \qquad \sigma_B = 0.315 \qquad \text{[Lee/Neubert]}\,. \quad (2.86)$$

The expansion coefficients a_k can be calculated numerically for different ξ. For example, for $\xi = 1$ we find

$$a_0 \simeq 1.050\,, \quad a_1 \simeq 0.096\,, \quad a_2 \simeq -0.007\,, \quad a_3 \simeq 0.035\,, \quad a_4 \simeq -0.051\,, \quad a_5 \simeq 0.047\,.$$

The higher-order coefficients remain almost constant in magnitude while their signs alternate.

In Fig. 2.4a and Fig. 2.4b, we show the coefficients a_0 to a_3 as a function of ξ and the resulting approximation of the model, respectively. While the plotted results look qualitatively identical to the exponential model, the tail requires special attention. In Fig. 2.5a, we focus on the medium-high region, $4 < \omega/\lambda_B < 12$, and consider higher truncation levels $K = 2, 3, 8$. We find that the uncertainty band at $K = 3$, within the benchmark interval, already contains the model even for large values of ω, whereas the precision at the high end can be systematically improved by including more terms in the expansion. Note that – by construction – the parametrization is not designed to reproduce the radiative tail at values $\omega \gg \mu$ (see also Section 2.4).

The integral bound of the Lee-Neubert model numerically yields

$$2\omega_0\chi = 0.547\,\xi + 0.608\,\xi^3 \qquad \text{[Lee/Neubert]}\,, \quad (2.87)$$

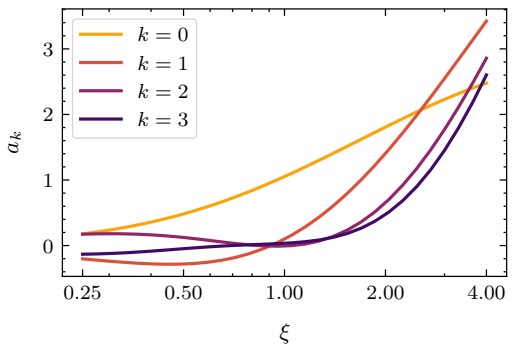

(a) Values for the expansion coefficients a_k

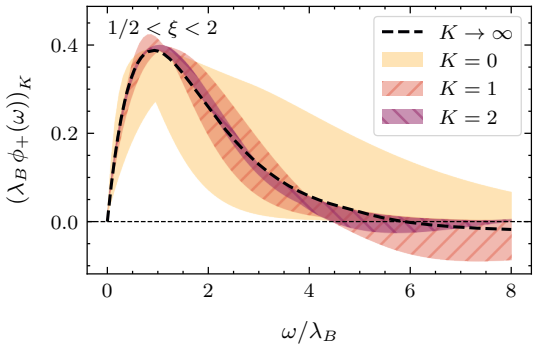

(b) Variability of the momentum-space LCDA for different truncations K in the interval $1/2 < \xi < 2$

Figure 2.4.: Plots illustrating the parametrization's truncation effects for the Lee-Neubert model in Eq. (2.85). We use the ratio $\xi = \omega_0/\lambda_B$ plotted on a logarithmic scale.

which is close to the exponential model. Notably, the bound is finite despite the derivative in Eq. (2.50) acting on the Heaviside distribution because of the continuous construction of the model. In Fig. 2.5b and Fig. 2.5c, we plot the saturation and relative growth of the bound, respectively. First, the saturation is below one because the truncated parametrization does not exactly reproduce the model for any value of ξ. Second, the curves are tilted in comparison to the exponential model: small values of ξ result in slower convergence, while best convergence is achieved for $\xi \gtrsim 1$. The peaking behavior (in contrast to the symmetrical plateau for the exponential model) reflects that higher-order coefficients are needed, such that the curve flattens and the dependence on the auxiliary scale becomes weak. The relative growth of the bound plotted in Fig. 2.5c decreases reasonably within the benchmark interval.

In Fig. 2.5d and Fig. 2.5e, we show the saturation for the inverse moment $L_0 = \lambda_B^{-1}$ and the value of σ_B, respectively, as functions of ξ and for different levels of truncation. In both cases, we find reasonable convergence, however, with a significantly lower rate than with the exponential model and a clear preference for larger values of ξ.

We omit the discussion for the quantities $\phi'_+(0)$ and ℓ_5, which are predominantly sensitive to the low-momentum region where the radiative tail has no effect.

The model additionally presents a test case for RG evolution since Ref. [35] includes the model parameters for different choices of the renormalization scale alongside a plot of their exact result after evolution. We compare this against the RG evolution of the parameters as defined in Eq. (2.58). In Fig. 2.5f, we show the model at $\mu = 1$ GeV and our exact result of the 1-loop RGE to $\mu = 2.5$ GeV. We further plot the approximation of the model at the lower scale at truncation level $K = 3$ and the result of the parameter evolution

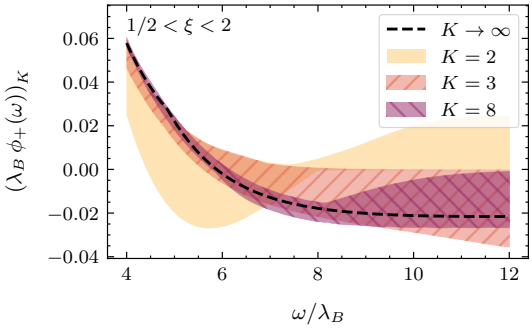

(a) Extension of 2.4b: variability of the momentum-space LCDA in the "tail region" for different truncations K in the interval $1/2 < \xi < 2$

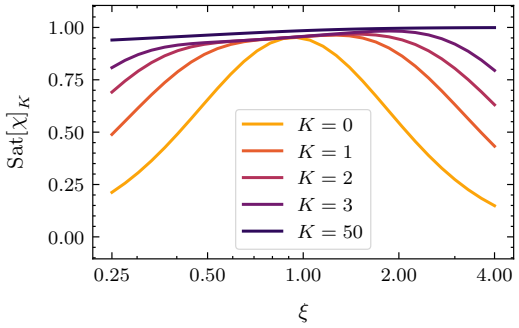

(b) Saturation of the integral bound χ

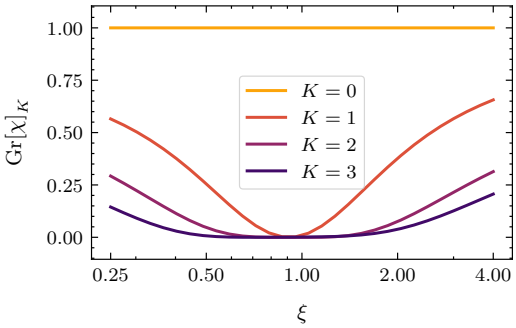

(c) Relative growth of the integral bound χ

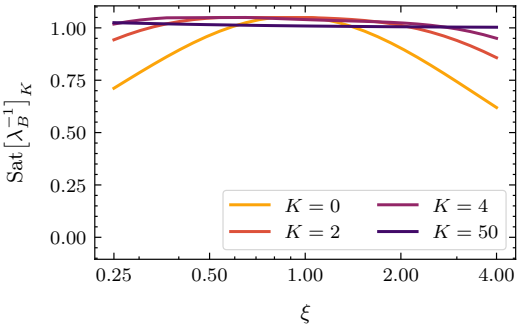

(d) Saturation of the inverse moment $L_0 = \lambda_B^{-1}$

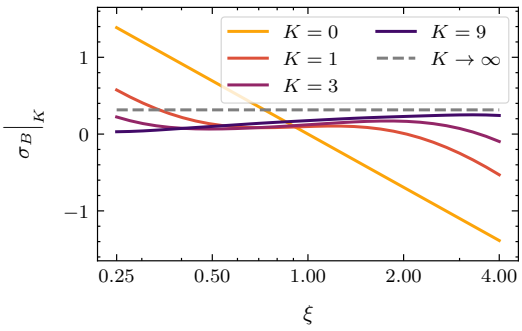

(e) Value of σ_B for different truncations K

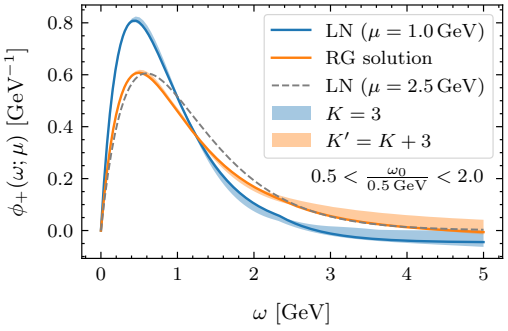

(f) Demonstration of the RG evolution

Figure 2.5.: Plots illustrating the parametrization's truncation effects for the Lee-Neubert model in Eq. (2.85). We use the ratio $\xi = \omega_0/\lambda_B$ plotted on a logarithmic scale.

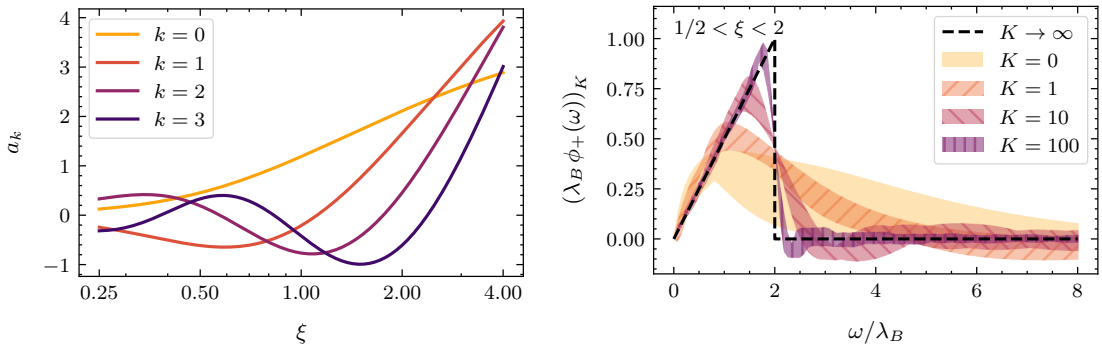

(a) Values for the expansion coefficients a_k

(b) Variability of the momentum-space LCDA for different truncations K in the interval $1/2 < \xi < 2$

Figure 2.6.: Plots illustrating the parametrization's truncation effects for the parton model Eq. (2.88). We use the ratio $\xi = \omega_0/\lambda_B$ plotted on a logarithmic scale.

to the higher scale at truncation level $K' = K + 3$. Both approximations take the usual variation within the benchmark interval into account as a handle for the truncation error. We also plot the model as provided at $\mu = 2.5$ GeV for reference. As a consistency check, we note that our plot is visually indistinguishable from the one provided in Ref. [35]. The uncertainty bands cover the model and its RGE result at both scales. Most importantly, the variation band is consistent for both scales, verifying the expectation that higher orders in the expansion remain negligible.

2.3.3. Naïve Parton Model

The naïve parton model [30] suggests the following momentum-space LCDA:

$$\phi_+(\omega) = \frac{\omega}{2\lambda_B^2}\,\theta(2\lambda_B - \omega) \qquad [\text{parton model}]\,. \tag{2.88}$$

In this model, the parameter λ_B is identical with the B meson's binding energy $\bar{\Lambda} \simeq M_B - m_b$. Transforming it into position space yields

$$\tilde{\phi}_+(\tau) = \frac{(1 + 2i\lambda_B\tau)\,\mathrm{e}^{-2i\lambda_B\tau} - 1}{2\lambda_B^2\tau^2} \qquad [\text{parton model}]\,, \tag{2.89}$$

which insufficiently falls off like $1/\tau$ for $|\tau| \to \infty$, in violation with **P4**; therefore, the parton model is a pathological example. It is nevertheless interesting to examine the behavior of the parametrization under extreme conditions.

In Fig. 2.6a and Fig. 2.6b, we show the numerical results for the expansion coefficients and the resulting momentum-space LCDA for different truncation levels, respectively,

within the benchmark interval. The coefficients a_k do not exhibit a contribution hierarchy across the benchmark interval, indicating poor convergence. The uncertainty bands in Fig. 2.6b confirm this since they are of comparable size between $K = 1$ and $K = 10$, whereas the exponential model yields a clearly visible improvement with each increment of K. Although the approximation improves with higher truncation levels, the convergence rate is qualitatively much slower than for the exponential model.

The integral bound χ in Eq. (2.28) does not exist because of the pathological asymptotic behavior of $\tilde{\phi}(\tau)$. In Fig. 2.7a, we therefore only show the diverging sum

$$2\omega_0 \chi\big|_K = \sum_{k=0}^{K} |a_k|^2 \,,$$

and in Fig. 2.7b its relative growth. The oscillatory behavior in the latter plot further indicates poor convergence of the expansion.

In Fig. 2.7c, we show the saturation of $L_0 = \lambda_B^{-1}$. It oscillates around unity, where the amplitude only slowly decreases as K increases. The normalized first logarithmic moment for the model yields

$$\sigma_B = 1 - \ln 2 - \gamma_\mathrm{E} \simeq -0.270 \qquad \text{[parton model]}\,. \tag{2.90}$$

In Fig. 2.7d, we show the result for different truncation levels K, again oscillating around the model value.

Finally, we examine the LCDA's convergence at small values of ω. We obtain

$$\begin{aligned} \phi_+'(0,\mu_0) &= \frac{1}{2\lambda_B^2}\,, \\ \ell_n(\mu_0, 1/\lambda_B) &= \frac{1}{2\lambda_B^2}\left(1 - (1+2n)\,\mathrm{e}^{-2n}\right) \end{aligned} \qquad \text{[parton model]}\,. \tag{2.91}$$

The derivative at the origin in Fig. 2.7e again oscillates for the whole range of ξ, while the normalized Laplace transform in Fig. 2.7f approaches unity for sufficiently large values of K and small values of ξ. The latter is less sensitive to oscillatory behavior since the momentum-space LCDA is integrated over, resulting in an averaging effect.

2.3.4. A Model with $\phi_+'(0) \to \infty$

In Ref. [16], Beneke et al. suggest to consider more general models for the B-meson LCDA, including cases where the derivative at the origin $\phi_+'(0)$ does not exist. Here, we use their following model to examine the consequences for the truncated expansion:

$$\phi_+(\omega,\mu_0) = \frac{1}{\Gamma(1+a)}\left(\frac{(1+a)\,\omega}{\lambda_B}\right)^{1+a} \frac{\mathrm{e}^{-(1+a)\,\omega/\lambda_B}}{\lambda_B} \qquad \text{[Beneke et al.]}\,. \tag{2.92}$$

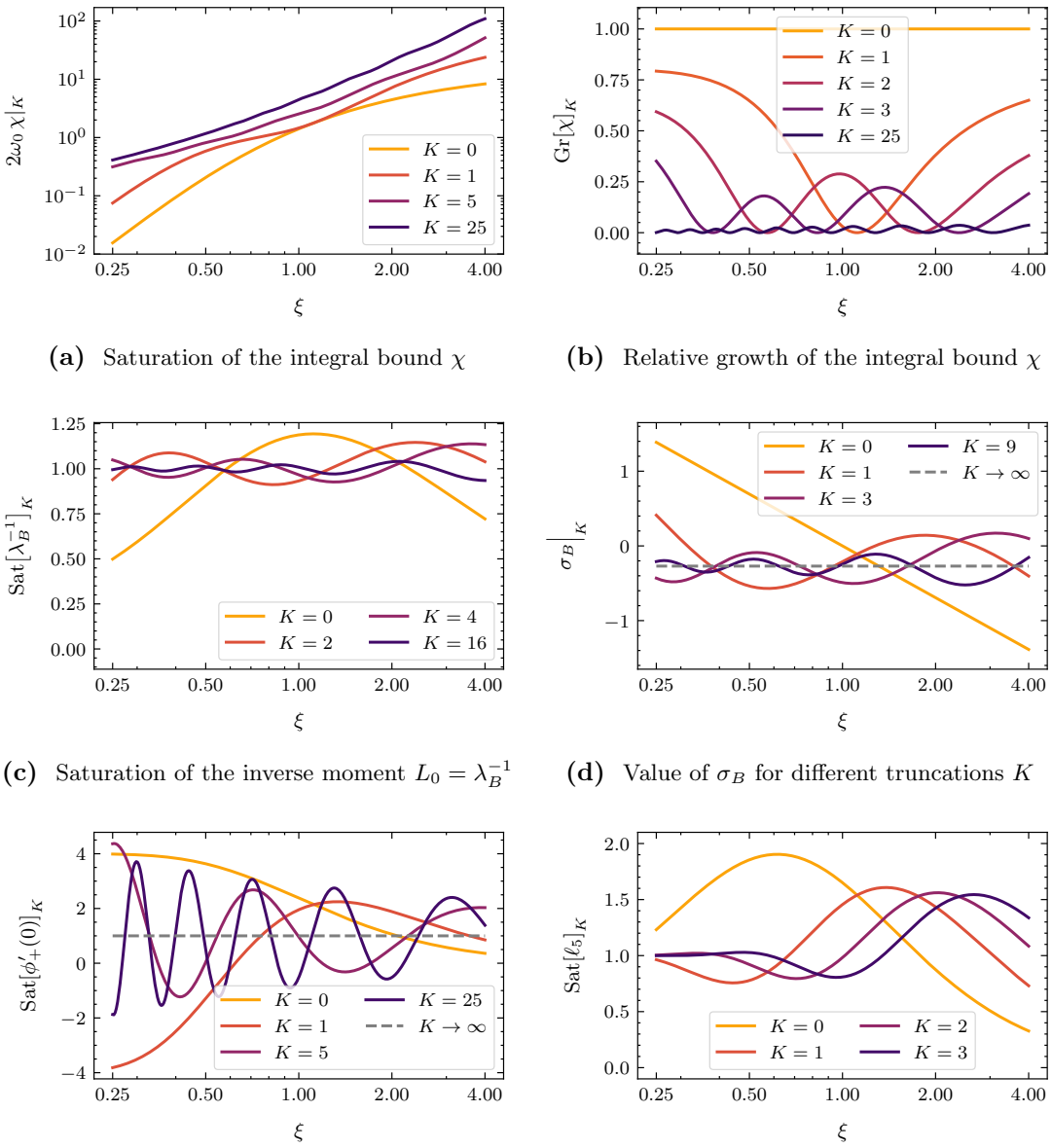

(a) Saturation of the integral bound χ

(b) Relative growth of the integral bound χ

(c) Saturation of the inverse moment $L_0 = \lambda_B^{-1}$

(d) Value of σ_B for different truncations K

(e) Saturation of the derivative of $\phi_+(\omega)$ at the origin

(f) Saturation of the normalized Laplace transform ℓ_5

Figure 2.7.: Plots illustrating the parametrization's truncation effects for the parton model Eq. (2.88). We use the ratio $\xi = \omega_0/\lambda_B$ plotted on a logarithmic scale.

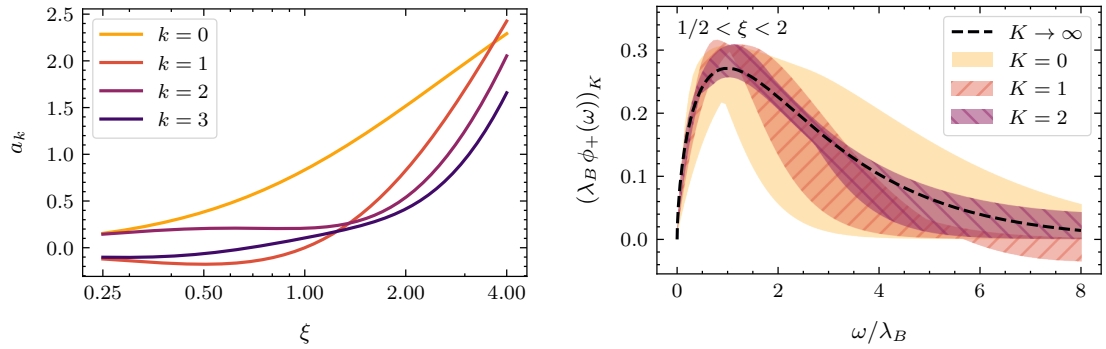

(a) Values for the expansion coefficients a_k

(b) Variability of the momentum-space LCDA for different truncations K in the interval $1/2 < \xi < 2$

Figure 2.8.: Plots illustrating the parametrization's truncation effects for the model Eq. (2.92) discussed by Beneke et al. [16]. We use the ratio $\xi = \omega_0/\lambda_B$ plotted on a logarithmic scale.

The domain of the model parameter is given by $-0.5 < a < 1$, where $a \to 0$ reduces the expression to the exponential model. As the model predicts $\phi'_+(\omega) \propto \omega^a$, the derivative's limit $\omega \to 0$ does not exist for $a < 0$. This presents another interesting pathological case for the parametrization because such behavior implicitly violates **P4**. We consider the concrete case $a = -0.4$ in the following.

In Fig. 2.8a and Fig. 2.8b, we show the coefficients a_k and the resulting shape of the LCDA, respectively, for different truncation levels. Although the precision is not as good as for the exponential model, already $K = 2$ results in a reasonable approximation, with the bands enveloping the model function.

The model predicts the following integral bound:

$$2\omega_0\chi = \frac{1}{2^{1+2a}}\frac{\Gamma(2+2a)}{\Gamma(1+a)^2}\left(\xi + \frac{(1+a)^2}{1+2a}\xi^3\right) \overset{a\to-0.4}{\simeq} 0.360\,\xi + 0.649\,\xi^3 \qquad \text{[Beneke et al.]}\,. \tag{2.93}$$

The saturation shown in Fig. 2.9a exhibits the opposite behavior to the Lee-Neubert model, i.e. the peak of the saturation appears on the lower side and best convergence is achieved for small values of ξ. The relative growth of the integral bound in Fig. 2.9b remains small in the benchmark interval around $\xi = 1$; however, it does not conclusively reflect the preference for smaller ξ.

In Fig. 2.9c and Fig. 2.9d, we show the saturation of the inverse moment $L_0 = \lambda_B^{-1}$ and the normalized first logarithmic moment,

$$\sigma_B = -\Psi(1+a) + \ln(1+a) - \gamma_\mathrm{E} \overset{a\to-0.4}{\simeq} +0.453 \qquad \text{[Beneke et al.]}\,, \tag{2.94}$$

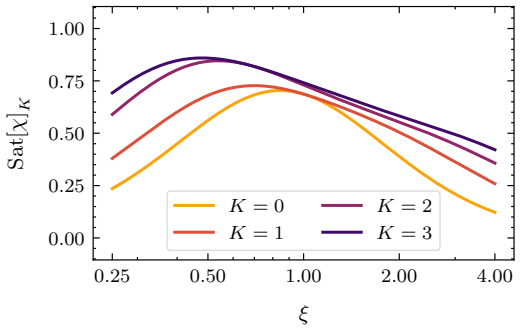

(a) Saturation of the integral bound χ

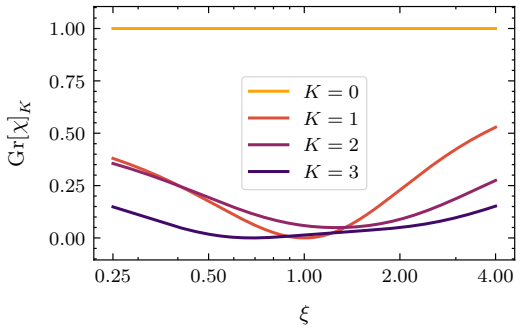

(b) Relative growth of the integral bound χ

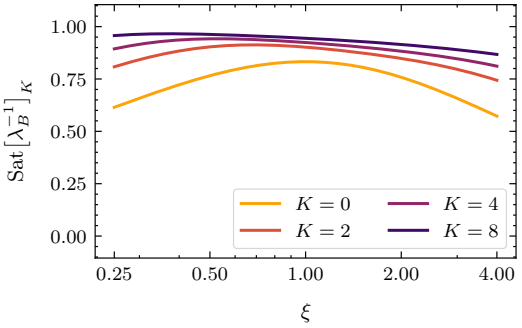

(c) Saturation of the inverse moment $L_0 = \lambda_B^{-1}$

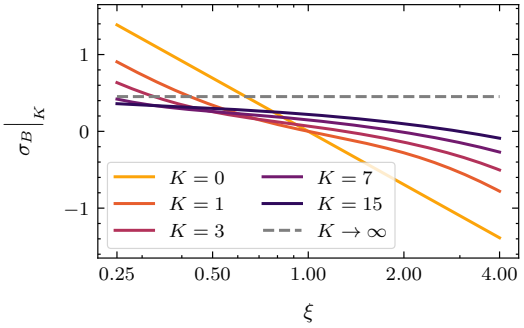

(d) Value of σ_B for different truncations K

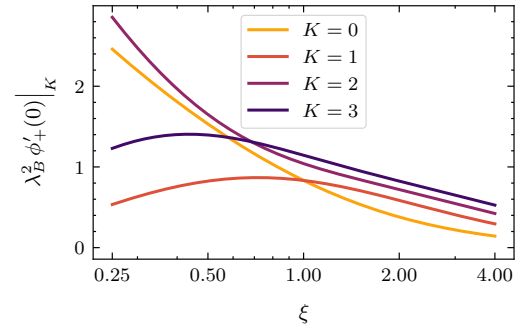

(e) Truncated expansion of the derivative at the origin

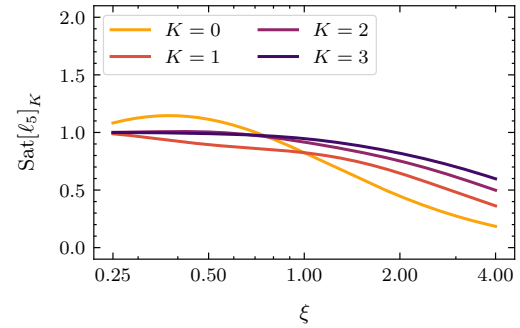

(f) Saturation of the normalized Laplace transform ℓ_5

Figure 2.9.: Plots illustrating the parametrization's truncation effects for the model Eq. (2.92) discussed by Beneke et al. [16]. We use the ratio $\xi = \omega_0/\lambda_B$ plotted on a logarithmic scale.

where $\Psi(z)$ is the standard digamma function. Compared to the exponential model, the saturation of L_0 converges slower, and the truncated result for σ_B remains sensitive to the value of ξ, even at moderate truncation levels K.

Finally, we examine the quantities that characterize the behavior of the LCDA at small momenta. In Fig. 2.9e, we show the truncated expansion for the derivative at the origin

$$\phi'_+(0)_K = \frac{1}{\omega_0^2} \sum_{k=0}^{K} a_k \,. \tag{2.95}$$

The plot indeed shows no convergence, as the model predicts. In Fig. 2.9f, we show the saturation of the normalized Laplace transform,

$$\ell_n(\mu_0, 1/\lambda_B) = \frac{n^2}{\lambda_B^2} \left(\frac{1+a}{n+1+a} \right)^{2+a} \qquad \text{[Beneke et al.]}\,, \tag{2.96}$$

at $n = 5$. Here, the saturation behavior is comparable to the exponential model.

2.4. Pseudo-phenomenology

In this section, we examine how the parametrization performs in a global analysis, considering various sources of information that constrain the LCDA in different ways. These sources include pseudo-observables (i.e., values derived from the LCDA used in predictions, although not experimentally observable) and purely theoretical information about the LCDA's short-distance behavior. A-priori one has to investigate whether certain inputs complement each other in a global analysis, leading to a more precise and consistent picture when combined. Hypothetically, constraints may be redundant, not improving the precision, or they may require a high truncation level for a consistency, which would render the parametrization impractical for such applications.

Generally, various methods probe different aspects of the LCDA. This can be visualized at the hand of the respective quantities expressed through the LCDA in position-space. In Fig. 2.10, we sketch the location of various quantities in the complex τ plane of $\tilde{\phi}_+(\tau)$. The logarithmic moments $L_0 = \lambda_B^{-1}$, L_1, etc., appearing in the QCD factorization approach, can be expressed as weighted integrals over the negative imaginary axis (see Eq. (2.19)), indicated by a red bar. The short-distance expansion, accessible through the OPE, provides information about a restricted band-like region in the lower-half plane close to the origin, which is drawn as a blue arc (see Chapter 3 for details). The Laplace transform ℓ_n, relevant in the QCD sum rules approach, corresponds to the values of $\tilde{\phi}_+(\tau)$ on the negative imaginary axis (see Eq. (2.26)), denoted for a single value by a cross.

In the following discussion, we do not conduct a rigorous statistical analysis of variables and constraints to draw quantitative conclusions. Instead, we address the above question qualitatively, emphasizing transparency, in a pseudo-phenomenological study.

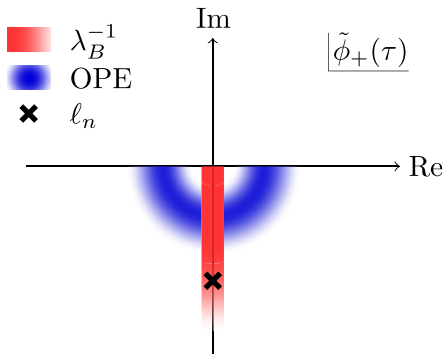

Figure 2.10.: The location of different quantities in the complex τ plane of the LCDA's position-space representation.

The parametrization allows estimating the impact of the constraints on the LCDA based on an ad-hoc assumption about the growth: Order by order, we constrain the bound's relative growth to remain below a certain threshold; in principle, this yields an arbitrary number of inequality constraints to yield a bounded region for the joint distributions of the parameters. Rather than an estimate, one can also view this procedure as a test of whether the parametrization can account for the physical constraints under "plausible" conditions, i.e., without large high-order coefficients or specific tuning of the auxiliary scale.

We conduct this study in two stages: in Section 2.4.1, we consider only typical phenomenological constraints. In Section 2.4.2, we extend the analysis using theory input to examine the effect when combining both sources.

2.4.1. Using λ_B and ℓ_5 as Phenomenological Constraints

We explore a hypothetical scenario where certain experimental or theoretical information constrains two specific pseudo-observables,

$$p_1 \equiv L_0(\mu_0, \mu_m) \qquad \text{and} \qquad p_2 \equiv \lambda_B^2\, \ell_5(\mu_0, 1/\lambda_B)\,, \tag{2.97}$$

at a low reference scale μ_0. These pseudo observables play a significant role in the theoretical description of the $\bar{B}^- \to \gamma\mu^-\bar{\nu}$ form factors (cf. Chapter 4), and it is anticipated that the Belle II experiment will provide measurements for this decay [9, 17, 36]. Additionally, they probe complementary aspects of the LCDA; while the inverse moment L_0 is sensitive to the bulk region of the LCDA, the Laplace transform ℓ_5 depends predominantly on the low-momentum behavior. We omit uncertainties in these parameters for simplicity, in contrast to a more rigorous analysis where uncertainties and correlations require careful treatment.

In the following, we consider $K = 2$, i.e., the parameters a_0, a_1, and a_2 as well as the scale ω_0. The two phenomenological constraints allow us to express two of the parameters through the others; we express a_0 and a_1 in terms of a_2, $\xi = \omega_0/\lambda_B = \omega_0\, p_1$, and p_2:

$$\begin{aligned} a_0 &= \xi - \frac{a_2}{3}\,, \\ a_1 &= \frac{(5\xi+1)^3}{25\,(5\xi-1)}\, p_2 - \frac{\xi\,(5\xi+1)}{5\xi-1} - \frac{2\,(25\xi^2-20\xi+1)}{3(5\xi+1)(5\xi-1)}\, a_2\,. \end{aligned} \tag{2.98}$$

This leaves the scale ratio ξ and the coefficient a_2 as free variables, which must be constrained by other means. Inspired by the model study in the previous subsection, we limit the coefficient bound's relative growth to 20% (for $K = 1$) and 10% (for $K = 2$),

$$\frac{|a_1|^2}{|a_0|^2+|a_1|^2} \le 0.2\,, \qquad\qquad \frac{|a_2|^2}{|a_0|^2+|a_1|^2+|a_2|^2} \le 0.1\,. \tag{2.99}$$

Combining the inequalities with Eq. (2.98) provides a bounded region in the parameter space for ξ and a_2. This allows us to determine minimal and maximal values for any given pseudo observable, expressed through the parametrization. For example, the normalized logarithmic moment at the reference scale $\mu_m = 1/p_1\, \mathrm{e}^{-\gamma_E}$ is given by

$$\sigma_B\big|_2 \equiv -\frac{1}{p_1}\, L_1(\mu_0, 1/p_1\, \mathrm{e}^{-\gamma_E})\Big|_{K=2} = -\ln\xi + \frac{a_1}{\xi}\,. \tag{2.100}$$

With this setup, at $K = 2$, we determine the resulting ranges for the normalized logarithmic moment σ_B, for the LCDA $\phi_+(\omega)$ at different values of $x = \omega\, p_1$, and the normalized Laplace transformation ℓ_n at different (real) values of n. For the input, p_1 and p_2, we consider several scenarios based on the predictions of each of the four models discussed in Section 2.3.

Exponential Model The exponential model, given in Eq. (2.79), predicts

$$p_2 = \frac{25}{36} \simeq 0.694\,, \qquad [\text{exp. model}]\,. \tag{2.101}$$

We determine the maximal range of σ_B according to the variation of the free parameters ξ and a_2 within the growth criterion. This results in

$$\begin{aligned} \sigma_B\big|_2^{\min} &= -0.073 \qquad \text{for } \xi \to 1.332 \text{ and } a_2 \to +0.410\,, \\ \sigma_B\big|_2^{\max} &= +0.172 \qquad \text{for } \xi \to 1.489 \text{ and } a_2 \to -0.625\,, \end{aligned} \tag{2.102}$$

which contains the exponential model's exact prediction $\sigma_B = 0$. In Fig. 2.11a and Fig. 2.12a, we show the momentum-space LCDA and its Laplace transform, respectively, along the curves corresponding to the extreme values of σ_B. The extreme values for both functions are determined through numerical optimization for each value of x and n, resulting in the parameter intervals $0.607 < \xi < 1.499$, $-0.633 < a_2 < 0.477$ (for ϕ_+) and $0.607 < \xi < 1.636$, $-0.632 < a_2 < 0.539$ (for ℓ_n). We observe the following:

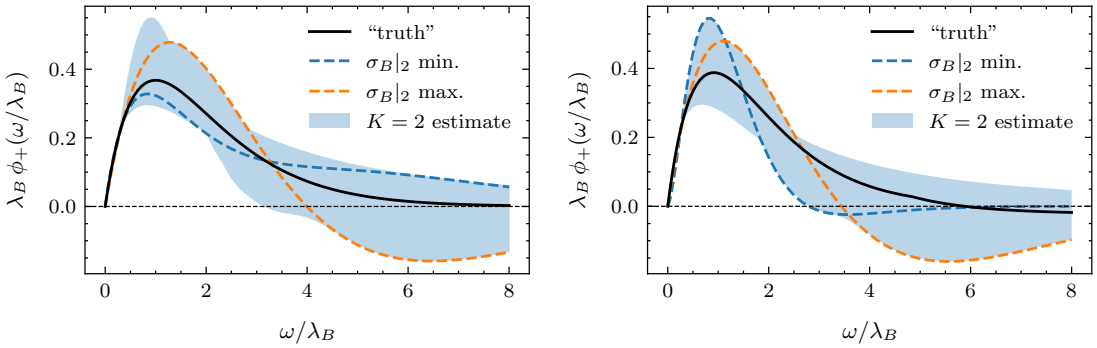

(a) Using the exponential model in Eq. (2.79) **(b)** Using the Lee-Neubert model Eq. (2.85)

Figure 2.11.: B-meson LCDA in momentum space using the two pseudo-observables $p_{1,2}$ as predicted by two models as a function of $x = \omega/\lambda_B$. We show the model ("truth"), the curves corresponding to extreme values of σ_B and the total variation of the parametrized LCDA.

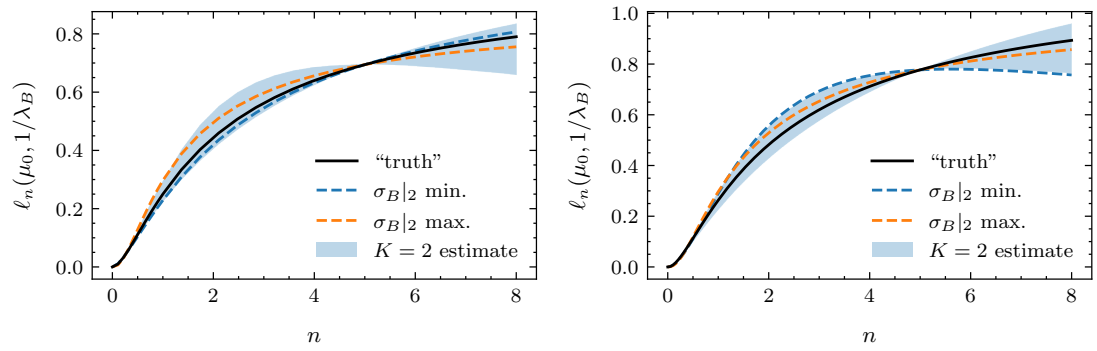

(a) Using the exponential model in Eq. (2.79) **(b)** Using the Lee-Neubert model in Eq. (2.85)

Figure 2.12.: Normalized Laplace transform $\ell_n(\mu_0, 1/\lambda_B)$ using the two pseudo-observables $p_{1,2}$ as predicted by two models as a function of $x = \omega/\lambda_B$. We show the model ("truth"), the curves corresponding to extreme values of σ_B and the total variation of the parametrized Laplace transform.

1. The pseudo-observables p_1 and p_2 strongly constrain the behavior of $\phi_+(\omega)$ at low momentum, as well as the behavior of its Laplace transform at large values of $\zeta = -i\tau \gg 1/\lambda_B$.
2. The shape of $\phi_+(\omega)$ at intermediate values of ω is sensitive to the variation of ξ; further constraints are needed to gain precision in this region.
3. The Laplace transform remains stable, reflecting a monotonous function (except around the origin). While the information is, by construction, precise for $n = 5$, the band becomes broader for both small and very large values of $\zeta = n/\lambda_B$.

Overall, this already indicates that a global fit would benefit from additional input about the Laplace transform at small values of ζ, corresponding to the position-space LCDA at small negative imaginary arguments, $\tilde{\phi}_+(-i\tau)$, $t \ll 1/\lambda_B$. We discuss a consistent implementation of short-distance behavior in the following Section 2.4.2.

Lee-Neubert Model with Radiative Tail The Lee-Neubert model, given in Eq. (2.85), predicts

$$p_2 \simeq 0.777 \qquad \text{[Lee/Neubert]}\,, \tag{2.103}$$

which is slightly larger than the exponential model's prediction. The corresponding ranges for the logarithmic moment follow as

$$\begin{aligned} \sigma_B\big|_2^{\min} &= 0.045 \quad \text{for } \xi \to 0.541 \text{ and } a_2 \to -0.225\,, \\ \sigma_B\big|_2^{\max} &= 0.321 \quad \text{for } \xi \to 1.283 \text{ and } a_2 \to -0.543\,, \end{aligned} \tag{2.104}$$

which includes the value $\sigma_B \simeq 0.315$ predicted by the model. The larger input value for p_2 results in an increase of σ_B. In Fig. 2.11b and Fig. 2.12b, we plot the momentum-space LCDA and its Laplace transform. The parameter ranges, extracted from numerical optimization of the observables at each point, are $0.498 < \xi < 1.342$, $-0.546 < a_2 < 0.439$ (for ϕ_+), and $0.540 < \xi < 1.381$, $-0.536 < a_2 < 0.458$ (for ℓ_n).

Naïve Parton Model The naïve parton model, given in Eq. (2.88), predicts

$$p_2 = (1 - 11\,\mathrm{e}^{-10})/2 \simeq 0.5 \qquad \text{[parton model]}\,, \tag{2.105}$$

which is, contrary to the Lee-Neubert model, smaller than the exponential model's prediction. The range of values for σ_B follow as

$$\begin{aligned} \sigma_B\big|_2^{\min} &= -0.565 \quad \text{for } \xi \to 1.810 \text{ and } a_2 \to +0.543\,, \\ \sigma_B\big|_2^{\max} &= -0.231 \quad \text{for } \xi \to 2.228 \text{ and } a_2 \to -0.943\,, \end{aligned} \tag{2.106}$$

which includes the model prediction $\sigma_B \simeq -0.270$. We find that the parameter values are constrained to the intervals $0.824 < \xi < 2.229$, $-0.948 < a_2 < 0.536$ (for ϕ_+), and $0.824 < \xi < 2.242$, $-0.947 < a_2 < 0.697$ (for ℓ_n). Again, the pseudo-fit shows a positive correlation between p_2 and σ_B.

Model with $\phi'_+(0) \to \infty$ The model in Eq. (2.92) results in the value

$$p_2 \simeq 0.701\,, \qquad \text{[Beneke et al.]} \tag{2.107}$$

very close to the prediction of the exponential model; based on this prediction alone, the two models cannot be distinguished. We note that the previous result based on the exponential model excludes this model's prediction, $\sigma_B = 0.453$. Since the model exhibits pathological behavior at $\omega \to 0$, the low-momentum region cannot be approximated well at low truncation order.

2.4.2. Including Theory Constraints from the Short-distance OPE

Contrary to the whole τ range of the position-space LCDA, the short-distance behavior for $|\tau| \sim 1/\mu \ll 1/\Lambda_{\text{QCD}}$ can be constrained by theoretical considerations. Essentially, the non-local operator of the LCDA can be expanded as a sum of local operators with coefficient weights. The hadronic matrix elements of the local operators can be reduced to a small set of parameters, while the coefficients can be extracted from a partonic matching calculation. Without going into further detail here, we use the following result [37]:

$$\begin{aligned}\tilde{\phi}_+(\tau,\mu) = 1 - \frac{\alpha_s C_F}{4\pi}\left(2L^2 + 2L + \frac{5\pi^2}{12}\right) \\ - i\tau\,\frac{4\bar{\Lambda}}{3}\left[1 - \frac{\alpha_s C_F}{4\pi}\left(2L^2 + 4L - \frac{9}{4} + \frac{5\pi^2}{12}\right)\right] + \mathcal{O}(\tau^2\Lambda^2_{\text{QCD}})\,.\end{aligned} \tag{2.108}$$

Here, $\bar{\Lambda}$ is a hadronic parameter (related to the HQET mass parameter in the on-shell scheme), and we abbreviate $L = \ln(i\tau\mu \mathrm{e}^{\gamma_E})$.

The Lee-Neubert model in Eq. (2.85) aims to incorporate short-distance information by extending the momentum-space representation with a tail. This extension is motivated by "cut off moments", $M_n(\Lambda_{\text{UV}}) = \int_0^{\Lambda_{\text{UV}}} \mathrm{d}\omega\, \omega^n\, \phi_+(\omega)$, also obtained through the operator product expansion. The large-ω tail is deduced based on the dependence of M_0 on the upper integration limit Λ_{UV}. Using the parametrization, on the other hand, offers a more straightforward way to incorporate short-distance information, as both the position- and momentum-space representations rely on a universal set of parameters. These parameters are directly constrained by comparing the LCDA parametrization with the OPE result in Eq. (2.108). To that end, we match the power counting of the OPE by expanding in $\omega_0/\mu_0 \ll 1$ for a fixed value of

$$x_0 \equiv i\tau_0\mu_0\, \mathrm{e}^{\gamma_E} \sim \mathcal{O}(1)\,. \tag{2.109}$$

As the theory input derived from the OPE, we consider the value and first derivative of $\tilde{\phi}_+(\tau)$ at a fixed value τ_0:

$$t_1 \equiv \tilde{\phi}(\tau_0,\mu_0)\,, \qquad t_2 \equiv i\frac{\mathrm{d}\tilde{\phi}(\tau,\mu_0)}{\mathrm{d}\tau}\bigg|_{\tau=\tau_0}\,. \tag{2.110}$$

It is instructive to study the minimal case at $K = 1$ first, where the parameters a_0 and a_1 are fixed by matching t_1 and t_2, based on Eq. (2.108), to the parametrization. The result reads

$$\begin{aligned} a_0 &= 2 - \frac{2\bar{\Lambda}}{3\omega_0} + \frac{\alpha_s C_F}{4\pi}\left(-\frac{1}{x_0}\,\frac{\mu_0 \mathrm{e}^{\gamma_E}}{\omega_0}\,(1 + 2\ln x_0) + \ldots\right), \\ a_1 &= 1 - \frac{2\bar{\Lambda}}{3\omega_0} + \frac{\alpha_s C_F}{4\pi}\left(-\frac{1}{x_0}\,\frac{\mu_0 \mathrm{e}^{\gamma_E}}{\omega_0}\,(1 + 2\ln x_0) + \ldots\right), \end{aligned} \tag{2.111}$$

showing only the α_s corrections that are enhanced by μ_0/ω_0. These terms can be absorbed by a convenient redefinition of the scheme-dependent parameter $\bar{\Lambda}$[5]:

$$\bar{\Lambda} \equiv \bar{\Lambda}_a(\mu, x_0)\left[1 + \frac{\alpha_s C_F}{4\pi}\left(10\,\ln x_0 + \frac{15}{4}\right)\right] - \frac{\alpha_s C_F}{4\pi}\,\frac{3\mu \mathrm{e}^{\gamma_E}}{2x_0}\,(1 + 2\ln x_0)\,. \tag{2.112}$$

The leading-order result for the parameters using this scheme is given by

$$\begin{aligned} a_0 &= Z(x_0)\left(2 - \frac{2\bar{\Lambda}_a}{3\omega_0} - \frac{8\alpha_s C_F}{3\pi}\,\frac{\bar{\Lambda}_a x_0}{\mu_0 \mathrm{e}^{\gamma_E}}\,(1 + \ln x_0)\right), \\ a_1 &= Z(x_0)\left(1 - \frac{2\bar{\Lambda}_a}{3\omega_0} - \frac{4\alpha_s C_F}{3\pi}\,\frac{\bar{\Lambda}_a x_0}{\mu_0 \mathrm{e}^{\gamma_E}}\,(1 + \ln x_0)\right), \end{aligned} \tag{2.113}$$

with

$$Z(x_0) = 1 + \frac{\alpha_s C_F}{4\pi}\left(-2\ln^2 x_0 + 2\ln x_0 + 2 - \frac{5\pi^2}{12}\right). \tag{2.114}$$

Our definitions of $\bar{\Lambda}_a$ and $Z(x_0)$ ensure the position-space LCDA at finite truncation K satisfies

$$\begin{aligned} \tilde{\phi}_+(0)\big|_K &= \sum_{k=1}^{K}(-1)^k\, a_k = Z(x_0) - \frac{4\alpha_s C_F}{3\pi}\,\frac{\bar{\Lambda}_a x_0}{\mu_0 \mathrm{e}^{\gamma_E}}\,(1 + \ln x_0)\,, \\ \tilde{\phi}'_+(0)\big|_K &= -2i\omega_0 \sum_{k=1}^{K}(-1)^k\,(1 + k)\, a_k = -Z(x_0)\,\frac{4i\bar{\Lambda}_a}{3}\,, \end{aligned} \tag{2.115}$$

extending the Grozin-Neubert relations for M_0 and M_1 in Ref. [18] from tree-level to 1-loop accuracy in our formalism. Our expressions can also be related to the corresponding ones for M_0 and M_1 in Ref. [35]. The perturbative relation for the mass parameter in their "distribution amplitude scheme" $\bar{\Lambda}_{\mathrm{DA}}$ and in our "parameter scheme" $\bar{\Lambda}_a$ reads

$$\begin{aligned} \bar{\Lambda}_a(\mu, x_0) = \bar{\Lambda}_{\mathrm{DA}}(\mu, \mu)\left[1 + \frac{\alpha_s C_F}{4\pi}\,(-10\,\ln x_0 - 2)\right] \\ + \mu\,\frac{\alpha_s C_F}{4\pi}\left(\frac{3\,\mathrm{e}^{\gamma_E}}{2x_0}\,(1 + 2\ln x_0) - \frac{9}{2}\right). \end{aligned} \tag{2.116}$$

[5]The authors of Ref. [35] similarly define a "distribution amplitude (DA) scheme" for $\bar{\Lambda}$, based on the quantities M_0 and M_1.

For instance, using $x_0 = 1$, $\mu_0 = 1\,\text{GeV}$, $\bar{\Lambda}_{\text{DA}}(\mu_0, \mu_0) = 519$ MeV, and $\alpha_s(\mu_0) = 0.5$ (as in Ref. [35]), the parameter numerically amounts to

$$\bar{\Lambda}_a(\mu_0, x_0) = 367\,\text{MeV}\,.$$

Using our scheme setup, we combine the theory input $t_{1,2}$ with the phenomenological constraints $p_{1,2}$. For legibility, we further introduce

$$n_0 \equiv i\tau_0\omega_0 = \frac{x_0\omega_0}{\mu_0 \mathrm{e}^{\gamma_E}}\,. \tag{2.117}$$

To use the theory constraint effectively, we need simultaneous convergence of the operator product expansion and the parametrization, such that a limited number of operators and parameters are sufficient. Quantitatively, that translates to the requirement $x_0 \sim \mathcal{O}(1)$ and small but finite $n_0 > 0$. In the following pseudo-fit, we choose

$$n_0 = 1/3\,, \quad \mu_0 = 1\ \text{GeV}\,,$$

while the value of ω_0 (i.e., x_0) varies within the fit under suitable constraints on the relative growth. For instance, a value $x_0 = 1$ corresponds to $\omega_0 \approx 600$ MeV, consistent with the observations from the model study in Section 2.3, assuming that (very roughly) $\lambda_B \approx 500\,\text{MeV}$. The value $n_0 = 1/3$ corresponds to $y_0 = -1/2$ of the conformal mapping in Eq. (2.29), located exactly halfway between the origin and $y = -1$ (corresponding to the local limit $\tau \to 0$), which implies reasonable convergence of the parametrization.

As the number of constraints doubles, we increase the truncation level of the pseudo-fit from $K = 2$ to $K = 4$, leaving the free parameters $a_4(\mu_0)$ and $\xi = \omega_0/\lambda_B$. For reference, we quote the resulting parameters for $\xi = 1$ and $x_0 = 1$:

$$\begin{aligned}
a_0 &= Z\left(-\frac{28}{25} + \frac{2\bar{\Lambda}_a p_1}{15}\right) + \frac{112\alpha_s C_F}{75\pi}\,\bar{\Lambda}_a n_0 p_1 + 3 - \frac{972\,p_2}{625} - \frac{4a_4}{15}\,,\\
a_1 &= Z\left(-2 + \frac{\bar{\Lambda}_a p_1}{3}\right) + \frac{8\alpha_s C_F}{3\pi}\,\bar{\Lambda}_a n_0 p_1 + \frac{3}{2} - \frac{4a_4}{5}\,,\\
a_2 &= Z\left(\frac{84}{25} - \frac{2\bar{\Lambda}_a p_1}{5}\right) - \frac{112\alpha_s C_F}{25\pi}\,\bar{\Lambda}_a n_0 p_1 - 6 + \frac{2916\,p_2}{625} + \frac{a_4}{5}\,,\\
a_3 &= Z\left(\frac{81}{25} - \frac{3\bar{\Lambda}_a p_1}{5}\right) - \frac{108\alpha_s C_F}{25\pi}\,\bar{\Lambda}_a n_0 p_1 - \frac{9}{2} + \frac{1944\,p_2}{625} + \frac{26a_4}{15}\,,
\end{aligned} \tag{2.118}$$

where $Z \equiv Z(x_0 = 1)$. The result for general ξ and x_0 is given in Appendix A.2. We constrain the parameter range for a_4 and ξ using generalized ad-hoc conditions on the relative growth, analogous to Eq. (2.99):

$$\text{Gr}[\chi]_K \leq \frac{20\%}{K}\,. \tag{2.119}$$

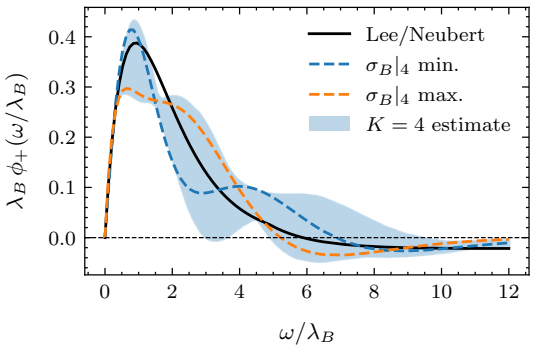

(a) Momentum-space LCDA

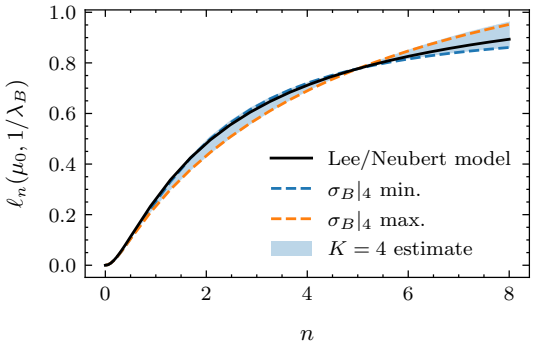

(b) Laplace transform ℓ_n

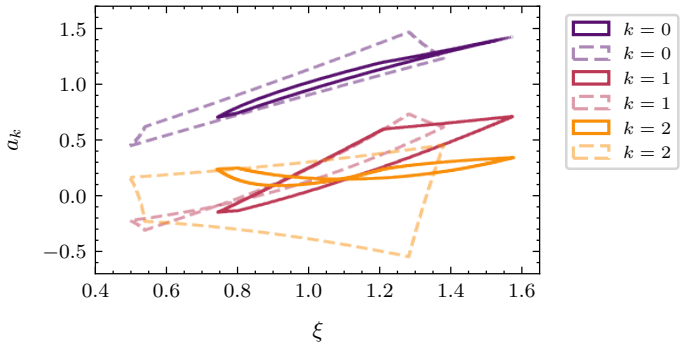

(c) Bounded regions for each parameter

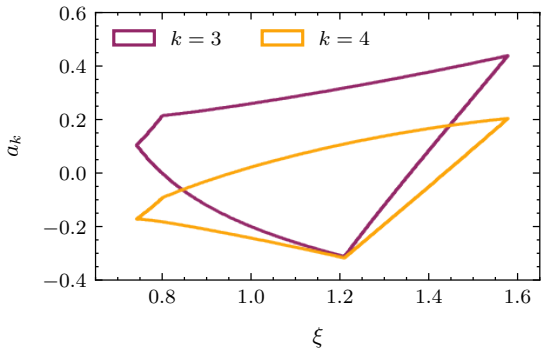

(d) Bounded regions for each parameter

Figure 2.13.: Results from the pseudo-fit using both theoretical inputs t_1 and t_2 as well as phenomenological inputs p_1 and p_2. The dashed regions in Fig. 2.13c correspond to the pseudo-fit *without* theoretical OPE constraints t_1 and t_2.

Among the models discussed in Section 2.3, only the Lee-Neubert model in Eq. (2.85) takes the local OPE information into account by means of the radiative tail. Therefore, this model is the appropriate reference here since it aims to reflect the various information we use as input and thus we expect consistency between the model and our result. Therefore, we use the model's predictions

$$p_1 = 1/\lambda_B = 2.085\,\text{GeV}^{-1}\,, \quad p_2 = 0.777 \qquad \text{[Lee/Neubert]}\,, \tag{2.120}$$

using the same parameter values as outlined below Eq. (2.85), while $\bar{\Lambda}_a$ is calculated from Eq. (2.116) as a function of x_0.

The parametrization of the normalized first logarithmic moment at $K = 4$ reads

$$\sigma_B\big|_4 = -\ln\xi + \frac{a_1 + 2/3\,a_3}{\xi}\,. \tag{2.121}$$

We find the following value ranges, constrained by the growth criterion,

$$\begin{aligned} \sigma_B\big|_4^{\text{min}} &= 0.114 \quad \text{for } \xi \to 0.961 \text{ and } a_2 \to -0.232\,, \\ \sigma_B\big|_4^{\text{max}} &= 0.217 \quad \text{for } \xi \to 0.905 \text{ and } a_2 \to -0.030\,. \end{aligned} \tag{2.122}$$

This interval is compatible with the previous estimate based only on p_1 and p_2; however, its size is decreased by more than 60%. The value $\sigma_B = 0.315$, as predicted by the Lee-Neubert model, is not contained in the range.

In Fig. 2.13a and Fig. 2.13b, we show the resulting momentum-space LCDA and its Laplace transform. Their respective extreme values numerically lead to the parameter ranges $0.745 < \xi < 1.577$, $-0.319 < a_4 < 0.201$ (for ϕ_+), and $0.743 < \xi < 1.522$, $-0.312 < a_4 < 0.120$ (for ℓ_n). The convergence window for ξ is shifted to higher values when adding the OPE information, in line with the analogous comparison of the exponential model with the Lee-Neubert model in Section 2.3. In Fig. 2.13c, we compare the resulting bounded regions for the coefficients a_0 through a_2 obtained with either four or the previous two constraints. Both results are consistent with each other: The respective regions largely overlap, with significantly reduced area for a_0 and a_2 and approximately the same area for a_1. Fig. 2.13d contains the regions for the additional coefficients a_3 and a_4.

Overall, the pseudo-fit setup suggests that incorporating theoretical constraints into a global fit of our parametrization indeed improves the accuracy. Even at low truncation levels we do not encounter consistency issues. It is important to note that this study's plots and numerical results demonstrate the potential for a global fit, but they should not be mistaken for predictions.

position-space LCDA	$\tilde{\phi}_+(\tau,\mu_0)$	$= \dfrac{1}{(1+i\omega_0\tau)^2}\sum_{k=0}^{K} a_k(\mu_0)\left(\dfrac{i\omega_0\tau-1}{i\omega_0\tau+1}\right)^k$
momentum-space LCDA	$\phi_+(\omega,\mu_0)$	$= \dfrac{\omega\,\mathrm{e}^{-\omega/\omega_0}}{\omega_0^2}\sum_{k=0}^{K} a_k(\mu_0)\,\dfrac{1}{1+k}\,L_k^{(1)}(2\omega/\omega_0)$
dual-space LCDA	$\eta_+(s,\mu_0)$	$= \mathrm{e}^{-s\omega_0}\sum_{k=0}^{K} a_k(\mu_0)\,\dfrac{(-1)^k}{1+k}\,L_k^{(1)}(2\omega_0 s)$
generating function	$F_{[\eta_+]}(t;\mu_0,\mu_m)$	$= \dfrac{\Gamma(1-t)}{\omega_0}\left(\dfrac{\hat{\mu}_m}{\omega_0}\right)^{-t}\sum_{k=0}^{K} a_k(\mu_0)\,{}_2F_1(-k,1+t,2,2)$
inverse moment	$\lambda_B^{-1}(\mu_0)$	$= \dfrac{1}{\omega_0}\sum_{k=0}^{K} a_k(\mu_0)\,\dfrac{1+(-1)^k}{2\,(1+k)}$ (only even k)
1st logarithmic moment	$\sigma_B(\mu_0)$	$= -\ln\dfrac{\omega_0}{\lambda_B} - \dfrac{\lambda_B}{\omega_0}\sum_{k=0}^{K} a_k(\mu_0)\left[\dfrac{\mathrm{d}}{\mathrm{d}t}\,{}_2F_1(-k,1+t;2;2)\right]_{t=0}$ (only odd k)
derivative at $\omega=0$	$\phi_+'(0,\mu_0)$	$= \dfrac{1}{\omega_0^2}\sum_{k=0}^{K} a_k(\mu_0)$

Table 2.1.: Summary of representations and pseudo observables related to the leading-twist B-meson LCDA expressed through our proposed parametrization at the low-energy reference scale μ_0. Here, $L_k^{(1)}$ denote associated Laguerre polynomials and $\xi = \omega_0/\lambda_B$.

2.5. Summary and Outlook

We introduced a new systematic parametrization of the leading-twist B-meson light-cone distribution amplitude (LCDA) in position space and other representations. The approach's core is a Taylor expansion of the LCDA using a carefully chosen variable called y, arising from the conformal transformation in Eq. (2.29). The coefficients of this expansion adhere to an integral bound, Eq. (2.35), which helps to estimate the error when the expansion is truncated. The numerical value of this bound is presently unknown. Our parametrization yields straightforward formulas for various LCDA-related quantities, such as its logarithmic moments and commonly used pseudo-observables which characterize the low-momentum behavior. We summarized the essential formulas in Table 2.1. In addition, we explored three different methods for implementing the renormalization-group evolution of the LCDA in our framework, including one approach that is particularly suitable for efficient numerical computations.

We conducted detailed numerical studies to demonstrate the versatility of our parametrization in capturing various benchmark models, including complex features such as the "radiative tail" occurring at large light-cone momenta. We further demonstrated the power of our approach to combine various phenomenological and theoretical constraints for the purpose of a global analysis. This was accomplished by matching the universal expansion parameters of the LCDA with hypothetical values of two pseudo-observables

outlined in Eq. (2.97), which are expected to be constrained by future experimental data on the photo-leptonic decay process $B \to \gamma\ell\nu$. In addition, we illustrated the integration of theoretical constraints derived from the operator product expansion at small but non-zero light-cone separations in a direct, transparent way. The successful proof-of-concept study in this chapter motivates the much more sophisticated analysis that is the subject of Chapter 4.

Our general framework allows us to readily accommodate future theoretical refinements. First, it can be applied to the higher-twist LCDAs of the B-meson, as we briefly discussed in relation to the Wandzura-Wilczek component of the twist-three LCDA ϕ_-. Second, we can incorporate 2-loop RG evolution into the truncated expansion. Third, we can implement improvements to the short-distance constraint, for example by including higher-dimensional local operators in the OPE or, for applications of the parametrization to the B_s LCDA, by including the effect of a finite spectator quark mass (see Chapter 3). Lastly, for phenomenological applications of the truncated expansion, determining the value of the integral bound in the future through QCD-based methods, such as lattice QCD or QCD sum rules, would enable us to quantify truncation errors more reliably (further detailed in Chapter 4).

3. Strange-Quark Mass Effects in the B_s Meson's Light-cone Distribution Amplitude

The main results in this chapter and Appendix B have been published in

> T. Feldmann, P. Lüghausen, and N. Seitz. "Strange-quark mass effects in the B_s meson's light-cone distribution amplitude". In: *JHEP* 08 (2023), p. 075. DOI: 10.1007/JHEP08(2023)075. arXiv: 2306.14686 [hep-ph].

The short-distance behavior of the leading-twist B-meson LCDA is accessible through the operator product expansion (OPE) in position space, imposing a genuine theory constraint. As discussed in Chapter 2, the short-distance behavior constrains the LCDA in a different region of the complex τ plane than the pseudo-observables that enter theoretical predictions of decays. Thus, it provides a valuable complementary information in a global analysis (see also Chapter 4).

We start with a brief overview of previous applications of the OPE for the LCDA's light-ray operator. Instead of the behavior at short distance in position space, one can derive the behavior at large light-cone momentum fraction ω in momentum space by studying the cut-off dependence of positive moments $\langle\omega^n\rangle = \int_0^{\Lambda_{\rm UV}} \mathrm{d}\omega\, \omega^n\, \phi_+(\omega;\mu)$ [35]. Here, the term "radiation tail" was coined for the model-independent prediction of the large-ω behavior induced by gluon exchange at next-to-leading order in perturbation theory. While this approach transparently addresses perturbative effects for pseudo-observables expressed as integrals of the momentum-space LCDA, it lacks control over the systematic uncertainty.

Later, the OPE was evaluated in position space directly, resulting in a systematic short-distance expansion of $\tilde{\phi}_+(\tau)$. Currently, this includes perturbative corrections at next-to-leading order and local operators in the OPE of mass dimension 3, 4, and 5 [37]. At leading order in perturbation theory, the result corresponds to an expansion in powers of $(-i\tau)$. At next-to-leading order, the expansion coefficients additionally depend on logarithms $\ln(-i\tau\mu\,\mathrm{e}^{\gamma_{\rm E}})$, with the renormalization scale μ and Euler's constant $\gamma_{\rm E}$. Consequently, the result is valid in a finite, band-like region in the complex τ plane: on the one hand, the absolute value must be sufficiently small so that higher-dimensional orders in the OPE are power-suppressed. On the other hand, the value of τ must be compatible with the

scale μ to keep the logarithms under control. Thus, the short-distance behavior obtained using the OPE can be used straightforwardly as a constraint for the LCDA in position space. However, the implications for the phenomenologically relevant pseudo-observables need to be clarified. We address this issue with the systematic parametrization proposed in Chapter 2 by expressing the position-space LCDA and the pseudo-observables by the same set of parameters.

The short-distance expansion depends on the separation of the scales between $1/\tau$ and the hadronic scales of the order of Λ_{had}, so that

$$|\tau\,\Lambda_{\text{had}}| \ll 1 \tag{3.1}$$

is a suitable expansion parameter. Taking $\Lambda_{\text{had}} \sim 1\,\text{GeV}$, one can roughly estimate the effect of the spectator-quark mass in such an expansion. For the B_q meson with a light spectator quark of mass m_q, the mass effect is roughly suppressed by $m_q/\Lambda_{\text{had}} \sim 1\,\%$ compared to other contributions. In the case of the B_s meson, however, the ratio $m_s/\Lambda_{\text{had}} \sim 10\,\%$ is more considerable and warrants closer attention.

We update the existing result for the LCDA's short-distance behavior with the effect of a non-zero spectator quark mass. This update enables the application of the short-distance constraint in global analyses involving the B_s-meson LCDA using the systematic parametrization. The range of applications that potentially benefit from this update include non-leptonic two-body decays [38–41] and rare radiative and semi-leptonic decays [42, 43]. For comprehensive reviews and additional references, see Refs. [9, 44]. As a notable example, our parametrization was already used (without the short-distance constraint) in Ref. [45] for QED corrections to $B_s \to \mu^+\mu^-$ decays, where internal photons resolve the hadronic structure of the B_s meson.

This chapter is organized as follows: in Section 3.1, we reiterate the definition of the 2-particle light-cone distribution amplitudes of the B-meson, introducing convenient notation that we use throughout this chapter. We proceed with a detailed description of the local OPE, including a brief review of literature results.

In Section 3.2, we focus on deriving the matching coefficient for the dimension-4 operator induced by the strange-quark mass. For this purpose, we use a convenient setup analogous to a non-relativistic model for the LCDA that has been considered in the literature previously. We obtain the matching coefficient in position space from momentum-space Feynman integrals using dimensional regularization. This involves straightforward subtractions at the stage of the Fourier transformation, before the expansion in $D-4$ dimensions, which suggests a simplified general procedure for the extraction of the matching coefficients from momentum-space Feynman integrals.

Building on the previous findings, we perform a comprehensive calculation of all matching coefficients in Section 3.3, which not only recovers our previous result for the mass-induced

operator coefficient, but also reproduces the known matching coefficients for the massless limit. We further obtain the matching coefficients for the OPE applied to the subleading twist 2-particle LCDA $\tilde{\phi}_-(\tau)$ up to dimension 4.

Section 3.4 discusses the implications of the short-distance behavior using the systematic parameterization for the leading-twist LCDA. To this end, we perform pseudo-fits similar to those in Chapter 2, this time comparing scenarios with massless and massive spectator quarks. We also compare our results with independent estimates obtained using QCD sum rules.

In Section 3.5, we briefly discuss the potential numerical impact of dimension-5 operators.

We conclude the chapter with a summary of our findings in Section 3.6. Appendix B contains additional detailed formulas concerning operator identities.

3.1. Preliminaries

After introducing convenient definitions related to the 2-particle LCDAs and the OPE, we briefly review the literature. We further introduce the "non-relativistic" setup used for the matching calculation to determine the effect of the spectator quark mass.

3.1.1. Leading and Subleading Twist 2-particle LCDAs

We define the leading-twist LCDA, appearing at leading power in QCD factorization theorems for exclusive B-decays, using a 2-particle light-ray operator in HQET [18],

$$\phi_+(\omega;\mu) = \Big(im_B f_B^{\rm HQET}(\mu)\Big)^{-1} \int \frac{\mathrm{d}\tau}{2\pi}\, \mathrm{e}^{i\omega\tau}\, \langle 0|\bar{q}(\tau n)\,[\tau n,0]\,\not{n}\gamma_5\, h_v(0)|\bar{B}(v)\rangle\,, \tag{3.2}$$

introducing $f_B^{\rm HQET}$, the B-meson decay constant in HQET in the static limit:

$$\langle 0|\bar{q}(0)\,\gamma^\mu\gamma_5\, h_v(0)|\bar{B}(v)\rangle \equiv im_B v^\mu f_B^{\rm HQET}(\mu)\,. \tag{3.3}$$

Above, v^μ with $v^2=1$ is the four-velocity of the heavy meson, the vector n^μ defines a light-ray direction such that $n^2=0$, and we consider the cases $B=B_q$ and B_s. The variable ω is the Fourier conjugate of the light-cone separation τ of the non-local operator[1]. For simplicity, we consider a reference frame where $v\cdot n = 1$. The analogous definition for the subleading-twist 2-particle LCDA, with a modification of the operator structure using $\bar{n}^\mu = 2v^\mu - n^\mu$, reads

$$\phi_-(\omega;\mu) = \Big(im_B f_B^{\rm HQET}(\mu)\Big)^{-1} \int \frac{\mathrm{d}\tau}{2\pi}\, e^{i\omega\tau}\, \langle 0|\bar{q}(\tau n)\,[\tau n,0]\,\not{\bar{n}}\gamma_5\, h_v(0)|\bar{B}(v)\rangle\,. \tag{3.4}$$

[1] At tree level, ω corresponds to the light-cone projection of the light quark's momentum, $\omega = n\cdot k$.

We first concentrate on the leading LCDA $\phi_+(\omega)$ to develop the calculation method at the hand of a concrete operator. This allows us to update the existing results for the short-distance behavior with the effect of a non-zero spectator-quark mass. We generalize our calculation in Section 3.3, where we further derive results for the case of the subleading LCDA $\phi_-(\omega)$.

3.1.2. Short-distance Operator Product Expansion

The short-distance OPE of the light-ray operator defining the leading-twist LCDA symbolically reads

$$\mathcal{O}_+(\tau) \equiv \bar{q}(\tau n)\,[\tau n, 0]\,\not{n}\gamma_5\, h_v(0) = \sum_{n=3}^{\infty}\sum_{k=1}^{K_n} c_k^{(n)}(\tau)\,\mathcal{O}_k^{(n)}(0)\,, \tag{3.5}$$

where the index n corresponds to the mass dimension of the local operator $\mathcal{O}_k^{(n)}$ and K_n counts the number of independent operators for a given dimension n. For practical applications such as here, the equation has to be understood as a plausible ansatz rather than a rigorous statement due to lack of mathematical proof [6]. Evaluated using a hadronic matrix element, the OPE separates hadronization effects related to confinement from partonic effects due to the interaction of quarks and gluons in the regime of asymptotic freedom. While the former relate to non-perturbative long-distance dynamics expressed through hadronic matrix elements of local operators $\mathcal{O}_k^{(n)}$, the latter are associated with the perturbative short-distance dynamics contained in the expansion coefficients $c_k^{(n)}(\tau)$.

On the right-hand side in Eq. (3.5), the coefficients are complex functions, $c_k^{(k)} : \mathbb{C} \mapsto \mathbb{C}$, while the local operators $\mathcal{O}_k^{(n)}$ form a complete set consistent with the transformation properties of the composite operator on the left-hand side. In particular, the operators must be gauge and Lorentz invariant. We can justify the truncation of the sum over n because the operator's mass dimension implies that

$$c_k^{(n)} \propto \tau^{n-3}\,.$$

When τ is sufficiently small compared to all other dimensionful scales (depending on the application), and in the absence of other enhancements, higher orders n of the expansion are systematically suppressed.

The local operators in Eq. (3.5) must be composed using the four vectors appearing on the right-hand side, namely n^μ and v^μ, together with the covariant derivative D^μ (according to QCD gauge symmetry) and spinor-space matrices such as γ^μ. For the concrete case at hand, including all operators up to mass dimension 4[2], the expansion in local operators

[2]See also Ref. [37] for the massless case up to dimension 5.

reads

$$\begin{aligned}\mathcal{O}_+(\tau) = {} & c_1^{(3)}(\tau)\,\bar q\,\not n\gamma_5\,h_v && \text{(dim-3)}\\ & + c_1^{(4)}(\tau)\,\bar q\,(in\cdot\overleftarrow{D})\,\not n\gamma_5\,h_v + c_2^{(4)}(\tau)\,\bar q\,(iv\cdot\overleftarrow{D})\,\not n\gamma_5\,h_v && \text{(dim-4, massless)}\\ & + c_3^{(4)}(\tau)\,m\,\bar q\,\not v\not n\gamma_5\,h_v && \text{(dim-4, massive)}\\ & + \ldots && \text{(dim-5 etc.)}\end{aligned} \tag{3.6}$$

The Dirac structure of the additional dimension-4 operator for the massive case follows from general considerations based on the Feynman rules of HQET. Owing to heavy-quark spin symmetry[3], the generic Dirac structure for the OPE can be cast into the form

$$\bar q(\tau n)[\tau n,0]\Gamma h_v(0) = \sum_i \bar q(0)\,A_i(\tau,n,v,iD)\,\Gamma h_v(0)\,.$$

In the context of the following matching calculation, it becomes clear that only operators of this form receive non-zero matching coefficients. The matrices A_i contain a product of an even number of γ matrices in the massless case [35], whereas terms linear in the spectator mass m must have an odd number of γ matrices. The Dirac structure in A_i can only be one of four,

$$A_i \quad\propto\quad \not n\,,\quad \not v\,,\quad \not n\not v\,,\quad \not v\not n\,,$$

because any product of those matrices can be decomposed again. If a string of matrices strictly contains either $\not n$ or $\not v$, it simplifies using $n^2=0$, $v^2=1$, and $n\cdot v=1$:

$$\begin{aligned}\not n\ldots\not n &= 0\,, && \text{any number}\\ \not v\ldots\not v &= \mathbb{1}\,, && \text{even number}\\ \not v\ldots\not v\not n &= \not n\,. && \text{odd number}\end{aligned}$$

If a string of matrices contains both $\not n$ and $\not v$, it can be rearranged and decomposed using the anti-commutation relation $\not n\not v = -\not v\not n + 2\,\mathbb{1}$:

$$\begin{aligned}\not v\not n\not v &= -\not n + 2\not v\,,\\ \not n\not v\not n &= 2\not n\,.\end{aligned}$$

This determines the single mass term in Eq. (3.6). We rederive the Dirac structures of all operators systematically in Section 3.3; the structures in Eq. (3.6) are specifically simplified for $\mathcal{O}_+$. Moreover, we explicitly include the mass dependence in the operator's definition to maintain a consistent power counting.

[3] Specifically, the manifestation of the symmetry in the property $\not v h_v(x) = h_v(x)$ and the Feynman rules of HQET.

3.1.3. Short-distance Light-cone Distribution Amplitude

The short-distance expansion of the position-space LCDA follows from the OPE by applying the hadronic matrix element $\langle 0|\ldots|\bar{B}(v)\rangle$ on both sides of Eq. (3.6). However, the matrix elements of the local operators on the right-hand side are not independent degrees of freedom. On the one hand, this is due to constraints from the quark field's equations of motion in QCD and leading-power HQET,

$$\left(i\not{D} - m\right) q(x) = 0\,, \tag{3.7}$$

$$(iv\cdot D)\, h_v(x) = 0\,. \tag{3.8}$$

On the other hand, it is due to the hadronic matrix element's properties related to spin, potentially imposing relations between operators containing different Dirac structures. A convenient way to represent the meson's spinor degrees of freedom in the effective theory is through the *covariant trace formalism* [18, 33, 34, 46]. For a generic dimension-3 operator, this amounts to

$$\langle 0|\,\bar{q}_\beta\,(h_v)_\alpha\,\big|\bar{B}\big\rangle \equiv -\frac{F(\mu)}{2}\,\left[\frac{1+\not{v}}{2}\gamma_5\right]_{\alpha\beta}\,, \tag{3.9}$$

where the single free parameter $F(\mu) = im_B f_B^{\text{HQET}}(\mu) = \langle 0|\,\bar{q}\,\not{n}\gamma_5\,h_v\,\big|\bar{B}\big\rangle$ is fixed by the definition of the decay constant in Eq. (3.3). For dimension 4, the equations of motion pose two constraints to fix the parameters a and b of the following generic decomposition:

$$\langle 0|\,\bar{q}_\beta\,i\overleftarrow{D}^\mu\,(h_v)_\alpha\,\big|\bar{B}\big\rangle \equiv -\frac{F(\mu)}{2}\,\left[\frac{1+\not{v}}{2}\,(a\,v^\mu + b\,\gamma^\mu)\,\gamma_5\right]_{\alpha\beta}\,. \tag{3.10}$$

First, we use the adjoint equation of motion for the light quark, $\bar{q}i\overleftarrow{\not{D}} = -m\,\bar{q}$,

$$\begin{aligned}(\gamma_\mu\not{n}\gamma_5)_{\beta\alpha}\,\langle 0|\,\bar{q}_\beta\,i\overleftarrow{D}^\mu\,(h_v)_\alpha\,\big|\bar{B}\big\rangle &= \langle 0|\,\bar{q}\,i\overleftarrow{\not{D}}\not{n}\gamma_5\,h_v\,\big|\bar{B}\big\rangle = -m\,\langle 0|\,\bar{q}\,\not{n}\gamma_5\,h_v\,\big|\bar{B}\big\rangle \\ &\overset{!}{=} -\frac{1}{4}\,\langle 0|\,\bar{q}\,\not{n}\gamma_5\,h_v\,\big|\bar{B}\big\rangle\;\mathrm{tr}\left[(1+\not{v})\,(a\,v^\mu + b\,\gamma^\mu)\,\gamma_5\gamma_\mu\not{n}\gamma_5\right]\,.\end{aligned} \tag{3.11}$$

Evaluating the trace yields the condition $a + 4b = m$. Second, employing the heavy quark's equation of motion requires relating the action of the covariant derivative on the light quark field to the action on the heavy quark field. To this end, consider the total derivative acting on the composite operator:

$$i\partial^\mu\,\bar{q}\Gamma h_v = \bar{q}\,i\overleftarrow{D^\mu}\,\Gamma h_v + \bar{q}\,\Gamma\,iD^\mu\,h_v\,. \tag{3.12}$$

We provide details in Appendix B.1. Taking the hadronic matrix element on the left-hand side of Eq. (3.12) results in [46]

$$\langle 0|\,i\partial^\mu(\bar{q}\Gamma h_v)\,\big|\bar{B}\big\rangle = (m_B - m_b)v^\mu\,\langle 0|\,\bar{q}\Gamma h_v\,\big|\bar{B}\big\rangle\,, \tag{3.13}$$

because the current carries the total momentum minus $m_b v$ due to the field definition of h_v in HQET. The mass difference, conventionally defined as $\bar{\Lambda} \equiv m_B - m_b$, is a non-trivial observable of the effective theory. Contracting both sides with v_μ and using with the heavy quark's equation of motion results in the matrix-element identity

$$\langle 0|\, \bar{q}(iv\cdot \overleftarrow{D})\Gamma h_v \,|\bar{B}\rangle = \bar{\Lambda}\, \langle 0|\, \bar{q}\Gamma h_v \,|\bar{B}\rangle \,. \tag{3.14}$$

Comparison to the decomposition leads to

$$\begin{aligned} v_\mu\, (\not{v}\gamma_5)_{\beta\alpha}\, \langle 0|\, \bar{q}_\beta\, i\overleftarrow{D}^\mu\, (h_v)_\alpha \,|\bar{B}\rangle = \langle 0|\, \bar{q}\, (iv\cdot \overleftarrow{D})\not{v}\gamma_5\, h_v \,|\bar{B}\rangle = \bar{\Lambda}\, \langle 0|\, \bar{q}\, \not{v}\gamma_5\, h_v \,|\bar{B}\rangle \\ \stackrel{!}{=} -\frac{1}{4}\, \langle 0|\, \bar{q}\, \not{v}\gamma_5\, h_v \,|\bar{B}\rangle\ \mathrm{tr}\left[(1+\not{v})\,(a+b\not{v})\,\gamma_5 \not{v}\gamma_5\right] \,, \end{aligned} \tag{3.15}$$

implying $a + b = \bar{\Lambda}$. Altogether, the solution for the generic matrix element reads

$$\langle 0|\, \bar{q}_\beta\, i\overleftarrow{D}^\mu\, (h_v)_\alpha \,|\bar{B}\rangle \equiv -\frac{F(\mu)}{2}\left[\frac{1+\not{v}}{2}\left(\frac{4\bar{\Lambda}-m}{3}\, v^\mu - \frac{\bar{\Lambda}-m}{3}\,\gamma^\mu\right)\gamma_5\right]_{\alpha\beta} \,. \tag{3.16}$$

Evaluating the local operators' hadronic matrix elements using Eq. (3.9) and Eq. (3.16) leads to

$$\frac{\langle 0|\mathcal{O}_1^{(4)}|\bar{B}(v)\rangle}{\langle 0|\mathcal{O}_1^{(3)}|\bar{B}(v)\rangle} = \frac{4\bar{\Lambda}-m}{3} \,, \quad \frac{\langle 0|\mathcal{O}_2^{(4)}|\bar{B}(v)\rangle}{\langle 0|\mathcal{O}_1^{(3)}|\bar{B}(v)\rangle} = \bar{\Lambda} \,, \quad \frac{\langle 0|\mathcal{O}_3^{(4)}|\bar{B}(v)\rangle}{\langle 0|\mathcal{O}_1^{(3)}|\bar{B}(v)\rangle} = -m \,, \tag{3.17}$$

which yields the OPE result for the position-space LCDA:

$$\tilde{\phi}_+(\tau) = c_1^{(3)}(\tau) + \bar{\Lambda}\left(\frac{4}{3}\, c_1^{(4)}(\tau) + c_2^{(4)}(\tau)\right) - m\left(c_3^{(4)}(\tau) + \frac{1}{3}\, c_1^{(4)}(\tau)\right) + \mathcal{O}(\tau^2) \,. \tag{3.18}$$

Note that we renormalize the local operators in the $\overline{\mathrm{MS}}$ scheme, and accordingly, the light quark mass $m \equiv \overline{m}(\mu)$ is to be understood in the same scheme.

3.1.4. Review of Existing Results and Outline of the Setup

Here we provide, for convenience, the existing result for the massless case and outline the setup we use to obtain the new result for the massive case.

The 1-loop contributions to the OPE coefficients up to dimension 5 for the massless case are provided in Ref. [37]. For the study of the leading mass effect, we are only interested in the OPE up to dimension 4, where the coefficients read

$$\begin{aligned} c_1^{(3)}(\tau) &= 1 - \frac{\alpha_s C_F}{4\pi}\left(2L^2 + 2L + \frac{5\pi^2}{12}\right) + \mathcal{O}(\alpha_s^2) \,, \\ c_1^{(4)}(\tau) &= -i\tau\left[1 - \frac{\alpha_s C_F}{4\pi}\left(2L^2 + L + \frac{5\pi^2}{12}\right) + \mathcal{O}(\alpha_s^2)\right] \,, \\ c_2^{(4)}(\tau) &= -i\tau\left[-\frac{\alpha_s C_F}{4\pi}\,(4L-3) + \mathcal{O}(\alpha_s^2)\right] \,, \end{aligned} \tag{3.19}$$

with $L = \ln(i\tau\mu e^{\gamma_E})$ and $C_F = 4/3$. Obviously, our additional operator $\mathcal{O}_3^{(4)}$ receives no contribution in the massless limit.

Generally, the coefficients follow from a matching calculation based on the universality of the OPE coefficients. While it is impossible to calculate hadronic matrix elements in perturbation theory, one can access on-shell matrix elements with asymptotic parton states. Although such asymptotic states are not realized in nature since they are not singlets under $\mathrm{SU}(3)_c$, QCD can describe them consistently. Therefore, evaluating both sides of the OPE using suitable partonic matrix elements allows determining the coefficients $c_k^{(n)}$ as an expansion in the strong coupling α_s.

We perform the matching calculation using the known coefficients in Eq. (3.19) as input, such that only the single coefficient $c_3^{(4)}$ is left undetermined. This enables us to work in a minimal setup, as opposed to a generic, more complicated setup that would allow us to obtain the coefficients of each operator individually. We consider partonic amplitudes between an incoming heavy quark with velocity v^μ and a light anti-quark with momentum $k^\mu = mv^\mu$ and the vacuum. We choose the external (on-shell) heavy quark to carry zero momentum, which is consistent with the definition of the HQET field; the velocity v^μ remains an essential parameter of the effective theory. Introducing no further kinematic scales other than the essential scale m promotes simple loop integrals.

As another advantage of this setup, the results for the non-trivial perturbative expressions are already known in a different context: Ref. [33] discusses a model for the B-meson LCDA through a non-relativistic bound state of a heavy quark and a light anti-quark. In this picture, the overall momentum of the B-meson is split up into the quarks according to their respective masses. Essentially, this corresponds to a perturbative calculation of

$$\phi_+^{\mathrm{NR}}(\omega;\mu) = \int_{-\infty}^{\infty} \frac{\mathrm{d}\tau}{2\pi}\, \mathrm{e}^{\mathrm{i}\omega\tau}\, \frac{\langle 0|\, \bar{q}(\tau n)\, [\tau n, 0] \not{n}\gamma_5\, h_v(0)\, |\bar{q}(mv) h_v(0)\rangle}{\langle 0|\, \bar{q}(0)\, \not{n}\gamma_5\, h_v(0)\, |\bar{q}(mv) h_v(0)\rangle} \tag{3.20}$$

directly in momentum space and up to order next-to-leading order, $\mathcal{O}(\alpha_s)$. The reference contains intermediate results for individual diagrams, which also appear in our matching calculation, however, in position space. Performing the transformation of these results is not trivial, even when considering the expansion to linear order in the quark mass m.

As a byproduct, our calculation further allows us to infer the perturbative 1-loop relationship between the HQET mass parameter $\bar{\Lambda}$ in the non-relativistic limit and the spectator quark mass,

$$\bar{\Lambda}_{\mathrm{NR}} = m\,(1 + \mathcal{O}(\alpha_s))\ . \tag{3.21}$$

The limit is defined analogously to Eq. (3.13) with the hadronic external state replaced by the partonic one.

3.2. Matching Coefficients for the Massive Case

We derive the matching relation using on-shell matrix elements of both sides of the OPE in Eq. (3.6). For simplicity, we project onto a particular spin configuration, such that for light-quark momentum $k^\mu = mv^\mu$ the outer product of the quark spinors can be replaced as

$$u(v,s)\,\bar{v}(k,s') \longrightarrow -\frac{1+\not{v}}{2}\,\gamma_5\,, \tag{3.22}$$

up to a normalization constant which is irrelevant in our context because it appears as a global factor on both sides of the operator expansion in Eq. (3.6). This prescription is analogous to the covariant trace formalism introduced before. Our use case relies on the spinor products

$$\begin{aligned}\bar{v}(k,s')\,\not{n}\gamma_5\,u(v,s) &\longrightarrow -\frac{1}{2}\,\mathrm{tr}\,[\not{n}\gamma_5(1+\not{v})\gamma_5] = +2\,,\\ \bar{v}(k,s')\,\not{v}\not{n}\gamma_5\,u(v,s) &\longrightarrow -\frac{1}{2}\,\mathrm{tr}\,[\not{v}\not{n}\gamma_5(1+\not{v})\gamma_5] = -2\,.\end{aligned} \tag{3.23}$$

For the partonic matrix element of the left-hand side of Eq. (3.6), the non-local operator, we define the 1-loop contribution in position space, $\tilde{I}^+$, via

$$\frac{\langle 0|\,\mathcal{O}_+(\tau)\,|\bar{q}(mv)h_v(0)\rangle}{\langle 0|\,\mathcal{O}_+(0)\,|\bar{q}(mv)h_v(0)\rangle} \equiv 1 - im\tau + \frac{\alpha_s C_F}{4\pi}\tilde{I}^+(\tau) + \mathcal{O}\big(\tau^2,\alpha_s^2\big)\,. \tag{3.24}$$

At the leading order, the Wilson line is trivial, i.e., $[\tau n,0] = 1 + \mathcal{O}(\alpha_s)$, and the matrix element can be calculated using the Fourier decomposition of the fields acting on the Fock state of the matrix element. The light-quark operator at position τn yields the exponential $\mathrm{e}^{-im\tau}$, which we already expanded to linear order in the above equation. Note that the coefficient function $\tilde{I}^+$ contains contributions not only from diagrams involving the non-local operator in the numerator, but also from the local operator in the denominator.

For the partonic matrix elements of the right-hand side of Eq. (3.6), the 1-loop contributions to the matrix elements of local operators $\mathcal{O}_k^{(n)}$ have to be taken into account, which we denote by $\tilde{I}_k^{(n)}$. Altogether, the resulting matching relation reads

$$\begin{aligned}&1 - im\tau + \frac{\alpha_s C_F}{4\pi}\,\tilde{I}^+(\tau) + \mathcal{O}(\tau^2,\alpha_s^2)\\ &\quad= c_1^{(3)}(\tau)\left(1+\frac{\alpha_s C_F}{4\pi}\,\tilde{I}_1^{(3)}\right) + m\,c_1^{(4)}(\tau)\left(1+\frac{\alpha_s C_F}{4\pi}\,\tilde{I}_1^{(4)}\right) + m\,c_2^{(4)}(\tau) - m\,c_3^{(4)}(\tau)\\ &\qquad\qquad + \mathcal{O}(\tau^2,\alpha_s^2)\,.\end{aligned} \tag{3.25}$$

Here, we already factor in that the coefficients $c_{2,3}^{(4)}$ start at order α_s. The contributions from the local operators on the right-hand side can be expressed as moments of the non-local contribution's holomorphic Fourier transform, $I^+(\omega) = \int_0^\infty \mathrm{d}\omega\,\mathrm{e}^{-i\omega\tau}\,\tilde{I}^+(\tau)$, such that

$$\tilde{I}_1^{(3)} = \int_0^\infty \mathrm{d}\omega\, I^+(\omega) \quad\text{and}\quad \tilde{I}_1^{(4)} = \frac{1}{m}\int_0^\infty \mathrm{d}\omega\,\omega\, I^+(\omega)\,. \tag{3.26}$$

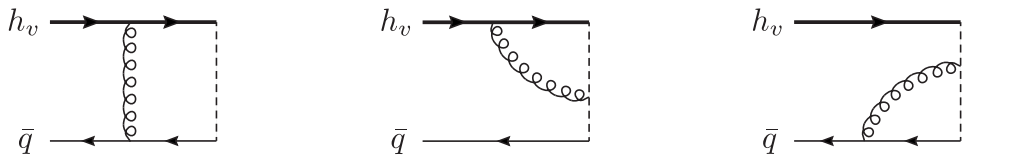

(a) Vertex like **(b)** Heavy quark with WL **(c)** Light quark with WL

Figure 3.1.: The three 1-loop Feynman diagrams contributing to the matching calculation. The dashed line indicates the Wilson line (WL).

Importantly, the $\overline{\text{MS}}$ subtraction (expanding in the dimensional regulator) of I^+ must be performed *after* the ω integration, in order to account for the renormalization of *local* operators. Rearranging the terms makes explicit how the 1-loop effects for the non-local and local operators combine,

$$\begin{aligned}\frac{\alpha_s C_F}{4\pi}\left(\tilde{I}^+(\tau) - \tilde{I}_1^{(3)} + im\tau\,\tilde{I}_1^{(4)}\right) &= \frac{\alpha_s C_F}{4\pi}\int_0^\infty \mathrm{d}\omega\,\left(\mathrm{e}^{-i\omega\tau} - 1 + i\omega\tau\right) I^+(\omega) \\ &= \left(c_1^{(3)}(\tau) - 1\right) + m\left(i\tau + c_1^{(4)}(\tau) + c_2^{(4)}(\tau) - c_3^{(4)}(\tau)\right) + \mathcal{O}(\tau^2, \alpha_s^2)\,. \quad (3.27)\end{aligned}$$

We refer to this systematic mechanism as "local subtractions" in the matching relation. Comparing the OPE treatment and the non-relativistic toy model – both partonic calculations based on the same diagrams – the local subtractions are a key difference because they render the result free of IR divergences in the limit $m \to 0$. We emphasize that $I^+(\omega)$ must be understood as a *bare* quantity; the matching coefficients are non-trivial because the Laurent expansion in the dimensional regulator and the short-distance limit $\tau \to 0$ do not commute.

3.2.1. Analysis of the Individual Diagrams in Feynman Gauge

The three diagrams contributing to the matrix element of the non-local operator are shown in Fig. 3.1. We consider each individually in this section using dimensional regularization and Feynman gauge. Notice that the 1-loop diagram where two gluon fields from the Wilson line are contracted with each other vanishes on the light cone. In the following, we treat each contributing diagram, (a), (b), and (c), separately,

$$I^+(\omega) \equiv I_a^+(\omega) + I_b^+(\omega) + I_c^+(\omega)\,, \quad (3.28)$$

and analogous for the local contributions.

The diagrams' expressions rely on Feynman rules for the insertion of the non-local operator, where the Wilson line is expanded in the strong coupling g_s [47]:

$$[\tau n, 0] = 1 - ig_s \int_0^\tau \mathrm{d}\lambda\, n \cdot A(\lambda n) + \mathcal{O}\big(g_s^2\big)\,. \tag{3.29}$$

In the following, we consider an incoming light quark with momentum p. To leading order, without gluon emission from the Wilson line, the operator leads to the following vertex rule in momentum space [47]:

$$\bar{q}(\tau n)\,\Gamma\, h_v(0) \to \delta(n \cdot p - \omega)\,\Gamma\,. \tag{3.30}$$

At the next order in the expansion, the operator contains one additional gluon field (with incoming momentum k, Lorentz-index μ, and color index a), leading to the momentum-space rule [47]

$$-ig_s \int_0^\tau \mathrm{d}\lambda\; \bar{q}(\tau n)\,(n \cdot A(\lambda n))\,\Gamma\, h_v(0) \to \frac{\delta(n \cdot p + n \cdot k - \omega) - \delta(n \cdot p - \omega)}{n \cdot k} g_s t^a n^\mu\,\Gamma\,. \tag{3.31}$$

The vertex rules can be derived using the standard method through functional derivatives or, as demonstrated in Ref. [47], using certain operator representations. Because the operators are non-local, the resulting vertex rules are distributions rather than mere factors.

We use the following short-hand notation for the integration measure of the loop momentum in the context of dimensional regularization in $D = 4 - 2\epsilon$ space-time dimensions and the $\overline{\text{MS}}$-subtraction scheme:

$$[\mathrm{d}\ell] = \left(\frac{\mu^2 \mathrm{e}^{\gamma_\mathrm{E}}}{4\pi}\right)^\epsilon \frac{\mathrm{d}^{4-2\epsilon}\ell}{(2\pi)^{4-2\epsilon}}\,. \tag{3.32}$$

Because of the two elemental directions n (introduced by the light-ray operator) and $v = (n + \bar{n})/2$ (entering the definition of HQET), it is useful to decompose the loop momentum into components $n \cdot \ell$, $\bar{n} \cdot \ell$ and $\ell_\perp = \ell - (n + \bar{n}) \cdot \ell$. In D dimensions, including the Jacobian determinant $1/2$, the measure reads

$$\frac{\mathrm{d}^D\ell}{(2\pi)^D} = \frac{1}{2} \frac{\mathrm{d}^{D-2}\ell_\perp}{(2\pi)^{D-2}} \frac{\mathrm{d}n \cdot \ell}{2\pi} \frac{\mathrm{d}\bar{n} \cdot \ell}{2\pi}\,. \tag{3.33}$$

When substituting the measure, one needs to ensure the integral over each component is well defined. Otherwise, it is necessary to introduce additional regulators, where the limit that corresponds to the original expression can be taken after all component integrals are carried out.

Vertex-like contribution First, we consider the vertex-like contribution, where a gluon connects the light quark with the heavy quark. The expression for the diagram in Fig. 3.1a reads

$$I_a^+(\omega) = -i \int [\mathrm{d}\ell]\, \delta(\omega - n\cdot(k-\ell))\, \frac{\bar v(k)\, \not v (-\not k + \not \ell + m)\, \not n \gamma_5\, u(v)}{[(k-\ell)^2 - m^2 + i0][v\cdot\ell + i0][\ell^2 + i0]}\,, \tag{3.34}$$

where, according to the prescription in Eq. (3.22), the spinor bilinear amounts to

$$-\frac{1}{2}\,\mathrm{tr}\left[\not v(-\not k + \not \ell + m)\, \not n \gamma_5 (1+\not v)\gamma_5\right] = 2\,(n\cdot l - n\cdot k) - 2m = 2n\cdot l - 4m\,.$$

After the trivial integration of $\mathrm{d}n\cdot\ell$ using the delta distribution, one can use the Cauchy's residue theorem to integrate $\mathrm{d}\bar n\cdot\ell$. The pole structure depends on the sign of $\omega - m$, which yields Heaviside distributions. The integrand only depends quadratically on $\ell_\perp$ such that the leftover (Euclidean) integration in $\mathrm{d}^{2-2\epsilon}\ell_\perp$ is straightforward. The regularized result in momentum space reads [33]

$$I_a^+(\omega) = 2\omega\,\Gamma(1+\epsilon)\left(\frac{\mu^2 \mathrm{e}^{\gamma_E}}{(m-\omega)^2}\right)^{\epsilon}\left\{\frac{2}{(m-\omega)^2} - \frac{\theta(m-\omega)}{m\,(m-\omega)} - \frac{\theta(\omega-m)}{\omega\,(\omega-m)}\right\}. \tag{3.35}$$

The holomorphic Fourier transform yields

$$\begin{aligned}\tilde I_a^+(\tau) &= \int_0^\infty \mathrm{d}\omega\, \mathrm{e}^{-i\omega\tau}\, I_a^+(\omega)\\ &= \mathrm{e}^{-im\tau}\left(\frac{2}{\epsilon} + 4L - 6\,\mathrm{Ei}(im\tau) + 4im\tau\,\mathrm{Ei}(im\tau)\right) - 4 + \frac{2-2\,\mathrm{e}^{-im\tau}}{im\tau} + \mathcal{O}(\epsilon)\\ &= \frac{2}{\epsilon} - 2L + 3\,\ln\frac{\mu^2}{m^2} - 2 - i\tau m\left(\frac{2}{\epsilon} - 6L + 5\,\ln\frac{\mu^2}{m^2} + 7\right) + \mathcal{O}(m^2,\epsilon)\,,\end{aligned} \tag{3.36}$$

where L is defined as before and $\mathrm{Ei}(z)$ is the exponential integral function. Similarly, we obtain the vertex correction to the local operator $\mathcal{O}_1^{(3)}$ (also provided in Ref. [33]) as

$$\tilde I_{1,a}^{(3)} = \int_0^\infty \mathrm{d}\omega\, I_a^+(\omega) = \frac{3}{\epsilon} + 3\,\ln\frac{\mu^2}{m^2} - 2 + \mathcal{O}(\epsilon)\,. \tag{3.37}$$

The vertex correction to the local operator $\mathcal{O}_1^{(4)}$ corresponds to the linear moment of $I_a^+(\omega)$,

$$\tilde I_{1,a}^{(4)} = \frac{1}{m}\int_0^\infty \mathrm{d}\omega\,\omega\, I_a^+(\omega) = \frac{5}{\epsilon} + 5\,\ln\frac{\mu^2}{m^2} + 3 + \mathcal{O}(\epsilon)\,. \tag{3.38}$$

Altogether, the contribution of the vertex-like diagram to the matching relation is

$$\begin{aligned}\tilde I_a^+(\tau) - \tilde I_{1,a}^{(3)} + im\tau\,\tilde I_{1,a}^{(4)} &= \int_0^\infty \mathrm{d}\omega\left(\mathrm{e}^{-i\omega\tau} - 1 + i\omega\tau\right) I_a^+(\omega)\\ &= -\frac{1}{\epsilon} - 2L - i\tau m\left(-\frac{3}{\epsilon} - 6L + 4\right) + \mathcal{O}(m^2,\epsilon)\,.\end{aligned} \tag{3.39}$$

Notice that the IR logarithms $\ln \mu^2/m^2$ no longer appear in the sum of the three terms. Consequently, the matching coefficients solely rely on the UV logarithms L, which aligns with the concept of the operator product expansion, separating the scales.

Since the subtraction terms lift the non-analytic behavior at $m = 0$, the total perturbative result can be expanded for small m already *prior* to the Fourier transform:

$$I_a^+(\omega) \simeq \Gamma(1+\epsilon) \left(\frac{\mu^2 \mathrm{e}^{\gamma_E}}{\omega^2}\right)^\epsilon \left(\frac{2}{\omega} + (6+4\epsilon)\,\frac{m}{\omega^2} + \mathcal{O}(m^2/\omega^3)\right). \tag{3.40}$$

Doing so presents a useful simplification when a more generic calculation is necessary, involving more dimensionful scales than the mass m. The subtractions appear as a *general feature* in the matching calculation since they originate from the expansion of the Fourier factor due to the light quark field's displacement. The factor generates leading-order terms on the left-hand side of the matching relation such that 1-loop contributions to the corresponding local matrix elements on the right-hand side enter at the next-to-leading order. To mass dimension N in the OPE, this amounts to the following replacement within the Fourier transform of the non-local contributions:

$$\mathrm{e}^{-i\omega\tau} \to \mathrm{e}^{-i\omega\tau} - \sum_{n=0}^{N} \frac{(-i\omega\tau)^n}{n!}\,.$$

We use this strategy to compute the matching contribution of the vertex diagram for a generic strange-quark momentum k in Section 3.3, where the additional scales $n \cdot k$ and $v \cdot k$ complicate the procedure.

Wilson line with heavy quark Next, we consider the diagram in Fig. 3.1b, coupling of a gluon from the Wilson-line to the heavy quark. Omitting intermediate results, the diagram yields ($k = n \cdot \ell$) [33]

$$I_b^+(\omega) = 2\,\Gamma(\epsilon) \int_0^\infty \mathrm{d}k \left(\frac{\mu^2 \mathrm{e}^{\gamma_E}}{k^2}\right)^\epsilon \frac{\delta(\omega - m - k) - \delta(\omega - m)}{k}\,. \tag{3.41}$$

The Fourier transform reads

$$\begin{aligned} \tilde{I}_b^+(\tau) &= \int_0^\infty \mathrm{d}\omega\, \mathrm{e}^{-i\omega\tau}\, I_b^+(\omega) \\ &= \mathrm{e}^{-im\tau} \left(-\frac{1}{\epsilon^2} - \frac{2L}{\epsilon} - 2L^2 - \frac{5\pi^2}{12}\right) + \mathcal{O}(\epsilon)\,, \end{aligned} \tag{3.42}$$

while the local subtractions cancel,

$$\int_0^\infty \mathrm{d}\omega\,(1 - i\omega\tau)\, I_b^+(\omega) = 2\,\Gamma(\epsilon) \int_0^\infty \mathrm{d}k \left(\frac{\mu^2 \mathrm{e}^{\gamma_E}}{k^2}\right)^\epsilon (-i\tau) = 0\,. \tag{3.43}$$

This is another generic feature of the matching calculation because any term from the Taylor expansion of the exponential results in scaleless integrals in dimensional regularization. As a consequence, the short-distance expansion for $\tilde{I}_b^+(\tau)$ in Eq. (3.42) factorizes into the trivial expansion of $\mathrm{e}^{-im\tau}$ and a *universal* 1-loop contribution, including the double-logarithmic dependence on τ, which affects all tree-level matching coefficients in the same way.

Wilson line with light quark Finally, the diagram in Fig. 3.1c with the Wilson-line gluon coupling to the light quark yields ($k = n \cdot \ell$) [33]

$$I_c^+(\omega) = 2\Gamma(\epsilon) \int_0^m \mathrm{d}k \, \frac{m-k}{m} \left(\frac{\mu^2 \mathrm{e}^{\gamma_E}}{k^2}\right)^\epsilon \frac{\delta(k-m+\omega) - \delta(\omega-m)}{k}\,, \tag{3.44}$$

where the Fourier transform is given by

$$\begin{aligned} \tilde{I}_c^+(\tau) &= \int_0^\infty \mathrm{d}\omega \, \mathrm{e}^{-i\omega\tau} \, I_c^+(\omega) \\ &= i\tau m \left(\frac{1}{\epsilon} + \ln\frac{\mu^2}{m^2} + 3\right) + \mathcal{O}\left((i\tau m)^2, \epsilon\right)\,. \end{aligned} \tag{3.45}$$

The local contributions amount to $\tilde{I}_{1,c}^{(3)} = 0$ and

$$\begin{aligned} \tilde{I}_{1,c}^{(4)} &= -\frac{2\Gamma(\epsilon)}{m} \int_0^m \mathrm{d}k \, \frac{m-k}{m} \left(\frac{\mu^2 e^{\gamma_E}}{k^2}\right)^\epsilon \\ &= \left(\frac{\mu^2 e^{\gamma_E}}{m^2}\right)^\epsilon \frac{\Gamma(\epsilon-1)}{2\epsilon-1} = -\left(\frac{1}{\epsilon} + 3 + \ln\frac{\mu^2}{m^2}\right) + \mathcal{O}(\epsilon)\,. \end{aligned} \tag{3.46}$$

As $I_c^+(\omega)$ only involves the low-momentum region, $\omega < m$, the short-distance expansion of the Fourier exponential and dimensional regularization commute, and thus, the net contribution to the matching relation is zero,

$$\tilde{I}_c^+(\tau) - \tilde{I}_{1,c}^{(3)} + im\tau\, \tilde{I}_{1,c}^{(4)} = \int_0^\infty \mathrm{d}\omega \left(\mathrm{e}^{-i\omega\tau} - 1 + i\omega\tau\right) I_c^+(\omega) = 0\,. \tag{3.47}$$

3.2.2. 1-loop Result for the Matching Coefficient $c_3^{(4)}(\tau)$

Using the massive 1-loop contributions and the known Wilson coefficients from the massless case in the matching relation Eq. (3.27), we obtain the following result for the remaining Wilson coefficient $c_3^{(4)}(\tau)$ after renormalization in the $\overline{\mathrm{MS}}$ scheme:

$$c_3^{(4)}(\tau) = -i\tau \left[\frac{\alpha_s C_F}{4\pi}\,(L-1) + \mathcal{O}(\alpha_s^2)\right]\,. \tag{3.48}$$

This is the primary new theoretical result of this chapter. In the following, we rederive all matching coefficients using our method with momentum-space Feynman integrals and we further derive the short-distance expansion for the subleading twist LCDA $\tilde{\phi}_-$.

3.2.3. 1-loop Result for $\bar{\Lambda}$ in the Non-relativistic Limit

As a cross-check and byproduct, we can infer the 1-loop corrections to the parameter $\bar{\Lambda}$ of the non-relativistic model for the LCDA. Inserting the result for the Wilson coefficients into the OPE result for the LCDA in Section 3.1.3, we find

$$\tilde{\phi}_+(\tau) = \left[1 - i\tau\,\frac{4\bar{\Lambda} - m}{3}\right]\left[1 - \frac{\alpha_s C_F}{4\pi}\left(2L^2 + 2L + \frac{5\pi^2}{12}\right)\right] + i\tau\bar{\Lambda}\,\frac{\alpha_s C_F}{4\pi}\left(\frac{8}{3}\,L - 3\right) + i\tau m\,\frac{\alpha_s C_F}{4\pi}\left(\frac{4}{3}\,L - 1\right) + \mathcal{O}(\alpha_s^2, \tau^2)\,. \quad (3.49)$$

On the other hand, the 1-loop contributions to the non-relativistic LCDA model in position space amount to (see also Ref. [33] for the momentum-space computation)

$$\tilde{\phi}_+(\tau)\Big|_{\rm NR} = 1 - i\tau m + \frac{\alpha_s C_F}{4\pi}\left(\tilde{I}_a^+(\tau) + \tilde{I}_b^+(\tau) + \tilde{I}_c^+(\tau) - \tilde{I}_{1,a}^{(3)}\right)_{\overline{\rm MS}} + \ldots \quad (3.50)$$

For consistency, both expressions must coincide in the limit $\bar{\Lambda} \to \bar{\Lambda}\big|_{\rm NR} = \gamma_m\, m$, where the factor $\gamma_m = 1 + \mathcal{O}(\alpha_s)$ can be inferred to 1-loop accuracy. Comparing the two expressions yields

$$\bar{\Lambda}\Big|_{\rm NR} = m\left[1 + \frac{\alpha_s C_F}{4\pi}\left(3\ln\frac{\mu^2}{m^2}\right) + \mathcal{O}(\alpha_s^2)\right], \quad (3.51)$$

with $m = \overline{m}(\mu)$ in the $\overline{\rm MS}$ scheme.

As a cross-check, being a non-trivial mass parameter of the effective theory, one expects no scale dependence when using the on-shell renormalization scheme. The relation between the quark mass in the $\overline{\rm MS}$ scheme and the pole mass scheme reads[4]

$$m = m_{\rm pole}\left[1 - \frac{\alpha_s C_F}{4\pi}\left(4 + 3\ln\frac{\mu^2}{m_{\rm pole}^2}\right) + \mathcal{O}\big(\alpha_s^2\big)\right], \quad (3.52)$$

which confirms that the relation $\mathrm{d}\bar{\Lambda}/\mathrm{d}\ln\mu = 0$ holds to the considered order in α_s.

3.3. Generic Calculation and Radiative Tail of $\tilde{\phi}_-(\tau)$

In this section, we generalize the calculation of the OPE coefficients based on the insights from Section 3.2. Taking the local subtractions into account early on allows us to obtain the radiative corrections using momentum-space expressions, even when several kinematic scales beyond the spectator-quark mass m are involved. We further consider a generic

[4] The provided relation for QCD follows analogously to the QED case discussed in Ref. [6, Sec. 18.4], amounting to the replacement $\alpha \to \alpha_s C_F$ at 1-loop level.

2-particle light ray operator, from which results for both the leading and subleading-twist 2-particle LCDAs can be extracted.

Instead of the leading-twist operator, we perform the short-distance expansion of a 2-particle HQET light-ray operator with arbitrary Dirac structure Γ. The possible Dirac structures involved with the matching of the local operators, as discussed in detail in Section 3.1.2, remain explicit in the generic case:

$$\begin{aligned}
\mathcal{O}_\Gamma(\tau) &= \bar{q}(\tau n)\,[\tau n, 0]\,\Gamma\, h_v(0) \\
&= c_1^{(3)}(\tau)\,\bar{q}(0)\,\frac{\not{n}\not{v}}{2}\,\Gamma\, h_v(0) + d_1^{(3)}(\tau)\,\bar{q}(0)\,\frac{\not{v}\not{n}}{2}\,\Gamma\, h_v(0) \\
&\quad + c_1^{(4)}(\tau)\,\bar{q}(0)\,(in\cdot\overleftarrow{D})\,\frac{\not{n}\not{v}}{2}\,\Gamma\, h_v(0) + d_1^{(4)}(\tau)\,\bar{q}(0)\,(in\cdot\overleftarrow{D})\,\frac{\not{v}\not{n}}{2}\,\Gamma\, h_v(0) \\
&\quad + c_2^{(4)}(\tau)\,\bar{q}(0)\,(iv\cdot\overleftarrow{D})\,\frac{\not{n}\not{v}}{2}\,\Gamma\, h_v(0) + d_2^{(4)}(\tau)\,\bar{q}(0)\,(iv\cdot\overleftarrow{D})\,\frac{\not{v}\not{n}}{2}\,\Gamma\, h_v(0) \\
&\quad + c_3^{(4)}(\tau)\,m\,\bar{q}(0)\,\frac{2\not{v}-\not{n}}{2}\,\Gamma\, h_v(0) + d_3^{(4)}(\tau)\,m\,\bar{q}(0)\,\frac{\not{n}}{2}\,\Gamma\, h_v(0) + \mathcal{O}(\tau^2)\,.
\end{aligned} \tag{3.53}$$

We note that the additional Dirac structures can be expressed in terms of the conventional light-cone projectors,

$$P_+ = \frac{\not{n}\not{v}}{2} = \frac{\not{n}\bar{\not{n}}}{4}\,, \qquad P_- = \frac{\not{v}\not{n}}{2} = \frac{\bar{\not{n}}\not{n}}{4}\,, \tag{3.54}$$

with the properties $P_\pm^2 = P_\pm$ and $P_+ + P_- = 1$. For $\Gamma = \not{n}\gamma_5$, the definition above reduces to the OPE for $\mathcal{O}_+(\tau)$ in 3.6. The case $\Gamma = \bar{\not{n}}\gamma_5$, on the other hand, corresponds to the subleading twist LCDA $\tilde{\phi}_-(\tau) \propto \langle 0|\,\mathcal{O}_-(\tau)\,\big|\bar{B}(v)\big\rangle$,

$$\begin{aligned}
\mathcal{O}_-(\tau) &= \bar{q}(\tau n)\,[\tau n, 0]\,\bar{\not{n}}\gamma_5\, h_v(0) = \sum_{n=3}^{\infty}\sum_{k=1}^{K_n} d_k^{(n)}(\tau)\,\mathcal{O}_k^{\prime(n)}(0) \\
&= d_1^{(3)}(\tau)\,\bar{q}\,\bar{\not{n}}\gamma_5\, h_v \\
&\quad + d_1^{(4)}(\tau)\,\bar{q}\,(in\cdot\overleftarrow{D})\,\bar{\not{n}}\gamma_5\, h_v + d_2^{(4)}(\tau)\,\bar{q}\,(iv\cdot\overleftarrow{D})\,\bar{\not{n}}\gamma_5\, h_v \\
&\quad + d_3^{(4)}(\tau)\,m\,\bar{q}\,\not{v}\bar{\not{n}}\gamma_5\, h_v + \ldots
\end{aligned} \tag{3.55}$$

The short-distance expansion of the LCDA $\tilde{\phi}_-(\tau)$ follows by taking the operators' hadronic matrix elements

$$\tilde{\phi}_-(\tau) = d_1^{(3)}(\tau) + \bar{\Lambda}\left(\frac{2}{3}\,d_1^{(4)}(\tau) + d_2^{(4)}(\tau)\right) - m\left(d_3^{(4)}(\tau) - \frac{1}{3}\,d_1^{(4)}(\tau)\right) + \mathcal{O}(\tau^2)\,, \tag{3.56}$$

relying on the local operator's matrix elements according to Eq. (3.9) and Eq. (3.16),

$$\langle 0|\mathcal{O}_1^{\prime(3)}|\bar{B}(v)\rangle = im_B f_B^{\mathrm{HQET}}\,, \tag{3.57}$$

and

$$\frac{\langle 0|\mathcal{O}_1^{\prime(4)}|\bar{B}(v)\rangle}{\langle 0|\mathcal{O}_1^{\prime(3)}|\bar{B}(v)\rangle} = \frac{2\bar{\Lambda}+m}{3}\,, \quad \frac{\langle 0|\mathcal{O}_2^{\prime(4)}|\bar{B}(v)\rangle}{\langle 0|\mathcal{O}_1^{\prime(3)}|\bar{B}(v)\rangle} = \bar{\Lambda}\,, \quad \frac{\langle 0|\mathcal{O}_3^{\prime(4)}|\bar{B}(v)\rangle}{\langle 0|\mathcal{O}_1^{\prime(3)}|\bar{B}(v)\rangle} = -m\,. \tag{3.58}$$

Vertex-like contribution The contribution of the vertex-like diagram to the matching coefficients results from a Fourier integral with subtractions[5],

$$\int_0^\infty \mathrm{d}\omega \left(\mathrm{e}^{-i\omega\tau} - 1 + i\omega\tau + \ldots\right) I_a^\Gamma(\omega, m, k)\,, \tag{3.59}$$

where in the integrand, the function $I_a^\Gamma(\omega, m, k)$ is now calculated using momentum-space Feynman rules for general external on-shell quark states with light-quark momentum k^μ:

$$I_a^\Gamma(\omega, m, k) = -i \int [\mathrm{d}\ell]\, \delta(\omega - n\cdot(k-\ell))\, \frac{\bar{v}(k)\,\not{v}(-\not{k}+\not{\ell}+m)\,\Gamma\,u(v)}{[(k-\ell)^2 - m^2 + i0][v\cdot\ell + i0][\ell^2 + i0]}\,. \tag{3.60}$$

We treat the $\ell_\perp$ integral explicitly using Feynman parameters to decompose integrand into even and odd terms in $\ell_\perp^\mu$,

$$\begin{aligned}&\frac{1}{(k-\ell)^2 - m^2 + i0}\frac{1}{\ell^2 + i0}\\ &\quad= \int_0^1 \mathrm{d}u\, \frac{1}{[u((k-\ell)^2 - m^2) + (1-u)\ell^2 + i0]^2} = \int_0^1 \mathrm{d}u\, \frac{1}{[\ell^2 - 2u\,k\cdot\ell + i0]^2}\,.\end{aligned} \tag{3.61}$$

Shifting the integral as $\ell \mapsto \ell + uk$ eliminates the linear term in the denominator,

$$\begin{aligned}I_a^\Gamma(\omega, m, k) = -i \int_0^1 \mathrm{d}u \int [\mathrm{d}\ell]\, \delta(\omega - n\cdot[(1-u)k - \ell]) \times\\ \times \frac{\bar{v}(k)\,\not{v}[-(1-u)\not{k} + \not{\ell} + m]\,\Gamma\,u(v)}{[v\cdot\ell + u\,v\cdot k + i0][\ell^2 - u^2 m^2 + i0]^2}\,.\end{aligned} \tag{3.62}$$

The equation of motion of the light-quark spinor simplifies the $\not{k}$ term as

$$\bar{v}(k)\not{v}\not{k} = \bar{v}(k)(-\not{k}\not{v} + 2\,v\cdot k\,\mathbb{1}) = \bar{v}(k)(m\not{v} + v\cdot k\,[\not{v}\not{n} + \not{n}\not{v}])\,, \tag{3.63}$$

while term term with the loop momentum $\not{\ell}$ must be decomposed into light-cone components:

$$\not{v}\not{\ell} = \frac{1}{2}(n\cdot\ell\,\not{v}\not{v} + [2v - n]\cdot\ell\,\not{v}\not{n}) + \not{v}\not{\ell}_\perp\,. \tag{3.64}$$

Because the last term linear in $\ell_\perp$ is odd under reflection, it yields no contribution to the integral. Solving the loop integral is straightforward for $n\cdot k < 0$ to avoid a non-trivial distribution in ω induced by the pole structure. After loop integration with the dimensional regulator, the integrand can be expanded to linear order in $n\cdot k$, $v\cdot k$, and m to match the OPE. To that end, we rescale each of those parameters formally by an auxiliary parameter

[5] We use the ellipsis to emphasize that additional subtractions arise when calculating the OPE to a mass dimension larger than 4.

λ and compute the Taylor series, which yields

$$\begin{aligned} I_a^\Gamma(\omega, m, k) = \frac{\Gamma(1+\epsilon)}{\omega} \left(\frac{\mu^2 \mathrm{e}^{\gamma_E}}{\omega^2}\right)^\epsilon \\ \times \bar{v}(k) \left\{ \left(2 + (1+2\epsilon)\,\frac{n\cdot k}{\omega} + (4+2\epsilon)\,\frac{v\cdot k}{\omega}\right) \frac{\not{n}\not{v}}{2} \right. \\ + \left(-2 - (1+2\epsilon)\,\frac{n\cdot k}{\omega} + (2-2\epsilon)\,\frac{v\cdot k}{\omega}\right) \frac{\not{v}\not{n}}{2} \\ \left. - \frac{m}{\omega}\not{v} + \mathcal{O}(\omega^{-2}) \right\} \Gamma\, u(v)\,. \end{aligned} \tag{3.65}$$

The subtracted Fourier integral results in

$$\begin{aligned} &\int_0^\infty \mathrm{d}\omega \left(\mathrm{e}^{-i\omega\tau} - 1 + i\omega\tau\right) I_a^\Gamma(\omega, m, k) \\ &= \bar{v}(k) \left\{ \left(-\frac{1}{\epsilon} - 2L + \left(\frac{1}{2\epsilon} + L\right) i\tau(n\cdot k) + \left(\frac{2}{\epsilon} + 4L - 3\right) i\tau(v\cdot k)\right) \frac{\not{n}\not{v}}{2} \right. \\ &\quad + \left(\frac{1}{\epsilon} + 2L - \left(\frac{1}{2\epsilon} + L\right) i\tau(n\cdot k) + \left(\frac{1}{\epsilon} + 2L - 3\right) i\tau(v\cdot k)\right) \frac{\not{v}\not{n}}{2} \\ &\quad \left. - \left(\frac{1}{2\epsilon} + L - 1\right) i\tau m \not{v} + \mathcal{O}(\tau^2) \right\} \Gamma\, u(v)\,, \end{aligned} \tag{3.66}$$

which allows a comparison of coefficients to extract the contribution of the vertex diagram (a) to the individual Wilson coefficients. One can formally use specific values for the momentum k and the Dirac structure Γ to isolate the individual matching coefficients.

Wilson line with heavy quark The contribution from the diagram (b), where the Wilson-line couples to the heavy quark, reads

$$I_b^\Gamma(\omega, k) = i \int [\mathrm{d}\ell]\, \frac{\delta(\omega - n\cdot k + n\cdot\ell) - \delta(\omega - n\cdot k)}{n\cdot\ell}\, \frac{\bar{v}(k)\,\Gamma\, u(v)}{[v\cdot\ell + i0][\ell^2 + i0]}\,. \tag{3.67}$$

For the matching calculation, it is sufficient to consider the case $n\cdot k < 0$, eliminating the second delta distribution to avoid the treatment of non-trivial cancellations between the two terms. It is then straightforward to perform the loop integration, to expand in $n\cdot k$, and to perform the Fourier transform:

$$\begin{aligned} &\int_0^\infty \mathrm{d}\omega \left(\mathrm{e}^{i\omega\tau} - 1 + i\omega\tau\right) I_b^\Gamma(\omega, k) \\ &\qquad = \left(1 - i\tau(n\cdot k) + \mathcal{O}(\tau^2)\right) \left(-\frac{1}{\epsilon^2} - \frac{2L}{\epsilon} - 2L^2 - \frac{5\pi^2}{12}\right) \bar{v}(k)\,\Gamma\, u(v)\,. \end{aligned} \tag{3.68}$$

Using the light-cone projectors, $(\not{n}\not{v} + \not{v}\not{n})/2 = \mathbb{1}$, allows to extract the matching coefficients.

Wilson line with light quark The diagram (c) with the Wilson line coupled to the light quark yields the expression

$$I_c^\Gamma(\omega,m,k) = i\int[\mathrm{d}\ell]\,\frac{\delta(\omega-n\cdot k)-\delta(\omega-n\cdot(k-\ell))}{n\cdot\ell}\,\frac{\bar v(k)\,\not n(-\not k+\not\ell+m)\,\Gamma\,u(v)}{[(k-\ell)^2-m^2+i0][\ell^2+i0]}\,. \tag{3.69}$$

Notice that diagrams (a) and (c) are similar, only replacing v by n in the nominator and denominator; the pole structure in the $\bar n\cdot\ell$ component, however, changes essentially. The quark spinor's equation of motion allows writing

$$\bar v(k)\not n\not k = \bar v(k)(m\not n + n\cdot k\,[\not v\not n + \not n\not v])\,,$$

while decomposing the linear term in the numerator into light-cone components in this case amounts to

$$\not n\not\ell = n\cdot\ell\,\not n\not v + \not n\not\ell_\perp\,.$$

It is convenient to calculate the diagram for $n\cdot k>0$ and $k_\perp=0$, whereas the procedure performed for diagram (a) requires an additional regulator to decompose the loop integration into well-defined separate integrals over light-cone components. Performing the $\ell_\perp$ and $\bar n\cdot\ell$ integrations results in

$$\begin{aligned} I_c^\Gamma(\omega,m,k) = \Gamma(\epsilon)\int_0^{n\cdot k}\mathrm{d}(n\cdot\ell)\left[\frac{n\cdot k\,\mu^2\mathrm{e}^{\gamma_E}}{(2\,v\cdot k-n\cdot k)(n\cdot\ell)^2}\right]^\epsilon\times \\ \times\,\frac{\delta(\omega-n\cdot k)-\delta(n\cdot\ell-n\cdot k+\omega)}{(n\cdot k)(n\cdot\ell)}\,\bar v(k)\,\{n\cdot(k-\ell)\,\not n\not v + n\cdot k\,\not v\not n\}\,\Gamma u(v)\,. \end{aligned} \tag{3.70}$$

Evaluating the expression yields no contribution to the matching because, as for the non-relativistic setup, only the low-momentum region $\omega<n\cdot k$ is involved.

We verify the coefficients for the expansion of $\mathcal{O}_+(\tau)$ already provided in Eq. (3.19) for known coefficients and Eq. (3.48) for the additional coefficient in the massive case. Unlike the approach using the specific "non-relativistic" setup, the results in this section are independent of external input. Our approach offers the benefit that one can resort to well-known techniques to solve the Feynman integrals in momentum space before transforming the result into position space (referring to the conjugate variables ω and τ) in a simplified way.

We obtain the following new result for the matching coefficients relevant to the subleading

LCDA ϕ_- after renormalization in the $\overline{\text{MS}}$ scheme:

$$\begin{aligned}
d_1^{(3)}(\tau) &= 1 - \frac{\alpha_s C_F}{4\pi}\left(2L^2 - 2L + \frac{5\pi^2}{12}\right) + \mathcal{O}(\alpha_s^2)\,,\\
d_1^{(4)}(\tau) &= -i\tau\left[1 - \frac{\alpha_s C_F}{4\pi}\left(2L^2 - L + \frac{5\pi^2}{12}\right) + \mathcal{O}(\alpha_s^2)\right]\,,\\
d_2^{(4)}(\tau) &= -i\tau\left[-\frac{\alpha_s C_F}{4\pi}\left(2L - 3\right) + \mathcal{O}(\alpha_s^2)\right]\,,\\
d_3^{(4)}(\tau) &= -i\tau\left[\frac{\alpha_s C_F}{4\pi}\left(L - 1\right) + \mathcal{O}(\alpha_s^2)\right]\,.
\end{aligned} \tag{3.71}$$

Applying this result to the expression for the LCDA $\tilde{\phi}_-(\tau)$, we obtain

$$\begin{aligned}
\tilde{\phi}_-(\tau) = &\left[1 - i\tau\,\frac{2\bar{\Lambda} + m}{3}\right]\left[1 - \frac{\alpha_s C_F}{4\pi}\left(2L^2 - 2L + \frac{5\pi^2}{12}\right)\right]\\
&+ i\tau\bar{\Lambda}\,\frac{\alpha_s C_F}{4\pi}\left(\frac{8}{3}\,L - 3\right) + i\tau m\,\frac{\alpha_s C_F}{4\pi}\left(\frac{4}{3}\,L - 1\right) + \mathcal{O}(\alpha_s^2, \tau^2)\,.
\end{aligned} \tag{3.72}$$

3.4. Constraints on the LCDA Parametrization

In this section, we explore the impact of our result when used together with the systematic parameterization developed in Chapter 2. To that end, we resort to the "pseudo-phenomenological" procedure outlined in Section 2.4. Consequently, the same limitations apply as for the study in the previous section: this analysis intends to determine whether the theoretical information about the short-distance behavior is compatible with complementary studies of the inverse moments of the LCDAs from QCD sum rules. We stress that, inherently, the perturbative tail *alone* cannot provide comprehensive predictions for the LCDAs; instead, the implication is that the constraints can be used together with other independent theoretical information from sum rules or lattice in future analyses of B_s decays in QCD factorization or QCD light-cone sum rules.

3.4.1. Determination of the Expansion Parameters

Following Section 2.4, the short-distance expansion for the LCDA $\tilde{\phi}_+(\tau)$ in Eq. (3.49) translates to constraints onto the expansion coefficients a_k:

$$\begin{aligned}
\tilde{\phi}_B^+(\tau,\mu_0) &= \frac{1}{(1 + i\omega_0\tau)^2}\sum_{k=0}^{K} a_k(\mu_0)\left(\frac{i\omega_0\tau - 1}{i\omega_0\tau + 1}\right)^k\\
&= \sum_{k=0}^{K}(-1)^k\, a_k(\mu_0)\left[1 - 2\,(k+1)\,i\omega_0\tau - (3 + 4k + 2k^2)\,\omega_0^2\tau^2 + \mathcal{O}(i\omega_0\tau)^3\right]\,.
\end{aligned} \tag{3.73}$$

We compare this with the OPE result at an imaginary-valued reference point $\tau = \tau_0$ such that

$$x_0 \equiv i\mu_0 \mathrm{e}^{\gamma_E}\, \tau_0 \overset{!}{=} \mathcal{O}(1)\,,$$

for a given reference scale, which we fix as $\mu_0 = 1$ GeV. This ensures that the logarithms $L = \log x_0$ in the matching coefficients of the OPE remain under control. In the numerical analysis below, we fix $x_0 \equiv 1$ for simplicity. For the expansion in Eq. (3.73) to converge, we further require that the auxiliary reference momentum ω_0 in the parameterization of the B_s or B_q LCDA satisfies

$$n_0 \equiv i\tau_0\, \omega_0 \overset{!}{\ll} 1\,.$$

Finally, as becomes apparent below, we require $\omega_0 \gtrsim \bar{\Lambda}_a, m_a$ to avoid large enhancement factors in the resulting expressions for the expansion parameters a_k. We use $n_0 \equiv 1/3$ in the numerical analysis, which satisfies these requirements.

As before, we consider the parameterization of the LCDA truncated at $K = 2$. The OPE results for the LCDA and its first derivative at the point τ_0 provide two independent conditions that determine the parameters a_0 and a_1, while a_2 remains as a free parameter:

$$\begin{aligned} a_0 &= 2 + a_2 - \frac{4\bar{\Lambda} - m}{6\omega_0} + \frac{\alpha_s C_F}{4\pi}\left(-\frac{1}{x_0}\,\frac{\mu_0 \mathrm{e}^{\gamma_E}}{\omega_0}\,(1 + 2\ln x_0) + \ldots\right), \\ a_1 &= 1 + 2a_2 - \frac{4\bar{\Lambda} - m}{6\omega_0} + \frac{\alpha_s C_F}{4\pi}\left(-\frac{1}{x_0}\,\frac{\mu_0 \mathrm{e}^{\gamma_E}}{\omega_0}\,(1 + 2\ln x_0) + \ldots\right), \end{aligned} \tag{3.74}$$

Above, only the α_s corrections enhanced by μ_0/ω_0 are shown. Because they are independent of the light quark mass, we absorb them the same way as before in Section 2.4, defining

$$\bar{\Lambda} \equiv \bar{\Lambda}_a(\mu_0, x_0)\left[1 + \frac{\alpha_s C_F}{4\pi}\left(10\,\ln x_0 + \frac{15}{4}\right)\right] - \frac{\alpha_s C_F}{4\pi}\,\frac{3\mu_0 \mathrm{e}^{\gamma_E}}{2x_0}\,(1 + 2\ln x_0)\,. \tag{3.75}$$

Thus, the result for the expansion parameters with $K = 2$ to order $\mathcal{O}(\alpha_s)$ reads

$$\begin{aligned} a_0 &= Z(x_0)\left(2 - \frac{4\bar{\Lambda}_a(\mu_0, x_0) - m_a(x_0)}{6\omega_0} - 2\,r(x_0)\right) + a_2\,, \\ a_1 &= Z(x_0)\left(1 - \frac{4\bar{\Lambda}_a(\mu_0, x_0) - m_a(x_0)}{6\omega_0} - r(x_0)\right) + 2\,a_2\,. \end{aligned} \tag{3.76}$$

Here we introduce the short-hand notation

$$r(x_0) \equiv \frac{\alpha_s C_F}{6\pi}\,\frac{8\bar{\Lambda}_a\, x_0(1 + \ln x_0) + m_a\, x_0(1 - 2\ln x_0)}{\mu_0\, \mathrm{e}^{\gamma_E}} = \mathcal{O}(\alpha_s n_0)\,, \tag{3.77}$$

$$Z(x_0) \equiv 1 + \frac{\alpha_s C_F}{4\pi}\left(-2\ln^2 x_0 + 2\ln x_0 + 2 - \frac{5\pi^2}{12}\right), \tag{3.78}$$

and

$$m_a(x_0) \equiv m\left(1 - \frac{\alpha_s C_F}{4\pi}\,(3 + 4\ln x_0)\right). \tag{3.79}$$

Those definitions of $\bar{\Lambda}_a$, m_a and Z are such that the parameterization for the position-space LCDA with finite truncation K satisfies the following relation analogous to the massless case:

$$\begin{aligned}\tilde{\phi}_+(0)\big|_K &= \sum_{k=0}^{K}(-1)^k\, a_k = Z(x_0) - r(x_0) + \mathcal{O}(\alpha_s^2,\, n_0^2)\,,\\ \tilde{\phi}'_+(0)\big|_K &= -2i\omega_0 \sum_{k=0}^{K}(-1)^k\,(1+k)\, a_k = -Z(x_0)\,\frac{4i\bar{\Lambda}_a - im_a}{3} + \mathcal{O}(\alpha_s^2,\, \bar{\Lambda}_a n_0)\,.\end{aligned} \tag{3.80}$$

3.4.2. Numerical Results

The following numerical study aims to explore the extent to which theoretical constraints from the radiative tail can be employed in future phenomenological studies. To achieve this, we focus on the inverse moments λ_{B_q} and λ_{B_s}, which hold significant importance in QCD factorization to exclusive B decays. The plots presented in the following sections are intended to provide semi-quantitative results, omitting a rigorous discussion of uncertainty estimates. Thus, we use only the central values of the input parameters, although we quote their uncertainties when possible.

As outlined in the previous section, we take $x_0 \equiv 1$ and $n_0 = 1/3$ for the dimensionless combinations of τ_0, μ_0 and ω_0. The renormalization scale is fixed to $\mu_0 = 1$ GeV resulting in $\omega_0 \simeq 594$ MeV. We take the corresponding value of the strong coupling as $\alpha_s(\mu_0) = 0.5$.

The effective mass parameter for the B_q meson (i.e., without mass effects, see Section 2.4) reads

$$\bar{\Lambda}_a^{(q)}(\mu_0, x_0 = 1) \simeq 367 \text{ MeV}\,.$$

From this, we derive the value for the massive case according to the hadronic mass difference of the B_q and B_s. Using the values $M_{B_s} = 5.367$ GeV and $M_{B_q} = 5.279$ GeV [48], together with Eq. (3.75), leads to

$$\bar{\Lambda}_a^{(s)}(\mu_0, 1) \simeq \bar{\Lambda}_a^{(q)}(\mu_0, 1) + \left(1 - \frac{\alpha_s C_F}{4\pi}\,\frac{15}{4}\right)(M_{B_s} - M_{B_q}) \simeq 437 \text{ MeV}\,.$$

We take the value $m_s(\mu_0) = 126^{+15}_{-7}$ MeV [48] for the strange-quark mass in the $\overline{\text{MS}}$ scheme, which translates via Eq. (3.79) to

$$m_a^{(s)}(\mu_0) \simeq (106 \pm 10) \text{ MeV}\,.$$

B_q meson's inverse moment Evaluating the parameter expressions in Eq. (3.76) for the B_q meson, we find

$$\begin{aligned} a_0^{(q)} &\simeq 1.78 - 0.47\,\frac{\bar{\Lambda}_a^{(q)}}{367\text{ MeV}} + a_2^{(q)} \simeq 1.31 + a_2^{(q)}\,, \\ a_1^{(q)} &\simeq 0.89 - 0.42\,\frac{\bar{\Lambda}_a^{(q)}}{367\text{ MeV}} + 2a_2^{(q)} \simeq 0.47 + 2a_2^{(q)}\,. \end{aligned} \tag{3.81}$$

To establish upper and lower limits for $a_2^{(q)}$, we employ the ad-hoc criterion for the bound's growth as in Section 2.4,

$$\frac{\left|a_1^{(q)}\right|^2}{\left|a_0^{(q)}\right|^2 + \left|a_1^{(q)}\right|^2} < 0.25\,, \qquad \frac{\left|a_2^{(q)}\right|^2}{\left|a_0^{(q)}\right|^2 + \left|a_1^{(q)}\right|^2 + \left|a_2^{(q)}\right|^2} < 0.1\,, \tag{3.82}$$

to select only parameter values that fulfill "reasonable" convergence of the bound in Eq. (2.35). With this setup, we test if such a selection at low truncation level is compatible with independent results. Numerically, the growth criterion constrains the value of the free parameter as

$$-0.33 < a_2^{(q)} < 0.20\,. \tag{3.83}$$

The estimate for the inverse moment $\lambda_B = L_0^{-1}$ in Eq. (2.44),

$$\lambda_{B_q} \simeq \frac{445\text{ MeV}}{1.33 - 0.35\,\frac{\bar{\Lambda}_a^{(q)}}{367\text{ MeV}} + a_2^{(q)}} \simeq \frac{445\text{ MeV}}{0.98 + a_2^{(q)}}\,, \tag{3.84}$$

is shown in Fig. 3.2 as a function of $a_2^{(q)}$ within the selected interval. We compare this estimate with the latest sum-rule result $\lambda_{B_q} = 383 \pm 153$ MeV [49], shown as a gray band. Both estimates agree for a large region of the considered $a_2^{(q)}$ interval. Anticipating the comparison with the B_s case, we note a slight preference for positive values of $a_2^{(q)}$[6]. Moreover, we note a positive correlation between the inverse moment λ_{B_q} and the HQET parameter $\bar{\Lambda}_a^{(q)}$, while the two parameters are not simply proportional to each other.

B_s meson's inverse moment Similarly, the coefficients for the B_s meson numerically amount to

$$\begin{aligned} a_0^{(s)} &\simeq 1.78 - 0.56\,\frac{\bar{\Lambda}_a^{(s)}}{437\text{ MeV}} + 0.023\,\frac{m_a^{(s)}}{105\text{ MeV}} + a_2^{(s)} \simeq 1.24 + a_2^{(s)}\,, \\ a_1^{(s)} &\simeq 0.89 - 0.50\,\frac{\bar{\Lambda}_a^{(s)}}{437\text{ MeV}} + 0.025\,\frac{m_a^{(s)}}{106\text{ MeV}} + 2a_2^{(s)} \simeq 0.42 + 2a_2^{(s)}\,. \end{aligned} \tag{3.85}$$

[6] Although the isolated statement critically depends on the external reference value for the inverse moment, the values for the B_q and B_s are obtained consistently such that a comparison between the two cases is sensible.

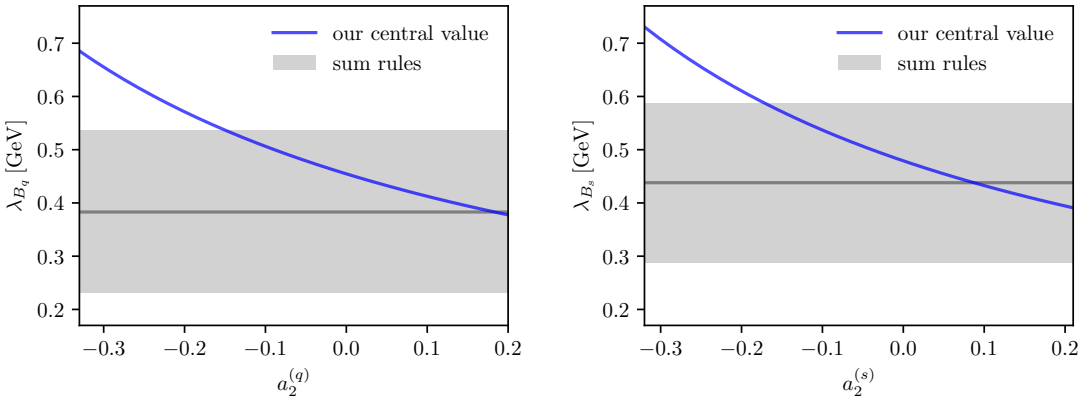

Figure 3.2.: Estimates for the inverse moment λ_B of the B_q (left) and the B_s (right). Blue solid line: central value as a function of the expansion coefficient a_2. Gray band: estimate from the latest sum-rule analysis [49].

Compared to the B_q meson, the resulting flavor-symmetry-breaking effect for the coefficients $a_{0,1}^{(s)}$ lies in the range of 10% to 15%. The moderate effect here suggests that the yet undetermined coefficients $a_2^{(s)}$ can be estimated based on $a_2^{(q)}$ under the assumption of flavor symmetry violation of that size. Independent of flavor symmetry, we can use the growth criterion in Eq. (3.82) as before to constrain the interval for $a_2^{(s)}$, leading to

$$-0.32 < a_2^{(s)} < 0.21\,. \tag{3.86}$$

Considering the inverse moment of the B_s-meson LCDA, we find

$$\lambda_{B_s} \simeq \frac{455\text{ MeV}}{1.33 - 0.42\frac{\bar{\Lambda}_a^{(s)}}{437\text{ MeV}} + 0.017\,\frac{m_a^{(s)}}{106\text{ MeV}} + a_2^{(s)}} \simeq \frac{455\text{ MeV}}{0.93 + a_2^{(s)}}\,. \tag{3.87}$$

On the right-hand side of Fig. 3.2, we show our result as a function of $a_2^{(s)}$ in comparison with the value $\lambda_{B_s} = 438 \pm 150$ MeV determined through QCD sum rules [49]. We again find good compatibility between our approach to implement the constraints from the short-distance behavior and the sum-rule estimates. The positive correlation between the inverse moment and $\bar{\Lambda}_a$ remains, while the explicit effect of the strange-quark mass turns out to be marginal compared to the effect through $\bar{\Lambda}_a$.

Ratio $\boldsymbol{\lambda_{B_s}/\lambda_{B_q}}$ Considering the ratio of inverse moments, we find

$$\frac{\lambda_{B_s}}{\lambda_{B_q}} \simeq \frac{1.33 - 0.35\,\frac{\bar{\Lambda}_a^{(q)}}{367\text{ MeV}} + a_2^{(q)}}{1.33 - 0.42\,\frac{\bar{\Lambda}_a^{(s)}}{437\text{ MeV}} + 0.017\,\frac{m_a^{(s)}}{106\text{ MeV}} + a_2^{(s)}} \simeq \frac{0.98 + a_2^{(q)}}{0.93 + a_2^{(s)}}\,. \tag{3.88}$$

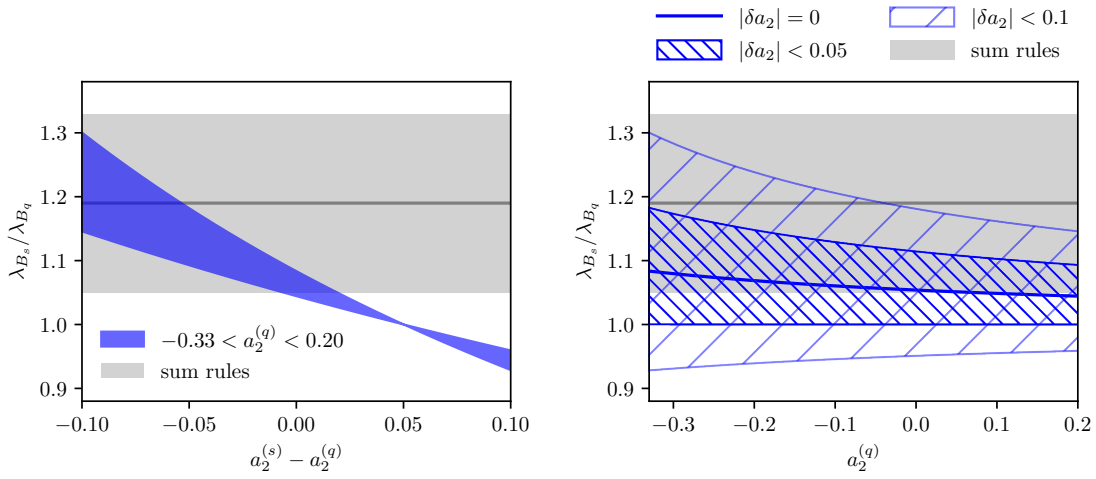

Figure 3.3.: Estimates for the ratio of inverse moments $\lambda_{B_s}/\lambda_{B_q}$ of the $B_{s,q}$-meson LCDAs Left: as a function $a_2^{(s)} - a_2^{(q)} \equiv \delta a_2$. Right: as a function of $a_2^{(q)}$. Blue (hatched) bands: value ranges under the given additional constraint. Gray band: estimate from the latest sum-rule analysis [49].

Again, the main flavor-symmetry breaking effect originates from $\bar{\Lambda}_a^{(q,s)}$, while the explicit effect of the strange-quark mass is numerically small. The ratio depends on two undetermined coefficients $a_2^{(q,s)}$ which we vary on a compact parameter space, constrained through both the bound growth and flavor symmetry. For the latter, given that the maximal values for $a_2^{(q,s)}$ allowed by our convergence criterion are about 0.3, and since we do not expect flavor-symmetry violation to be larger than 30%, we consider $|a_2^{(q)} - a_2^{(s)}| < 0.1$ as a conservative bound. In Fig. 3.3, we plot the result for the ratio in Section 3.4.2 in two different ways: On the left-hand side, we show the ratio as a function of the difference $\delta a_2 = a_2^{(s)} - a_2^{(q)}$, where the band illustrates the range allowed by the growth criterion in Eq. (3.82). On the right-hand side, we show the ratio as a function of $a_2^{(q)}$, where the bands correspond to different values of $|\delta a_2|$ equal to 0 or smaller than 0.05 and 0.1. In both cases, we find good agreement with the sum-rule estimate for the ratio of 1.19 ± 0.14 [49] (with smaller uncertainty than the estimates for the individual inverse moments). While $\delta a_2 = 0$ is included, the comparison shows a slight preference for $a_2^{(s)} - a_2^{(q)} < 0$, consistent with, on the one hand, the previous results and, on the other hand, the estimate obtained for $a_2^{(q,s)}$ based on dimension-5 contributions in the following Section 3.5.

Summarizing the numerical study, for both the B_q and B_s meson, we find a consistent picture when confronting information from the short-distance behavior of the LCDAs with the inverse moments obtained in an independent study. This holds for an analysis based on a systematic parametrization, even at a low truncation order. We find a clear correlation between the inverse moments and the HQET mass parameter $\bar{\Lambda}$. The explicit effect of the

light quark mass in the short-distance expansion turns out to be marginal.

3.4.3. Extrapolation for the B_c Meson

We briefly explore the case of the B_c meson analogously to Section 3.4.2, where we found that the explicit effect due to the quark mass is quantitatively small. In the context of the charmed meson, however, we require a larger renormalization scale due to the larger quark mass (related to convergence of the OPE). The effect of the increased scale needs to be investigated. We consider $\mu_0 = 2$ GeV such that $\alpha_s(\mu_0) \simeq 0.3$, and $\omega_0 = 1.18$ GeV (for $x_0 = 1$ and $n_0 = 1/3$). We further take $M_{B_c} = 6274.47 \pm 0.32$ MeV and $m_c(m_c) = 1.27 \pm 0.2$ GeV [48], from which we obtain $m_c(\mu_0) \simeq 1.10$ GeV using the software `RunDec` [50]. In our scheme, this corresponds to

$$\bar{\Lambda}_a^{(c)}(\mu_0, x_0 = 1) \simeq 1244 \text{ MeV}\,, \quad m_a^{(c)}(\mu_0, x_0 = 1) \simeq 995 \text{ MeV}\,, \tag{3.89}$$

yielding the coefficients

$$\begin{aligned} a_0^{(c)} &\simeq 1.87 - 0.77\,\frac{\bar{\Lambda}_a^{(c)}}{1244 \text{ MeV}} + 0.12\,\frac{m_a^{(c)}}{995 \text{ MeV}} + a_2^{(c)} &&= 1.22 + a_2^{(c)}\,, \\ a_1^{(c)} &\simeq 0.93 - 0.71\,\frac{\bar{\Lambda}_a^{(c)}}{1244 \text{ MeV}} + 0.13\,\frac{m_a^{(c)}}{995 \text{ MeV}} + 2a_2^{(c)} &&= 0.35 + 2\,a_2^{(c)}\,. \end{aligned} \tag{3.90}$$

The convergence criterion leads to the interval

$$-0.32 < a_2^{(c)} < 0.25\,, \tag{3.91}$$

and the inverse moment reads

$$\lambda_{B_c} \;\simeq\; \frac{885 \text{ MeV}}{1.40 - 0.57\frac{\bar{\Lambda}_a^{(c)}}{1244 \text{ MeV}} + 0.090\frac{m_a^{(c)}}{995 \text{ MeV}} + a_2^{(c)}} = \frac{885 \text{ MeV}}{0.91 + a_2^{(c)}}\,. \tag{3.92}$$

The left panel in Fig. 3.4 shows the inverse moment as a function of $a_2^{(c)}$. The expansion parameters $a_k^{(c)}$ lie quantitatively close to the light-quark case. Due to the vastly different renormalization scale μ_0 and reference momentum ω_0, however, the resulting inverse moment is considerably larger, close to the non-relativistic limit (where $m_c \approx \bar{\Lambda}_{B_c} \approx \lambda_{B_c}$). The relevant quantities are collected in Table 3.1 for comparison. We further extend the numerical discussion by illustrating the resulting LCDAs in the right panel of Fig. 3.4 to show the strong effect of the different scales despite the similar parameter values. The bulk region of the B_c LCDA is shifted significantly towards higher momenta. The plot does not include the variation due to $a_2^{(q,s,c)}$, which we set to zero. Notably, the three curves for the scaled quantity $\lambda_B\,\phi_B^+(\omega/\lambda_B)$ (not shown) are virtually indistinguishable.

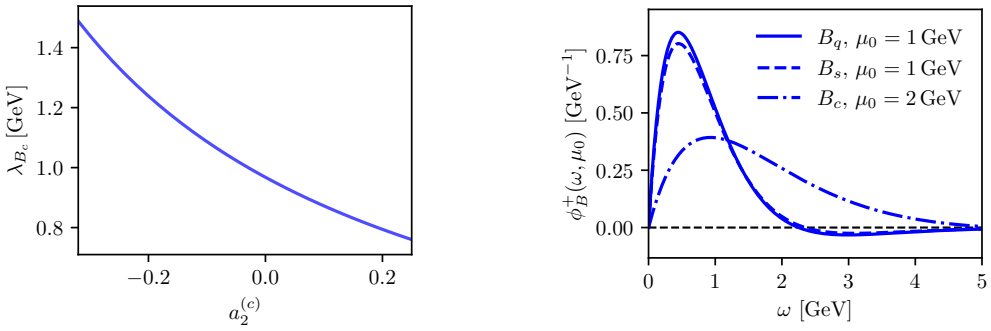

Figure 3.4.: Left: estimate for the inverse moment λ_{B_c} of the B_c-meson LCDA as a function of the expansion coefficient a_2 (central value). Right: comparison of the estimates of the B_q, B_s, and B_c LCDAs (central values).

	B_q	B_s	B_c
μ_0	1 GeV	1 GeV	2 GeV
ω_0	594 MeV	594 MeV	1.18 GeV
$\bar{\Lambda}_a$	367 MeV	437 MeV	1.24 GeV
m_a	0	106 MeV	1.00 GeV
$a_0 - a_2$	1.31	1.24	1.22
$a_1 - 2a_2$	0.47	0.42	0.35
a_2	$(-0.33, 0.20)$	$(-0.32, 0.21)$	$(-0.32, 0.25)$
λ_B	$(380, 690)$ MeV	$(390, 730)$ MeV	$(0.76, 1.49)$ GeV

Table 3.1.: Comparison between the quantities of the numerical study for the LCDAs of B_q, B_s, and B_c mesons.

3.5. Potential Impact of Dimension-5 Operators

This section deals with the possible impact on the determination of the parameters a_k from operators appearing at mass dimension 5 in the OPE. We partially include radiative effects, although not to the full extend. As such, the following results can be seen as a rough estimate and a consistency check of our approach. We investigate the stability and consistency under variation of the parametrization's truncation level K, the mass dimension of the OPE, and the impact of radiative corrections.

The following discussion is a direct extension of Section 3.1.3, where we constrained the local matrix elements at dimension 3 and 4, introducing the parameter $\bar{\Lambda}$. At tree level, the following local operators with mass dimension 5 have non-vanishing Wilson coefficients [18],

$$\bar{q}\, iG^{\mu\nu}\, h_v\,, \qquad \frac{1}{2}\,\bar{q}\{i\overleftarrow{D}^{\mu}, i\overleftarrow{D}^{\nu}\}\, h_v\,,$$

with the gluon field strength tensor $iG^{\mu\nu} = [iD^{\mu}, iD^{\nu}]$. At dimension 5, there appear only two more independent hadronic matrix elements in addition to the binding energy $\bar{\Lambda}$ at dimension 4 and the decay constant f_B^{HQET} at dimension 3. The B-meson matrix element of the first operator does not have an explicit mass dependence, which generally originates from covariant derivatives acting on the light-quark field. Translating the definition from Ref. [18] in terms of the parameters λ_E^2 and λ_H^2 into the covariant trace formalism, we have

$$\frac{\langle 0|\bar{q}_\beta\, iG^{\mu\nu}\,(h_v)_\alpha|\bar{B}(v)\rangle}{\langle 0|\mathcal{O}_1^{(3)}|\bar{B}(v)\rangle} = \frac{1}{4}\left[(1+\not{v})\left(\frac{\lambda_H^2-\lambda_E^2}{3}\,(\gamma^\mu v^\nu - \gamma^\nu v^\mu) - \frac{\lambda_H^2}{3}\, i\sigma^{\mu\nu}\right)\gamma_5\right]_{\alpha\beta}\,. \tag{3.93}$$

We obtain the mass dependence for the second operator by accounting for the quark mass in the spectator quark's Dirac equation, $\bar{q}\, i\overleftarrow{\not{D}} = -\bar{q}m$. There are three independent Lorentz structures (see the result in Eq. (3.95) below) whose coefficients are fully determined by the above parameter definition and the equations of motion,

$$\begin{aligned}
\langle 0|\,\bar{q}\, i\overleftarrow{\not{D}}\, i\overleftarrow{\not{D}}\,\Gamma h_v\,|\bar{B}\rangle &= m^2\,\langle 0|\,\bar{q}\Gamma h_v\,|\bar{B}\rangle\,,\\
\langle 0|\,\bar{q}\, i\overleftarrow{\not{D}}\,(iv\cdot\overleftarrow{D})\,\Gamma h_v\,|\bar{B}\rangle &= -m\bar{\Lambda}\,\langle 0|\,\bar{q}\Gamma h_v\,|\bar{B}\rangle\,,\\
\langle 0|\,\bar{q}\,(iv\cdot\overleftarrow{D})(iv\cdot\overleftarrow{D})\,\Gamma h_v\,|\bar{B}\rangle &= \bar{\Lambda}^2\,\langle 0|\,\bar{q}\Gamma h_v\,|\bar{B}\rangle\,.
\end{aligned} \tag{3.94}$$

Deriving the above conditions, we have to bear in mind the action of the four derivative acting on the gluon field contained in the covariant derivatives (see Appendix B.1). Overall, we obtain the following generic result for the local dimension-5 operator including the

spectator quark mass:

$$\begin{aligned}
&\frac{\frac{1}{2}\,\langle 0|\bar{q}_\beta\,\{i\overleftarrow{D}^\mu, i\overleftarrow{D}^\nu\}\,(h_v)_\alpha|\bar{B}(v)\rangle}{\langle 0|\mathcal{O}_1^{(3)}|\bar{B}(v)\rangle} \\
&\quad = -\frac{1}{4}\left[(1+\not{v})\left(\frac{6\bar{\Lambda}^2+2\lambda_E^2+\lambda_H^2-2m\bar{\Lambda}-m^2}{3}\,v^\mu v^\nu\right.\right. \\
&\qquad \left.\left. -\frac{\bar{\Lambda}^2+\lambda_E^2+\lambda_H^2-m^2}{3}\,g^{\mu\nu}-\frac{2\bar{\Lambda}^2+\lambda_E^2-2m\bar{\Lambda}}{6}\,(\gamma^\mu v^\nu+\gamma^\nu v^\mu)\right)\gamma_5\right]_{\alpha\beta}\,.
\end{aligned} \tag{3.95}$$

Therefore, the LCDA's second Mellin moment at tree level reads

$$\begin{aligned}
\langle\omega^2\rangle_+ \equiv \int_0^\infty d\omega\,\omega^2\,\phi_B^+(\omega)\Big|_{\text{tree}} &= \frac{\langle 0|\,\bar{q}\,(in\cdot\overleftarrow{D})^2\,\not{n}\gamma_5 h_v\,|\bar{B}(v)\rangle}{\langle 0|\mathcal{O}_1^{(3)}|\bar{B}(v)\rangle} \\
&= \frac{6\bar{\Lambda}^2+2\lambda_E^2+\lambda_H^2-2m\bar{\Lambda}-m^2}{3}\,,
\end{aligned} \tag{3.96}$$

$$\begin{aligned}
\langle\omega^2\rangle_- \equiv \int_0^\infty d\omega\,\omega^2\,\phi_B^-(\omega)\Big|_{\text{tree}} &= \frac{\langle 0|\,\bar{q}\,(in\cdot\overleftarrow{D})^2\,\not{\bar{n}}\gamma_5 h_v\,|\bar{B}(v)\rangle}{\langle 0|\mathcal{O}_1'^{(3)}|\bar{B}(v)\rangle} \\
&= \frac{2\bar{\Lambda}^2+\lambda_H^2+2m\bar{\Lambda}-m^2}{3}\,,
\end{aligned} \tag{3.97}$$

generalizing the findings in Ref. [18] to the massive case. The limit to the non-relativistic model corresponds to $\bar{\Lambda}\to m$ and $\lambda_{E,H}^2\to 0$, resulting in $\langle\omega^2\rangle_\pm = m^2$. This is indeed consistent with the respective model of the LCDA, $\phi_B^\pm(\omega)\big|_{\text{tree}} = \delta(\omega-m)$ [33].

We now extend our previous result for the short-distance LCDA derived from the massive OPE up to dimension 4 with OPE contributions of dimension 5. To that end, we neglect certain suppressed terms such that an explicit calculation of the Wilson coefficients is not required. On the one hand, we make use of the *massless* dimension-5 result given in Eq. (7) of Ref. [37]. On the other hand, we supplement the tree-level result for the massive dimension-5 contribution with the universal 1-loop correction. Overall, this leads to

$$\begin{aligned}
\tilde{\phi}_+(\tau) = &\left[1-i\tau\,\langle\omega\rangle_+-\tau^2\,\frac{\langle\omega^2\rangle_+}{2}\right]\left[1-\frac{\alpha_s C_F}{4\pi}\left(2L^2+2L+\frac{5\pi^2}{12}\right)\right] \\
&+i\tau\bar{\Lambda}\,\frac{\alpha_s C_F}{4\pi}\left(\frac{8}{3}\,L-3\right)+i\tau m\,\frac{\alpha_s C_F}{4\pi}\left(\frac{4}{3}\,L-1\right) \\
&+\tau^2\bar{\Lambda}^2\frac{\alpha_s C_F}{4\pi}\left(\frac{10}{3}L-\frac{35}{9}+\mathcal{O}\left(\frac{m}{\bar{\Lambda}}\right)+\mathcal{O}\left(\frac{\lambda_{E,H}^2}{\bar{\Lambda}^2}\right)\right) \\
&+\mathcal{O}(\alpha_s^2)+\mathcal{O}(\tau^3)\,,
\end{aligned} \tag{3.98}$$

where the first Mellin moment is given by $\langle\omega\rangle_+ = (4\bar{\Lambda}-m)/3$. In the first line, we include the universal double-logarithmic corrections proportional to $\langle\omega^2\rangle_+$, while for the single-logarithmic corrections to the dimension-5 contributions, we only account for terms

proportional to $\bar{\Lambda}^2$. The remaining α_s corrections at dimension-5, indicated in the third line, are numerically suppressed due to the small values for light quark masses and $\lambda^2_{E,H}$.

Using this result, we perform a similar study as in Section 3.4, constraining the coefficients of the parametrization based on the OPE input. While in Section 3.4, we determined two parameters while varying a third one according to a convergence criterion, we now take the OPE to dimension 5 into account to fix up to three coefficients. This presents a consistency check for our previous approach as well as the opportunity to test the behavior under variation of the truncation level (corresponding to the mass dimension) and the impact of the radiative corrections.

For the HQET parameters, we consider the pole-mass scheme here, with the central value for the b-quark pole mass taken as $m_b \simeq 4.78$ GeV from Ref. [48], which corresponds to

$$\bar{\Lambda}^{(q)} \simeq 500 \text{ MeV}\,, \qquad \bar{\Lambda}^{(s)} \simeq 590 \text{ MeV}\,,$$

together with $\lambda_E^2 = 0.01$ GeV^2 and $\lambda_H^2 = 0.15$ GeV^2 provided in Ref. [51]. We use a different scheme than the one previously introduced because its generalization is not straightforward when including higher mass dimensions. Note that the value for $\bar{\Lambda}_a$ calculated perturbatively from the value in the pole mass scheme is significantly larger than the one used in Section 3.4.2, relying on Ref. [35][7]. Besides that, the (possible) difference between the two treatments of the HQET mass parameters may give some handle to estimate the scheme dependence of our results. In the same spirit, for the light quarks, we simply use the $\overline{\text{MS}}$ mass values (see Section 3.4.2).

The dimension-5 result allows to match the parameters of the parametrization in Eq. (3.73) at truncation level $K = 2$ to the OPE expression to determine the coefficients. At tree level, this results in

$$\begin{aligned} a_0 &= 1 + \left(1 - \frac{\langle\omega\rangle_+}{2\omega_0}\right) + \frac{3}{4}\left(1 - \frac{\langle\omega_+\rangle}{\omega_0} + \frac{\langle\omega^2\rangle_+}{6\omega_0^2}\right) + \dots\,, \\ a_1 &= \left(1 - \frac{\langle\omega\rangle_+}{2\omega_0}\right) + \frac{3}{2}\left(1 - \frac{\langle\omega_+\rangle}{\omega_0} + \frac{\langle\omega^2\rangle_+}{6\omega_0^2}\right) + \dots\,, \\ a_2 &= \frac{3}{4}\left(1 - \frac{\langle\omega_+\rangle}{\omega_0} + \frac{\langle\omega^2\rangle_+}{6\omega_0^2}\right) + \dots \end{aligned} \tag{3.99}$$

We provide the numerical results in the first three columns of Table 3.2, where we also give the results for lower truncation levels $K = 0, 1$. The expressions for the lower truncation levels correspond to dropping the respective columns in the above formula, maintaining the triangular shape. This serves as a reference to compare against when further taking radiative corrections into account.

[7] They obtain a value $\bar{\Lambda}_{\text{DA}}$ (in their "distribution amplitude" scheme) using the perturbative relation to $\bar{\Lambda}_{\text{SF}}$ (in the "shape function" scheme), which was extracted from moment analyses of experimental data. The purpose is to avoid the renormalon problem surrounding the pole scheme for quark masses.

$n_0 = 1/3$	tree-level, pole-scheme dim-3 $K=0$	dim-4 $K=1$	dim-5 $K=2$	1-loop$^{(*)}$, pole-scheme dim-3 $K=0$	dim-4 $K=1$	dim-5 $K=2$	1-loop, a-scheme dim-4 $K=2$
$a_0^{(q)}$	1	1.44	1.54	0.78	1.07	1.07	$(0.98, 1.51)$
$a_1^{(q)}$	–	0.44	0.65	–	0.26	0.23	$(-0.19, 0.87)$
$a_2^{(q)}$	–	–	0.11	–	–	-0.03	$(-0.33, 0.20)$
$a_0^{(s)}$	1	1.37	1.43	0.78	0.99	0.96	$(0.92, 1.45)$
$a_1^{(s)}$	–	0.37	0.49	–	0.20	0.10	$(-0.22, 0.84)$
$a_2^{(s)}$	–	–	0.06	–	–	-0.06	$(-0.32, 0.21)$

Table 3.2.: Comparison of different estimates for the expansion parameters, depending on the loop order, the highest mass dimension of the OPE, and the parametrization's truncation level K. The last column refers to the results of Section 3.4.2. $^{(*)}$ Not including all 1-loop corrections at dimension 5 (see the discussion of Eq. (3.98)).

Using the expression in Eq. (3.98), we calculate the 1-loop expansion coefficients for truncation levels $K = 0, 1, 2$. The resulting numerical values are compiled in Table 3.2. Comparing the 1-loop corrections to the tree-level case, we observe an improved convergence in the sense that the absolute values of the parameters overall become smaller. The parameter values also exhibit better stability under varying levels of truncation. The parameter values $a_{1,2}$ are consistently decreased when accounting for mass effects which is in line with the results based on the comparison with QCD sum rule results for λ_{B_q} and λ_{B_s} in Section 3.4.2.

At last, in the right column of Table 3.2, we quote again the estimated ranges for the expansion coefficients obtained in Section 3.4.2, where the parameter a_2 is varied within an interval fixed by an ad-hoc convergence criterion, and the mass parameters are taken in the a-scheme. Note that, as functions of a_2, the parameters a_0 and a_1 also lie within an interval. All resulting central values obtained in this section for the expansion coefficients are compatible with the intervals we found before, indicating that our convergence criterion is sensible and that our (qualitative) results are insensitive to the renormalization scheme used for the mass parameters.

Altogether, the findings in this section further support the conclusion that information from the OPE can be consistently incorporated into a global phenomenological analysis that relies on quantities within the QCD factorization framework and the parametrization proposed in Chapter 2.

3.6. Summary

In this chapter, we studied the short-distance behavior of the 2-particle light-cone distribution amplitudes (LCDAs) of the B_s meson, which differs from the known behavior for the B meson because of the considerable mass of the strange quark. We reconsidered the short-distance expansion of 2-particle light-ray operators in HQET, updating the 1-loop matching coefficients of the leading-twist LCDA $\tilde{\phi}_+(\tau)$ with a new contribution at dimension 4 arising for a non-vanishing spectator quark mass, see Eq. (3.48). We also determined the complete set of 1-loop matching coefficients for the subleading 2-particle LCDA $\tilde{\phi}_-(\tau)$ up to dimension 4, see Eq. (3.71). These results were obtained using a convenient procedure based on the asymptotic behavior of Feynman integrals for on-shell matrix elements in momentum space, which allows us to perform local subtractions at the level of the Fourier transform to position space prior to the $\overline{\text{MS}}$ subtraction, greatly simplifying this critical step.

We studied the numerical effect of our result in the context of a global analysis based on the systematic parametrization developed in Chapter 2. We evaluated the short-distance behavior of the LCDA at a suitable small but non-zero light-cone separation τ, together with an imposed convergence criterion for the LCDA parameters, to constrain finite ranges of the leading three parameters. These parameter ranges led to limits for the inverse moment of the leading B_q and B_s LCDAs, which were compatible with independent results based on light-cone sum rules, supporting the consistency of our approach using the parametrization. We found that the dominant flavor-symmetry breaking effect is not due to the explicit mass dependence but rather the HQET mass parameters, $\bar{\Lambda}_{B_s} > \bar{\Lambda}_{B_q}$. This observation motivated us to extrapolate the results to the case of the B_c meson in the limit $m_c \ll m_b$. In summary, we found that the systematic parametrization of the leading-twist LCDA provides a consistent framework even at low truncation levels to combine information from the short-distance regime with and the inverse moment, which constrains the essentially non-perturbative regime of the LCDA.

4. Constraints from $B \to \gamma\ell\nu$ Decay

The results in chapter and Appendix C are unpublished at the time of writing this thesis. A key development featured here is the extension of the publicly available open-source software `EOS` by the author of this thesis. This extension enables the execution of the numerical studies presented herein. For further context, a comprehensive overview of `EOS` has been previously published in

> D. van Dyk, P. Lüghausen, et al. "EOS: a software for flavor physics phenomenology". In: *Eur. Phys. J. C* 82.6 (2022), p. 569. DOI: 10.1140/epjc/s10052-022-10177-4. arXiv: 2111.15428 [hep-ph].

In this chapter, we turn to the decay channel $B \to \gamma\ell\nu$[1] in light of the systematic parametrization proposed in Chapter 2. The decay mode is most promising for the extraction of the leading-twist B LCDA, being both accessible experimentally and well developed from a theory point of view. Reconstructing the invisible neutrino in the final state requires precise knowledge of the initial state. Therefore, an electron-positron collider such as SuperKEKB at KEK running the Belle-II experiment is better suited than a hadron collider like the LHC at CERN with the LHCb experiment. The Belle-II collaboration already anticipates the measurement of the decay [17]. Notably, the LHCb collaboration is keen to contribute data, e.g., on $B \to 3\ell\nu$ [52], which is gaining interest due to recent advancements on the theoretical side [53–55].

Historically, the radiative decay mode has already been investigated since the late 1990s, yet primarily not to probe the LCDA but as the most suitable decay channel to access the decay constant f_B and the CKM matrix element $|V_{ub}|$ [56]. Although the decay $B \to \ell\nu$ is simpler theoretically, because the two-particle final state does not require form factors but merely a decay constant, its event rate suffers from helicity suppression [56]. The back-to-back lepton pair in the final state must combine to spin 0 (equal to the initial state), but the right-handed antineutrino forces the same helicity for the massive charged lepton; as a result, the decay amplitude receives an overall factor m_ℓ^2/m_B^2. The akin process with an additional photon in the final state, $B \to \gamma\ell\nu$, is not overall suppressed this way, but its theory prediction is more complicated due to photon emission from the B-meson system, probing the internal hadronic structure beyond just the decay constant. Apart

[1] We restrict the discussion to B^-, ℓ, and $\bar{\nu}$ whenever the charge and parity properties are relevant. The conjugate case with B^+, $\bar{\ell}$ and ν behaves analogously.

from the direct phenomenological relevance, developing the theory of the radiative leptonic decay mode was also interesting since many ingredients for the more complicated hadronic decays $B \to V\gamma$ already appear in a simplified setting.

The radiative leptonic decay $B \to \gamma\ell\nu$ can be described in the framework of QCD factorization [57, 58]. The goal of this framework is to express the amplitude as a convolution of a process-specific hard scattering kernel, which can be calculated using perturbation theory, with the leading-twist B LCDA, which contains only process-independent, non-perturbative information that is universal for the B meson. To that end, factorization requires large photon energies, $2E_\gamma \gg \Lambda_{\rm QCD}$, as the method relies on the separation of these scales. Shortly after its conception, the factorization theorem was reformulated in terms of soft-collinear effective theory (SCET) [59, 60], which simplifies and generalizes its proof: a complicated diagrammatic analysis can be reduced to a study of field transformations acting on operators in the effective Lagrangian [59, 61–63]. The SCET approach has further achieved to relax the necessary scale hierarchy $m_b \gg 2E_\gamma \gg \Lambda_{\rm QCD}$ (initial formulation) to allow higher photon energies, $m_b, 2E_\gamma \gg \Lambda_{\rm QCD}$ (SCET formulation). At the present, the factorization formula for the $B \to \gamma\ell\nu$ decay includes renormalization group resummation of enhanced logarithms of $m_b/\Lambda_{\rm QCD}$ at the next-to-leading logarithm accuracy [14].

To further improve the accuracy, the factorization approach needs to be supplemented with other non-perturbative QCD methods. While it has been shown that factorization holds at leading power of the expansion in $\Lambda_{\rm QCD}/m_b$ to all orders in the perturbative expansion in α_s [59], the subleading power corrections already contain non-factorizable contributions suffering from end-point divergences. Those power-suppressed "soft overlap" contributions can be estimated using QCD-based methods, combining hadronic dispersion relations with the operator product expansion and light-cone sum rules [15, 64]. In addition to the leading-twist LCDA, the power corrections also involve the higher-twist LCDAs, although the numerical study performed in Ref. [16] suggests that the dominant power corrections stem from the leading-twist LCDA.

We begin this chapter with a review of the state-of-the-art prediction for the $B \to \gamma\ell\nu$ decay amplitude in terms of the dominant contributions from the leading-twist B LCDA $\phi_+(\omega)$ in Section 4.1. We apply the systematic parametrization proposed in Chapter 2 and provide analytic formulas to obtain the expansion of the observables in terms of the parameters a_k to all orders in k in Section 4.2. We discuss technical aspects concerning the implementation of the parametrized expressions into the software `EOS` in Section 4.3. Using the software implementation and the Bayesian analysis tools accessible through `EOS`, we study the efficacy of experimental constraints and form factor predictions potentially available from lattice estimates in combination with theory input from the short-distance expansion in Section 4.4. We summarize the findings in Section 4.5 and provide supplementary formulas and figures in Appendix C.

4.1. Review of the $B \to \gamma\ell\nu$ Decay

We recapitulate the theory description of the decay amplitude based on Ref. [16]. Recent publications have revisited their findings, detailing subleading effects or employing different approaches beyond the scope of our analysis [65–67]. One can define the radiative leptonic decay amplitude of the B meson for a massless lepton $\ell = e, \tau$ using the QCD matrix element [14, 16, 64, 68]

$$\mathcal{A}(B^- \to \gamma\ell\bar{\nu}_\ell) = \frac{G_F V_{ub}}{\sqrt{2}} \big\langle \gamma(p) \ell \bar{\nu}_\ell \big| \big[\bar{\ell}\,\gamma^\nu (1-\gamma_5)\,\nu_\ell\big] \big[\bar{u}\,\gamma_\nu (1-\gamma_5)\,b\big] \big| B^-(p+q) \big\rangle \,, \tag{4.1}$$

with the B meson at rest, $p + q = m_B\, v$, using its four velocity $v_\mu = (1, 0, 0, 0)$, and the momentum of the lepton pair q. We use the following definition of the hadronic tensor in terms of independent Lorentz structures, introducing vector and axial-vector form factors, F_V and F_A:

$$\begin{aligned} T_{\mu\nu}(p,q) &= -i \int \mathrm{d}^4x\, \mathrm{e}^{ip\cdot x} \,\langle 0|\, T\left\{ j_\mu^{\mathrm{em}}(x)\; \bar{u}(0)\, \gamma_\nu (1-\gamma_5)\, b(0) \right\} \big| B^-(p+q) \big\rangle \\ &= (\epsilon_{\mu\nu\tau\rho}\, p^\tau v^\rho)\, F_V + i\,(-g_{\mu\nu}\, v\cdot p + v_\mu p_\nu)\; F_A - i \frac{v_\mu v_\nu}{v\cdot p} f_B m_B + (p_\mu \text{ terms})\,. \end{aligned} \tag{4.2}$$

Above, $j_\mu^{\mathrm{em}} = \sum_q e_q\, \bar{q}\gamma_\mu q$ is the electromagnetic current. Because of the photon's Ward identity, $\epsilon^*(p) \cdot p = 0$, the terms proportional to p_μ indicated in braces are irrelevant for the decay amplitude. The term proportional to $v_\mu v_\nu$ is fixed by the Ward identity $p^\mu T_{\mu\nu} = -i f_B m_B v_\nu$ [14, 69] in the massless lepton limit (see, e.g., Ref. [54] for a discussion of the massive case).

Convenient choices for the form factor's kinematic variable are the squared invariant mass of the lepton pair, q^2, or the photon energy $E_\gamma = v \cdot p$ in the B-meson rest frame:

$$q^2 = (m_B\, v - p)^2 = m_B^2 + p^2 - 2 m_B E_\gamma \,. \tag{4.3}$$

For the case of a real photon, $p^2 = 0$, the kinematic range is bounded by the condition

$$E_\gamma = \frac{m_B^2 - q^2}{2 m_B} \qquad \text{such that} \qquad 0 \le E_\gamma \le \frac{m_B}{2} \qquad \text{or} \qquad 0 \le q^2 \le m_B^2 \,. \tag{4.4}$$

The doubly differential decay width in the B-meson rest frame reads (see also Ref. [14])

$$\frac{\mathrm{d}^2\Gamma}{\mathrm{d}E_\gamma\, \mathrm{d}E_\ell} = \frac{\alpha_{\mathrm{em}} G_F^2 |V_{ub}|^2}{16\pi^2} m_B^3 (1-x_\gamma) \left[(1-x_\nu)^2 \big| F_V + \hat{F}_A \big|^2 + (1-x_\ell)^2 \big| F_V - \hat{F}_A \big|^2 \right] , \tag{4.5}$$

using the abbreviation $x_i = 2E_i/m_B$ for $i = \gamma, \ell, \nu$ and with $\hat{F}_A = F_A + e_\ell f_B / E_\gamma$. The second term in $\hat{F}_A$ corresponds to final state radiation, where the photon is emitted off the charged lepton. The two form factors depend on the photon energy E_γ but not on the

lepton energy E_ℓ. The following single differential decay width of the amplitude results from integrating the lepton energy E_ℓ over its entire kinematic range $[m_B/2 - E_\gamma, m_B/2]$:

$$\frac{\mathrm{d}\Gamma}{\mathrm{d}E_\gamma} = \frac{\alpha_{\mathrm{em}} G_F^2 |V_{ub}|^2}{6\pi^2} m_B E_\gamma^3 \left(1 - \frac{2E_\gamma}{m_B}\right) \left(\left|F_V\right|^2 + \left|\hat{F}_A\right|^2\right) . \tag{4.6}$$

The integrated forward-backward asymmetry is an experimental observable that characterizes the angular distribution of the lepton emission. Adopting the angular coordinate system provided in Ref. [54], Appendix D, the relation between the lepton energy and the polar angle θ in the center of mass system of the lepton and neutrino reads $2E_\ell = (\cos\theta - 1)E_\gamma + m_B$. Accordingly, we define the normalized differential forward-backward asymmetry as

$$a_{\mathrm{FB}}(E_\gamma) \equiv \left(\frac{\mathrm{d}\Gamma}{\mathrm{d}E_\gamma}\right)^{-1} \int \mathrm{d}\cos(\theta)\ \mathrm{sgn}[\cos(\theta)]\, \frac{\mathrm{d}^2\Gamma}{\mathrm{d}E_\gamma\, \mathrm{d}\cos(\theta)} = \frac{3}{2} \frac{\mathrm{Re}\, F_V \hat{F}_A^*}{\left|F_V\right|^2 + \left|\hat{F}_A\right|^2} . \tag{4.7}$$

It is useful to organize the contributions to the form factors according to

$$F_{V,A}(E_\gamma) \equiv \frac{e_u m_B}{2E_\gamma} \frac{f_B}{\lambda_B(\mu)} R(E_\gamma, \mu) + \left[\xi(E_\gamma) \pm \Delta\xi(E_\gamma)\right] \tag{4.8}$$

into a leading-power (LP) contribution proportional to R and next-to-leading power (NLP) contributions in the expansion in $1/m_B$, $1/(2E_\gamma)$, denoted in square brackets. The latter are either "symmetry preserving", collected in ξ, i.e., entering both form factors with equal signs, or "symmetry breaking", collected in $\Delta\xi$, i.e., entering them with opposite signs. Apart from the dominant LP (non-local) contribution, which can be calculated in QCD factorization to all orders in the perturbative expansion, there are three classes of subleading power corrections: local corrections; non-local, factorizable corrections; and non-local, non-factorizable (i.e., "soft") corrections. In the following, we review each of the contributions.

4.1.1. Leading-power Contribution (Factorization Formula)

At LP in the heavy quark expansion (i.e., the heavy quark limit $m_B \to \infty$), the form factors can be expressed using QCD factorization and read

$$F_{V,A}(E_\gamma)\big|_{\mathrm{LP}} = \frac{e_u m_B}{2E_\gamma} \frac{f_B}{\lambda_B(\mu)} R(E_\gamma, \mu) \tag{4.9}$$

with the inverse moment $1/\lambda_B(\mu) = \int_0^\infty \frac{\mathrm{d}\omega}{\omega} \phi_+(\omega, \mu)$. The LP contribution, sketched in Fig. 4.1a at tree level, originates only from photon emission off the light spectator quark, while the emission off the b quark shown in Fig. 4.1b is power suppressed (see the discussion of subleading contributions). The function R results from the convolution of a "hard scattering kernel" T and the leading-twist LCDA ϕ_+,

$$R(E_\gamma, \mu) = \lambda_B(\mu) \int_0^\infty \frac{\mathrm{d}\omega}{\omega}\, T(E_\gamma, \omega, \mu)\, \phi_+(\omega, \mu) = 1 + \mathcal{O}(\alpha_s) , \tag{4.10}$$

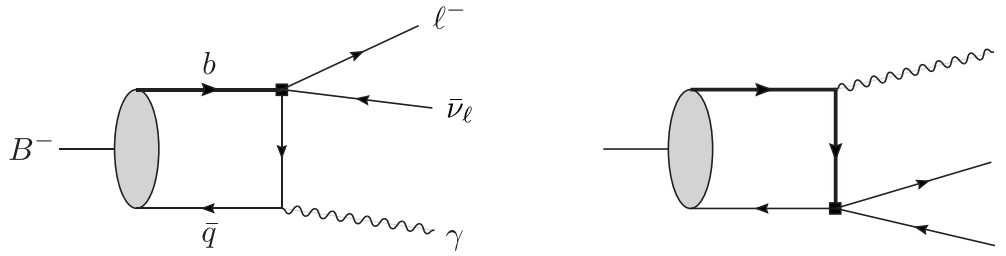

(a) Leading power **(b)** Subleading power

Figure 4.1.: Sketches of $B \to \gamma\ell\nu$ contributions at the leading perturbative order.

where we indicate the normalization at the tree level. At leading power in $1/m_b$ and leading order in α_s, the inverse moment is the only quantity derived from the LCDA that enters the amplitude. Therefore, it is the most significant non-perturbative parameter associated with the substructure of the B meson in the factorization approach.

Currently, the most advanced result for R includes next-to-leading logarithmic summation of logarithms of m_b/Λ_{QCD}, which consists of several contributions [14, 60]:

$$R(E_\gamma, \mu) = C(E_\gamma, \mu_{h1})\, K^{-1}(\mu_{h2})\, U(E_\gamma, \mu_{h1}, \mu_{h2}, \mu)\, J(E_\gamma, \mu) \tag{4.11}$$

The factors have various origins:

C arises when matching the QCD heavy-to-light current onto the corresponding SCET current [70]. This function is associated to the hard scale m_B.

K^{-1} converts the physical B-meson decay constant f_B as defined using QCD to its scale-dependent definition using HQET in the static limit by [16]

$$f_B^{\text{HQET}}(\mu) = K^{-1}(\mu)\, \sqrt{m_B}\, f_B\,. \tag{4.12}$$

U connects, via the RGE (see, e.g., Ref. [60]), the other pieces dependent of their respective scales to resum large logarithms to next-to-leading accuracy.

J is the radiative correction factor, i.e., a convolution with $\phi_+(\omega)$. At 1-loop order, in addition to the inverse moment at tree level, the formula [14]

$$J(E_\gamma, \mu) = 1 + \frac{\alpha_s C_F}{4\pi}\left(\ln^2\frac{2E_\gamma\mu_0}{\mu^2} - 2\sigma_1(\mu)\ln\frac{2E_\gamma\mu_0}{\mu^2} - 1 - \frac{\pi^2}{6} + \sigma_2(\mu)\right), \tag{4.13}$$

includes the LCDA's first and second logarithmic moments $\sigma_{1,2}$,

$$\sigma_n(\mu) = \lambda_B(\mu)\int_0^\infty \frac{\mathrm{d}\omega}{\omega}\, \ln^n\frac{\mu_0}{\omega}\, \phi_+(\omega, \mu)\,, \tag{4.14}$$

where μ_0 serves as a reference scale for the logarithmic moments. This factor is associated with the hard-collinear scale $\sqrt{m_B \Lambda_{\rm QCD}}$. Derivations of the expression can be found in Refs. [59] and [60]. Note that J can be related to the inverse moment of an "effective LCDA" (defined later in the context of soft corrections in Eq. (4.22)) [16],

$$\frac{J(E_\gamma,\mu)}{\lambda_B(\mu)} = \int_0^\infty \frac{\mathrm{d}\omega}{\omega}\, \phi_+^{\rm eff}(\omega,\mu)\,. \tag{4.15}$$

Explicit expressions for the ingredients of Eq. (4.11) are provided in Ref. [14]. Details on the resummation procedure can also be found in the recent publication Ref. [67].

4.1.2. Subleading-power Contributions

Power-suppressed contributions to the form factors in Eq. (4.8) are accounted for in ξ and $\Delta\xi$, for pieces that enter each form factor with equal or opposite sign, respectively. Again, there are several different sources for the subleading corrections, which we discuss individually. In the following, we adopt the notation from Ref. [16],

$$\xi = \xi^{\rm ht} + \xi^{\rm soft}_{\rm (NLO)} + \left[\xi^{\rm soft}_{\rm (tw-3,4)} + \xi^{\rm soft}_{\rm (tw-5,6)}\right], \tag{4.16}$$

$$\Delta\xi = \Delta\xi^{\rm ht} + \left[\Delta\xi^{\rm soft}_{\rm (tw-3,4)} + \Delta\xi^{\rm soft}_{\rm (tw-5,6)}\right], \tag{4.17}$$

which contains factorizable higher-twist ("ht") contributions and non-factorizable "soft" ones. The numerical study in Ref. [16] reveals a suppression of the higher-twist pieces marked in square brackets, which we therefore not include in our numerical analysis. We note, however, that it is straightforward to adopt the ansatz laid out in Appendix A of Ref. [16] to estimate the higher-twist contributions based on only a single "profile function" $f(\omega)$. It is defined as $\phi_+(\omega) = \omega\, f(\omega)$, translating to

$$f(\omega;\omega_0,\mu_0) = \frac{\mathrm{e}^{-\omega/\omega_0}}{\omega_0^2} \sum_{k=0}^{K} \frac{a_k(\mu_0)}{1+k}\, L_k^{(1)}(2\omega/\omega_0)$$

using the LCDA parametrization. The equations of motion relate the higher-twist LCDAs to the same profile function; e.g., for the 3-particle LCDAs $\phi_3(\omega_1,\omega_2) \propto \omega_1\omega_2^2\, f'(\omega_1+\omega_2)$ and $\phi_4(\omega_1,\omega_2) \propto \omega_2^2\, f(\omega_1+\omega_2)$ up to hadronic constants such as $\bar\Lambda$, λ_E, and λ_H. This is valid only at the tree level and therefore not suitable for extracting quantitative predictions. Instead, it can provide an estimate of the neglected higher-twist corrections for diagnostic purposes.

The factorizable higher-twist contributions can be further split as

$$\xi^{\rm ht} = \xi^{\rm ht}_{1/E_\gamma} + \xi^{\rm ht}_{1/m_b}\,, \tag{4.18}$$

$$\Delta\xi^{\rm ht} = \frac{e_u f_B m_B}{(2E_\gamma)^2} + \frac{e_b f_B m_B}{2E_\gamma m_b}\,. \tag{4.19}$$

The origins of the above terms are most easily explained at the hand of the two sketches in Fig. 4.1. Since the spectactor-quark momentum $k \sim \Lambda_{\rm QCD}$ is soft, the internal propagator joining the lepton and photon vertices has hard-collinear virtuality $m_b\,\Lambda_{\rm QCD}$ when the photon is emitted off the light anti-quark (Fig. 4.1a) but hard virtuality m_b^2 when it is emitted off the heavy quark (Fig. 4.1b) [14]. The last term in Eq. (4.19) proportional to e_b accounts for the subleading contribution from the diagram in Fig. 4.1b. The other terms in Eq. (4.18) and Eq. (4.19) stem from the diagram Fig. 4.1a but evaluated in HQET to subleading power. Without providing the exact expressions for $\xi^{\rm ht}_{1/E_\gamma}$ and $\xi^{\rm ht}_{1/m_b}$ as functionals of the LCDAs, we quote their estimates obtained using the profile function ansatz. They only depend on hadronic parameters, but not on the shape of the LCDAs:

$$\begin{aligned}
\xi^{\rm ht}_{1/E_\gamma}(E_\gamma) &= -\frac{e_u f_B m_B}{2E_\gamma^2}\left\{\frac{2(\lambda_E^2+2\lambda_H^2)}{6\bar\Lambda^2+2\lambda_E^2+\lambda_H^2}+\frac{1}{2}\right\},\\
\xi^{\rm ht}_{1/m_b}(E_\gamma) &= +\frac{e_u f_B m_B}{4E_\gamma m_b}\left\{\frac{\bar\Lambda}{\lambda_B}-2+\frac{4(\lambda_E^2-\lambda_H^2)}{6\bar\Lambda^2+2\lambda_E^2+\lambda_H^2}\right\}.
\end{aligned} \tag{4.20}$$

The non-factorizable (soft) contributions complement the light-cone expansion used to obtain the LP factorization formula. They also take into account distances x between the currents in Eq. (4.2) that lie outside the light cone, $x^2 \sim 1/\Lambda^2_{\rm QCD}$. This case is accessible using the light-cone sum rules approach [71], based on dispersion relations and quark-hadron duality. The latter refers to a certain equivalency between two representations of the correlation function in Eq. (4.2). On the one hand, it can be expressed in terms of quarks and gluons and, on the other hand, in terms of physical hadrons as the intermediate states. Omitting the derivation details provided in Ref. [16], we proceed to discuss the results.

Soft contributions related to only the leading-twist LCDA, including perturbative corrections, can be cast into the form (see also [64])

$$\begin{aligned}
\xi^{\rm soft}_{\rm (NLO)}(E_\gamma) = \frac{e_u f_B m_B}{2E_\gamma}\, C(E_\gamma,\mu_{h1})\, K^{-1}(\mu_{h2})\, U(E_\gamma,\mu_{h1},\mu_{h2},\mu)\,\times\\
\times\int_0^{\frac{s_0}{2E_\gamma}} {\rm d}\omega'\left[\frac{2E_\gamma}{m_\rho^2}\,{\rm e}^{-(2E_\gamma\omega'-m_\rho^2)/M^2}-\frac{1}{\omega'}\right]\,\phi_+^{\rm eff}(\omega',\mu)\,,
\end{aligned} \tag{4.21}$$

where M is a free parameter introduced by a Borel transform, and s_0 is a duality threshold parameter used in dispersion relations. The prefactors are equal to the ones in the leading-power factorization formula discussed in Section 4.1.1. This contribution is identical for both form factors, i.e., $\Delta\xi^{\rm soft}_{\rm (NLO)}(E_\gamma) = 0$. The "effective LCDA" $\phi_+^{\rm eff}$ is defined to account for the convolution of ϕ_+ with a hard-collinear kernel at NLO, including the LO term:

$$\phi_+^{\rm eff}(\omega') = \phi_+(\omega') + \frac{\alpha_s(\mu)C_F}{4\pi}\,\Delta\phi_+^{(1)}(\omega')\,. \tag{4.22}$$

Here, we further decompose $\Delta\phi_+^{(1)}$ as the sum of the following four pieces in order to break down the following computations:

$$\Delta\phi_+^{(1a)}(\omega') = \left(\ln^2\frac{\mu^2}{2E_\gamma\omega'} + \frac{\pi^2}{6} - 1\right)\phi_+(\omega',\mu)\,, \tag{4.23}$$

$$\Delta\phi_+^{(1b)}(\omega') = \left(2\ln\frac{\mu^2}{2E_\gamma\omega'} + 3\right)\omega'\int_{\omega'}^{\infty}\mathrm{d}\omega\ln\frac{\omega-\omega'}{\omega'}\frac{\mathrm{d}}{\mathrm{d}\omega}\frac{\phi_+(\omega,\mu)}{\omega}\,, \tag{4.24}$$

$$\Delta\phi_+^{(1c)}(\omega') = -2\ln\frac{\mu^2}{2E_\gamma\omega'}\int_0^{\omega'}\mathrm{d}\omega\ln\frac{\omega'-\omega}{\omega'}\frac{\mathrm{d}}{\mathrm{d}\omega}\phi_+(\omega,\mu)\,, \tag{4.25}$$

$$\Delta\phi_+^{(1d)}(\omega') = \int_0^{\omega'}\mathrm{d}\omega\ln^2\frac{\omega'-\omega}{\omega'}\frac{\mathrm{d}}{\mathrm{d}\omega}\left[\frac{\omega'}{\omega}\phi_+(\omega,\mu) + \phi_+(\omega,\mu)\right]. \tag{4.26}$$

The other soft higher-twist contributions with subscripts $(\mathrm{tw}-3,4)$ and $(\mathrm{tw}-5,6)$ can be brought into a form similar to Eq. (4.21) at LO, involving the higher-twist LCDAs. In contrast to the soft LP, NLO piece, soft higher-twist corrections also include symmetry-breaking contributions. A model-based numerical study suggests, however, that "among the different contributions to the soft correction the part related to the leading-twist LCDA, $\xi^{\mathrm{soft}}_{(\mathrm{NLO})}$ [...], is dominant in all cases" [16]. Therefore, we do not expect any significant effect for our qualitative study and assume in the following

$$\xi^{\mathrm{soft}}_{(\mathrm{tw}-3,4)}\,,\ \Delta\xi^{\mathrm{soft}}_{(\mathrm{tw}-3,4)}\,,\ \xi^{\mathrm{soft}}_{(\mathrm{tw}-5,6)}\,,\ \Delta\xi^{\mathrm{soft}}_{(\mathrm{tw}-5,6)} \approx 0\,.$$

For quantitative results, however, these contributions should be taken into account, at least by estimation using the profile function approach.

4.2. Convolutions Beyond the Inverse Moment λ_B^{-1}

The leading contribution in Eq. (4.9) with $R = 1$, i.e., without perturbative or power corrections, only depends on the LCDA's inverse moment $L_0 = \lambda_B^{-1}$. Beyond the leading piece, further integrals involving the LCDA come into play: the logarithmic moments $\sigma_{1,2}$ enter the radiative corrections at leading power through the 1-loop expression for R in Eq. (4.11), which alternatively can be expressed as the inverse moment of the effective LCDA at NLO. The "incomplete inverse moment", L_0^{inc}, and the "incomplete Laplace transform", denoted by $\mathcal{L}^{\mathrm{inc}}$, appear in the soft power corrections in Eq. (4.21). Because the finite upper integration limit stems from soft kinematics, we use the term "incomplete" (in the sense of "partial") rather than "cut off" which is usually associated with a large scale serving as a UV regulator. We find it convenient to denote the functional dependence explicitly in order to treat the terms for $\phi = \phi_+^{\mathrm{eff}}$ in Eq. (4.23) individually. In summary,

the following integrals with $\phi = \phi_+, \Delta\phi_+^{(i)}$ appear in the form factors:

$$L_0[\phi] = \int_0^\infty \frac{\mathrm{d}\omega}{\omega}\, \phi(\omega)\,, \tag{4.27}$$

$$L_0^{\mathrm{inc}}[\phi;\Omega] = \int_0^\Omega \frac{\mathrm{d}\omega}{\omega}\, \phi(\omega)\,, \tag{4.28}$$

$$\mathcal{L}^{\mathrm{inc}}[\phi;\Omega,\sigma] = \int_0^\Omega \mathrm{d}\omega\, \mathrm{e}^{-\sigma\omega}\, \phi(\omega)\,, \tag{4.29}$$

with parameters $\Omega = s_0/(2E_\gamma)$ and $\sigma = 2E_\gamma/M^2$.

Computing these integrals in terms of the parametrization for ϕ_+ can be done order-by-order in the coefficient expansion in a_k or, more efficiently, using the associated Laguerre polynomial's generating function. This function encodes the polynomials as its series coefficients [72],

$$\sum_{n=0}^\infty t^n\, L_n^{(\alpha)}(x) = \frac{\mathrm{e}^{-tx/(1-t)}}{(1-t)^{\alpha+1}}\,. \tag{4.30}$$

Applied to the parametrization, we define[2] the "generator formalism",

$$\phi_+(\omega) = \frac{\omega\, \mathrm{e}^{-\omega/\omega_0}}{\omega_0^2} \sum_k \frac{a_k}{1+k}\, L_k^{(1)}(2\omega/\omega_0) = \sum_k \frac{a_k}{1+k} \left[\frac{1}{k!}\frac{\partial^k}{\partial t^k}\, [\phi_+(\omega)](t)\right]_{t=0}\,, \tag{4.31}$$

where the LCDA in square brackets denotes the generator

$$[\phi_+(\omega)](t) = \frac{1}{(1-t)^2}\frac{\omega}{\omega_0^2} \exp\!\left(-\frac{1+t}{1-t}\frac{\omega}{\omega_0}\right)\,. \tag{4.32}$$

Given that integration and differentiation commute, for any quantity X that is derived from the LCDA, we define the generator of X, denoted as $[X](t)$, by substituting $\phi_+(\omega) \to [\phi_+(\omega)](t)$ in the formula of X. Doing so implies the replacement of X by its coefficient expansion as

$$X \to \sum_k \frac{a_k}{1+k} \left[\frac{1}{k!}\frac{\partial^k}{\partial t^k}\, [X](t)\right]_{t=0}\,. \tag{4.33}$$

This formalism highlights one of the parametrization's key advantages: the choice of basis functions is convenient for the computation of observables since they are mere products of polynomials with an exponential. Here, we further reduce the order-by-order computation of integrations to a single special case, as remarkably simple as the exponential model.

[2] Retaining the weight factor $1/(1+k)$ in the sum instead of absorbing it into the generator results in a more compact formula, similar to the exponential model. Another advantage is the obvious limit $t \to 0$. The weighted polynomial's generating function for the other case (lacking those features) reads

$$\sum_{n=0}^\infty t^n\, \frac{L_n^{(1)}(x)}{1+n} = \frac{1-\mathrm{e}^{-tx/(1-t)}}{tx}\,.$$

The differentiations to recover the order-by-order expressions are typically easy to perform (especially using computer algebra software). Note that the parametrization allows us to account for renormalization scale dependence through the coefficient values $a_k(\mu)$, see Eq. (2.58) and the discussion in Section 2.2.3.

4.2.1. Leading-order Expressions

We illustrate the generator formalism using the LCDA's inverse moment, where the explicit order-by-order result is already given in Eq. (2.44). The generator yields the compact expression

$$[L_0[\phi_+]](t) = \int_0^\infty \frac{\mathrm{d}\omega}{\omega}\, [\phi_+(\omega)](t) = \frac{1}{\omega_0}\frac{1}{1-t^2}\,. \tag{4.34}$$

We recover the previous result by computing the derivatives at $t = 0$,

$$L_0 = \frac{1}{\omega_0}\sum_k \frac{a_k}{1+k}\left[\frac{1}{k!}\frac{\partial^k}{\partial t^k}\frac{1}{1-t^2}\right]_{t=0} = \frac{1}{\omega_0}\left(a_0 + \frac{a_2}{3} + \frac{a_4}{5} + \frac{a_6}{7} + \ldots\right). \tag{4.35}$$

The other quantities for ϕ_+ are similarly compact,

$$\left[L_0^{\mathrm{inc}}[\phi_+;\Omega]\right](t) = \frac{1}{\omega_0}\frac{1}{1-t^2}\left(1 - \exp\left\{-\frac{1+t}{1-t}\frac{\Omega}{\omega_0}\right\}\right), \tag{4.36}$$

$$\left[\mathcal{L}^{\mathrm{inc}}[\phi_+;\Omega,\sigma]\right](t) = \frac{1}{(1-t)^2}\frac{1}{g^2}\left[1 - \left(1 + g\,\frac{\Omega}{\omega_0}\right)\exp\left\{-g\frac{\Omega}{\omega_0}\right\}\right], \tag{4.37}$$

using the abbreviation $g = \frac{1+t}{1-t} + \omega_0\,\sigma$.

4.2.2. Subleading-order Expressions

The effective LCDA accounts for radiative corrections at NLO, which manifest as a convolution of the LCDA with a perturbative kernel. Therefore, double integrals of the parametrized LCDA ϕ_+ appear. We proceed to calculate the inverse moment of the effective LCDA term by term, starting with the single integral

$$\begin{aligned}\left[L_0[\Delta\phi_+^{(1a)}]\right](t) &= \int_0^\infty \frac{\mathrm{d}\omega}{\omega}\left(\ln^2\frac{\mu^2}{2E_\gamma\omega} + \frac{\pi^2}{6} - 1\right)\,[\phi_+(\omega)]\,(t)\\ &= \frac{1}{\omega_0}\frac{1}{1-t^2}\left[-1 + \frac{\pi^2}{3} + \ln^2\left(\frac{\mu^2\mathrm{e}^{\gamma_\mathrm{E}}}{2E_\gamma\omega_0}\frac{1+t}{1-t}\right)\right],\end{aligned} \tag{4.38}$$

while the remaining pieces require integration twice. The second piece reads

$$\begin{aligned}\left[L_0[\Delta\phi_+^{(1b)}]\right](t) &= \int_0^\infty \frac{\mathrm{d}\omega'}{\omega'}\left(2\ln\frac{\mu^2}{2E_\gamma\omega'} + 3\right)\omega'\int_{\omega'}^\infty \mathrm{d}\omega\,\ln\frac{\omega-\omega'}{\omega'}\frac{d}{d\omega}\frac{[\phi_+(\omega,\mu)]\,(t)}{\omega}\\ &= -\frac{\pi^2}{3}\,\frac{1}{\omega_0}\frac{1}{1-t^2}\,.\end{aligned} \tag{4.39}$$

The other pieces only differ up to a sign,

$$\left[L_0[\Delta\phi_+^{(1c)}]\right](t) = \frac{\pi^2}{3}\,\frac{1}{\omega_0}\,\frac{1}{1-t^2}\,, \tag{4.40}$$

$$\left[L_0[\Delta\phi_+^{(1d)}]\right](t) = -\frac{\pi^2}{3}\,\frac{1}{\omega_0}\,\frac{1}{1-t^2}\,. \tag{4.41}$$

Overall, the NLO part of the effective LCDA yields the generator of the inverse moment

$$\left[L_0[\Delta\phi_+^{(1)}]\right](t) = \frac{1}{\omega_0}\,\frac{1}{1-t^2}\left[-1+\ln^2\left(\frac{\mu^2 \mathrm{e}^{\gamma_\mathrm{E}}}{2E_\gamma\omega_0}\,\frac{1+t}{1-t}\right)\right]\,. \tag{4.42}$$

The expressions for the incomplete inverse moment at NLO,

$$\left[L_0^{\mathrm{inc}}[\Delta\phi_+^{(1)};\Omega]\right](t) \tag{4.43}$$

are provided as machine-copyable code for Mathematica 13 in Appendix C.1. They involve the exponential integral function $\mathrm{Ei}(z)$, hypergeometric functions ${}_pF_q(a;b;z)$, and their derivatives.

The generator of the incomplete Laplace transform

$$\left[\mathcal{L}^{\mathrm{inc}}[\Delta\phi_+^{(1)};\Omega,\sigma]\right](t) \tag{4.44}$$

contains terms which, as of the writing of this thesis, we cannot express using standard functions. This concerns the two pieces associated with $\Delta\phi_+^{(1c)}$ and $\Delta\phi_+^{(1d)}$. Rearranging the terms in ϕ_+^{eff} using partial integration and expansion of the logarithms allows us to obtain all pieces but the last in closed form. To that end, we express $\Delta\phi_+^{(1)}$ as the sum of

$$\Delta\phi_+^{(1a\star)}(\omega') = \left(\frac{\pi^2}{6}-1\right)\phi_+(\omega',\mu)\,, \tag{4.45}$$

$$\Delta\phi_+^{(1b\star)}(\omega') = \Delta\phi_+^{(1b)}(\omega') = \left(2\ln\frac{\mu^2}{2E_\gamma\omega'}+3\right)\omega'\int_{\omega'}^{\infty}\mathrm{d}\omega\,\ln\frac{\omega-\omega'}{\omega'}\,\frac{\mathrm{d}}{\mathrm{d}\omega}\,\frac{\phi_+(\omega,\mu)}{\omega}\,, \tag{4.46}$$

$$\Delta\phi_+^{(1c\star)}(\omega') = \int_0^{\omega'}\mathrm{d}\omega\,\ln^2\left[\frac{\omega'-\omega}{\omega'}\,\frac{2E_\gamma\omega'}{\mu^2}\right]\,\frac{\mathrm{d}}{\mathrm{d}\omega}\phi_+(\omega,\mu)\,, \tag{4.47}$$

$$\Delta\phi_+^{(1d\star)}(\omega') = \int_0^{\omega'}\mathrm{d}\omega\,\ln^2\frac{\omega'-\omega}{\omega'}\,\frac{\mathrm{d}}{\mathrm{d}\omega}\left[\frac{\omega'}{\omega}\phi_+(\omega,\mu)\right]\,. \tag{4.48}$$

The known partial results for $\left[\mathcal{L}^{\mathrm{inc}}[\Delta\phi_+^{(1)};\Omega,\sigma]\right](t)$ using the above decomposition are also provided as code in Appendix C.1.

If no closed form is available, numerical integration can be used in practical applications. However, doing so might result in undesirable computation times for applications requiring many evaluations such as sampling-based statistical methods. As a more efficient option, one can approximate the exact solution using a truncated series, which is the subject of Section 4.2.3. The terms of the rapidly converging series are more accessible in closed form than the sum of the entire series.

4.2.3. Series Expansion of $\Delta\phi_+^{(1d\star)}$

Even though the functional form of the LCDA's parametrization is simple, complicated integrals may arise when several dimensionful scales are present and because of the convolution with a perturbative kernel. At present, we have no expression in terms of standard functions for the double integral with external scales Ω and σ

$$\Big[\mathcal{L}^{\text{inc}}[\Delta\phi_+^{(1d\star)};\Omega,\sigma]\Big](t) = \int_0^\Omega \mathrm{d}\omega'\, \mathrm{e}^{-\sigma\omega'} \Big[\Delta\phi_+^{(1d\star)}(\omega')\Big](t) \tag{4.49}$$

with a logarithmic factor in

$$\Big[\Delta\phi_+^{(1d\star)}(\omega')\Big](t) = \int_0^{\omega'} \mathrm{d}\omega \ln^2\frac{\omega'-\omega}{\omega'} \frac{\mathrm{d}}{\mathrm{d}\omega}\Big[\frac{\omega'}{\omega}\,[\phi_+(\omega)](t)\Big]\,. \tag{4.50}$$

The latter integral, related to the effective LCDA, is dominated by the region where $\omega \to \omega'$ because of the logarithm's behavior. This can be exploited by Taylor expanding the remaining integrand around that region to obtain a rapidly converging series. We have

$$\frac{\mathrm{d}}{\mathrm{d}\omega}\Big[\frac{\omega'}{\omega}\,[\phi_+(\omega)](t)\Big] = \frac{t+1}{t-1}\frac{1}{\omega_0}\frac{\omega'}{\omega}\,[\phi_+(\omega)](t) \tag{4.51}$$

and further

$$\frac{\omega'}{\omega}\,[\phi_+(\omega)](t) = \exp\left\{\frac{1+t}{1-t}\frac{\omega'}{\omega_0}\frac{\omega'-\omega}{\omega'}\right\}\big[\phi_+(\omega')\big](t)\,. \tag{4.52}$$

Taken all together, expanding the exponential leads to the sum

$$\Big[\Delta\phi_+^{(1d\star)}(\omega')\Big](t) = \frac{t+1}{t-1}\,\frac{\omega'}{\omega_0}\,\big[\phi_+(\omega')\big](t)\sum_{n=0}^{\infty}\int_0^1 \mathrm{d}x\ln^2(1-x)\frac{1}{n!}\left[\frac{1+t}{1-t}\frac{\omega'}{\omega_0}(1-x)\right]^n \tag{4.53}$$

$$= -2\,\big[\phi_+(\omega')\big](t)\sum_{n=0}^{\infty}\frac{1}{(1+n)^3}\frac{1}{n!}\left[\frac{1+t}{1-t}\frac{\omega'}{\omega_0}\right]^{n+1}\,. \tag{4.54}$$

The sum in Eq. (4.54) corresponds to a hypergeometric function ${}_3F_3$. More importantly, the effect of the logarithmic convolution becomes transparent: the generator shows that even the unsuppressed term at $n = 0$ modifies the LCDA's series expansion. Whereas the contribution a_k of $\phi_+(\omega)$ comes with a polynomial $\mathcal{O}\big(\omega^{k+1}\big)$, the n^{th} term above generates a polynomial weight of $\mathcal{O}\big(\omega^{k+2+n}\big)$[3]. On the one hand, the expression is helpful as a compact, intermediate result for further calculation. On the other hand, it suggests an approximation of the LCDA's effective term, which can replace inefficient numerical integration in practical applications.

[3]Note this contains terms not only with ω^{k+2+n} but also with lower powers down to ω^{k+2} with the same suppression factor $1/[(1+n)^3\,n!]$.

We can account for the convolution's leading effect with a minimal modification of the basis functions used for the LCDA's series expansion. For the moment, we use the notation

$$\phi_+(\omega) = \sum_{k=0}^{K} a_k \, f_k(\omega) \,, \tag{4.55}$$

such that the piece the effective LCDA can be brought into the form

$$\Delta\phi_+^{(1\mathrm{d}\star)}(\omega) = \lim_{K'\to\infty} \frac{\omega}{\omega_0} \sum_{k=0}^{K} \sum_{k'=0}^{K'} a_k \, \mathcal{M}_{kk'}^{(1\mathrm{d}\star)} f_{k'}(\omega) \,, \tag{4.56}$$

where, for practical purposes, K' must be truncated. However, the suppression in n and convergence of the a_k ensure that a finite K' is sufficient for a given accuracy. As a minimally viable approximation, we need $K' = K$ to capture the leading contribution $n = 0$. Note that the additional factor ω is not strictly necessary but significantly improves the convergence of the expansion. We obtain the matrix via Eq. (2.49) from the generating function,

$$\mathcal{M}_{kk'}^{(1\mathrm{d}\star)} = \left[\frac{1}{(1+k)!} \frac{\partial^k}{\partial t^k} \frac{1}{k'!} \frac{\partial^{k'}}{\partial s^{k'}} \frac{4}{(1-s)^2} \int_0^\infty \mathrm{d}\omega \exp\left\{ \frac{(s+1)}{(s-1)} \frac{\omega}{\omega_0} \right\} \left(\frac{\omega}{\omega_0} \right)^{-1} \left[\Delta\phi_+^{(1\mathrm{d}\star)}(\omega) \right](t) \right]_{t,s=0} . \tag{4.57}$$

Integration over ω leads to

$$\mathcal{M}_{kk'}^{(1\mathrm{d}\star)} = \left[\frac{1}{(1+k)!} \frac{\partial^k}{\partial t^k} \frac{1}{k'!} \frac{\partial^{k'}}{\partial s^{k'}} \frac{2}{(s\,t-1)^2} \frac{t+1}{t-1} \sum_{n=0}^{\infty} \frac{1}{2^n \, (1+n)^2} \left(\frac{(s-1)(t+1)}{s\,t-1} \right)^n \right]_{t,s=0} . \tag{4.58}$$

Note that for any given k, k', the sum over n can be (at least by numerical approximation) carried out to infinity. As illustration, the case $K = 3$, $K' = 5$ amounts to

$$\mathcal{M}_{kk'}^{(1\mathrm{d}\star)} \simeq \begin{bmatrix} -2.33 & 0.444 & -0.17 & 0.0875 & -0.0527 & 0.0351 \\ -2.55 & -1.72 & 0.364 & -0.147 & 0.0781 & -0.0481 \\ -1.91 & -2.94 & -1.38 & 0.312 & -0.131 & 0.0709 \\ -1.49 & -2.59 & -2.95 & -1.17 & 0.276 & -0.118 \end{bmatrix} . \tag{4.59}$$

The convergence is evident in the entries: for a coefficient a_k, the contribution weight of the function $\omega/\omega_0 \, f_{k'}(\omega)$ decreases rapidly as soon as $k' > k$.

We turn to a brief numerical study to demonstrate that a moderate $K' \gtrsim K$ is sufficient for practical applications. The contribution of the coefficient a_k to the quantity $\mathcal{L}^{\mathrm{inc}}[\Delta\phi_+^{(1\mathrm{d}\star)}; \Omega, \sigma]$ reads

$$\int_0^\Omega \mathrm{d}\omega' \, \mathrm{e}^{-\sigma\omega'} \int_0^{\omega'} \mathrm{d}\omega \ln^2 \frac{\omega' - \omega}{\omega'} \frac{\mathrm{d}}{\mathrm{d}\omega} \Big[\frac{\omega' \, \mathrm{e}^{-\omega/\omega_0}}{\omega_0^2} \frac{L_k^{(1)}(2\omega/\omega_0)}{1+k} \Big] \tag{4.60}$$

which we approximate using a finite K' such that

$$\approx \sum_{k'=0}^{K'} \mathcal{M}_{kk'}^{(1\mathrm{d}\star)} \int_0^\Omega \mathrm{d}\omega' \, \mathrm{e}^{-\sigma\omega'} \, \frac{\omega'}{\omega_0} \, \frac{\omega' \, \mathrm{e}^{-\omega'/\omega_0}}{\omega_0^2} \, \frac{L_{k'}^{(1)}(2\omega'/\omega_0)}{1+k'} \,. \tag{4.61}$$

For the parameters $\Omega = s_0/(2E_\gamma)$ and $\sigma = 2E_\gamma/M^2$, we use realistic central values $s_0 = 1.5\,\mathrm{GeV}^2$ and $M^2 = 1.25\,\mathrm{GeV}^2$, in addition to the (arbitrary) value $\omega_0 = 0.7\,\mathrm{GeV}$.

In Fig. C.1, we show the contributions associated to the coefficients $a_0, a_1, \ldots, a_8$ and the absolute truncation error for $K' = 8$ as a function of E_γ in a large interval $[1.0, 3.0]\,\mathrm{GeV}$. The plot confirms the truncation error becomes larger for a_k as k approaches K', e.g., it is largest for the a_8 contribution. The contributions might have zero crossings; however, below the interval $1.5\,\mathrm{GeV} < E_\gamma < m_B/2$, relevant for practical applications. At the lower boundary, the factorization approach becomes unreliable [16] while the upper boundary is kinematic. Therefore, we proceed to examine the *relative* truncation errors for a more realistic interval $E_\gamma \in [1.5, 2.7]\,\mathrm{GeV}$. In Fig. C.2, we show the cases $K' = 8, 12$ and 16 for each coefficient $a_0, a_1, \ldots, a_8$. While the relative error for $K' = 8$ lies already in the low percent range, it falls off to a few 10^{-4} for $K' = 12$, which is more than sufficient for practical purposes. The last case, $K' = 16$, shows diminishing benefits for larger values of K', as the order of magnitude of the maximum relative error is identical for the previous case, $K' = 12$.

In conclusion, we find that $\mathcal{L}^{\mathrm{inc}}[\Delta\phi_+^{(1\mathrm{d}\star)}; \Omega, \sigma]$ may be implemented for numerical applications using the parametrization at (primary) truncation level $K = 8$ using the expansion Eq. (4.56) with the (secondary) truncation level $K' = 12$. The presented technique, expressing the effective LCDA as a series, can also be applied to the other pieces, not only for numerical evaluation but also as compact intermediate results as in Eq. (4.54) for analytical calculations.

4.3. Implementation in the `EOS` Software

The observables of $B \to \gamma\ell\nu$ listed in Table 4.1 have been implemented in the open-source software[4] `EOS` [3] using the programming language `C++` as part of this thesis. It provides means for numerical evaluation, particularly tools for Bayesian inference to perform sophisticated global fits. The software project facilitates a high level of independence between the various parts of the code to ensure future extendibility. For example, the code for the branching ratio is agnostic about lower-level quantities, such as the implementation of the form factors or the renormalization group evolution of the LCDA.

[4] The source code of release version 1.0.10 is permanently available under `https://github.com/eos/eos/tree/v1.0.10`. Note that any implementation details discussed here, including file names, are only guaranteed to pertain to this version.

EOS qualified name	observable	description
`B_u->gammalnu::BR(E_gamma_min)`	$\mathcal{B}(B^- \to \gamma\ell^-\bar{\nu})$	integrated branching ratio
`B_u->gammalnu::A_FB(E_gamma_min)`	$A_{\rm FB}(B^- \to \gamma\ell^-\bar{\nu})$	forward-backward asymmetry
`B->gamma::F_V(E_gamma)`	$F_V^{B\to\gamma}(E_\gamma)$	vector form factor
`B->gamma::F_A(E_gamma)`	$F_A^{B\to\gamma}(E_\gamma)$	axial-vector form factor

Table 4.1.: User-accessible observables provided in EOS.

We use the LCDA's parametrization at truncation level $K = 8$, i.e., the observables are implemented up to the first nine terms. This choice ensures that there is sufficient headroom to account for RG evolution while keeping the implementation overhead manageable when fitting a small number of parameters. The code is written such that the number of coefficients and terms, if necessary, can easily be increased in the future.

4.3.1. Physical Observables

The files `eos/b-decays/b-to-gamma-l-nu.{hh,cc}` of the EOS source code contain the implementation of the physical observables. Here, we provide the relevant definitions but omit auxiliary functions.

The branching ratio

$$\mathcal{B}(B^- \to \gamma\ell^-\bar{\nu}) = \frac{\tau_B}{\hbar}\int_{E_{\gamma,\min}}^{m_B/2} \mathrm{d}E_\gamma \,\frac{\mathrm{d}\Gamma}{\mathrm{d}E_\gamma} \tag{4.62}$$

is implemented using Eq. (4.6) through numerical integration over the photon energy in the member function `integrated_decay_width(E_gamma_min)`.

We define the integrated forward-backward asymmetry

$$A_{\rm FB} \equiv \left[\int_{E_{\gamma,\min}}^{m_B/2} \mathrm{d}E_\gamma \,\frac{\mathrm{d}\Gamma}{\mathrm{d}E_\gamma}\right]^{-1} \int_{E_{\gamma,\min}}^{m_B/2} \mathrm{d}E_\gamma \; a_{\rm FB}(E_\gamma)\,\frac{\mathrm{d}\Gamma}{\mathrm{d}E_\gamma}\,, \tag{4.63}$$

which is implemented using Eq. (4.7) through numerical integration over the photon energy in the member function `forward_backward_asymmetry(E_gamma_min)`.

4.3.2. Form Factors

The files `eos/form-factors/analytic-b-to-gamma-qcdf.{hh,cc}` of the EOS source code contain the implementation of the form factors F_V and F_A in the member functions `F_V(Egamma)` and `F_A(Egamma)`, respectively, according to the definition in Eq. (4.8). We omit the discussion

of auxiliary functions, which mirror the previous definitions. Instead, we focus on the technical aspects of the implementation using the LCDA parametrization.

Each ingredient, L_0 in Eq. (4.27), L_0^{inc} in Eq. (4.28), and $\mathcal{L}^{\text{inc}}$ in Eq. (4.29) is implemented as a scalar product of a coefficient vector $\vec{a} = (a_0, a_1, \dots, a_k)$ with a quantity-specific weight vector with the same dimension. For example, the code implementation for L_0 is given in Listing 4.1. In line 4, we assign the weight vector, where the numerical values are calculated beforehand from the generator according to Eq. (4.35). In line 8, we get the iterators provided by the class member `blcdas` that give access to the coefficient values. In line 9, we return the result of the vector product of the coefficients with the weights.

Listing 4.1: Implementation of the parametrized L_0 as a vector product.

```
1  double
2  AnalyticFormFactorBToGammaQCDF::L0() const
3  {
4      const Weights c = {
5          1.0, 0.0, 1.0 / 3.0, 0.0, 1.0 / 5.0, 0.0, 1.0 / 7.0, 0.0, 1.0 / 9.0
6      };
7
8      auto [a_begin, a_end] = blcdas->coefficient_range(mu);
9      return 1.0 / omega_0 * std::inner_product(a_begin, a_end, c.begin(), 0.0);
10 }
```

While the code for the weight vector, which generally depends on parameters such as Ω and ω_0, can be generated automatically using Mathematica's `CForm`, the quantities typically benefit from optimization. For example, the generator of L_0^{inc} in Eq. (4.36) yields expressions composed of the exponential function and powers of Ω/ω_0. We compute them just once before composing the entries of the weight vector, aiming to minimize the number of operations and function calls:

Listing 4.2: We are optimizing the number of operations and function calls. In line 20, we indicate the omission of some lines containing lengthy expressions for the higher-order weights.

```
1  double
2  AnalyticFormFactorBToGammaQCDF::L0_incomplete(const double & omega_cut) const
3  {
4      const double xom = omega_cut / omega_0;
5      const double xom2 = xom  * xom;
6      const double xom3 = xom2 * xom;
7      const double xom4 = xom3 * xom;
8      const double xom5 = xom4 * xom;
9      const double xom6 = xom5 * xom;
10     const double xom7 = xom6 * xom;
11     const double xom8 = xom7 * xom;
12
13     const double exp_xom = std::exp(-xom);
14
15     const Weights c = {
16         1. - exp_xom,
17         xom * exp_xom,
18         0.3333333333333333 + (exp_xom * (-1 + 2 * xom - 2 * xom2)) / 3.,
19         (xom * exp_xom * (3 - 3 * xom + xom2)) / 3.,
```

```
        [...]
    };

    auto [a_begin, a_end] = blcdas->coefficient_range(mu);
    return 1.0 / omega_0 * std::inner_product(a_begin, a_end, c.begin(), 0.0);
}
```

For the numerical evaluation of polynomials, Horner's form results in a minimal number of evaluations and stored intermediate results. It consists of nested expressions using multiplication and addition, e.g.,

$$a\,x^3 + b\,x^2 + c\,x + d = x(x(a\,x + b) + c) + d\,.$$

The ingredient's expressions of the parametrization terms often involve generalized hypergeometric functions and their derivatives. These are implemented using cubic spline interpolation, approximating the function by piece-wise cubic polynomials ("splines"), which interpolate values calculated once beforehand. We obtain the sampling points using dynamic sampling provided by the Python library `Adaptive` [73] such the sampling frequency adapts to the rapidity of change of the function. Compared to a constant sampling rate, fewer points are required to achieve the same global accuracy. To evaluate the functions, we use the "Wolfram Client library for Python" by Wolfram Research[5] as an interface between the Mathematica kernel and the Python runtime environment. The infinite domain of the functions needs to be mapped onto a finite interval using a suitable map, for example, the map g,

$$\begin{aligned} g : [0, \infty] &\to [0, 1] \\ x &\mapsto \frac{x}{1 + x}\,. \end{aligned}$$

The ingredient $\mathcal{L}^{\text{inc}}[\Delta\phi_+^{(1d\star)}; \Omega, \sigma]$ is implemented in `lapltr_incomplete_effective(Egamma, omega_cut, sigma, use_approximation)` using the approximation of Eq. (4.56) truncated at $K' = 12$. An alternative implementation is available through an optional argument, which uses numerical integration instead of the approximation by the truncated series.

4.3.3. B-LCDA ϕ_+

The files `eos/form-factors/b-lcdas-flvd2022.{hh,cc}` of the EOS source code contain the code related to the leading-twist B LCDA using the parametrization.

The central input parameters used by this class are the LCDA coefficients $a_k(\mu_0)$, their reference scale ω_0, and the renormalization scale μ_0. Their qualified names in EOS are

[5] See `wolfr.am/wolframclientdoc`.

`B_u::a^phi+_<k>@FLvD2022` (where `<k>` must be replaced by the index $k = 0, \ldots, 8$), `B_u::omega_0@FLvD2022`, and `B_u::mu_0@FLvD2022`, respectively.

The member function `coefficient_range(mu)` provides access to the coefficients through iterators. Using iterators instead of a fixed-size container such as an array ensures that the users of this method do not assume a specific number of parameters. Minimal coupling allows us to increase the truncation level K later with the ability to update the code users (such as the form factors) incrementally. The coefficient values are provided at the renormalization scale μ, which is implemented using the RG evolution according to Eq. (2.58).

While the form factors for $B \to \gamma\ell\nu$ in our calculation are directly expressed in terms of the parameters, the LCDA class also includes methods that give access to the LCDA representations in momentum and position space. The position-space representation $\tilde{\phi}_+$ is needed to employ the OPE result as a constraint in a global fit. Otherwise, the LCDA as a function can be used in `EOS` with numerical integration for existing applications of ϕ_+ or simply for diagnostic purposes.

4.4. Phenomenological Analysis

We use the `EOS` software to perform a sensitivity study based on Bayesian inference methods. Without empirical data like experimental measurements or lattice predictions for the form factors, it's unfeasible to accurately determine the LCDA parameters. However, one can study the potential impact of such data, highlighting the importance of further research in this area.

We use a Bayesian framework for the analysis. Bayes' theorem states how to infer knowledge about a set of fit parameters, denoted as ϑ, from a given dataset, symbolized as D. The analysis result is the posterior probability density function (PDF), given by

$$P(\vartheta \,|\, D, M) = \frac{P(D, M \,|\, \vartheta)\, P_0(\vartheta \,|\, M)}{Z(D, M)}\,. \tag{4.64}$$

Here, $P(D, M \,|\, \vartheta)$ is known as the "likelihood" of observing the data D under the model M given the parameters ϑ, allowing us to implement fit constraints. The factor $P_0(\vartheta \,|\, M)$ denotes the prior probability distribution of the parameters, representing the already available knowledge about the parameters independent of D. For the LCDA parameters, our lack of prior knowledge is represented by a product of uniform distributions. In the denominator, the "evidence" $Z(D, M)$ is a normalization factor, ensuring the posterior PDF is normalized when integrating all possible values of ϑ.

For complicated data and models, calculating the posterior PDF in closed form is often unfeasible, at which point numerical methods become indispensable. We use the `EOS`

software [3], which has been extended to this purpose as part of this thesis. Our analysis involves the optimization of the posterior in order to determine the best-fit point (or points, if there are several modes) of the parameters. Even though we do not provide best fit points in the following, we use them to derive p values to qualify the setup in statistical terms. We also produce samples for the model parameters, i.e., the fit and nuisance parameters. It allows to obtain "posterior-predictive distributions" for dependent observables, including those that appear in the likelihood as constraints, but also predictions of observables where no data is available. To that end, we interface `EOS` with the open-source third-party software `dynesty` [74, 75] to calculate importance samples using a dynamical nested sampling algorithm [76].

4.4.1. Constraint Through the Short-distance OPE

We turn again to the short-distance OPE, already used in the pseudo-fits in Section 2.4 and Section 3.4, using the OPE result on the negative imaginary axis as input. In contrast to the previous sections, we use a more sophisticated statistical framework, allowing us to account for correlations and uncertainties.

For the reader's convenience, we quote the full result given in Ref. [37], which includes local operators up to mass dimension 5:

$$\begin{aligned}\tilde{\phi}_+(\tau;\mu) = 1 &- \frac{\alpha_s C_F}{4\pi}\left(2L^2 + 2L + \frac{5\pi^2}{12}\right) \\ &- i\tau\,\frac{4\bar{\Lambda}}{3}\left[1 - \frac{\alpha_s C_F}{4\pi}\left(2L^2 + 4L - \frac{9}{4} + \frac{5\pi^2}{12}\right)\right] \\ &- \tau^2\bar{\Lambda}^2\left[1 - \frac{\alpha_s C_F}{4\pi}\left(2L^2 + \frac{16}{3}L - \frac{35}{9} + \frac{5\pi^2}{12}\right)\right] \\ &- \tau^2\frac{\lambda_E^2(\mu)}{3}\left[1 - \frac{\alpha_s C_F}{4\pi}\left(2L^2 + 2L - \frac{2}{3} + \frac{5\pi^2}{12}\right) + \frac{\alpha_s C_G}{4\pi}\left(\frac{3}{4}L - \frac{1}{2}\right)\right] \\ &- \tau^2\frac{\lambda_H^2(\mu)}{6}\left[1 - \frac{\alpha_s C_F}{4\pi}\left(2L^2 + \frac{2}{3} + \frac{5\pi^2}{12}\right) - \frac{\alpha_s C_G}{8\pi}\,(L-1)\right] \\ &+ (-i\tau\,\Lambda_{\text{had}})^3\,\delta\,.\end{aligned} \tag{4.65}$$

Above, $\bar{\Lambda}$ is the HQET mass parameter in the on-shell scheme, and we abbreviate $L = \ln(i\tau\mu e^{\gamma_E})$. In the last line, we add an error estimate for the next-higher order in the short-distance expansion via the parameter δ and a generic hadronic scale Λ_{had}. Aiming to remove the pole mass in $\bar{\Lambda} = m_B - m_b^{\text{pole}}$ in favor of a renormalon-free low-energy parameter, we follow Ref. [37] and use

$$\bar{\Lambda} = \bar{\Lambda}_{\text{DA}}\left(1 + \frac{7}{16\pi}\alpha_s C_F\right) - \frac{9}{8\pi}\mu\,\alpha_s C_F\,. \tag{4.66}$$

μ	$1\,\mathrm{GeV}$
$\alpha_s(\mu)$	0.466
Λ_{had}	$0.5\,\mathrm{GeV}$
$\bar{\Lambda}_{\mathrm{DA}}$	$0.52\,\mathrm{GeV}$ [35]
λ_{E}^2	$0.01 \pm 0.01\,\mathrm{GeV}^2$ [51]
λ_{H}^2	$0.15 \pm 0.05\,\mathrm{GeV}^2$ [51]

Table 4.2.: Numerical values of the OPE input parameters.

In order for the OPE to be a valid estimate of the LCDA at some point $\tau = -it_0$, it is first necessary that the power expansion converges rapidly, i.e.,

$$|t_0 \Lambda_{\mathrm{had}}| \ll 1\,. \tag{4.67}$$

Fig. 1 of Ref. [37] shows the individual contributions to the OPE result for $\mu = 1\,\mathrm{GeV}$ as a function of $-i\tau$. The plots suggests that the OPE "works up to moderate LC distances τ of order $1\,\mathrm{GeV}^{-1} \sim 1/\mu$" [37], after which the contribution hierarchy breaks down. Second, we require that radiative corrections, obtained at fixed order in perturbation theory, are not subject to strong logarithmic enhancement,

$$\ln(t_0 \mu \mathrm{e}^{\gamma_{\mathrm{E}}}) \sim \mathcal{O}(1)\,. \tag{4.68}$$

Allowing the logarithm to take values ranging from -1 to 1, suggests the range $t_0 \in [0.207, 1.53]\,\mathrm{GeV}^{-1}$. In the following, we consider the interval $t_0 \in [0.25, 1.0]\,\mathrm{GeV}^{-1}$, in compliance with both the short-distance expansion and ensuring that the fixed-order logarithms do not lead to strong enhancement.

In Fig. 4.2, we plot the OPE result for the LCDA on the negative imaginary axis, $\tilde{\phi}_+(\tau = -it, \mu)$, using the numerical values in Table 4.2. For $\bar{\Lambda}_{\mathrm{DA}}$, we assume a relative error of 10 %, which is in line with the numerical reference provided in Ref. [35]. We show the overall result obtained using central values as a dashed line. The dotted line corresponds to the limit $\lambda_{E,H} \to 0$, illustrating the small impact of these parameters compared to the mass parameter $\bar{\Lambda}$. The colored blue bands illustrate the overall uncertainty using the central 68% probability interval obtained through random sampling according to Gaussian distributions of the parameters. To illustrate the impact of the truncation error, we consider the three cases $\delta = 0, 0 \pm 1, 0 \pm 2$. The truncation error estimate quickly dominates the hadronic parameter's uncertainty for larger values of t.

To access as much of the OPE's information as possible in an analysis, one can either (a) evaluate the LCDA at multiple points in the complex τ plane, (b) evaluate the functional behavior through the value and derivatives at a single point, or (c) consider a mixture of both. We chose the first option, as it is the most straightforward one. To keep the

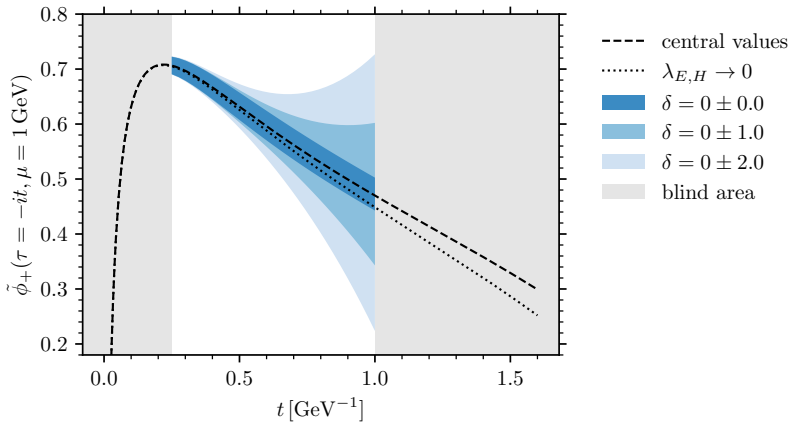

Figure 4.2.: The OPE result of the LCDA on the negative imaginary axis $\tilde{\phi}_+(\tau = -it, \mu = 1\,\mathrm{GeV})$ as a function of t. The dashed line corresponds to the curve using central values, while the blue bands indicate the parametric uncertainty. The dotted line corresponds to the limit $\lambda_{E,H} \to 0$, demonstrating the parameters' small numerical impact. Shaded in gray is the "blind area" where the OPE prediction of the LCDA becomes unreliable.

truncation error minimal, small values of t are favorable, however, considering several points close to each other results in highly correlated constraints. What limits the maximum useful number of data points is the overall structure of the OPE result in Eq. (4.65) and the fact that it (numerically) predominantly depends on the single parameter $\bar{\Lambda}$, giving rise to substantial correlations between any pair of pseudo-observables. The number of independent input parameters suggests that at most three independent constraints may be used as a multivariate Gaussian constraint. Aiming to balance minimal correlation with an acceptable truncation error, we consider three equidistant points in the interval $t_0 \in [0.25, 0.75]\,\mathrm{GeV}^{-1}$.

Because the precise form of the dimension-6 order in the OPE is unknown, we treat the variation due to the parameter δ as uncorrelated for each data point. Taking $\delta = 0 \pm 1$ in the following results in

$$\begin{aligned}
\tilde{\phi}_+(-i0.25\,\mathrm{GeV}^{-1}) &= 0.707 \pm 0.016 \pm 0.002\,, \\
\tilde{\phi}_+(-i0.50\,\mathrm{GeV}^{-1}) &= 0.632 \pm 0.025 \pm 0.016\,, \\
\tilde{\phi}_+(-i0.75\,\mathrm{GeV}^{-1}) &= 0.547 \pm 0.029 \pm 0.053\,,
\end{aligned} \tag{4.69}$$

where the first uncertainty stems from the hadronic parameters, and the second represents the truncation error. Formulated more precisely as a multivariate Gaussian distribution for the three points, we calculate the covariance matrix based on the hadronic parameter's variation and, afterward, add the uncertainty due to δ in quadrature to its diagonal entries. The resulting covariance matrix is provided in Table C.5. Adding the uncorrelated truncation error relaxes the overall correlations between the data points, which improves

μ_0	1 GeV
μ	1 GeV to 2 GeV
μ_{h1}, μ_{h2}	$m_b/2$ to $2\,m_b$
M^2	(1.25 ± 0.25) GeV^2
s_0	(1.5 ± 0.1) GeV^2
m_B	5.27925 GeV [48]
m_b	(4.8 ± 0.1) GeV [16]
m_ρ	0.77526 GeV [48]
f_B	(192.0 ± 4.3) MeV [77]
τ_B	$1.638 \times 10^{-12} s$ [48]
$\lvert V_{ub}\rvert^{\text{excl}}$	3.70×10^{-3} [48]
G_F	1.166378×10^{-5} GeV^{-2} [48]

Table 4.3.: Numerical values of the $B \to \gamma\ell\nu$ decay's nuisance parameters. We omit uncertainties when only central values enter the analysis. The first section, related to factorization and sum rules, is adopted from the original publication [16]. The b-quark mass is understood in the pole scheme.

the stability of numerical evaluations. The corresponding correlation matrix has eigenvalues 2.12, 0.16, and 0.67 and determinant 0.23, indicating the degree of correlation.

Numerical Impact

The numerical input for the decay's nuisance parameters is provided in Table 4.3. We treat parameters given as central value and standard deviation as Gaussian priors, while scales such as μ follow a probability density function that yields a uniform distribution of logarithms of the scale. It reflects that the scales are arbitrary as long as the value of their logarithms remains of a certain moderate size. We state and use only the central value of a parameter if the uncertainty is negligible in our analysis or when they enter (trivially) as a global factor.

To cover a wide range of applications, we consider the following set of six (pseudo-) observables:

- $\mathcal{B}$ and A_{FB}, the integrated branching ratio and the forward-backward asymmetry for $E_{\gamma,\text{min}} = 2\,\text{GeV}$ as the lower integration boundary (in compliance with factorization),
- $F_V(m_B/2)$ and $F_A(m_B/2)$, the form factors at maximum recoil energy, $E_\gamma = m_B/2$, which might become accessible using lattice calculations in the future,
- and L_0 and L_1, the first two logarithmic moments of the LCDA, crucial in phenomenological applications.

In the Bayesian framework, the result is a multivariate posterior distribution, which we numerically approximate through weighted samples. It is necessary to marginalize the posterior to infer information about only a subset of variables independent of the remaining ones. This process involves integrating the other variables across their entire domain, considering all possible values; for example, in the case of a one-dimensional marginalized distribution, all other variables are integrated over. The one-dimensional probability density functions obtained in this manner generally do not exhibit a Gaussian shape. In the following, we quantify the distribution's central tendency and variability through the median value and the central 68 % interval of probability, which may be asymmetric. The lower boundary of the central interval, the median value, and the upper boundary of the central interval correspond, respectively, to the 16^{th}, 50^{th}, and 84^{th} percentiles of the probability density. We further provide, when sensible, the p value associated with the minimum χ^2 to characterize a given setup consisting of a statistical model and a likelihood.

We start off using only the OPE constraint (three degrees of freedom) in an analysis with $K = 1$, i.e., LCDA parameters a_0 and a_1, with a fixed value of ω_0, resulting in the total degree of freedom of one. The resulting setups in this section all exhibit a p value in excess of 74 %.

We compare the effect of the multivariate constraint with and without correlation between the three data points from the OPE result using $\omega_0 = 0.8\,\text{GeV}$. The latter case corresponds to the covariance matrix given in Table C.5 where the off-diagonal entries are zero. Fig. 4.3 shows the distributions of the fit parameters' posterior samples in the two-dimensional a_0-a_1 plane (in the corner) alongside the one-dimensional marginalized histograms for each parameter (on the diagonal). Using the constraint with correlation tends to result in narrower posterior distributions; however, the effect is negligible. The posterior distributions inherit the input's Gaussian shape because of the underlying linear relationship between the LCDA parameters and its value in position space at a certain point in the complex plane. This is further manifest in the correlation of the posterior samples, illustrated in the upper right panel, which are shaped like narrow ellipses. In the following, we use the correlated multivariate Gaussian constraint.

We repeat the Bayesian procedure for several values of ω_0 to examine its influence on the posterior result and the corresponding observable predictions. Table 4.4a contains the results for $a_0(\mu_0)$ and $a_1(\mu_0)$ for several $\omega_0 \in \{0.4, 0.6, 0.8, 1.0, 1.2\}\,\text{GeV}$. The values correspond to the sample's median and boundaries of the 68 % probability interval. The boundaries are approximately symmetrical because of the Gaussian-like shape of the posterior. Fig. 4.4 shows the resulting posterior prediction of the LCDA $\tilde{\phi}_+(\tau = -it, \mu_0)$ as a function of t in comparison to the complete OPE prediction and the extracted constraints. The blue bands indicate the width of the posterior distribution within the central 68 % probability interval. We find the prediction adheres to the constraints for all

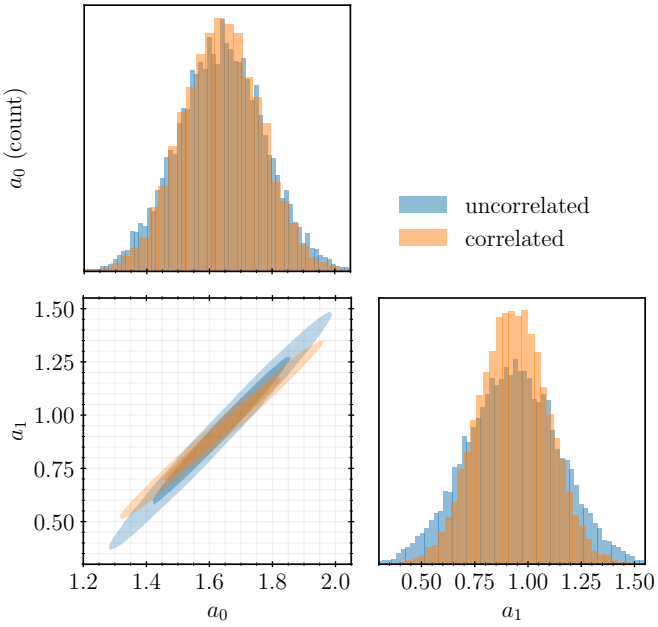

Figure 4.3.: On the diagonal, we show histograms of the one-dimensional marginalized samples of the fit parameters obtained using correlated and uncorrelated inputs from the OPE. In the corner, contours indicate estimates of the 68 % and 95 % probability intervals of the two-dimensional marginalized samples.

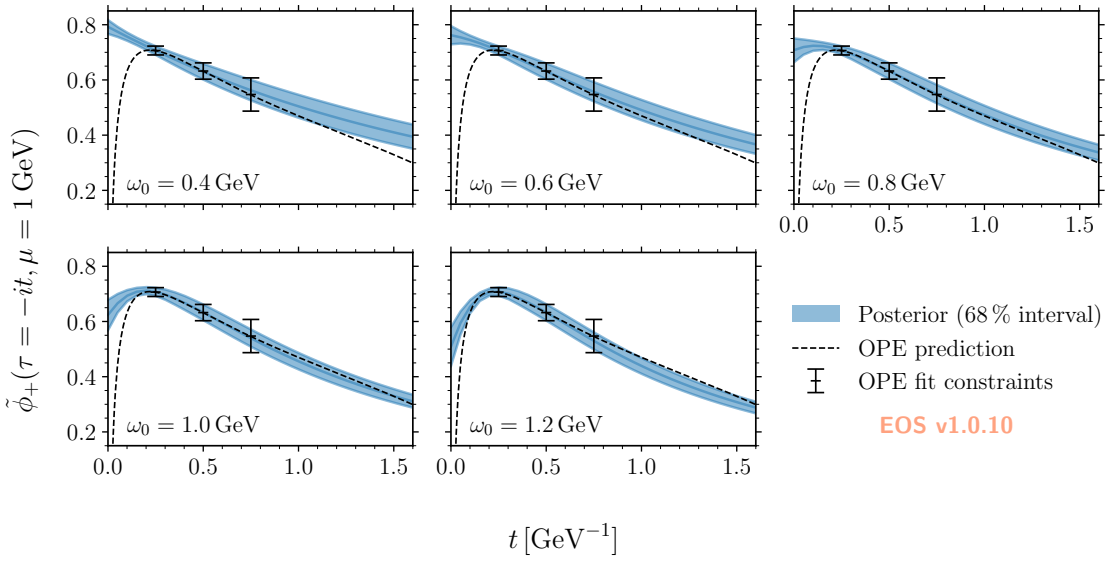

Figure 4.4.: Comparing the input constraints with the corresponding posterior prediction for $K = 1$ and different values for ω_0.

ω_0 [GeV]	$a_0(\mu_0)$	$a_1(\mu_0)$	p value
0.4	$1.53^{+0.87}_{-0.59}$	$0.55^{+0.07}_{-0.12}$	74 %
0.6	$0.98^{+0.47}_{-0.33}$	$0.44^{+0.10}_{-0.15}$	84 %
0.8	$0.66^{+0.31}_{-0.21}$	$0.29^{+0.14}_{-0.21}$	97 %
1.0	$0.47^{+0.20}_{-0.14}$	$0.11^{+0.19}_{-0.26}$	88 %
1.2	$0.36^{+0.15}_{-0.09}$	$-0.09^{+0.24}_{-0.29}$	74 %

(a) Posterior results for the $a_k(\mu_0)$ fit.

ω_0 [GeV]	$\mathcal{B}$ $[10^{-7}]$	A_{FB}
0.4	$1.53^{+0.87}_{-0.59}$	$0.55^{+0.07}_{-0.12}$
0.6	$0.98^{+0.47}_{-0.33}$	$0.44^{+0.10}_{-0.15}$
0.8	$0.66^{+0.31}_{-0.21}$	$0.29^{+0.14}_{-0.21}$
1.0	$0.47^{+0.20}_{-0.14}$	$0.11^{+0.19}_{-0.26}$
1.2	$0.36^{+0.15}_{-0.09}$	$-0.09^{+0.24}_{-0.29}$

(b) Poster-predictive results for experimental observables.

ω_0 [GeV]	$F_V(m_B/2)$	$F_A(m_B/2)$	$L_0\,[\text{GeV}^{-1}]$	$L_1\,[\text{GeV}^{-1}]$
0.4	$0.183^{+0.038}_{-0.034}$	$0.161^{+0.038}_{-0.034}$	$2.84^{+0.39}_{-0.39}$	$-0.86^{+0.44}_{-0.44}$
0.6	$0.151^{+0.027}_{-0.025}$	$0.129^{+0.027}_{-0.025}$	$2.37^{+0.22}_{-0.22}$	$-1.10^{+0.27}_{-0.27}$
0.8	$0.127^{+0.023}_{-0.021}$	$0.105^{+0.023}_{-0.021}$	$2.05^{+0.16}_{-0.16}$	$-1.16^{+0.21}_{-0.20}$
1.0	$0.110^{+0.019}_{-0.018}$	$0.088^{+0.019}_{-0.018}$	$1.82^{+0.12}_{-0.12}$	$-1.20^{+0.17}_{-0.17}$
1.2	$0.096^{+0.017}_{-0.016}$	$0.074^{+0.017}_{-0.016}$	$1.66^{+0.10}_{-0.10}$	$-1.23^{+0.15}_{-0.16}$

(c) Posterior-predictive results for pseudo observables.

Table 4.4.: Results for varying ω_0 using only the OPE input. We provide the median value and boundaries of the 68 % probability interval.

values of ω_0 while the resulting LCDA's behavior varies, especially for small $t \lesssim 0.25\,\text{GeV}$, indicating a significant truncation error in that regime. The plot suggests that additional constraints for larger values of t would not significantly improve the result at this truncation level, even using an estimate of the OPE's truncation error that is more conservative than indicated in Fig. 4.2. Notably, as ω_0 increases, the parametrized LCDA follows the OPE's pathological behavior more closely in the limit $t \to 0$. This observation aligns with the study of the Lee-Neubert model discussed in Section 2.3.2, in terms of the parametrization's capability to reproduce the radiative tail, which derives from the short-distance behavior. Again, however, we stress that the fixed-order result of the OPE is unreliable in limit $t \to 0$ because of the logarithmic enhancement. In Table 4.4b and Table 4.4c, we provide posterior-predictive results for the experimental observables (branching ratio and A_{FB}) and the pseudo observables (form factors and first logarithmic moments), respectively. All predictions are additionally illustrated in Fig. C.4. Because the form factors and logarithmic moments depend linearly on the parameters, they inherit their Gaussian-like distribution. The same is not the case for the experimental observables, which are asymmetrically distributed (cf. Fig. C.3, which includes the one-dimensional marginalized posteriors for $\omega_0 = 0.8\,\text{GeV}$). All (pseudo) observables are sensitive to the value of ω_0 at this low truncation order, making them suitable to constrain the optimal value at the hand of a statistical test. Based on the p values provided in Table 4.4a (i.e., relying solely on the OPE constraint) we select $\omega_0 = 0.8\,\text{GeV}$ for the following sections. The associated maximum p value indicates the best compatibility of higher-order coefficients a_k with zero.

4.4.2. Adding Experimental Data

We fix $\omega_0 = 0.8\,\text{GeV}$ and increase the truncation level to $K = 2$, i.e., fitting the LCDA parameters a_0, a_1 and a_2. The value of ω_0 results in a central value for a_2 close to zero, which imposes consistency with the previous setup at $K = 1$. Without input beyond the OPE, this setup has zero total degrees of freedom, resulting in a minimum $\chi^2 \to 0$. Despite of the lack of degrees of freedom, Bayesian inference allows us to obtain a well-defined posterior probability density, albeit with substantial uncertainties of the parameter's marginalized distributions:

$$a_0(\mu_0) = 1.63^{+0.51}_{-0.55}\,, \quad a_1(\mu_0) = 0.90^{+1.98}_{-2.09}\,, \quad a_2(\mu_0) = -0.03^{+1.82}_{-1.94}\,.$$

More important than the one-dimensional marginalized distributions, however, are the two-dimensional ones, showing the correlations between the fit parameters and predictions in order to estimate the impact of supplementing the OPE information with data.

In the following, we discuss the resulting distribution of the posterior samples for the fit parameters and predictions at the hand of a "corner plot". It shows the one-dimensional marginalized samples of each parameter on the diagonal, where the median value and

lower and upper bound of the 68 % probability interval are indicated with dashed lines (we omit them in the following if the distribution has several significant modes). The off-diagonal plots show the two-dimensional marginalized samples between each pair of parameters as a two-dimensional histogram, complemented by blue contours for the 68 % and 95 % probability intervals obtained using Gaussian kernel density estimation (we omit them if this estimate is not applicable). The purpose of the two-dimensional plots is to show correlation between two parameters. Note that a third parameter can drive this correlation.

In Fig. 4.5, we show the corner plot for the LCDA parameters and the predictions of the experimental observables. While the distributions of the LCDA parameter appear Gaussian, the posterior-predictive samples of the experimental observables are non-Gaussian with local maxima at the boundaries. For this reason, we omit the Gaussian kernel density estimates in the two-dimensional distributions. The structure of the branching ratio's posterior results from a local minimum that lies in the broad range of values for the LCDA parameters. Numerically, we find $\mathcal{B} = 0.89^{+2.10}_{-0.62} \times 10^{-7}$ while fewer than 0.01 % of the importance samples lie below 0.18×10^{-7}. A sharp correlation between the branching ratio and the forward-backward asymmetry suggests they complement each other as fit constraints (rather than being redundant). The complete set of observables can be seen in Fig. C.5. The impact of information about the additional pseudo-observables is clear due to the linear relationship to the parameters. The complete corner plot further illustrates how the constraints can introduce correlation between variables that are a priori unrelated in the statistical model: using the parametrization, L_0 only depends on a_0 and a_2 but not a_1. We still observe a correlation between L_0 and a_1, driven indirectly by the correlation between a_1 and the other parameters by the OPE constraints. Similarly, L_1 only depends on a_1 (hence, the two-dimensional marginalized distribution takes the form of a line); correlation of L_1 with a_0 and a_2 is driven via the third variable a_1.

We now add the following mock data for the experimental observables:

$$\mathcal{B} = (0.66 \pm 0.31) \times 10^{-7}\,, \quad A_{\mathrm{FB}} = 0.29 \pm 0.21\,. \qquad \text{[mock input]}$$

These values are compatible with the posterior predictions from the previous section to ensure consistency. We further assume the measurement results are provided as (symmetrical) Gaussian distributions. For the analyses in this section, taking one or both of the mock measurements into account, we determined that the respective p values exceed 82 %. Note that experimental results for the branching ratio are already available in Ref. [9]; however, using $E_{\gamma,\mathrm{min}} = 1\,\mathrm{GeV}$, which is incompatible with the QCD factorization description. We show the posterior distributions associated with the parameters and the experimental observables in Fig. 4.6. The full set of posteriors is available in Fig. C.6. Due to the quadratic relationship with the experimental observables, the parameters' posterior features a primary and a secondary mode, which are well-separated at the level of the 68 % probability interval. The two-dimensional marginalized samples between the inverse

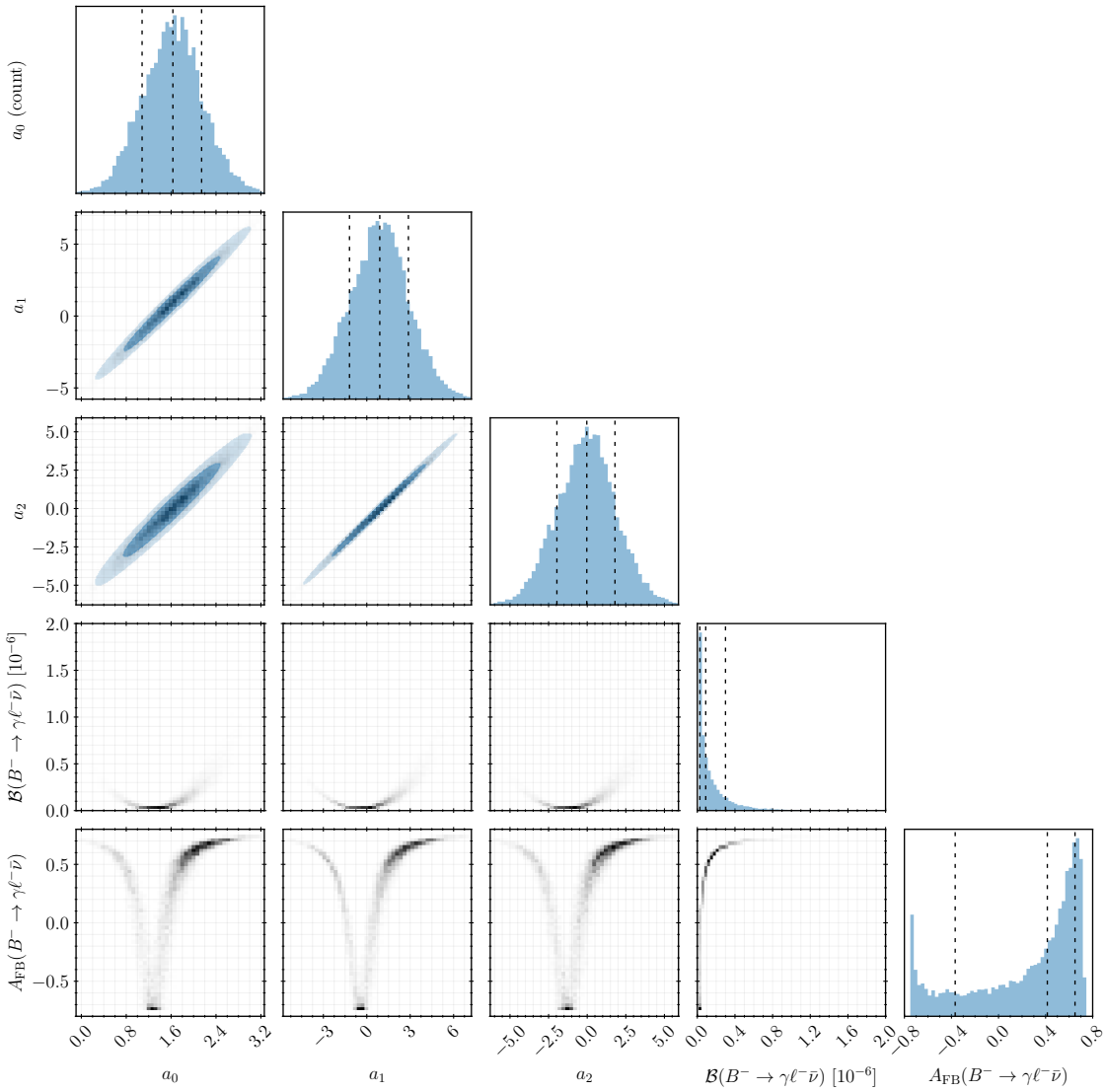

Figure 4.5.: Corner plot of the posterior for $K = 2$ and $\omega_0 = 0.8\,\text{GeV}$ showing the LCDA parameters and predictions of the experimental observables based on inputs from the OPE. Blue areas in the two-dimensional histograms indicate estimates of the 68 % and 95 % probability contours.

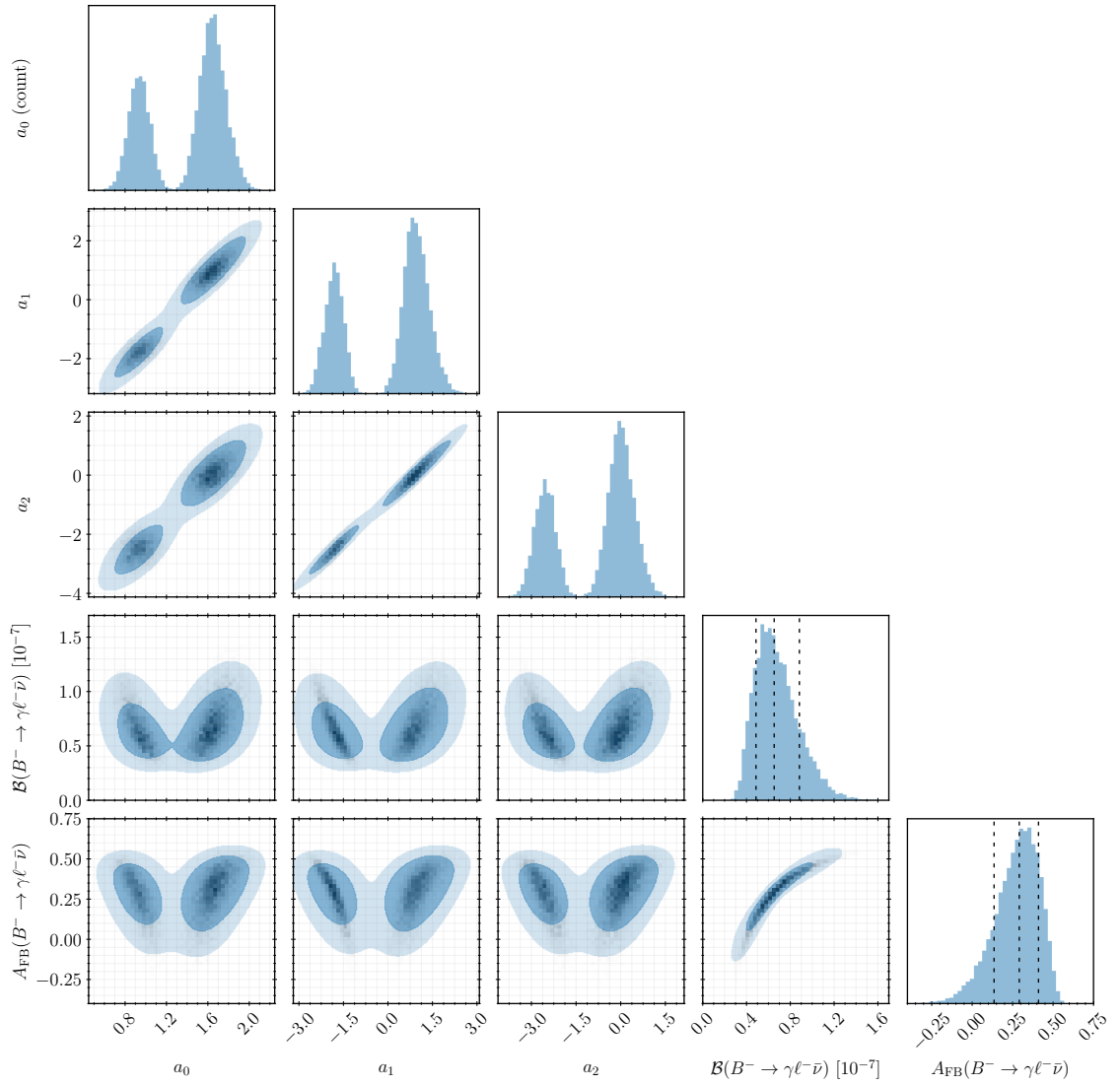

Figure 4.6.: Corner plot of the posterior for $K = 2$ and $\omega_0 = 0.8\,\mathrm{GeV}$ showing the LCDA parameters and the experimental observables based on inputs from the OPE and mock input for the experimental observables. Blue areas in the two-dimensional histograms indicate estimates of the 68 % and 95 % probability contours.

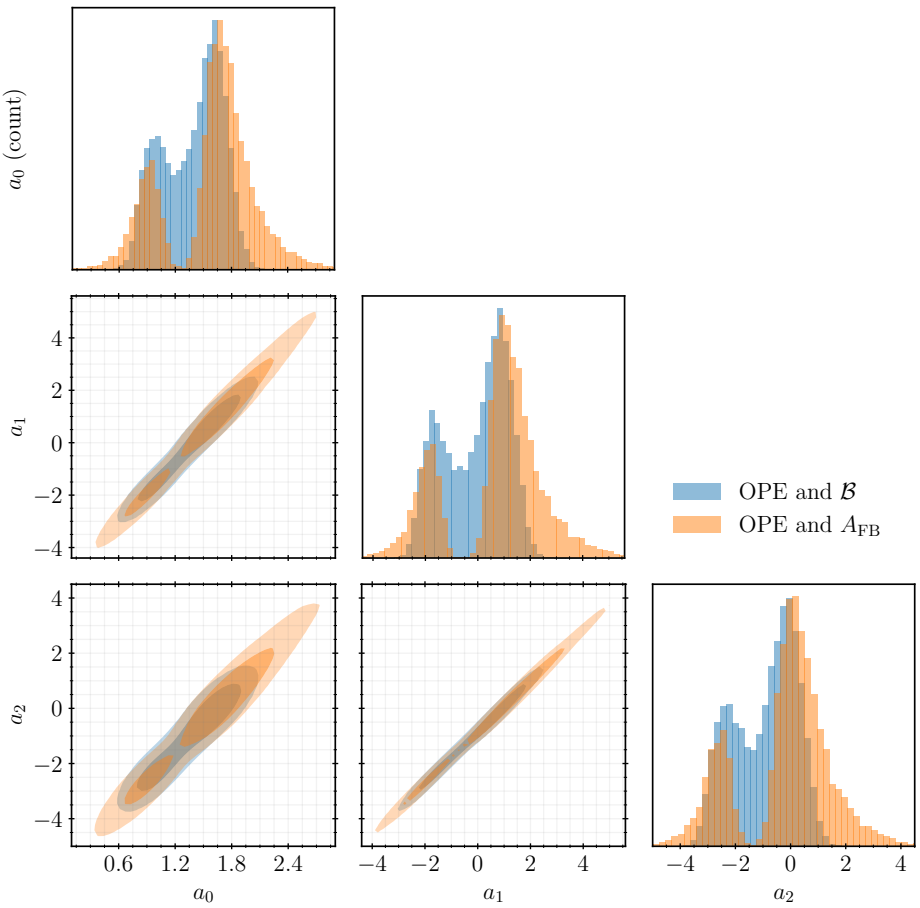

Figure 4.7.: Combined corner plot of the posteriors for $K = 2$ and $\omega_0 = 0.8\,\mathrm{GeV}$ comparing the LCDA parameters when using either the branching ratio or the forward-backward asymmetry as an experimental constraint together with inputs from the OPE. Shaded areas in the off-diagonal plots indicate estimates of the 68 % and 95 % probability contours.

moment $L_0 = \lambda_B^{-1}$ and the parameters reveal that input about L_0, e.g., from a sum rule estimate, can discriminate the two modes in favor of the primary one, since the secondary mode corresponds to $L_0 \sim 0$. Alternatively, form factor data can be used to the same effect when it becomes available. The posterior distributions of the experimental observables do not strictly follow the Gaussian shape of their priors due to the effect of the likelihood. Again, we find a striking correlation between the pair of experimental observables, affirming their complementary potential in a global fit. We explicitly confirm (not shown) that the qualitative result remains the same when using an input value for the branching ratio $\mathcal{B} = (0.18 \pm 0.18) \times 10^{-7}$ at the lower boundary.

The striking correlation between the two experimental observables warrants closer inspection. In Fig. 4.7, we show a combined corner plot, overlaying the posteriors for two cases:

combining inputs from the OPE with either only the branching ratio $\mathcal{B}$ or only the forward-backward asymmetry A_{FB} as constraints in the analysis. We find that both posteriors feature the primary and secondary mode. The location of the modes agree by construction of our setup. The overlap region, however, is significantly reduced in comparison to the individual distributions. While $\mathcal{B}$ overall narrows the distributions, A_{FB} drives the clear separation of the modes. Using both constraints together thus improves the accuracy of the analysis, i.e., the constraints are complementary.

Extending the analysis with input from the latest sum rule estimate for the inverse moment [49][6],

$$L_0(\mu_0) = 2.6 \pm 1.1\,\mathrm{GeV}^{-1}\,, \qquad \text{[input]}$$

indeed leads to a strong suppression of the posterior's secondary mode shown in Fig. C.7. For the LCDA parameters, we now find

$$a_0(\mu_0) = 1.66^{+0.13}_{-0.13}\,, \quad a_1(\mu_0) = 1.01^{+0.45}_{-0.43}\,, \quad a_2(\mu_0) = 0.08^{+0.46}_{-0.45}\,.$$

Notably, after eliminating the secondary mode, experimental information and lattice QCD estimates of the form factors lead to similarly correlated posteriors (comparison not shown). This observation naïvely implies the less precise set of inputs is somewhat redundant, while the set of inputs with higher precision drives the posterior's accuracy. The conclusion, however, only holds if there is no tension between the two sets of inputs in the given analysis setup.

4.4.3. Adding the Parameter Bound

As a fundamental advantage of the Bayesian analysis, in contrast to the frequentist approach, the fit parameters are not required to be over-constrained. The LCDA's parameter bound

$$\chi(\mu_0) = \frac{1}{2\omega_0} \sum_{k=0}^{\infty} |a_k(\mu_0)|^2 < \infty$$

serves as a regulator in such a scenario, ensuring that the posterior distributions remain localized while increasing the number of fit parameters to the same level or even beyond the constraints' degree of freedom.

In the absence of a value for $\chi(\mu_0)$, we use the following model assumption with $\sigma > 0$ to obtain an estimate:

$$|a_k(\mu_0)| < \frac{\sigma}{k+1}\,. \qquad \text{[model ansatz]} \tag{4.70}$$

[6] As suggested in the Ref. [49], we account for the condensate contribution's model uncertainty by increasing the total error by the quadrature of the difference between the two estimates.

The criterion implies the upper limit of the bound

$$\chi(\mu_0) < \frac{1}{2\omega_0}\frac{\pi^2\sigma^2}{6} \tag{4.71}$$

and similarly for the inverse moment (cf. Eq. (2.44))

$$L_0(\mu_0) < \frac{1}{\omega_0}\sum_{k=0}^{\infty}\frac{1-(-1)^{k+1}}{2}\frac{\sigma}{(k+1)^2} = \frac{1}{\omega_0}\frac{\pi^2\sigma}{8}\,. \tag{4.72}$$

Taking the reference value for L_0 in Section 4.4.2 at the upper uncertainty limit restricts the model parameter as $\sigma \gtrsim 2.40$.

Going forward, we use $\sigma = 2.5$, which numerically implies $\chi(\mu_0) < 6.43\,\mathrm{GeV}^{-1}$. Note that each parameter is thereby limited as

$$|a_k| < \frac{\pi\sigma}{\sqrt{6}} \approx 3.21\,.$$

We refer to this condition as a "weak bound" as opposed to the more restrictive criterion for the entire sum. In the analysis, this range also serves as a guide to determine the finite support range of the parameter's uniform priors. This model's weak bounding condition is consistent with the previous results for the parameters. The software `EOS` provides means to employ a parameter bound, including an uncertainty, as a component of the likelihood. However, the conventional χ^2 test statistic does not apply for this type of likelihood component and thus we cannot assign a p value. In the following, we take the bound's upper limit and assume a relative error of 10 %,

$$\chi(\mu_0) = 6.43 \pm 0.64\,\mathrm{GeV}^{-1}\,, \qquad \text{[mock input]}$$

while increasing the truncation level from $K = 2$ to $K = 5$, doubling the number of parameters. This results in

$$\begin{aligned} a_0(\mu_0) &= 1.60^{+0.18}_{-0.19}\,, \quad a_1(\mu_0) = 0.83^{+0.51}_{-0.52}\,, \quad a_2(\mu_0) = 0.13^{+0.97}_{-0.98}\,, \\ a_3(\mu_0) &= 0.39^{+1.16}_{-1.18}\,, \quad a_4(\mu_0) = 0.20^{+1.18}_{-1.19}\,, \quad a_5(\mu_0) = 0.04^{+1.31}_{-1.32}\,. \end{aligned} \tag{4.73}$$

We show the marginalized posteriors of the LCDA parameters in Fig. C.8. The posterior distributions of a_0 and a_1 remain localized with only minor broadening by virtue of the constraints despite significantly increasing the number of varied parameters. Similarly, the location of their central intervals remains stable since the parameterization at $K = 2$ (for the specific ω_0) already fulfilled the OPE constraints reasonably well. Hence, we find that the employed set of constraints is suitable to determine a_0 and a_1, while for a_2, one might overestimate the result's significance in the setup without the parameter bound. Comparing Fig. C.8 to the previous case without the parameter bound in Fig. C.7, we observe additional suppression of the secondary mode, rendering it virtually invisible.

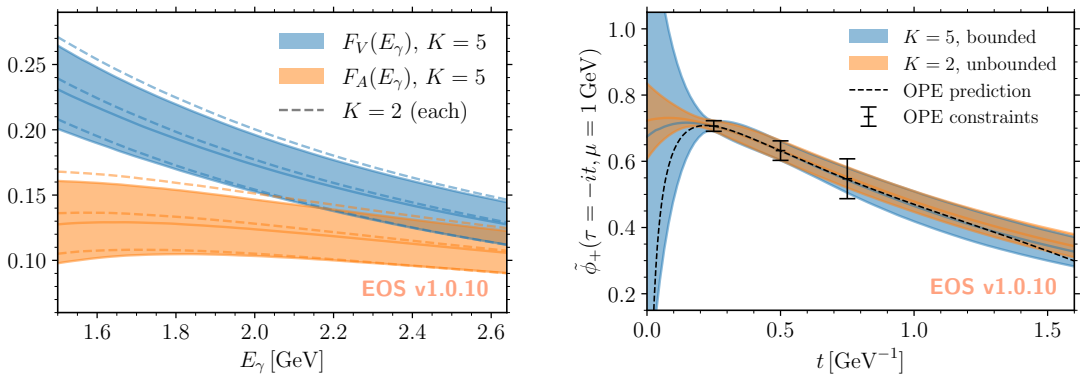

(a) Form factors over their entire kinematic range compared with the case $K = 2$ (without bound).

(b) Position-space LCDA compared with the case $K = 2$ (without bound), the central OPE prediction, and the concrete OPE inputs.

Figure 4.8.: Prediction of the form factors at $K = 5$ and $\omega_0 = 0.8\,\text{GeV}$, using inputs from the OPE, mock data for the experimental observables, and a model for the parameter bound. Bands indicate the 68 % probability interval.

The similar widths of the distributions of the higher-order parameters suggest they are constrained mainly by the parameter bound rather than by the other inputs. Their widths correspond to a weak bound for the higher-order parameters. It remains after the lower-order contributions, which statistically tend to be non-zero, are effectively subtracted from the total bound χ. In the posterior-predictive results, the broad distributions of the higher-order parameters become a handle of the truncation error: the error only remains under control for observables that primarily depend on the sharply determined parameters, i.e., if interpolating the information from the constraints to the predictions is valid. This way, our approach allows to qualify the reliability of predictions.

To demonstrate the last point, we predict the form factors over their entire kinematic range (given by the limits of the factorization approach and maximum recoil) in our setup at $K = 5$ using inputs from the OPE, mock experimental data, and the inverse moment from QCD sum rule analysis together with the parameter bound obtained from a model. The result is shown in Fig. 4.8a as a plot of the median values within the 68 % probability interval. For comparison, the dashed lines indicate the result of the previous setup at truncation level $K = 2$ and without the bound. The lines for the different truncation levels are similar (but not identical) because the parametrization at $K = 2$ already fulfills the constraints, by construction, reasonably well so that the central tendencies are consistent. More importantly, the widths of the uncertainty bands remain virtually identical when increasing the number of parameters, i.e., the form factors' truncation error is well under control. This behavior can be anticipated at a qualitative level, as it effectively results from interpolating data that includes the experimental observables directly linked to the

integrated form factors.

The LCDA itself presents another instructive example. In Fig. 4.8b, we show its posterior prediction as a function of $\tau = -it$ on the negative imaginary axis, complemented, for reference only, with the central OPE prediction and the concrete data points that constrain the analysis. The plot further includes the analogous result for $K = 2$ without the parameter bound. Comparing the bands for both truncation levels, we find that the uncertainty remains consistent for larger values of $t \gtrsim 0.25\,\mathrm{GeV}^{-1}$, reflecting the suppression of higher-order coefficients in that region. On the contrary, the increased uncertainty at lower t values for $K = 5$ shows the initial underestimation of uncertainties at a low truncation level without the bound. We further compare the new result with the previous case at $K = 1$ shown in Fig. 4.4. There, we varied the scale ω_0 which indeed gives a similar impression of the truncation error of the prediction as a function of t. However, this method has certain limitations. It only allows for the identification of predictions with high uncertainty, indicated by significant variation; it does not, conversely, guarantee the reliability of predictions with minimal variation. Furthermore, the scale variation method is prone to subjective bias. The selection of the ω_0 interval for this method either relies on heuristic judgment to estimate typical hadronic scales or it takes inspiration from model-based studies such as in Section 2.3. In contrast, using the parameter bound as a regulator at high truncation levels in a Bayesian analysis offers a more objective and quantitative approach to assessing the truncation error, allowing a clearer interpretation of the results.

4.4.4. Conclusions

The model-independent theory information from the operator product expansion proves to be valuable input for constraining the LCDA parameters. All observables considered here, i.e., the experimental observables, the form factors, and the logarithmic moments, are suitable to constrain the value of the parametrization's reference scale ω_0 that leads to optimal convergence. Input about the $B \to \gamma\ell\nu$ form factors or the logarithmic moments has a straightforward impact on determining the LCDA parameters due to simple linear correlation. Experimental data for the branching ratio and forward-backward asymmetry of $B \to \gamma\ell\nu$ also provide effective constraints. Although they induce both a primary and prominent secondary mode, the latter can be effectively eliminated using additional input. In particular, we find that the inverse moment, accessible via the QCD Light-Cone Sum Rule method, is suitable for this purpose at the accuracy already available in the literature. We emphasize that data for the branching ratio and the forward-backward asymmetry complement each other to improve the accuracy of a global analysis and thus both observables should be measured. Lastly, we demonstrated a major feature of the LCDA parametrization, the ability to control the truncation error of predictions based on the parameter bound in a Bayesian setup.

4.5. Summary and Outlook

We detailed the theoretical aspects of the $B \to \gamma\ell\nu$ decay, employing QCD Factorization, complemented with the QCD Light-Cone Sum Rule approach, to predict the decay amplitude through the leading-twist B LCDA.

For the first time, we applied the systematic parametrization proposed in Chapter 2 to a decay prediction, introducing a tailored method, termed the "generator formalism." This formalism streamlines the computational process by reducing the need for multiple integrals to a single integral, which can then be differentiated to obtain the coefficient expansion order by order. This approach is complemented by a compact series expansion for incorporating perturbative corrections, which manifest as logarithmic convolutions of the LCDA, offering a practical solution to efficiently approximate results where closed forms are unavailable.

Furthermore, the chapter outlined the integration of this decay process into the `EOS` software, a central development of this thesis. It allowed us to perform a comprehensive phenomenological study using tools for Bayesian analysis provided in `EOS`, to assess the effectiveness of using $B \to \gamma\ell\nu$ decay constraints alongside theoretical information about the LCDA's short-distance behavior. We employed mock data because no experimental data (compatible with the factorization approach) is available at present, but a suitable measurement is already anticipated from the Belle-II experiment. This analysis demonstrated the potential of the decay observables to constrain the LCDA parameters and also showcased the utility of the parameter bound within a Bayesian framework to manage the parametrization's truncation error.

We note that lattice QCD estimates for the $B \to \gamma$ form factors might become available in the foreseeable future. Methods for the determination of radiative-leptonic decay form factors using lattice QCD are currently under investigation. See, for recent examples, Refs. [78–80].

In conclusion, we established the feasibility of a global analysis with experimental data to determine the B-LCDA parameters, with the expectation that future data will elevate the analysis to a quantitative level. Our proof-of-concept study also highlights the role of the parameter bound in accounting for truncation errors, which enhances the robustness of the analysis.

Conclusion

Descriptions of hadronic particles such as the B meson need inputs that can presently not be derived from first principles in QCD. Among these inputs, the leading-twist B-meson Light-Cone Distribution Amplitude (LCDA) is pivotal for theoretical predictions of exclusive, energetic B decays, as it encodes the internal structure of the hadron in accordance with QCD Factorization and QCD Light-Cone Sum Rules. These frameworks allow for a multifaceted analysis of the LCDA, complemented by the theoretical short-distance behavior, altogether providing substantial constraints of various aspects. In this thesis, we developed a new approach to infer information about the LCDA through a global analysis, aiming to integrate all available data sources. This approach seeks to maximize the accuracy and completeness of the predictions while minimizing any potential bias, thereby offering a more reliable framework for the study of B-meson decays. We addressed the principal ingredients of our approach in three main parts.

First, we developed a systematic parametrization for the leading-twist B-meson LCDA, which can serve as the vehicle for a comprehensive analysis. The primary goal of the parametrization approach, in contrast to previous model-based approaches, is to avoid unquantifiable systematic uncertainties. This parametrization fulfills established mathematical properties and satisfies a parameter bound to manage truncation. Using the flexibility in the choice of the expansion's functional basis, we selected a form that facilitates straightforward and compact closed-form expressions. Notably, at the elementary truncation level $K = 0$, the expansion aligns with a widely recognized single-parameter model. Therefore, our parametrization can be viewed as a systematic extension of this model, albeit with a different underlying philosophy. The renormalization scale dependence of the LCDA can be accounted for in several ways, one of which involves variation of the parameters while keeping the basis functions invariant. This implementation of the RGE significantly simplifies the development of numerical codes. Analyzing the parameterization across various models has shown the capability to reproduce diverse behaviors and offered heuristic benchmarks for convergence. A first rudimentary study of the interplay between phenomenological inputs and theoretical information from the short-distance behavior led to consistent and encouraging results.

Second, we derived the short-distance behavior of the leading-twist B_s-meson LCDA, where the mass of the spectator quark has a considerable effect. Our matching calculation takes advantage of the techniques for evaluating Feynman integrals in momentum space before

transforming the result to the desired representation in position space. We simplified this critical step by using systematic "local subtractions" to perform an asymptotic expansion of the Feynman integrals for on-shell matrix elements at the level of the Fourier transform. Based on this technique, we further obtained results for the matching coefficients of the *subleading-twist* 2-particle LCDA up to dimension 4 in the OPE. To test the consistency of our results, we extrapolated the short-distance behavior using the parametrization for the LCDA. Estimating the inverse moment this way led to results consistent with independent estimates from QCD rum rules, and a brief study of the potential impact of local operators of dimension 5 again confirmed the consistency of our approach. The updated short-distance behavior can directly benefit applications with the B_s-meson LCDA using our parametrization.

Third, we applied the LCDA parametrization to the $B \to \gamma\ell\nu$ decay, which is the benchmark decay mode to probe the leading-twist LCDA experimentally. The theory prediction is based on QCD Factorization, supplemented by QCD Light-Cone Sum Rules for power corrections. Both methods rely on integrals of the LCDA which we express in terms of the parametrization. To this end, we introduced the "generator formalism" to streamline the computation of order-by-order expressions. We briefly discussed the technical implementation of observables using the parametrization in the `EOS` software, which enabled a comprehensive proof-of-concept study based on Bayesian inference. Here, our systematic approach proved to be feasible and practical for combining inputs from various sources to constrain the LCDA. We demonstrated the role of the parameter bound as a regulator using a model-based mock value for the bound. Using examples, we showed how our approach allows us to straightforwardly quantify truncation errors to test the reliability of predictions.

We established the feasibility of our approach for systematic analysis of the leading-twist B-meson LCDA using available theoretical inputs and future experimental inputs from the benchmark $B \to \gamma\ell\nu$ decay channel. The analysis tools described in this thesis are publicly available in the `EOS` software. Quantitative analysis will become feasible in the foreseeable future with the availability of experimental $B \to \gamma\ell\nu$ decay data or lattice estimates for the $B \to \gamma$ form factors. The value of the parameter bound has yet to be determined using QCD-based methods to fully utilize the parametrization and more accurately quantify systematic uncertainties. Until the bound is determined, variation of the auxiliary scale ω_0 offers a practical method to provide a heuristic estimate. Thoroughly testing various aspects of our parameterization has consistently produced promising results. Therefore, we conclude that our approach has significant potential to improve the reliability of predictions based on QCD Factorization and QCD Light-Cone Sum Rules which depend on the B-meson LCDA.

A. Supplementary Material for the Parametrization

A.1. Useful Definitions and Formulas

We define the renormalization group functions along Ref. [81] as

$$V(\mu,\mu_0) = -\int_{\alpha_s(\mu_0)}^{\alpha_s(\mu)} \frac{\mathrm{d}\alpha}{\beta(\alpha)} \left[\gamma_+(\alpha) + \Gamma_\mathrm{c}(\alpha) \int_{\alpha_s(\mu_0)}^{\alpha} \frac{\mathrm{d}\alpha}{\beta(\alpha)}\right], \tag{A.1}$$

$$g(\mu;\mu_0) = \int_{\alpha_s(\mu_0)}^{\alpha_s(\mu)} \frac{d\alpha}{\beta(\alpha)} \Gamma_\mathrm{c}(\alpha)\,. \tag{A.2}$$

Bessel function obey the following useful integral identity (cf. Ref. [31]):

$$\int_0^\infty \mathrm{d}\omega \mathrm{e}^{-i\omega z} \left(\frac{\omega}{s}\right)^{j-1/2} J_{2j-1}(2\sqrt{s\omega}) = \mathrm{e}^{-i\pi j} \frac{\mathrm{e}^{is/z}}{z^{2j}}\,. \tag{A.3}$$

They can be expressed using a weighted sum of associated Laguerre polynomials by

$$J_\alpha(x) = \left(\frac{x}{2}\right)^\alpha \frac{\mathrm{e}^{-t}}{\Gamma(1+\alpha)} \sum_{k=0}^{\infty} \frac{\alpha!}{(k+\alpha)!} L_k^{(\alpha)}\left(\frac{x^2}{4t}\right) t^k\,, \tag{A.4}$$

with an arbitrary parameter t. For the parametrization, a useful special case with $t = \omega/\omega_0$ reads

$$J_1(2\sqrt{\omega s}) = \sqrt{\omega s}\,\mathrm{e}^{-\omega/\omega_0} \sum_{k=0}^{\infty} \frac{1}{(1+k)!} L_k^{(1)}(s\omega_0) \left(\frac{\omega}{\omega_0}\right)^k. \tag{A.5}$$

To unambiguously define the Laguerre polynomials, we provide explicit formulas here. They can be written in closed form as

$$L_n^{(\alpha)}(x) = \sum_{i=0}^{n} (-1)^i \binom{n+\alpha}{n-i} \frac{x^i}{i!}\,. \tag{A.6}$$

For $\alpha = 1$, the lowest order polynomials read

$$\begin{aligned} L_0^{(1)} &= 1\,, & L_1^{(1)} &= -x+2\,, \\ L_2^{(1)} &= \frac{1}{2}\left(x^2-6x+6\right)\,, & L_3^{(1)} &= \frac{1}{6}\left(-x^3+12x^2-36x+24\right)\,. \end{aligned} \tag{A.7}$$

They obey the orthogonality relation

$$\int_0^\infty \mathrm{d}x\, x^\alpha\, \mathrm{e}^{-x} L_n^{(\alpha)}(x)\, L_m^{(\alpha)}(x) = \frac{\Gamma(n+\alpha+1)}{n!}\,\delta_{nm}\,. \tag{A.8}$$

Their "generating function", containing the polynomials as its Taylor series coefficients, reads

$$\sum_{n=0}^{\infty} t^n L_n^{(\alpha)}(x) = \frac{1}{(1-t)^{\alpha+1}} \mathrm{e}^{-tx/(1-t)}\,. \tag{A.9}$$

A.2. Coefficients a_k from Pseudo-phenomenology and OPE

We obtain solutions for the expansion coefficients a_k for $k = 0, \ldots, 3$ using the constraints from the pseudo-observables p_1 and p_2 and two theory inputs t_1 and t_2 (see Section 2.4) in dependence of ξ, x_0, n_0 and a_4 as

$$\begin{aligned} a_0 = Z\Bigg(&-\frac{(5\xi-1)(1+30\xi+25\xi^2)}{100\xi^2(5\xi-3)} + \frac{5\xi-1}{15\xi^2(5\xi-3)}\,\bar{\Lambda}_a\, p_1\Bigg) \\ &+ \frac{3\xi(5\xi-1)}{2(5\xi-3)} - \frac{(5\xi+1)^5}{2500\xi^2(5\xi-3)}\,p_2 - \frac{(9-5\xi)(5\xi-1)}{5(5\xi-3)(5\xi+1)}\,a_4 \\ &+ \frac{(5\xi-1)(1+30\xi+25\xi^2)\,\alpha_s C_F}{75\pi\xi^3(5\xi-3)}\,\bar{\Lambda}_a\, n_0\, p_1\,(1+\ln x_0)\,, \end{aligned} \tag{A.10}$$

$$a_1 = Z\left(-2+\frac{1}{3\xi}\,\bar{\Lambda}_a\, p_1\right) + \frac{3\xi}{2} + \frac{8\alpha_s C_F}{3\pi}\,\frac{\bar{\Lambda}_a n_0}{\xi}\,(1+\ln x_0)\, p_1 - \frac{4a_4}{5}\,, \tag{A.11}$$

$$\begin{aligned} a_2 = Z\Bigg(&\frac{3\,(5\xi-1)(1+30\xi+25\xi^2)}{100\xi^2(5\xi-3)} - \frac{5\xi-1}{5\xi^2(5\xi-3)}\,\bar{\Lambda}_a\, p_1\Bigg) \\ &- \frac{3\xi(5\xi+3)}{2(5\xi-3)} + \frac{3(5\xi+1)^5}{2500\xi^2(5\xi-3)}\,p_2 + \frac{6(-3+30\xi-25\xi^2)}{5(5\xi-3)(5\xi+1)}\,a_4 \\ &- \frac{(5\xi-1)(1+30\xi+25\xi^2)\alpha_s C_F}{25\pi\xi^3(5\xi-3)}\,\bar{\Lambda}_a\, n_0\, p_1\,(1+\ln x_0)\,, \end{aligned} \tag{A.12}$$

$$\begin{aligned} a_3 = Z\Bigg(&\frac{(5\xi+1)(-1-20\xi+75\xi^2)}{50\xi^2(5\xi-3)} - \frac{(5\xi-2)(5\xi+1)}{15\xi^2(5\xi-3)}\,\bar{\Lambda}_a\, p_1\Bigg) \\ &- \frac{3\xi(5\xi+1)}{2(5\xi-3)} + \frac{(5\xi+1)^5}{1250\xi^2(5\xi-3)}\,p_2 + \frac{4(-9+10\xi+25\xi^2)}{5(5\xi-3)(5\xi+1)}\,a_4 \\ &- \frac{2(5\xi+1)(-1-20\xi+75\xi^2)\,\alpha_s C_F}{75\pi\xi^3(5\xi-3)}\,\bar{\Lambda}_a\, n_0\, p_1\,(1+\ln x_0)\,. \end{aligned} \tag{A.13}$$

B. Supplementary Material for the Short-distance Expansion

B.1. Derivatives Acting on 2-particle Operators

The equations of motion of the light and heavy quark fields impose conditions on the hadronic matrix elements of local operators. To employ them effectively, the following identities are central, which involve the four-derivative acting on the 2-particle operator.

The action of the derivative on the composite operator can be complemented with gluon fields as follows:

$$i\partial^\mu\,\bar q\Gamma h_v = \bar q\, i\overleftarrow{\partial^\mu}\,\Gamma h_v + \bar q\,\Gamma\, i\partial^\mu\, h_v = \bar q\, i\overleftarrow{D^\mu}\,\Gamma h_v + \bar q\,\Gamma\, iD^\mu\, h_v\,. \tag{B.1}$$

Above, we use the covariant derivative $iD^\mu = i\partial^\mu + A^\mu$ with the gluon field $A^\mu = g_s t_a A^\mu_a$, we use the notation $i\overleftarrow{D^\mu}{=}i\overleftarrow{\partial^\mu} - A^{\mu\dagger}$ to account for the Dirac adjoint [47], and g_s denotes the bare coupling.

A similar identity holds for the second derivative, with additional terms where the derivative acts only on the gauge field:

$$\begin{aligned} i\partial^\nu i\partial^\mu\,\bar q\Gamma h_v &= \bar q\Big(i\overleftarrow{\partial^\mu}i\overleftarrow{\partial^\nu} + i\partial^\mu i\partial^\nu + i\overleftarrow{\partial^\mu}\,i\partial^\nu + i\overleftarrow{\partial^\nu}\,i\partial^\mu\Big)\Gamma h_v \\ &= \bar q\Big(i\overleftarrow{D^\mu}i\overleftarrow{D^\nu} + (i\partial^\nu A^\mu) - A^\mu A^\nu \\ &\quad + iD^\mu iD^\nu - (i\partial^\mu A^\nu) - A^\mu A^\nu \\ &\quad + i\overleftarrow{D^\mu}iD^\nu + A^\mu A^\nu + i\overleftarrow{D^\nu}iD^\mu + A^\nu A^\mu\Big)\Gamma h_v \end{aligned} \tag{B.2}$$

These can be expressed using the field strength tensor $iG^{\mu\nu} = [iD^\mu, iD^\nu]$ acting on the light quark field:

$$\bar q\,[i\overleftarrow{D^\mu}, i\overleftarrow{D^\nu}]\,\Gamma h_v = \bar q\,\big((i\partial^\mu A^\mu) - (i\partial^\nu A^\mu) + [A^\mu, A^\nu]\big)\,\Gamma h_v\,. \tag{B.3}$$

Together, this yields the compact identity

$$i\partial^\nu i\partial^\mu\,\bar q\Gamma h_v = \bar q\,\big(i\overleftarrow{D^\mu}i\overleftarrow{D^\nu} + iD^\mu iD^\nu + i\overleftarrow{D^\mu}iD^\nu + i\overleftarrow{D^\nu}iD^\mu - [i\overleftarrow{D^\mu}, i\overleftarrow{D^\nu}]\big)\,\Gamma h_v\,. \tag{B.4}$$

C. Supplementary Material for $B \to \gamma \ell \nu$ Decay

C.1. NLO Integration Results

Here, we provide machine-copyable code for Mathematica 13 for the quantities

$$\left[L_0^{\text{inc}}[\Delta\phi_+^{(1a)};\Omega]\right](t)\,,\quad \left[L_0^{\text{inc}}[\Delta\phi_+^{(1b)};\Omega]\right](t)\,,\quad \left[L_0^{\text{inc}}[\Delta\phi_+^{(1c)};\Omega]\right](t)\,,\quad \left[L_0^{\text{inc}}[\Delta\phi_+^{(1d)};\Omega]\right](t)\,,$$

and

$$\left[\mathcal{L}^{\text{inc}}[\Delta\phi_+^{(1a\star)};\Omega,\sigma]\right](t)\,,\qquad \left[\mathcal{L}^{\text{inc}}[\Delta\phi_+^{(1b\star)};\Omega,\sigma]\right](t)\,,\qquad \left[\mathcal{L}^{\text{inc}}[\Delta\phi_+^{(1c\star)};\Omega,\sigma]\right](t)\,.$$

A helpful identity to obtain the following formulas is

$$\ln^n x = \left[\frac{\mathrm{d}^n}{\mathrm{d}t^n}\, x^t\right]_{t=0}\,. \tag{C.1}$$

The expressions are composed of special functions, namely the exponential integral function,

$$\mathrm{Ei}(z) := \texttt{ExpIntegralEi[z]}\,,$$

the generalized hypergeometric function,

$${}_pF_q(a_1,\dots a_p;b_1,\dots b_q;z) := \texttt{HypergeometricPFQ[\{a[1], ...a[p]\}, \{b[1], ...b[q]\}, z]}\,,$$

and the Meijer G-function,

$$G_{p,q}^{m,n}\left(\begin{matrix}a_1,\dots a_p\\ b_1,\dots b_q\end{matrix}\,\middle|\, z\right) :=$$

$$\texttt{MeijerG[\{\{a[1], ...a[n]\}, \{a[n+1], ...a[p]\}\}, \{\{b[1], ...b[m]\}, \{b[m+1], ...b[q]\}\}, z]}\,.$$

The concrete cases of the Meijer G-function appearing in the code can be written as (less compact) combinations of logarithms and the aforementioned special functions using Mathematica's function `FunctionExpand`. The special constants are the Euler–Mascheroni constant $\gamma_E :=$ `EulerGamma` ≈ 0.577, the base of the natural logarithm e := `E`, and $\pi :=$ `Pi`.

In the code, we use the abbreviations

$$\ln\frac{\mu^2}{2E_\gamma\Omega} := \texttt{LNLO}\,,\qquad \frac{\Omega}{\omega_0} := \texttt{xOmega}\,,\qquad \sigma\,\omega_0 := \texttt{xsigma}\,.$$

$$\left[L_0^{\text{inc}}[\Delta\phi_+^{(1a)};\Omega]\right](t) :=$$

```
-1/24*(E^(((1 + t)*xOmega)/(-1 + t))*(-1 + t)*(1 - (1 + t)/(-1 + t))^2*(6 - 6*LNLO^2 - Pi^2 +
12*LNLO*Log[xOmega] - 6*Log[xOmega]^2 + (-6 + 6*LNLO*(2*EulerGamma + LNLO) + Pi^2 - (12*(1 + t)
*xOmega*HypergeometricPFQ[{1, 1, 1}, {2, 2, 2}, ((1 + t)*xOmega)/(-1 + t)])/(-1 + t) + 12*Log[-
((1 + t)/(-1 + t))]*(LNLO - Log[xOmega]) - 6*Log[xOmega]*(2*EulerGamma + Log[xOmega]) + 12*
ExpIntegralEi[((1 + t)*xOmega)/(-1 + t)]*(-LNLO + Log[xOmega]))/E^(((1 + t)*xOmega)/(-1 + t))))
/(1 + t)
```

$$\left[L_0^{\text{inc}}[\Delta\phi_+^{(1b)};\Omega]\right](t) :=$$

```
-(((4*(1 + t)*xOmega*HypergeometricPFQ[{1, 1, 1}, {2, 2, 2}, ((1 + t)*xOmega)/(-1 + t)])/(-1 +
t) + E^(((1 + t)*xOmega)/(-1 + t))*(EulerGamma + Log[-(((1 + t)*xOmega)/(-1 + t))])*(-3 + (2*
EulerGamma)/E^(((1 + t)*xOmega)/(-1 + t)) - 2*LNLO + 2*Log[xOmega] - ((2*ExpIntegralEi[((1 + t)
*xOmega)/(-1 + t)] + Log[-xOmega^(-1)] - Log[-xOmega] + 2*Log[xOmega])*(-2 + 3*xOmega + 2*LNLO*
xOmega + t*(2 + 3*xOmega + 2*LNLO*xOmega) - 2*(1 + t)*xOmega*Log[xOmega]))/(2*E^(((1 + t)*
xOmega)/(-1 + t))*(-1 + t)) + (2*Log[-(((1 + t)*xOmega)/(-1 + t))])/E^(((1 + t)*xOmega)/(-1 + t
))) + ((3 + 2*LNLO - 2*Log[xOmega])*(2*ExpIntegralEi[((1 + t)*xOmega)/(-1 + t)] + Log[-xOmega^(
-1)] - Log[-xOmega] + 2*Log[xOmega])*(-1 + t + EulerGamma*xOmega + EulerGamma*t*xOmega + (1 + t
)*xOmega*Log[-(((1 + t)*xOmega)/(-1 + t))]))/(2*(-1 + t)))/(-1 + t^2))
```

$$\left[L_0^{\text{inc}}[\Delta\phi_+^{(1c)};\Omega]\right](t) :=$$

```
(((-1 + t)*(-2*EulerGamma + 2*E^(((1 + t)*xOmega)/(-1 + t))*EulerGamma*LNLO + 2*ExpIntegralEi
[((1 + t)*xOmega)/(-1 + t)] + Log[(-1 + t)/((1 + t)*xOmega)] - 2*E^(((1 + t)*xOmega)/(-1 + t))*
ExpIntegralEi[-(((1 + t)*xOmega)/(-1 + t))]*(LNLO - Log[xOmega]) - 2*E^(((1 + t)*xOmega)/(-1 +
t))*EulerGamma*Log[xOmega] + E^(((1 + t)*xOmega)/(-1 + t))*LNLO*Log[-(((1 + t)*xOmega)/(-1 + t)
)] - E^(((1 + t)*xOmega)/(-1 + t))*Log[xOmega]*Log[-(((1 + t)*xOmega)/(-1 + t))] - Log[((1 + t)
*xOmega)/(-1 + t)] - E^(((1 + t)*xOmega)/(-1 + t))*LNLO*Log[(1 - t)/(xOmega + t*xOmega)] + E
^(((1 + t)*xOmega)/(-1 + t))*Log[xOmega]*Log[(1 - t)/(xOmega + t*xOmega)]))/(1 + t) - 2*xOmega*
Derivative[{0, 0}, {0, 1}, 0][HypergeometricPFQ][{1, 1}, {2, 2}, ((1 + t)*xOmega)/(-1 + t)])/(-
1 + t)^2
```

$$\left[L_0^{\text{inc}}[\Delta\phi_+^{(1d)};\Omega]\right](t) :=$$

```
(xOmega*(-(((-1 + t)*(2*EulerGamma - 2*ExpIntegralEi[((1 + t)*xOmega)/(-1 + t)] - Log[(-1 + t)
/((1 + t)*xOmega)] + Log[((1 + t)*xOmega)/(-1 + t)]))/((1 + t)*xOmega)) - 2*Derivative[{0, 0},
{0, 1}, 0][HypergeometricPFQ][{1, 1}, {2, 2}, ((1 + t)*xOmega)/(-1 + t)] + 2*Derivative[{0, 0},
 {0, 2}, 0][HypergeometricPFQ][{1, 1}, {2, 1}, ((1 + t)*xOmega)/(-1 + t)]))/(-1 + t)^2
```

$$\left[\mathcal{L}^{\text{inc}}[\Delta\phi_+^{(1a\star)};\Omega,\sigma]\right](t) :=$$

```
-1/6*((-6 + Pi^2)*(1 - t + E^((xOmega*(1 + t + xsigma - t*xsigma))/(-1 + t))*(-1 + t + t*xOmega
*(-1 + xsigma) - xOmega*(1 + xsigma))))/((-1 + t)*(1 + t + xsigma - t*xsigma)^2)
```

$$\left[\mathcal{L}^{\text{inc}}[\Delta\phi_+^{(1b\star)};\Omega,\sigma]\right](t) :=$$

```
(2 - Pi^2/3 - (-1 + EulerGamma)*(1 + 2*EulerGamma + 2*LNLO + 2*Log[(1 + t + xsigma - t*xsigma)
/(1 - t)]) + 2*Log[(xOmega*(-1 + t*(-1 + xsigma) - xsigma))/(-1 + t)]*MeijerG[{{}, {1, 1}},
{{0, 0, 2}, {}}, (xOmega*(-1 + t*(-1 + xsigma) - xsigma))/(-1 + t)] - (3 + 2*LNLO - 2*Log[
xOmega])*(Gamma[2, (xOmega*(-1 + t*(-1 + xsigma) - xsigma))/(-1 + t)]*Log[(xOmega*(-1 + t*(-1 +
 xsigma) - xsigma))/(-1 + t)] + MeijerG[{{}, {1, 1}}, {{0, 0, 2}, {}}, (xOmega*(-1 + t*(-1 +
xsigma) - xsigma))/(-1 + t)]) + EulerGamma*(1 + 2*EulerGamma + 2*LNLO + Gamma[2, (xOmega*(-1 +
t*(-1 + xsigma) - xsigma))/(-1 + t)]*(-3 - 2*LNLO + 2*Log[xOmega]) + 2*Log[(1 + t + xsigma - t*
xsigma)/(1 - t)] + 2*MeijerG[{{}, {1, 1}}, {{0, 0, 2}, {}}, (xOmega*(-1 + t*(-1 + xsigma) -
xsigma))/(-1 + t)]) + Log[1 + t]*(1 + 2*EulerGamma + 2*LNLO + Gamma[2, (xOmega*(-1 + t*(-1 +
xsigma) - xsigma))/(-1 + t)]*(-3 - 2*LNLO + 2*Log[xOmega]) + 2*Log[(1 + t + xsigma - t*xsigma)
/(1 - t)] + 2*MeijerG[{{}, {1, 1}}, {{0, 0, 2}, {}}, (xOmega*(-1 + t*(-1 + xsigma) - xsigma))/(
-1 + t)]) - Log[1 + t + xsigma - t*xsigma]*(1 + 2*EulerGamma + 2*LNLO + Gamma[2, (xOmega*(-1 +
t*(-1 + xsigma) - xsigma))/(-1 + t)]*(-3 - 2*LNLO + 2*Log[xOmega]) + 2*Log[(1 + t + xsigma - t*
xsigma)/(1 - t)] + 2*MeijerG[{{}, {1, 1}}, {{0, 0, 2}, {}}, (xOmega*(-1 + t*(-1 + xsigma) -
xsigma))/(-1 + t)]) + 4*MeijerG[{{}, {1, 1, 1}}, {{0, 0, 0, 2}, {}}, (xOmega*(-1 + t*(-1 +
xsigma) - xsigma))/(-1 + t)])/(1 + t + xsigma - t*xsigma)^2
```

$$\left[\mathcal{L}^{\rm inc}[\Delta\phi_+^{(1c\star)};\Omega,\sigma]\right](t) :=$$

```
-((E^((xOmega*(1 + t + xsigma - t*xsigma))/(-1 + t))*((-2*EulerGamma*(1 + t))/(-1 + t) - (2*
LNLO*(1 + t))/(-1 + t) + (2*LNLO*(1 + t))/(E^(((1 + t)*xOmega)/(-1 + t))*(-1 + t)) + (2*
EulerGamma*LNLO*(1 + t))/(-1 + t) - (2*E^(xOmega*((1 + t)/(1 - t) + xsigma))*EulerGamma*LNLO*(1
 + t))/(-1 + t) + (LNLO^2*(1 + t))/(-1 + t) - (E^(xOmega*((1 + t)/(1 - t) + xsigma))*LNLO^2*(1
+ t))/(-1 + t) - (2*EulerGamma*LNLO*(1 + t)^2*xOmega)/(-1 + t)^2 - (LNLO^2*(1 + t)^2*xOmega)/(-
1 + t)^2 + 2*EulerGamma*xsigma + 2*LNLO*xsigma - (2*LNLO*xsigma)/E^(((1 + t)*xOmega)/(-1 + t))
+ (2*EulerGamma*LNLO*(1 + t)*xOmega*xsigma)/(-1 + t) + (LNLO^2*(1 + t)*xOmega*xsigma)/(-1 + t)
+ (2*(1 + t)*ExpIntegralEi[-(((1 + t)*xOmega)/(-1 + t))])/(-1 + t) - (2*LNLO*(1 + t)*
ExpIntegralEi[-(((1 + t)*xOmega)/(-1 + t))])/(-1 + t) + (2*LNLO*(1 + t)^2*xOmega*ExpIntegralEi[
-(((1 + t)*xOmega)/(-1 + t))])/(-1 + t)^2 - 2*xsigma*ExpIntegralEi[-(((1 + t)*xOmega)/(-1 + t))
] - (2*LNLO*(1 + t)*xOmega*xsigma*ExpIntegralEi[-(((1 + t)*xOmega)/(-1 + t))])/(-1 + t) + (2*E
^(xOmega*((1 + t)/(1 - t) + xsigma))*LNLO*(1 + t)*ExpIntegralEi[-(xOmega*xsigma)])/(-1 + t) +
(2*(1 + t)^2*xOmega*(-1 + t + t*xOmega*(-1 + xsigma) - xOmega*(1 + xsigma))*HypergeometricPFQ
[{1, 1, 1}, {2, 2, 2}, -(((1 + t)*xOmega)/(-1 + t))])/(-1 + t)^3 - (2*E^(xOmega*((1 + t)/(1 - t
) + xsigma))*(1 + t)*xOmega*xsigma*HypergeometricPFQ[{1, 1, 1}, {2, 2, 2}, -(xOmega*xsigma)])/(
-1 + t) - (2*(1 + t)*Log[(1 + t)/(1 - t)])/(-1 + t) + (2*LNLO*(1 + t)*Log[(1 + t)/(1 - t)])/(-1
 + t) - (2*LNLO*(1 + t)^2*xOmega*Log[(1 + t)/(1 - t)])/(-1 + t)^2 + 2*xsigma*Log[(1 + t)/(1 - t
)] + (2*LNLO*(1 + t)*xOmega*xsigma*Log[(1 + t)/(1 - t)])/(-1 + t) - (2*(1 + t)*Log[xOmega])/(E
^(((1 + t)*xOmega)/(-1 + t))*(-1 + t)) - (2*EulerGamma*(1 + t)*Log[xOmega])/(-1 + t) + (2*E^(
xOmega*((1 + t)/(1 - t) + xsigma))*EulerGamma*(1 + t)*Log[xOmega])/(-1 + t) + (2*EulerGamma*(1
+ t)^2*xOmega*Log[xOmega])/(-1 + t)^2 + (2*xsigma*Log[xOmega])/E^(((1 + t)*xOmega)/(-1 + t)) -
(2*EulerGamma*(1 + t)*xOmega*xsigma*Log[xOmega])/(-1 + t) + (2*(1 + t)*ExpIntegralEi[-(((1 + t)
*xOmega)/(-1 + t))]*Log[xOmega])/(-1 + t) - (2*(1 + t)^2*xOmega*ExpIntegralEi[-(((1 + t)*xOmega
)/(-1 + t))]*Log[xOmega])/(-1 + t)^2 + (2*(1 + t)*xOmega*xsigma*ExpIntegralEi[-(((1 + t)*xOmega
)/(-1 + t))]*Log[xOmega])/(-1 + t) - (2*E^(xOmega*((1 + t)/(1 - t) + xsigma))*(1 + t)*
ExpIntegralEi[-(xOmega*xsigma)]*Log[xOmega])/(-1 + t) - (2*(1 + t)*Log[(1 + t)/(1 - t)]*Log[
xOmega])/(-1 + t) + (2*(1 + t)^2*xOmega*Log[(1 + t)/(1 - t)]*Log[xOmega])/(-1 + t)^2 - (2*(1 +
t)*xOmega*xsigma*Log[(1 + t)/(1 - t)]*Log[xOmega])/(-1 + t) - ((1 + t)*Log[xOmega]^2)/(-1 + t)
+ (E^(xOmega*((1 + t)/(1 - t) + xsigma))*(1 + t)*Log[xOmega]^2)/(-1 + t) + ((1 + t)^2*xOmega*
Log[xOmega]^2)/(-1 + t)^2 - ((1 + t)*xOmega*xsigma*Log[xOmega]^2)/(-1 + t) - (2*E^(xOmega*((1 +
 t)/(1 - t) + xsigma))*LNLO*(1 + t)*Log[xsigma])/(-1 + t) + (2*E^(xOmega*((1 + t)/(1 - t) +
xsigma))*(1 + t)*Log[xOmega]*Log[xsigma])/(-1 + t)))/((-1 + t^2)*((1 + t)/(1 - t) + xsigma)^2))
```

C.2. Tables

	$\times 10^{-3}$	1	2	3
$\tilde{\phi}_+(-i0.25\,\mathrm{GeV}^{-1})$	1	0.258	0.398	0.458
$\tilde{\phi}_+(-i0.50\,\mathrm{GeV}^{-1})$	2	0.398	0.871	0.723
$\tilde{\phi}_+(-i0.75\,\mathrm{GeV}^{-1})$	3	0.458	0.723	3.62

Table C.5.: Covariance matrix for the three data points taken from the OPE.

C.3. Figures

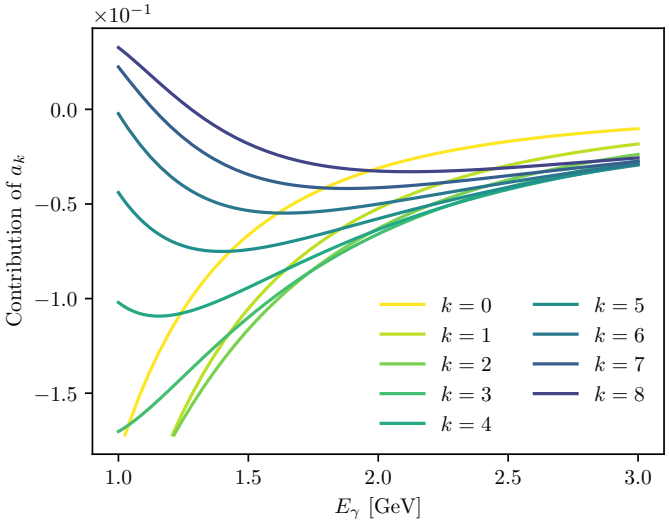

(a) Exact contributions

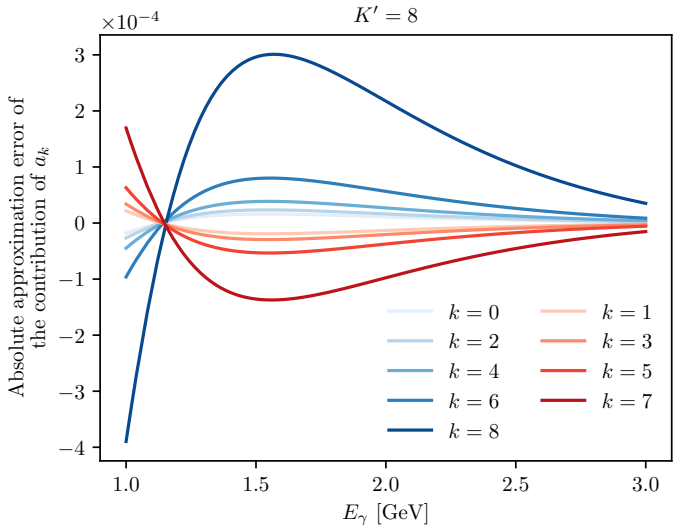

(b) Absolute errors in the minimal approximation $K' = 8$

Figure C.1.: Individual contributions associated to $a_0, a_1, \ldots, a_8$ in the parametrization of $\mathcal{L}^{\text{inc}}[\Delta\phi_+^{(1d\star)}; \Omega, \sigma]$.

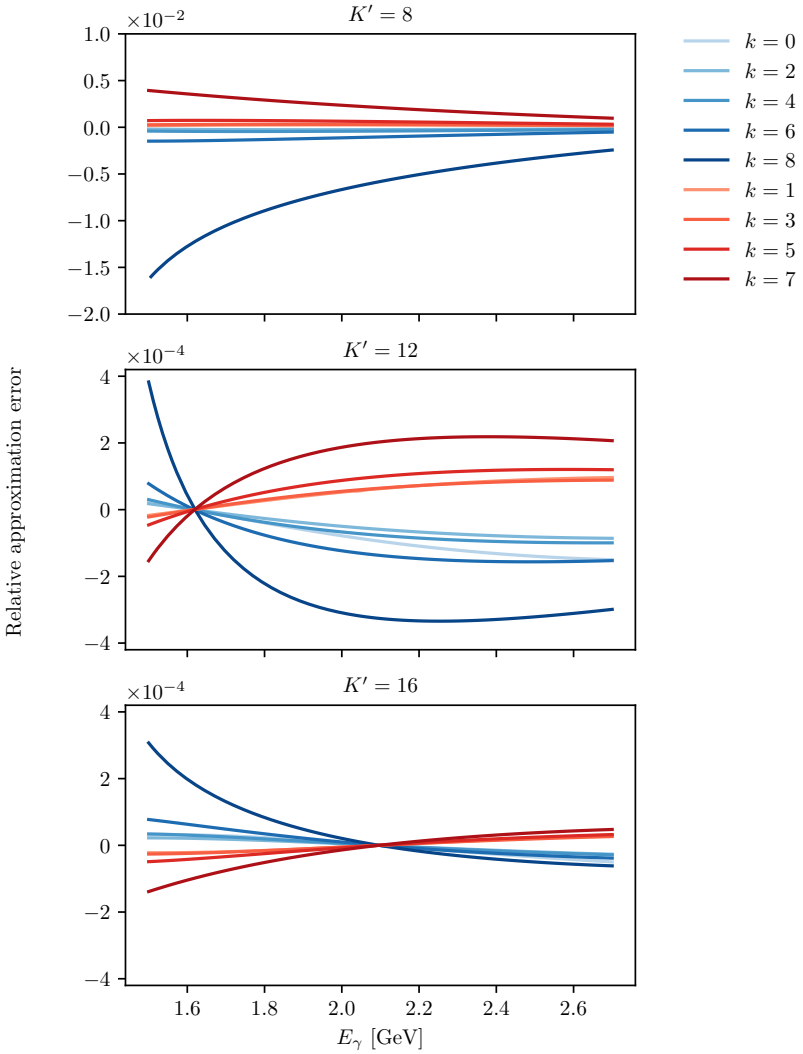

Figure C.2.: Relative truncation errors for the contribution associated to a_k in the parametrization of $\mathcal{L}^{\text{inc}}[\Delta\phi_+^{(1\text{d}\star)}; \Omega, \sigma]$ using different level approximations $K' = 8$, 12 and 16.

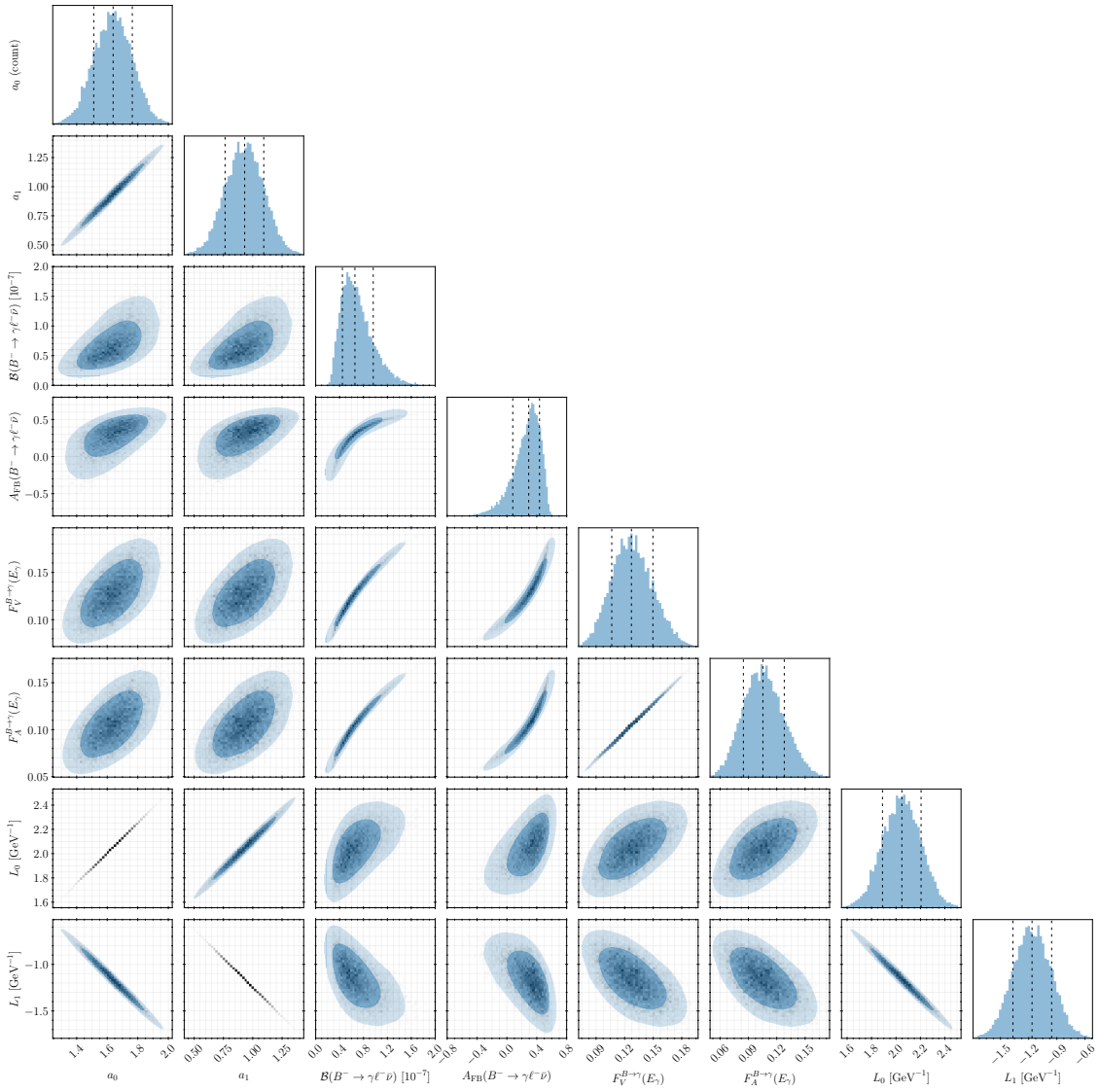

Figure C.3.: Corner plot of the posterior for $K = 1$ and $\omega_0 = 0.8\,\text{GeV}$ showing the LCDA parameters and predictions based on inputs from the OPE. Blue areas in the two-dimensional histograms indicate estimates of the 68 % and 95 % probability contours.

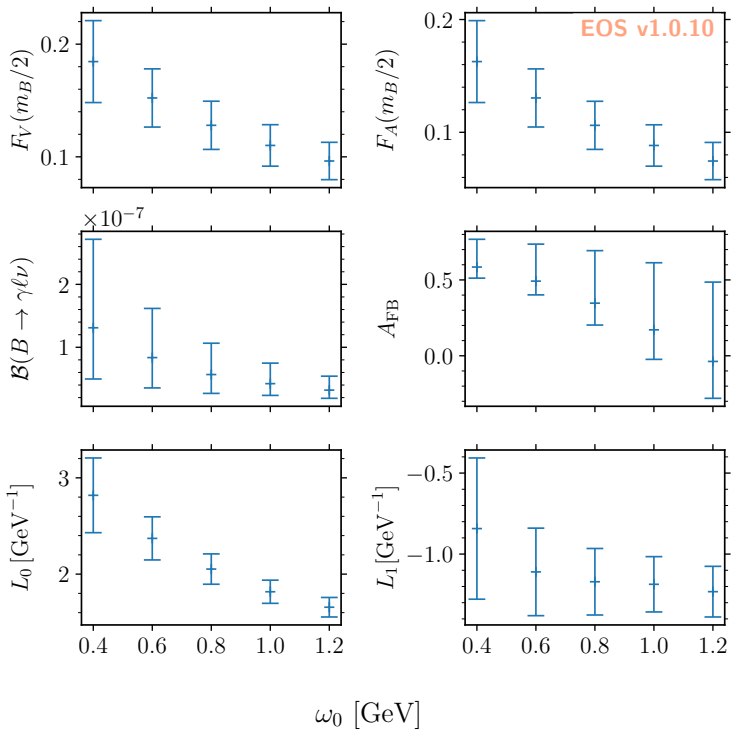

Figure C.4.: The (pseudo) observable's posterior-predictive results for $K = 1$ and varying ω_0 based on OPE input. Error bars show the median value and the limits of the 68 % probability interval.

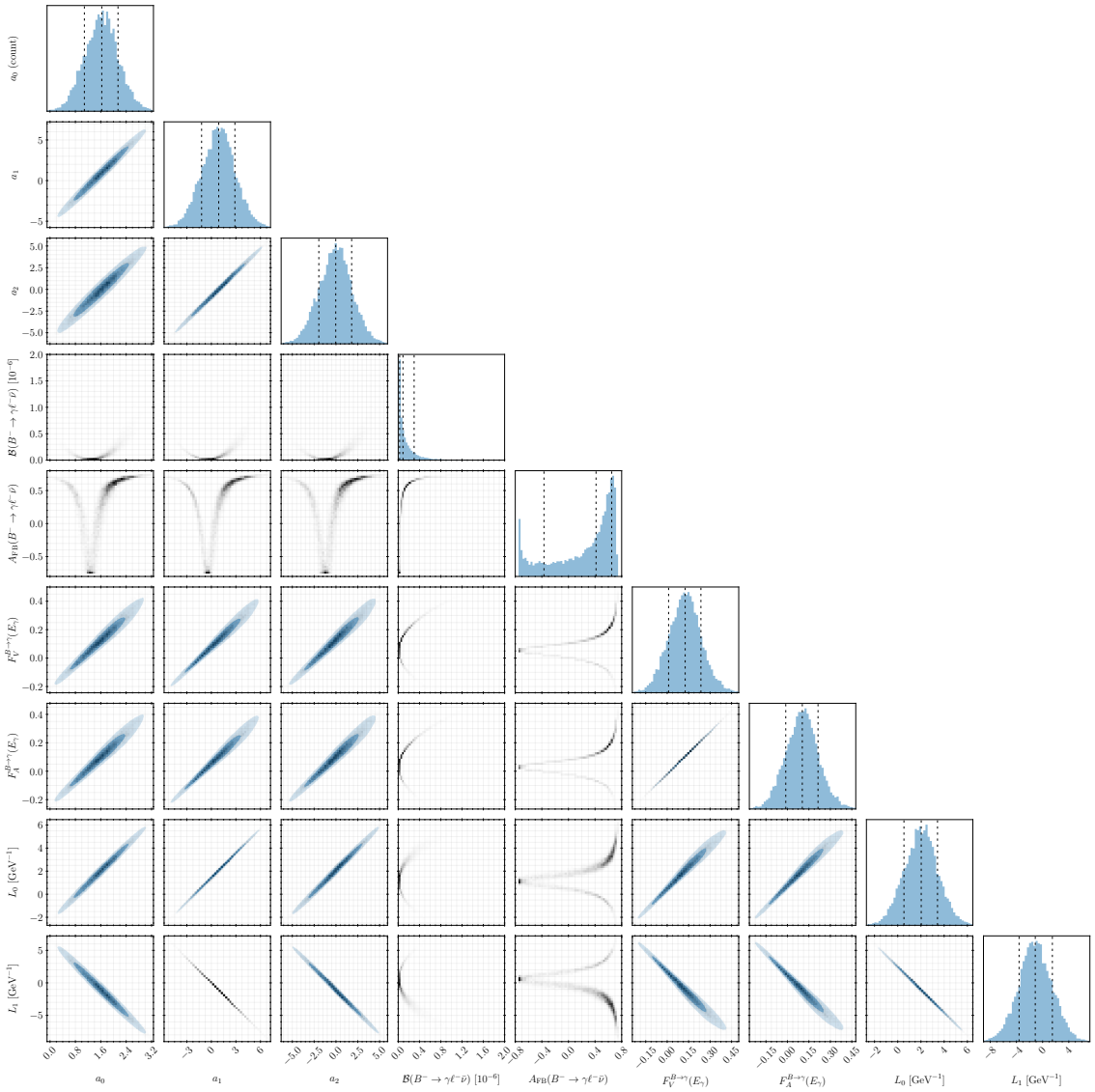

Figure C.5.: Corner plot of the posterior for $K = 2$ and $\omega_0 = 0.8\,\mathrm{GeV}$ showing the LCDA parameters and predictions based on inputs from the OPE. Blue areas in the two-dimensional histograms indicate estimates of the 68 % and 95 % probability contours.

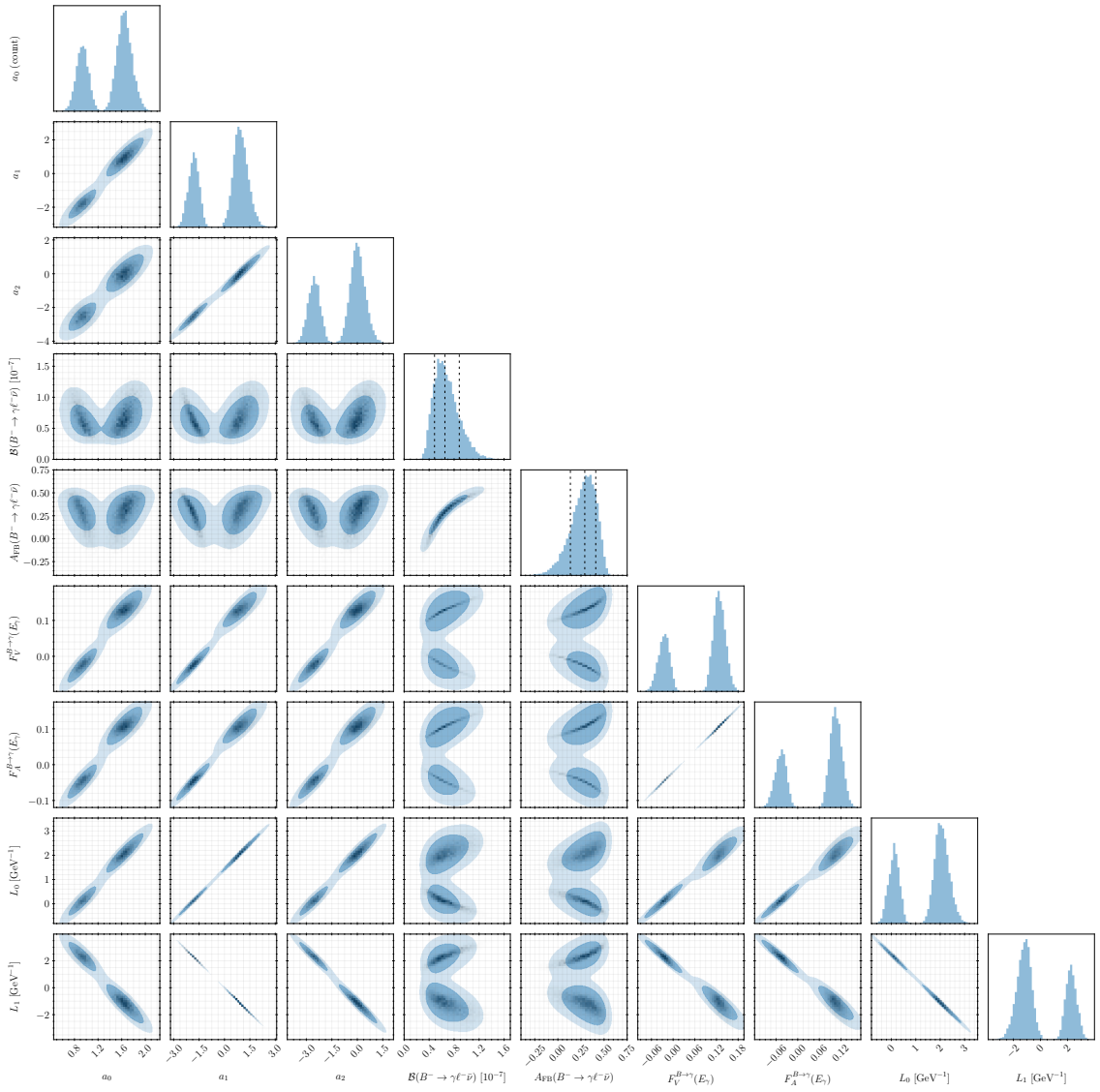

Figure C.6.: Corner plot of the posterior for $K = 2$ and $\omega_0 = 0.8\,\mathrm{GeV}$ showing the LCDA parameters and predictions based on inputs from the OPE and mock data for the experimental observables. Blue areas in the two-dimensional histograms indicate estimates of the 68 % and 95 % probability contours.

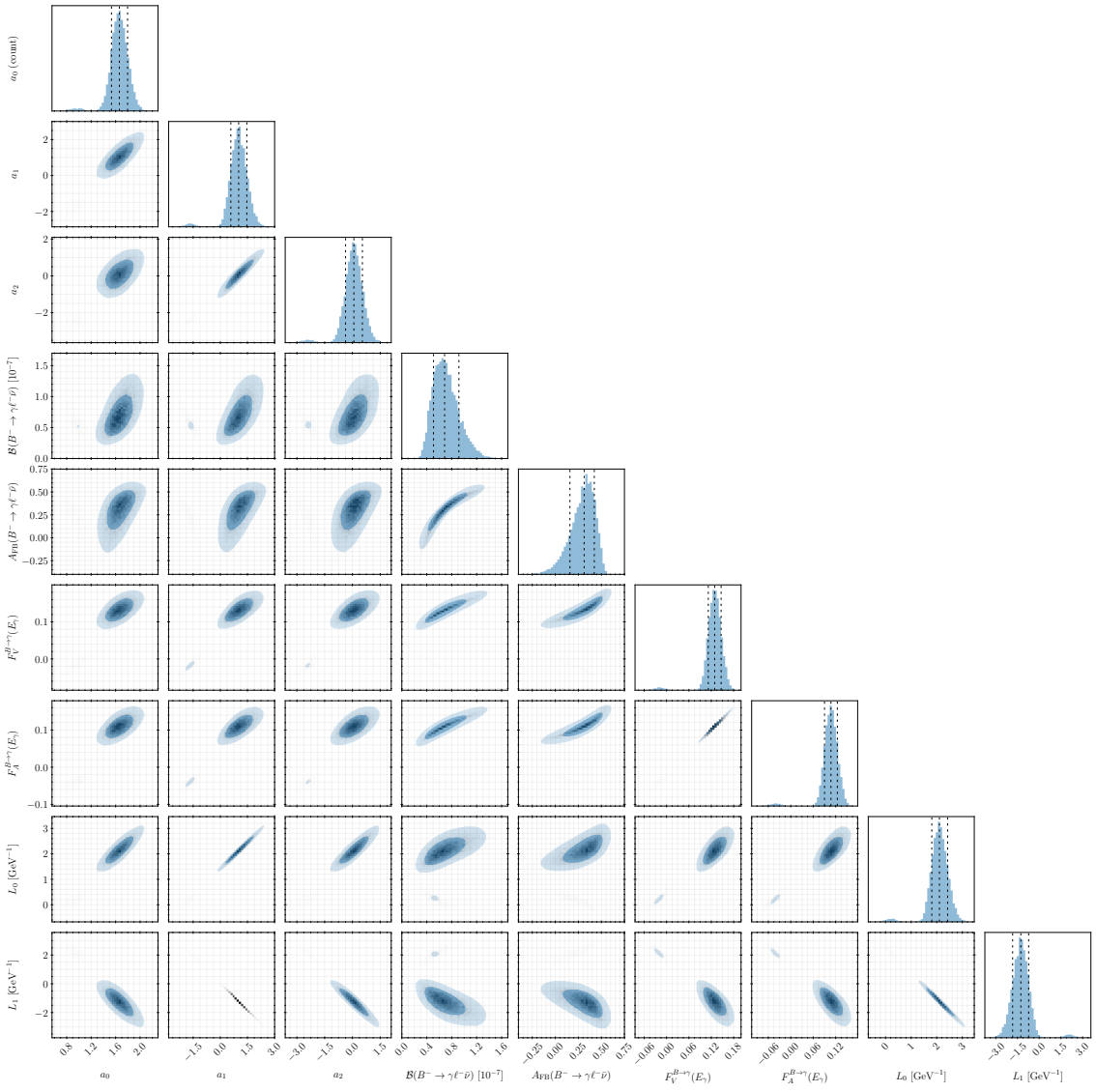

Figure C.7.: Corner plot of the posterior for $K = 2$ and $\omega_0 = 0.8\,\text{GeV}$ showing the LCDA parameters and predictions based on inputs from the OPE, mock data for the experimental observables, and data for L_0. Blue areas in the two-dimensional histograms indicate estimates of the 68 % and 95 % probability contours.

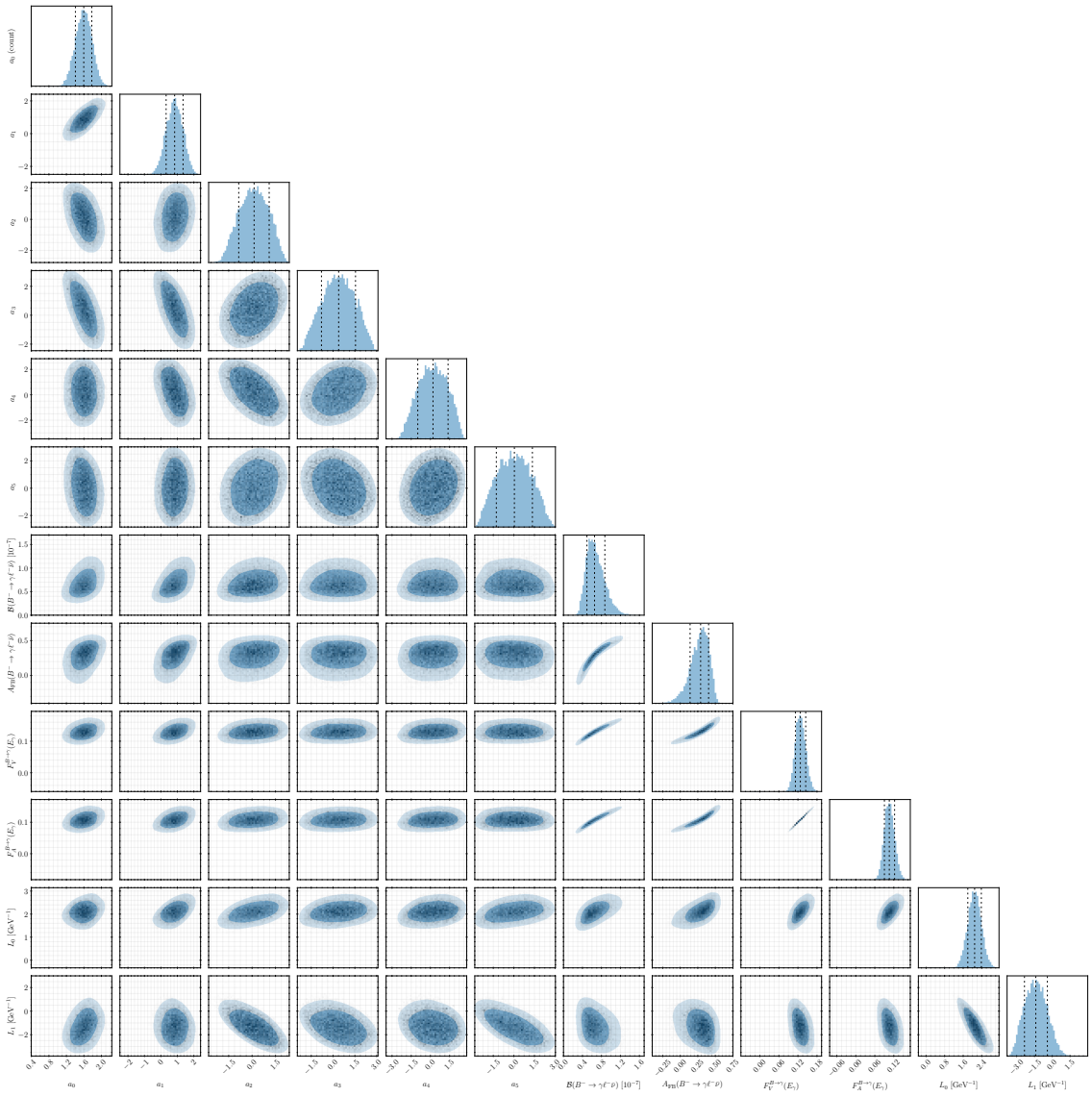

Figure C.8.: Corner plot of the posterior for $K = 5$, $\omega_0 = 0.8\,\text{GeV}$, and model for the parameter bound χ. It shows the LCDA parameters and predictions based on inputs from the OPE, mock data for the experimental observables, and data for L_0. Blue areas in the two-dimensional histograms indicate estimates of the 68 % and 95 % probability contours.

Acknowledgments

I thank my advisors, Danny van Dyk and Thorsten Feldmann, for scientific guidance, trust, and mentorship. It was a pleasure to work together on exciting and diverse problems in theoretical particle physics, software, and statistics. Engaging in this work at TU Munich and U Siegen, among some of the top researchers of the field, has been great. I thank Nicolas Seitz for the pleasant collaboration. Moreover, I thank Méril Reboud for many physics discussions, especially towards the final stages of this thesis.

Heartfelt thank yous are due to Vitalij Adam, Julian Günther, Stephan Kürten, Amélie Gonand, Méril Reboud (again), Peter Vander Griend, Daniel Greenwald, Vero Errasti Díez, Maria Laura Piscopo, Vlad Shtabovenko, Zac Wüthrich, Kevin Brune, Eleftheria Malami, and Marta Marchese: life's rich and wonderful.

I dedicate this thesis to my inspiring family.

Bibliography

[1] T. Feldmann, P. Lüghausen, and N. Seitz. "Strange-quark mass effects in the B_s meson's light-cone distribution amplitude". In: *JHEP* 08 (2023), p. 075. DOI: 10.1007/JHEP08(2023)075. arXiv: 2306.14686 [hep-ph] (cit. on pp. iii, 49).

[2] T. Feldmann, P. Lüghausen, and D. van Dyk. "Systematic parametrization of the leading B-meson light-cone distribution amplitude". In: *JHEP* 10 (2022), p. 162. DOI: 10.1007/JHEP10(2022)162. arXiv: 2203.15679 [hep-ph] (cit. on pp. iii, 7).

[3] D. van Dyk, P. Lüghausen, et al. "EOS: a software for flavor physics phenomenology". In: *Eur. Phys. J. C* 82.6 (2022), p. 569. DOI: 10.1140/epjc/s10052-022-10177-4. arXiv: 2111.15428 [hep-ph] (cit. on pp. iii, 81, 94, 99).

[4] T. Mannel. "Effective Field Theories in Flavor Physics". In: *Springer Tracts Mod. Phys.* 203 (2004), pp. 1–175. DOI: 10.1007/b62268 (cit. on pp. 3, 4).

[5] A. G. Grozin. "Heavy quark effective theory". In: *Springer Tracts Mod. Phys.* 201 (2004), pp. 1–213. DOI: 10.1007/b79301 (cit. on pp. 3, 4).

[6] M. D. Schwartz. *Quantum Field Theory and the Standard Model*. Cambridge University Press, 2014 (cit. on pp. 3, 4, 52, 63).

[7] M. Beneke, G. Buchalla, M. Neubert, and C. T. Sachrajda. "QCD factorization for $B \to \pi\pi$ decays: Strong phases and CP violation in the heavy quark limit". In: *Phys. Rev. Lett.* 83 (1999), pp. 1914–1917. DOI: 10.1103/PhysRevLett.83.1914. arXiv: hep-ph/9905312 [hep-ph] (cit. on pp. 5, 11).

[8] M. Beneke, G. Buchalla, M. Neubert, and C. T. Sachrajda. "QCD factorization in $B \to \pi K, \pi\pi$ decays and extraction of Wolfenstein parameters". In: *Nucl. Phys.* B606 (2001), pp. 245–321. DOI: 10.1016/S0550-3213(01)00251-6. arXiv: hep-ph/0104110 [hep-ph] (cit. on pp. 5, 11).

[9] W. Altmannshofer et al. "The Belle II Physics Book". In: *PTEP* 2019.12 (2019). Ed. by E. Kou and P. Urquijo. [Erratum: PTEP 2020, 029201 (2020)], p. 123C01. DOI: 10.1093/ptep/ptz106. arXiv: 1808.10567 [hep-ex] (cit. on pp. 5, 38, 50, 107).

[10] A. Khodjamirian, T. Mannel, and N. Offen. "B-meson distribution amplitude from the $B \to \pi$ form-factor". In: *Phys. Lett.* B620 (2005), pp. 52–60. DOI: 10.1016/j.physletb.2005.06.021. arXiv: hep-ph/0504091 [hep-ph] (cit. on pp. 5, 13).

[11] F. De Fazio, T. Feldmann, and T. Hurth. "Light-cone sum rules in soft-collinear effective theory". In: *Nucl. Phys.* B733 (2006). [Erratum: Nucl. Phys.B800,405(2008)], pp. 1–30. DOI: 10.1016/j.nuclphysb.2008.03.022,10.1016/j.nuclphysb.2005.09.047. arXiv: hep-ph/0504088 [hep-ph] (cit. on pp. 5, 13).

[12] A. Khodjamirian, T. Mannel, and N. Offen. "Form-factors from light-cone sum rules with B-meson distribution amplitudes". In: *Phys. Rev.* D75 (2007), p. 054013. DOI: 10.1103/PhysRevD.75.054013. arXiv: hep-ph/0611193 [hep-ph] (cit. on pp. 5, 13).

[13] F. De Fazio, T. Feldmann, and T. Hurth. "SCET sum rules for $B \to P$ and $B \to V$ transition form factors". In: *JHEP* 02 (2008), p. 031. DOI: 10.1088/1126-6708/2008/02/031. arXiv: 0711.3999 [hep-ph] (cit. on pp. 5, 13).

[14] M. Beneke and J. Rohrwild. "B meson distribution amplitude from $B \to \gamma\ell\bar{\nu}$". In: *Eur. Phys. J.* C71 (2011), p. 1818. DOI: 10.1140/epjc/s10052-011-1818-8. arXiv: 1110.3228 [hep-ph] (cit. on pp. 5, 82, 83, 85–87).

[15] V. M. Braun and A. Khodjamirian. "Soft contribution to $B \to \gamma\ell\nu_\ell$ and the B-meson distribution amplitude". In: *Phys. Lett.* B718 (2013), pp. 1014–1019. DOI: 10.1016/j.physletb.2012.11.047. arXiv: 1210.4453 [hep-ph] (cit. on pp. 5, 82).

[16] M. Beneke, V. M. Braun, Y. Ji, and Y.-B. Wei. "Radiative leptonic decay $B \to \gamma\ell\nu_\ell$ with subleading power corrections". In: (2018). arXiv: 1804.04962 [hep-ph] (cit. on pp. 5, 33, 35, 36, 82, 83, 85–88, 94, 102).

[17] M. Gelb et al. "Search for the rare decay of $B^+ \to \ell^+\nu_\ell\gamma$ with improved hadronic tagging". In: *Phys. Rev. D* 98.11 (2018), p. 112016. DOI: 10.1103/PhysRevD.98.112016. arXiv: 1810.12976 [hep-ex] (cit. on pp. 5, 38, 81).

[18] A. G. Grozin and M. Neubert. "Asymptotics of heavy meson form-factors". In: *Phys. Rev. D* 55 (1997), pp. 272–290. DOI: 10.1103/PhysRevD.55.272. arXiv: hep-ph/9607366 (cit. on pp. 8–10, 17, 25, 43, 51, 54, 76, 77).

[19] V. M. Braun, D. Y. Ivanov, and G. P. Korchemsky. "The B meson distribution amplitude in QCD". In: *Phys. Rev. D* 69 (2004), p. 034014. DOI: 10.1103/PhysRevD.69.034014. arXiv: hep-ph/0309330 (cit. on pp. 9, 10).

[20] A. G. Grozin and G. P. Korchemsky. "Renormalized sum rules for structure functions of heavy mesons decays". In: *Phys. Rev. D* 53 (1996), pp. 1378–1390. DOI: 10.1103/PhysRevD.53.1378. arXiv: hep-ph/9411323 (cit. on p. 9).

[21] B. O. Lange and M. Neubert. "Renormalization group evolution of the B meson light cone distribution amplitude". In: *Phys. Rev. Lett.* 91 (2003), p. 102001. DOI: 10.1103/PhysRevLett.91.102001. arXiv: hep-ph/0303082 (cit. on pp. 9, 10, 12).

[22] R. S. Strichartz. *A Guide To Distribution Theory And Fourier Transforms*. CRC Press, 2003 (cit. on p. 9).

[23] G. Bell, T. Feldmann, Y.-M. Wang, and M. W. Y. Yip. "Light-Cone Distribution Amplitudes for Heavy-Quark Hadrons". In: *JHEP* 11 (2013), p. 191. DOI: 10.1007/JHEP11(2013)191. arXiv: 1308.6114 [hep-ph] (cit. on pp. 10–12).

[24] V. M. Braun and A. N. Manashov. "Conformal symmetry of the Lange-Neubert evolution equation". In: *Phys. Lett. B* 731 (2014), pp. 316–319. DOI: 10.1016/j.physletb.2014.02.051. arXiv: 1402.5822 [hep-ph] (cit. on p. 10).

[25] V. M. Braun, Y. Ji, and A. N. Manashov. "Two-loop evolution equation for the B-meson distribution amplitude". In: *Phys. Rev. D* 100.1 (2019), p. 014023. DOI: 10.3204/PUBDB-2019-02451. arXiv: 1905.04498 [hep-ph] (cit. on pp. 11, 22).

[26] T. Feldmann, B. O. Lange, and Y.-M. Wang. "B-meson light-cone distribution amplitude: Perturbative constraints and asymptotic behavior in dual space". In: *Phys. Rev.* D89.11 (2014), p. 114001. DOI: 10.1103/PhysRevD.89.114001. arXiv: 1404.1343 [hep-ph] (cit. on pp. 11, 29).

[27] A. M. Galda and M. Neubert. "Evolution of the B-Meson Light-Cone Distribution Amplitude in Laplace Space". In: *Phys. Rev. D* 102 (2020), p. 071501. DOI: 10.1103/PhysRevD.102.071501. arXiv: 2006.05428 [hep-ph] (cit. on pp. 12, 13).

[28] H. Kawamura and K. Tanaka. "Evolution equation for the B-meson distribution amplitude in the heavy-quark effective theory in coordinate space". In: *Phys. Rev. D* 81 (2010), p. 114009. DOI: 10.1103/PhysRevD.81.114009. arXiv: 1002.1177 [hep-ph] (cit. on p. 12).

[29] I. Caprini. *Functional Analysis and Optimization Methods in Hadron Physics*. SpringerBriefs in Physics. Springer, 2019. DOI: 10.1007/978-3-030-18948-8 (cit. on p. 15).

[30] H. Kawamura, J. Kodaira, C.-F. Qiao, and K. Tanaka. "B-meson light cone distribution amplitudes in the heavy quark limit". In: *Phys. Lett.* B523 (2001). [Erratum: Phys. Lett.B536,344(2002)], p. 111. DOI: 10.1016/S0370-2693(01)01299-0,10.1016/S0370-2693(02)01866-X. arXiv: hep-ph/0109181 [hep-ph] (cit. on pp. 23, 32).

[31] V. M. Braun, Y. Ji, and A. N. Manashov. "Higher-twist B-meson Distribution Amplitudes in HQET". In: *JHEP* 05 (2017), p. 022. DOI: 10.1007/JHEP05(2017)022. arXiv: 1703.02446 [hep-ph] (cit. on pp. 23, 24, 119).

[32] S. Descotes-Genon and N. Offen. "Three-particle contributions to the renormalisation of B-meson light-cone distribution amplitudes". In: *JHEP* 05 (2009), p. 091. DOI: 10.1088/1126-6708/2009/05/091. arXiv: 0903.0790 [hep-ph] (cit. on p. 23).

[33] G. Bell and T. Feldmann. "Modelling light-cone distribution amplitudes from non-relativistic bound states". In: *JHEP* 04 (2008), p. 061. DOI: 10.1088/1126-6708/2008/04/061. arXiv: 0802.2221 [hep-ph] (cit. on pp. 23, 54, 56, 60–63, 77).

[34] M. Beneke and T. Feldmann. "Symmetry breaking corrections to heavy to light B meson form-factors at large recoil". In: *Nucl. Phys. B* 592 (2001), pp. 3–34. DOI: 10.1016/S0550-3213(00)00585-X. arXiv: hep-ph/0008255 (cit. on pp. 23, 54).

[35] S. J. Lee and M. Neubert. "Model-independent properties of the B-meson distribution amplitude". In: *Phys. Rev. D* 72 (2005), p. 094028. DOI: 10.1103/PhysRevD.72.094028. arXiv: hep-ph/0509350 (cit. on pp. 28–30, 32, 43, 44, 49, 53, 78, 100).

[36] A. Heller et al. "Search for $B^+ \to \ell^+ \nu_\ell \gamma$ decays with hadronic tagging using the full Belle data sample". In: *Phys. Rev. D* 91.11 (2015), p. 112009. DOI: 10.1103/PhysRevD.91.112009. arXiv: 1504.05831 [hep-ex] (cit. on p. 38).

[37] H. Kawamura and K. Tanaka. "Operator product expansion for B-meson distribution amplitude and dimension-5 HQET operators". In: *Phys. Lett. B* 673 (2009), pp. 201–207. DOI: 10.1016/j.physletb.2009.02.028. arXiv: 0810.5628 [hep-ph] (cit. on pp. 42, 49, 52, 55, 77, 99, 100).

[38] M. Beneke and M. Neubert. "QCD factorization for $B \to PP$ and $B \to PV$ decays". In: *Nucl. Phys. B* 675 (2003), pp. 333–415. DOI: 10.1016/j.nuclphysb.2003.09.026. arXiv: hep-ph/0308039 (cit. on p. 50).

[39] A. R. Williamson and J. Zupan. "Two body B decays with isosinglet final states in SCET". In: *Phys. Rev. D* 74 (2006). [Erratum: Phys.Rev.D 74, 03901 (2006)], p. 014003. DOI: 10.1103/PhysRevD.74.014003. arXiv: hep-ph/0601214 (cit. on p. 50).

[40] H.-Y. Cheng and C.-K. Chua. "QCD Factorization for Charmless Hadronic B_s Decays Revisited". In: *Phys. Rev. D* 80 (2009), p. 114026. DOI: 10.1103/PhysRevD.80.114026. arXiv: 0910.5237 [hep-ph] (cit. on p. 50).

[41] T. Huber and G. Tetlalmatzi-Xolocotzi. "Estimating QCD-factorization amplitudes through SU(3) symmetry in $B \to PP$ decays". In: *Eur. Phys. J. C* 82.3 (2022), p. 210. DOI: 10.1140/epjc/s10052-022-10068-8. arXiv: 2111.06418 [hep-ph] (cit. on p. 50).

[42] A. Ali, B. D. Pecjak, and C. Greub. "$B \to$ V γ Decays at NNLO in SCET". In: *Eur. Phys. J. C* 55 (2008), pp. 577–595. DOI: 10.1140/epjc/s10052-008-0623-5. arXiv: 0709.4422 [hep-ph] (cit. on p. 50).

[43] M. Beneke, C. Bobeth, and Y.-M. Wang. "$B_{d,s} \to \gamma \ell \bar{\ell}$ decay with an energetic photon". In: *JHEP* 12 (2020), p. 148. DOI: 10.1007/JHEP12(2020)148. arXiv: 2008.12494 [hep-ph] (cit. on p. 50).

[44] R. Aaij et al. "Implications of LHCb measurements and future prospects". In: *Eur. Phys. J. C* 73.4 (2013), p. 2373. DOI: 10.1140/epjc/s10052-013-2373-2. arXiv: 1208.3355 [hep-ex] (cit. on p. 50).

[45] T. Feldmann, N. Gubernari, T. Huber, and N. Seitz. "Contribution of the electromagnetic dipole operator O_7 to the $B_s \to \mu^+\mu^-$ decay amplitude". In: *Phys. Rev. D* 107.1 (2023), p. 013007. DOI: 10.1103/PhysRevD.107.013007. arXiv: 2211.04209 [hep-ph] (cit. on p. 50).

[46] M. Neubert. "Symmetry breaking corrections to meson decay constants in the heavy quark effective theory". In: *Phys. Rev. D* 46 (1992), pp. 1076–1087. DOI: 10.1103/PhysRevD.46.1076 (cit. on p. 54).

[47] A. G. Grozin. "B-meson distribution amplitudes". In: *Int. J. Mod. Phys. A* 20 (2005), pp. 7451–7484. DOI: 10.1142/S0217751X05028570. arXiv: hep-ph/0506226 (cit. on pp. 59, 121).

[48] R. L. Workman et al. "Review of Particle Physics". In: *PTEP* 2022 (2022), p. 083C01. DOI: 10.1093/ptep/ptac097 (cit. on pp. 70, 74, 78, 102).

[49] A. Khodjamirian, R. Mandal, and T. Mannel. "Inverse moment of the B_s-meson distribution amplitude from QCD sum rule". In: *JHEP* 10 (2020), p. 043. DOI: 10.1007/JHEP10(2020)043. arXiv: 2008.03935 [hep-ph] (cit. on pp. 71–73, 111).

[50] F. Herren and M. Steinhauser. "Version 3 of RunDec and CRunDec". In: *Comput. Phys. Commun.* 224 (2018), pp. 333–345. DOI: 10.1016/j.cpc.2017.11.014. arXiv: 1703.03751 [hep-ph] (cit. on p. 74).

[51] M. Rahimi and M. Wald. "QCD sum rules for parameters of the B-meson distribution amplitudes". In: *Phys. Rev. D* 104.1 (2021), p. 016027. DOI: 10.1103/PhysRevD.104.016027. arXiv: 2012.12165 [hep-ph] (cit. on pp. 78, 100).

[52] R. Aaij et al. "Search for the rare decay $B^+ \to \mu^+\mu^-\mu^+\nu_\mu$". In: *Eur. Phys. J. C* 79.8 (2019), p. 675. DOI: 10.1140/epjc/s10052-019-7112-x. arXiv: 1812.06004 [hep-ex] (cit. on p. 81).

[53] M. Beneke, P. Böer, P. Rigatos, and K. K. Vos. "QCD factorization of the four-lepton decay $B^- \to \ell\bar{\nu}_\ell\ell^{(\prime)}\bar{\ell}^{(\prime)}$". In: *Eur. Phys. J. C* 81.7 (2021), p. 638. DOI: 10.1140/epjc/s10052-021-09388-y. arXiv: 2102.10060 [hep-ph] (cit. on p. 81).

[54] S. Kürten, M. Zanke, B. Kubis, and D. van Dyk. "Dispersion relations for $B^- \to \ell^-\overline{\nu}_\ell\ell'^-\ell'^+$ form factors". In: *Phys. Rev. D* 107.5 (2023), p. 053006. DOI: 10.1103/PhysRevD.107.053006. arXiv: 2210.09832 [hep-ph] (cit. on pp. 81, 83, 84).

[55] M. A. Ivanov and D. Melikhov. "Theoretical analysis of the leptonic decays B$\to\ell\ell\ell\nu^-\ell$: Identical leptons in the final state". In: *Phys. Rev. D* 105.9 (2022), p. 094038. DOI: 10.1103/PhysRevD.105.094038. arXiv: 2204.02792 [hep-ph] (cit. on p. 81).

[56] G. Burdman, J. T. Goldman, and D. Wyler. "Radiative leptonic decays of heavy mesons". In: *Phys. Rev. D* 51 (1995), pp. 111–117. DOI: 10.1103/PhysRevD.51.111. arXiv: hep-ph/9405425 (cit. on p. 81).

[57] G. P. Korchemsky, D. Pirjol, and T.-M. Yan. "Radiative leptonic decays of B mesons in QCD". In: *Phys. Rev. D* 61 (2000), p. 114510. DOI: 10.1103/PhysRevD.61.114510. arXiv: hep-ph/9911427 (cit. on p. 82).

[58] S. Descotes-Genon and C. T. Sachrajda. "Factorization, the light cone distribution amplitude of the B meson and the radiative decay $B \to \gamma\ell\nu_\ell$". In: *Nucl. Phys. B* 650 (2003), pp. 356–390. DOI: 10.1016/S0550-3213(02)01066-0. arXiv: hep-ph/0209216 (cit. on p. 82).

[59] E. Lunghi, D. Pirjol, and D. Wyler. "Factorization in leptonic radiative B $\to \gamma e\nu$ decays". In: *Nucl. Phys. B* 649 (2003), pp. 349–364. DOI: 10.1016/S0550-3213(02)01032-5. arXiv: hep-ph/0210091 (cit. on pp. 82, 86).

[60] S. W. Bosch, R. J. Hill, B. O. Lange, and M. Neubert. "Factorization and Sudakov resummation in leptonic radiative B decay". In: *Phys. Rev. D* 67 (2003), p. 094014. DOI: 10.1103/PhysRevD.67.094014. arXiv: hep-ph/0301123 (cit. on pp. 82, 85, 86).

[61] C. W. Bauer, D. Pirjol, and I. W. Stewart. "Soft collinear factorization in effective field theory". In: *Phys. Rev. D* 65 (2002), p. 054022. DOI: 10.1103/PhysRevD.65.054022. arXiv: hep-ph/0109045 (cit. on p. 82).

[62] C. W. Bauer, S. Fleming, D. Pirjol, I. Z. Rothstein, and I. W. Stewart. "Hard scattering factorization from effective field theory". In: *Phys. Rev. D* 66 (2002), p. 014017. DOI: 10.1103/PhysRevD.66.014017. arXiv: hep-ph/0202088 (cit. on p. 82).

[63] R. J. Hill and M. Neubert. "Spectator interactions in soft collinear effective theory". In: *Nucl. Phys. B* 657 (2003), pp. 229–256. DOI: 10.1016/S0550-3213(03)00116-0. arXiv: hep-ph/0211018 (cit. on p. 82).

[64] Y.-M. Wang. "Factorization and dispersion relations for radiative leptonic B decay". In: *JHEP* 09 (2016), p. 159. DOI: 10.1007/JHEP09(2016)159. arXiv: 1606.03080 [hep-ph] (cit. on pp. 82, 83, 87).

[65] Y.-L. Shen, Z.-T. Zou, and Y.-B. Wei. "Subleading power corrections to $B \to \gamma l\nu$ decay in PQCD approach". In: *Phys. Rev. D* 99.1 (2019), p. 016004. DOI: 10.1103/PhysRevD.99.016004. arXiv: 1811.08250 [hep-ph] (cit. on p. 83).

[66] Y.-L. Shen, Y.-B. Wei, X.-C. Zhao, and S.-H. Zhou. "Revisiting radiative leptonic B decay". In: *Chin. Phys. C* 44.12 (2020), p. 123106. DOI: 10.1088/1674-1137/abb6df. arXiv: 2009.03480 [hep-ph] (cit. on p. 83).

[67] B.-Y. Cui, Y.-L. Shen, C. Wang, and Y.-B. Wei. "QCD factorization for the $B \to \gamma\ell\nu_\ell$ decay beyond leading power". In: (2023). arXiv: 2308.16436 [hep-ph] (cit. on pp. 83, 86).

[68] A. Khodjamirian. *Hadron Form Factors: From Basic Phenomenology to QCD Sum Rules*. Boca Raton, FL, USA: CRC Press, Taylor & Francis Group, 2020 (cit. on p. 83).

[69] A. Khodjamirian and D. Wyler. "Counting contact terms in $B \to V$ gamma decays". In: (2001). DOI: 10.1142/9789812777478_0014. arXiv: hep-ph/0111249 (cit. on p. 83).

[70] C. W. Bauer, S. Fleming, D. Pirjol, and I. W. Stewart. "An Effective field theory for collinear and soft gluons: Heavy to light decays". In: *Phys. Rev. D* 63 (2001), p. 114020. DOI: 10.1103/PhysRevD.63.114020. arXiv: hep-ph/0011336 (cit. on p. 85).

[71] I. I. Balitsky, V. M. Braun, and A. V. Kolesnichenko. "Radiative Decay $\sigma^+ \to p\gamma$ in Quantum Chromodynamics". In: *Nucl. Phys. B* 312 (1989), pp. 509–550. DOI: 10.1016/0550-3213(89)90570-1 (cit. on p. 87).

[72] S. Roman. *The Umbral Calculus*. Dover Books on Mathematics. Dover Publications, 2005 (cit. on p. 89).

[73] B. Nijholt, J. Weston, J. Hoofwijk, and A. Akhmerov. *Adaptive: parallel active learning of mathematical functions*. 2019. DOI: 10.5281/zenodo.1182437 (cit. on p. 97).

[74] J. S. Speagle. "dynesty: a dynamic nested sampling package for estimating Bayesian posteriors and evidences". In: *Monthly Notices of the Royal Astronomical Society* 493.3 (2020), pp. 3132–3158. DOI: 10.1093/mnras/staa278 (cit. on p. 99).

[75] S. Koposov, J. Speagle, K. Barbary, G. Ashton, E. Bennett, J. Buchner, C. Scheffler, B. Cook, C. Talbot, J. Guillochon, P. Cubillos, A. A. Ramos, B. Johnson, D. Lang, Ilya, M. Dartiailh, A. Nitz, A. McCluskey, and A. Archibald. *joshspeagle/dynesty: v2.1.3*. Version v2.1.3. 2023. DOI: 10.5281/zenodo.8408702 (cit. on p. 99).

[76] E. Higson, W. Handley, M. Hobson, and A. Lasenby. "Dynamic nested sampling: an improved algorithm for parameter estimation and evidence calculation". In: *Statistics and Computing* 29.5 (2018), pp. 891–913. DOI: 10.1007/s11222-018-9844-0 (cit. on p. 99).

[77] S. Aoki et al. "Review of lattice results concerning low-energy particle physics". In: *Eur. Phys. J. C* 77.2 (2017), p. 112. DOI: 10.1140/epjc/s10052-016-4509-7. arXiv: 1607.00299 [hep-lat] (cit. on p. 102).

[78] D. Giusti, C. F. Kane, C. Lehner, S. Meinel, and A. Soni. "Methods for high-precision determinations of radiative-leptonic decay form factors using lattice QCD". In: *Phys. Rev. D* 107.7 (2023), p. 074507. DOI: 10.1103/PhysRevD.107.074507. arXiv: 2302.01298 [hep-lat] (cit. on p. 115).

[79] R. Frezzotti, N. Tantalo, G. Gagliardi, F. Sanfilippo, S. Simula, V. Lubicz, F. Mazzetti, G. Martinelli, and C. T. Sachrajda. "Lattice calculation of the D_s meson radiative form factors over the full kinematical range". In: *Phys. Rev. D* 108.7 (2023), p. 074505. DOI: 10.1103/PhysRevD.108.074505. arXiv: 2306.05904 [hep-lat] (cit. on p. 115).

[80] R. Frezzotti, G. Gagliardi, V. Lubicz, G. Martinelli, C. T. Sachrajda, F. Sanfilippo, S. Simula, and N. Tantalo. "The $B_s \to \mu^+\mu^-\gamma$ decay rate at large q^2 from lattice QCD". In: (2024). arXiv: 2402.03262 [hep-lat] (cit. on p. 115).

[81] M. Neubert. "Renormalization-group improved calculation of the $B \to X(s)$ gamma branching ratio". In: *Eur. Phys. J. C* 40 (2005), pp. 165–186. DOI: 10.1140/epjc/s2005-02141-1. arXiv: hep-ph/0408179 (cit. on p. 119).